LARGE EDDY SIMULATION, PARTICLE IMAGE VELOCIMETRY IN THE STUDY OF MOLD TRANSIENTS IN CONTINUOUS CASTING OF STEEL AND HEAT TRANSFER THROUGH MOLTEN SLAG LAYERS

BY

SIVARAJ SIVARAMAKRISHNAN

B.Engr., University of Poona, 1998

THESIS

Submitted in partial fulfillment of the requirements
for the degree of Master of Science in Mechanical Engineering
in the Graduate College of the
University of Illinois at Urbana-Champaign, 2000

Urbana, Illinois

ABSTRACT

This thesis studies the fluid flow and heat transfer in the mold of a continuous caster in an attempt to better understand the process and prevent defect formation. The flow transients, which can significantly influence formation of defects have been quantified using Particle Image Velocimetry (PIV) and Large Eddy Simulations (LES) of the mold flow in a water model of a continuous caster. PIV measurements were done in the central wide face plane at LTV Steel (Cleveland, OH). For the simulations the Navier-Stokes equations were discretized using a fractional step procedure on a 1.5 million cell grid. The Smagorinsky model accounts for sub grid scale diffusion, although for the Reynolds number and grid fineness used its activation was not found necessary. The slide gate creates a strong swirl at the outlet ports of the nozzle, which is seen to persist more than halfway across the mold, causing a characteristic staircase velocity vector pattern in the PIV measurements when viewed in a plane parallel to the wide faces. Flow across the top surface was found in PIV to contain periods of 5-10s when the velocities were three to four times their mean values. This is likely related to inlet conditions and would likely exacerbate shear entrainment of the liquid flux at the top surface and level fluctuations. Simulations of the MFC output indicate that accurate flow prediction is not possible unless the sensors are located in a region of relatively uniform flow, such as near the top surface. In both LES and PIV, the upper roll structure evolves chaotically between a single large recirculation structure and a set of distinct vortices. The lower rolls in PIV are significantly asymmetric for very long periods of time (around 1-hour) and go through a repeating sequence of features. One of these features involves a short circuit between the upward and downward flow in the lower roll, which is also seen in the simulation. This appears to be inherent to the turbulent nature of the flow and is likely important to inclusion particle and bubble entrapment. Finite element simulations of the fluid flow and heat transfer of the liquid flux layer of a caster with natural convection effects were done using the commercial finite element software package FIDAP. A detailed parametric study was done to quantify the individual effects of flux properties and casting conditions. Over certain ranges, natural convection was found to substantially affect the fluid flow and heat transfer in liquid flux layers of continuous casters. For a given set of flux properties and caster dimensions a critical steel-flux interface velocity was identified beyond which natural convection no longer affects the fluid flow and heat transfer. The steel-flux interface velocity was correlated to the bulk velocity of steel flow beneath the liquid flux layer to facilitate reference of results.

ACKNOWLEDGEMENTS

I would like to express my sincere gratitude to my advisors Professor B.G. Thomas and Professor S.P. Vanka for their guidance and support throughout the course of this work. The work on this project was supported by the National Science Foundation. The computations for this project were done on the Origin 2000 machines at the National Center for Supercomputing Applications (NCSA) at UIUC. The commercial finite element software package FIDAP (v 7.5.2) by Fluid Dynamics International was used for simulating the slag layer flow. The support of these organizations is gratefully acknowledged.

I would like to thank Dr. Mohammad Assar, Dr. Pierre Dauby, Joe Sand and the technicians at LTV Steel (Cleveland, OH) for their help and guidance in the PIV measurements. Thanks are also extended to my lab mates, past and present, Dr. Aniruddha Mukhopadhyay, Prem Venugopal, Sarma Rani and Hua Bai whose help, guidance and company have made this a thoroughly enjoyable experience.

Last but not the least I am grateful to my parents and my brother to whom I owe all that I have accomplished.

TABLE OF CONTENTS

LIST OF TABLES

LIST OF FIGURES

NOMENCLATURE

A	Ratio of domain length to domain thickness
B	Ratio of domain length to domain depth
C_S	Smagorinsky constant
C_P	Specific Heat (J/kgK)
g	Gravitational acceleration (m/s^2)
Gr	Grashoff number = $rgb\Delta TH^3/n^2$
H	Liquid layer thickness(m) / Characteristic length
k	Thermal conductivity of fluid (W/mK)
k_R	Radiational thermal conductivity of fluid = $16\sigma\, n^2\, T^3 / 3\alpha$ (W/mK)
K	Turbulence kinetic energy (m^2/ s^2)
m	Von-Karman constant = 0.4
n	Refractive index
Nu	Nusselt Number (at y = C) = $(-(dT/dy)\|_{y\,=\,C}) / ((T_h-T_c)/H)$
Nu_R	Right Peak Nusselt number
Nu_{avg}	Average Nusselt number over top/bottom of liquid layer
p	Pressure at any point in the domain (N/m^2)
$\bar{p}$	Pressure at any point in the domain (N/m^2)
p*	Non-dimensional pressure gradient at any point in domain
Pr	Prandtl Number = n/α
Q_{cond}	Conduction heat transfer (W/m^2)
Q_{conv}	Convective heat transfer (W/m^2)
Ra	Rayleigh Number = $rgb\Delta TH^3/ua$

Ra_c	Critical Ra for onset of natural convection (Ra_c = 1707)
RF	Relaxation factor for successive substitution technique
R	Root mean square error in discretized finite element equations at any iteration
t	Time (s)
T	Temperature (K)
T_c	Temperature of top wall (K)
T_h	Temperature of bottom wall (K)
u	Velocity component in x direction at any point in domain (m/s)
u^+	Non-dimensional velocity in boundary layer = u/($\sqrt{\frac{t_o}{r}}$)
u*	Non-dimensional horizontal velocity at any point in domain
$\overline{u}_i, (i = 1,3)$	Filtered velocity components for Large Eddy Simulation (m/s)
$\overline{\tilde{u}}_i, (i = 1,3)$	Intermediate filtered velocity components for Large Eddy Simulation (m/s)
U	Imposed horizontal bottom velocity (m/s)
U_c	U at which multiple natural convection cells are annihilated (m/s)
U_o	Characteristic velocity based on natural convection = $\sqrt{gb\Delta TH / an}$ (m/s)
v	Velocity component in y direction at any point in domain (m/s)
v*	Non-dimensional vertical velocity at any point in domain
V_x	Horizontal velocity at any point in domain (m/s)
V_y	Vertical velocity at any point in domain (m/s)
V	Speed at any point in domain = $\sqrt{V_x{}^2 + V_y{}^2}$ (m/s)
V_o	Steel bulk velocity (m/s)
w	Velocity component in z direction at any point in domain (m/s)

W	Wideface width (m)
x	Coordinate direction, horizontal distance from left side wall (m)
y	Coordinate direction, vertical distance above bottom layer (m)
y^+	Non-dimensional distance from boundary within boundary layer = $y/(\frac{m}{\sqrt{t_o r}})$
z	Coordinate direction

Greek Symbols

α	Absorption coefficient
β	Volumetric expansion coefficient (K^{-1})
Δ	Filter width (m) for Large Eddy Simulation
Δ_x, Δ_y, Δ_z	Mesh sizes in three coordinate directions (m)
ΔT	Temperature difference across layer (K) / Characteristic temperature (K)
ε	Turbulent dissipation (m^2/ s^3)
Θ	Non-dimensional temperature at any point in domain
μ	Molecular viscosity (Pa-s)
ν	Kinematic viscosity (m^2/s)
ν_T	Turbulent viscosity (m^2/s)
Φ	Velocity and temperature interpolation function
Ψ	Pressure interpolation function
ρ	Density of the fluid (kg/m^3)
σ	Stefan Boltzmann constant = 5.67×10^{-8} W/m^2 K
τ_o	Characteristic shear stress (N/m^2) = $\mu U_o/H$

τ_b	Average shear stress over bottom of liquid flux layer (N/m^2)
τ_t	Average shear stress over top of liquid flux layer (N/m^2)

CHAPTER 1. INTRODUCTION

Continuous casting is used to solidify most of the several hundred million tons of steel produced in the world every year. Continuous casting of steel is a very complex process involving transport and two-phase flow. Figure 1.1 shows a representative picture of the continuous casting process. Molten steel flows from a ladle through a tundish into the mold. The flow from the tundish into the nozzle is turbulent and has a high Reynolds number, around 100,000. Flow through the submerged nozzle is gravity driven by the pressure difference between the liquid levels of the tundish and the mold free surface. In practice the flow into the nozzle is controlled either by a "stopper rod " or by a "slide gate". These flow control devices strongly influence the flow pattern in the nozzle and beyond. Argon gas is injected into the nozzle to prevent clogging. The resulting bubbles provide buoyancy that greatly affects the flow pattern both in the nozzle and the mold. The jet leaving the nozzle flows across the mold and impinges against the shell, solidifying at the narrow face. Here, the heat transfer is due to oblique impingement of the fluid, with the jet bifurcating into an upper wall jet and a lower wall jet. The jet carries superheat, which can erode the shell where it impinges on locally thin regions.

The upward flowing wall-jet travels towards the free surface, and may become transitional or laminar. Mold flux powder is added on the liquid steel surface from the open upper end of the mold. The melting point of this powder ranges from 800-1200^{o}C and is lower than the temperature of the liquid steel below (> 1550^{o}C). Thus the mold powder absorbs heat from the molten steel below, sinters and melts to form a liquid flux layer above the molten steel surface. A vertical cross section through the mold, Figure 1.1, reveals powder, sintered and liquid layers above the molten steel surface. The slag layer has much lower thermal conductivity than steel or the copper mold providing thermal insulation. In addition the slag layer provides chemical insulation to the steel by preventing the steel from contacting the atmosphere causing oxidation. The liquid flux layer absorbs alumina particles, added in the form of aluminum for deoxidizing steel. It also absorbs argon gas added in the nozzle and vents the gas to the atmosphere. Otherwise these would penetrate deep into the mold and form inclusions. The liquid flux infiltrates into the gap between the solidifying steel shell and the mold and lubricates the interface. Here it flows into air gaps and promotes low but uniform heat transfer in the mold-strand gap. The large temperature difference across the liquid flux layer coupled with temperature dependent density results in buoyancy driven convection, the strength of which depends on the flux properties and process variables. The presence of natural convection can significantly alter the fluid flow and heat transfer through the liquid flux layer. The horizontal velocity along the interface induces flow and controls heat transfer in the liquid and solid flux layers, which float on the top free surface. Beneath the jet, a large recirculation region is formed, which may be also transitional or mildly turbulent.

This flow pattern changes radically with increasing argon injection rate and with the application of electromagnetic forces used to brake and stir the liquid. The flow pattern can fluctuate with time, leading to defects, so transient behaviour is important. Lower in the caster, fluid flow is driven by thermal and solutal buoyancy effects, caused by density differences between the different compositions created by microsegregation. This flow leads to macrosegregation and associated defects such as centerline porosity, cracks and undesired property variations. Thus understanding the detailed fluid flow and heat transfer phenomena is of considerable importance to defect reduction in continuous casting.

Much of the previous analyses of the flow in the mold region and in the nozzle have been carried out using the Reynolds-averaged approach, which accounts for the turbulent mixing and momentum transport and solves for a mean flow field. However, as mentioned above, most of the phenomena which lead to defect formation are transient and cannot be predicted and hence controlled by a steady state approach. Among the various approaches to study transient fluid flow, those prominent include Large Eddy Simulation (LES) modeling, Particle Image Velocimetry (PIV) measurements in water models, unsteady Reynolds averaged modeling and using electromagnetic point velocity sensors on the actual caster. Unsteady Reynolds averaged modeling has been done by Huang and Thomas [1] and the significant results are discussed in chapter 2. In addition to mold flow the fluid flow and heat transfer in the liquid flux layer also controls defects such as surface and subsurface inclusions, non-uniform shell growth, sub-surface depressions, cracks and breakouts. The work of McDavid and Thomas [2] is one of the few studies of fluid flow and heat transfer through the liquid flux layer. The effect of natural convection, in the presence of shear from the steel flow beneath has not been investigated so far.

The present work aims to study the fluid flow and heat transfer in different parts of the continuous casting mold, in an attempt to better understand the process and prevent defect formation. First the transient fluid flow in the mold region of a water model of a continuous caster has been studied using PIV measurements. The fluid flow in the mold is also simulated using the LES approach. Signal outputs from an electromagnetic sensor mounted on a caster, on which the water model is based, provide further information about the transient flow in the mold region. The results of these three approaches with respect to the mean flow, turbulent statistics and flow transients are analyzed individually and together to get insight into the various transient phenomena in the mold region. The comparisons also serve to validate the LES approach and provide insight into the sensor predictions. Next the fluid flow and heat transfer in the liquid flux layer are simulated using a finite element approach, in the presence of natural convection effects and shear from the steel flow beneath. Parametric studies have been conducted to simulate a wide range of flux properties and casting conditions. The liquid flux layer in the caster is representative of slag layers in numerous materials processing applications. Hence the results are first analyzed from a fundamental standpoint, as applicable to slag layers in general. Following this, the specific implications of the results, to the flow and heat transfer in the continuous casting liquid flux layers and hence steel quality, are studied.

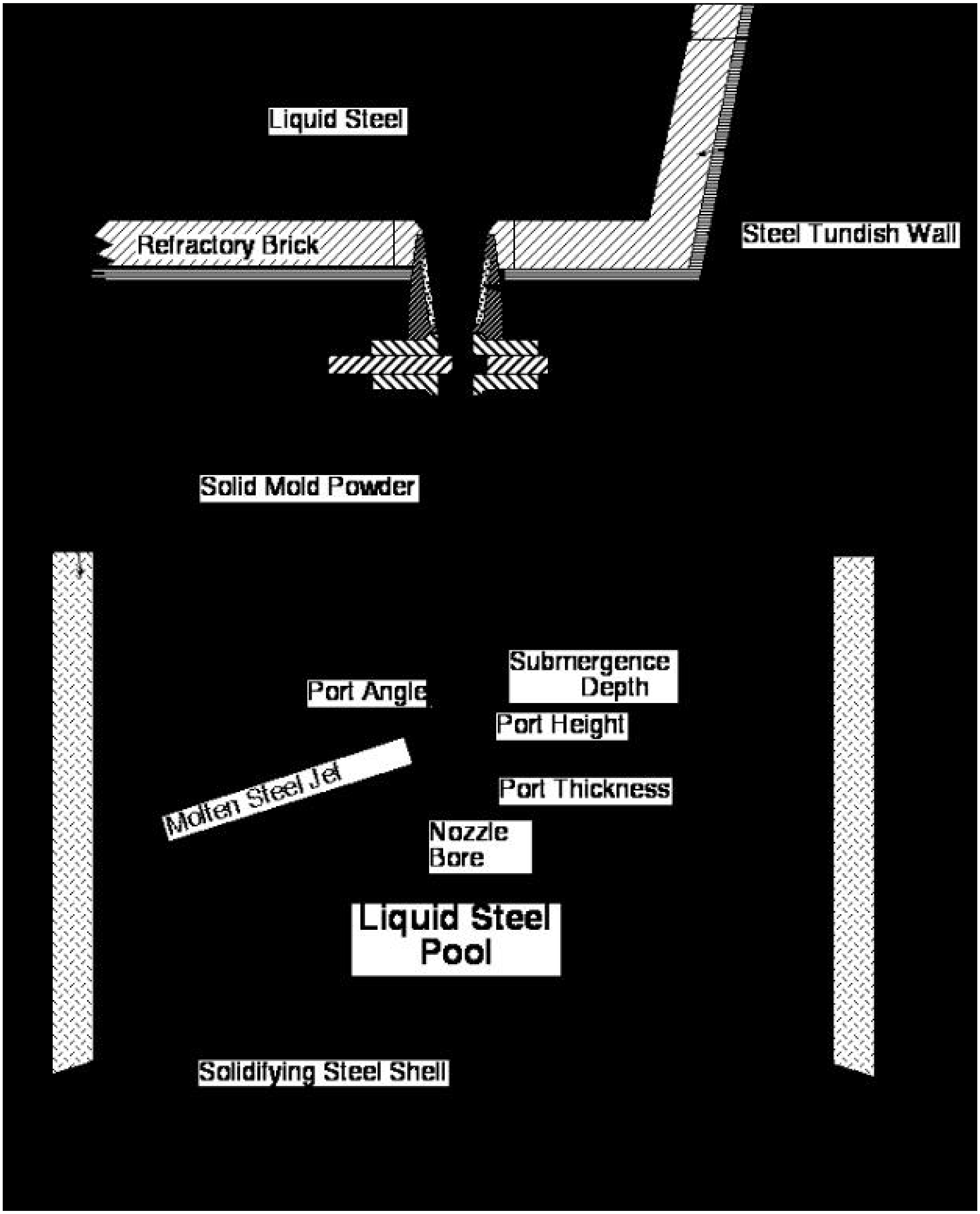

Figure 1.1 Schematic of continuous casting tundish, slide-gate nozzle, and mold

CHAPTER 2. STUDY OF FLOW TRANSIENTS IN CONTINUOUS CASTING USING PARTICLE IMAGE VELOCIMETRY MEASUREMENTS IN WATER MODELS

2.1 Introduction

Flow in the mold region during the continuous casting of steel is of great interest because it influences many important phenomena, which have far-reaching consequences on strand quality. These include the flow and entrainment of the top surface powder/flux layer, top-surface contour and level fluctuations, and the entrapment of subsurface inclusions and gas bubbles. Shear entrainment of the liquid flux layer is related to the top surface velocity, which in turn increases with the casting speed or inlet velocity [3-5]. Beyond a certain casting speed a surface discontinuity occurs which would result in emulsification between the liquid steel and the liquid flux layer [4]. After solidification the entrapped low strength flux would decrease the steel strength. The top surface velocity will be influenced by the presence of transient flow structures in the upper roll region, which have yet to be studied. Argon gas injected to reduce nozzle clogging needs to be aspirated through the liquid flux layer. If not, the bubbles get entrapped in the solidifying steel causing voids, which reduce the steel strength. Thomas et al [6] used a steady state numerical model to study the effect of argon injection on the fluid flow and heat transfer in continuous casting molds. Gas volume fraction distributions were used to predict bubble penetration for different bubble sizes and inlet gas volume fractions, which can then be correlated to possible bubble entrapment. Considering that the mold flow is transient and turbulent, involving asymmetries and oscillations [7, 8] the effect of flow transients on bubble entrapment needs to be investigated. The momentum of the flow along the narrowface and turbulent flow beneath the top surface cause local fluctuations in the location of the steel-flux interface. Huang and Thomas [1] simulated the fluid flow using a Reynolds averaged approach, with the steel-flux interface replaced by a rigid wall boundary. They found a good correlation between the level fluctuations in experiments and the top surface kinetic energy in simulations. The level fluctuations could prevent smooth flow of liquid flux into the shell-mold gap, reducing the lubrication and increased heat transfer provided by the liquid flux. This would increase the thermal stresses in the shell and friction between the shell and the mold leading to surface defects or cracks in the steel shell. Once again the flow transients in the mold could accentuate the level fluctuations and hence need to be studied.

Various tools can be used to study the fluid flow in the mold the prominent ones being mathematical modeling, water modeling and flow sensors. Extensive mathematical modeling of the fluid flow has been done and chapter 3 of this work provides a selective review. Water modeling is based on the near equal kinematic viscosities of water and molten steel resulting in Reynolds and Froude similarity. Water models are easy to construct and inexpensive. Flow visualization in water models can provide useful qualitative information and is made possible by injection of a suitable dye or gas before the nozzle outlet port. In addition to visualization, point measurements can be made with pitot tubes, ultrasonic sensors and hot wire anemometers. Gupta and Lahiri [9] used flow visualization to study the surface disturbances in a water model of varying aspect ratio (ratio of length to wideface width). A camera recording at 25 frames/s and an image analyzer were used. The effect of varying port diameter, port angle and immersion depth of the nozzle were studied. The meniscus was seen to be wavy with a crest close to the narrow face where the upper wall jet rises to the top surface. The wave amplitude was found to vary parabolically with the nozzle exit velocity. Another study of Gupta and Lahiri [7] used a similar set up with varying aspect ratio to study flow asymmetry. Dye and bubble injection was used to trace the flow pattern and a camera was used to record the images. The fluid was drained through multiple holes in the bottom. It was found that only if the recirculation region reached the bottom, the flow pattern in the lower roll was symmetric. Beyond an aspect ratio of 6.25 the lower recirculation region size does not change with aspect ratio causing asymmetry between the two lower rolls. A correlation was also found between the interaction of the swirling jet with the wide faces and asymmetry between the jets in the two halves of the mold.

Laser Doppler Velocimetry (LDV) is a non-intrusive technique, which can be used to measure flow velocities in water model. In LDV a velocity component at the intersection of two laser beams can measured knowing the frequency shift resulting from the Doppler effect [10]. Lan et al [11] have used LDV to study the fluid flow in a water model of a continuous casting billet mold. The billet mold essentially consists of a circular plexiglass cylinder with the flow entering the mold in the form a submerged circular jet from a nozzle. The results of this work compared favorably to six K-ε turbulence model simulations. Khodadadi et al [10] conducted LDV measurements on a similar setting but with a non-concentric inlet jet.

Particle Image Velocimetry (PIV) is another optical technique used to measure flow velocities at discrete points in the flow field and is the tool used in the present work. The details of PIV are discussed in later sections. Dong Xu et al[12] were among the first to apply PIV to study the fluid flow in a water model of a continuous caster. A Lexan mold with water as the fluid was used. The flow was illuminated using a high power laser (>10W). Neutrally buoyant particles of size in the range of 200-300 μm were used to seed the flow field. A CCD camera was used to record snapshots of the illuminated flow field with a 33.3ms interval. Time averaged flow patterns were obtained using 40 randomly selected frames. The flow fields in two planes parallel to the wide face were measured with and without argon gas injection for two downward nozzle angles. The measurements were found to be qualitatively accurate and compared favorably to a finite element calculation using the commercial finite element software package FIDAP. Dong Xu et al [13] also applied PIV to study the fluid flow in electromagnetic or direct-chill casting of aluminum. Neutral density latex particles were used for seeding the flow with similar image capturing technique.

Honeyands and Herbertson [8] used ultrasonic flow sensors in addition to flow visualization with dye injection to study the dynamic fluid flow phenomena in the mold region. The studies were done on a perspex model of the mold of a thin slab caster. The ultrasonic flow sensors mounted on top of the water surface measured the surface level fluctuations. Similar to the results of Gupta and Lahiri [9] the level was found to oscillate with time with periods of 5s and 50s for a closed bottom and open bottom nozzles respectively. The amplitude of the surface wave was found to increase with increasing casting speed.

Assar et al [14] have used electromagnetic flow sensors on a steel caster to measure the flow velocity near the meniscus. This study also includes PIV measurements in a water model of the caster. Nail-board experiments [14] were also done to study the shape and distribution of slag layers above the steel. MFC sensors are one of the few tools to directly quantify the fluid flow in the caster. The details of the principle of the MFC sensor can be found in chapter 3 of this work. The Mold Flow Control (MFC) sensor measured the velocity near the water surface on both halves of the mold. The direction of flow near the meniscus indicates the presence of single or double roll pattern. For low argon injection rates the classic double roll pattern was found to exist with single roll pattern for high argon injection rates. The results of PIV and MFC were found to correlate well for low argon injection rates. At high argon injections the flow was found to become unstable and the correlation no longer exists.

Despite the decisive effect of transient flow phenomena on continuous casting defects no previous experimental work has been done to quantify the flow transients in different parts of the mold and correlate them to defects. In the present work PIV measurements were done on a water model at LTV Steel (Cleveland, OH), to better understand and quantify the transient flow phenomena in the mold of a continuous caster. In the following sections the water model used for this study is described first. This is followed by the principle and details of the PIV measuring system. Finally the results of the study for the jet, upper roll and lower roll are examined.

2.2 Water model description

Figure 2.1 shows a schematic of the water model used in this study. It is constructed from formed transparent plexiglas plates. The flow from the tundish passes through a slide gate, which moves at right angles to the wideface to restrict the opening in the nozzle and thereby controls the flow rate. The flow then enters the mold cavity through downward-angled square ports of a bifurcated nozzle. The top and bottom angles on the port are 40^o and 15^o respectively. The top surface is uncovered resulting in a free surface between water and the atmosphere. Flow exits the bottom of the water model through three pipes attached to circular outlets in the bottom plate. The experimental mold is nominally symmetric with respect to the centerline shown in the figure. The thickness of the water model tapers from the top to the bottom in order to simulate only the liquid portion of the steel caster. Table 2.1 lists the main dimensions and casting conditions for the mold.

2.3 Particle Image Velocimetry (PIV)

2.3.1 Principle

PIV is a measurement technique for obtaining instantaneous velocities at discrete points in the flow field. Figure 2.2 is a schematic depicting the principle of PIV. A laser sheet is used to illuminate a plane in a flow field with particles. A CCD (Charge Couple Device) camera is used to capture two snapshots within a short time interval (~100μs). The light reflected by the particles in the laser sheet creates patterns on the camera. The region within the camera aperture is divided into a number of interrogation areas. Using a suitable correlation technique an average velocity is computed for each interrogation area using the average distance traveled by particles in that area and the known time interval between snapshots. The process can be repeated to obtain a sequence of instantaneous velocity vector plots, which can be used to study the flow.

2.3.2 Details

Adding particles to the flow is known as seeding and the particle used depends of the nature of the flow to be studied. To detect the particle at a given time instant, an area of the flow field is illuminated by a light-sheet generated by a laser and a system of optical components. The light-sheet is not continuous but is pulsed, freezing the movement of the seeding particles. To detect the position of the illuminated seeding particles, a Charge Coupled Device (CCD) camera is positioned at right angles to the light sheet. The particle positions appear as light specks on a dark background on each camera snapshot. The pulsing light-sheet and camera are synchronized so that particle positions at the instant of each light pulse are recorded as a separate snapshot by the camera. The camera images are divided into rectangular interrogation areas and for each of these the particle positions in the two snapshots are correlated to produce an average displacement vector.

The number of particles per interrogation area should be sufficient to give an accurate average vector. The camera can detect the presence or absence of a particle in each pixel based on whether the pixel is illuminated or not. It cannot distinguish more than one particle per pixel and hence there should be sufficient number of pixels within each interrogation area to resolve all particles. The particle density is adjusted to give a reasonable average for the entire flow field. Hence larger interrogation areas would need more number of pixels to resolve all particles. From experience the number of pixels per interrogation area varies from 16x16 to 64x64 for good particle resolution. The CCD camera used in this study was DANTEC - Double Image 700 with 768x480 pixels. To avoid problems arising from crossover to adjacent areas by particles close to the area edges the interrogation areas are made to overlap each other by 25%. With 32x32 pixels per interrogation area this results in a field of 31x19 vectors.

In order to capture the large scale structure motions a large measurement area has to be selected at the expense of the low resolution resulting from limited number of camera pixels and a minimum particle seeding density. In order to make detailed measurements such as close to the water surface a smaller measurement area can be selected at the expense of loosing information about the rest of the flow field during the measurement. Considering these limitations the flow field is divided into the three regions as seen in Figure 2.2: the top region of the mold containing the jet and the upper roll (A), the middle region containing both the lower rolls (B) and the bottom region containing part of the lower roll (C). The number of vectors in each of these areas is fixed at 31x19 to get 32x32 pixels per interrogation area. In some regions this may result in over-resolving whereas it may be under-resolved for others.

Dividing the average displacement vector by the time interval between the two snapshots gives the average velocity vector over the interrogation area for the time interval between the snapshots. This process is repeated at fixed intervals, which are generally much larger (>1000 times) than the time interval between the snapshots, resulting in a set of instantaneous vector plots.

In this study aluminum powder with particle diameter (~ 30μm) are used for seeding. The low particle diameter prevents the particles from affecting the flow field. A Nd:YAG laser was used. Auto Correlation was used to obtain the average displacement vectors in each interrogation area.

The average time interval between the light pulses depends on the flow rate and is adjusted such that the particles travel 1/3rd to 1/4th of the interrogation area. For this study it was set at 1ms. The time interval between each measurement varies from 0.2-1s. The number of snapshots collected and the time interval between them depends on the time scales of the flow in the respective regions. The data for the top region is a total of 900 snapshots spaced 0.2s apart, for the middle region is a 2000 snapshots of both halves of the water model spaced 1s apart and 400 snapshots of one half spaced 0.2s apart and for the bottom region is 200 snapshots spaced 0.2s apart.

Figure 2.3 is an instantaneous snapshot of the flow in the water model. A small fraction of gas is injected to make flow visualization possible without altering the flow field significantly. The downward momentum of the flow through the nozzle causes the jet to exit the port at an angle of 29^o, which is significantly greater than the bottom port angle of 15^o. Najjar et al. [15] have simulated the turbulent fluid flow through nozzles and have found similar results but for a different nozzle configuration. Also the jet is seen to diffuse as it travels across the mold. A certain measure of water-soluble dye was injected all-at-once near the slide gate to better visualize the flow field. It passes through the mold and the water-dye mixture is drained out the bottom without recycling. Figure 2.4 is an instantaneous snap shot with injected dye. The dye is deep purple in color with a white screen behind the transparent mold. The greater the dye concentration, the darker is the region in which it is present. At the instant shown in figure 2.4 the dye has traveled with the jets slightly beyond the impingement point. As the jet travels across the mold it diffuses and so does the dye dissolved in it. These regions appear gray with the darkness depending on the local dye concentration. Since the surrounding flow field does not contain any dye the boundary between the gray and white regions in the photograph indicates the extent to which the jet has diffused. The central region where the dye has retained its original concentration traces the path followed by the jet. From the paths traced by the two jets there appears to be considerable asymmetry between the jets on the two halves of the water model. The jet on the left penetrates deeper than the one on the right, which rises steeply after traveling halfway across the mold. More will be said about this later.

2.4 Results and discussion

PIV measurements were made in the different regions as mentioned earlier in the details section. Time averages were computed to study the mean flow field. Sequences of instantaneous velocity vector plots in time were animated to record the flow transients in different parts of the mold. Velocity variations at key points were used to examine the time scales involved in different parts of the flow field. An overview of the flow in the mold is first provided. This is followed by a detailed discussion of the flow in the jet, upper and lower roll.

2.4.1 Overview

Figure 2.5 is an instantaneous velocity vector plot of the flow field in the center plane of the water model. It is a composite of the top, middle and bottom regions depicted in figure 2.2, each for the two halves, taken at different instants in time. The flow is turbulent consisting of a range of flow scales, as witnessed by the velocity fluctuations across the flow field. The flow emerges from the nozzle as a jet directed at about 30^o downward. It is seen to have diffused as it traveled across the mold. The jet, at both instants seen, consists of alternate bands of vectors with angles substantially lower and higher than the 30^o inlet value. This is examined in later sections. There is a region of low velocity between the upper wall jet and the flow close to the water surface. The mean flow field needs to be examined to determine if this transient phenomenon persists in time. The flow velocities close to the water surface and the upper roll structure are seen to vary significantly between the two time instants. The flow from the lower wall jet is observed to recirculate into the flow entrained from below the nozzle at both instants, but at different distances below the top surface. Thus the shape and size of the lower roll appears significantly different at the two instants. Both lower and upper roll are seen to consist of numerous small flow structures. The details of the flow field will be discussed in subsequent sections.

2.4.1 Jet

Figure 2.6 is a time averaged velocity vector plot of the top region of the mold, averaged over 1min with 300 instantaneous measurements. The jet emerges from the nozzle at an angle of around 30^o. It diffuses and its downward angle is seen to decrease gradually as it travels across the mold finally impinging nearly horizontally on the narrow face. After impingement part of the flow is directed upwards forming the upper wall jet. This flows along the narrowface and top surface finally recirculating into the main jet and forming the upper roll. The region of low velocity vectors between the upper wall jet and flow close to the top surface observed earlier in the instantaneous velocity vector plot is seen to persist in the time average. Its appearance can be justified only by out of plane flow in order to satisfy mass continuity.

Figure 2.7 shows a schematic of the flow from the port that illustrates the swirl in the jet. The movement of the slide gate flow control positioned high in the nozzle tube, perpendicular to the wide face, allows flow through only 41% of the nozzle bore area. This causes stronger flow down the inner radius wide face side of the nozzle. This bias in flow over the cross section persists until the nozzle port outlet, causing a swirl in the experimental jet [15, 16]. The overall jet moves downward at an angle of 30^o and the swirl gradually diffuses. With respect to its centerline, the jet moves along a helix, as depicted in the figure. The swirling experimental jet moves both up and down and in and out of the center plane. This motion of swirling jets at high

Reynolds numbers and swirl rates is called precession and has been studied in detail [17, 18]. As a result of the helical motion, the flow has either an additional upward or downward component, the magnitude depending on the radial location. The motion of the jet in and out of the center plane results in this vertical component of flow to occur in the center plane. The net instantaneous jet angle is then significantly larger or smaller than 30^o depending on whether the portion of the helix in the center plane has downward or upward flow. Corresponding to the pitch of the helix alternate bands of flow with angles smaller and larger than 30^o will exist. The resulting staircase type of pattern is seen in figure 2.8, which is a sequence of instantaneous velocity vector plots of the top region spaced 0.2s apart. These particular sequences were chosen to best illustrate this phenomenon that is typically present in all 900 frames recorded.

From figure 2.8 it can be seen that the alternate regions of velocities directed at angles smaller and larger than 30^o form a staircase pattern. The steep downward regions might correspond with the downward part of the swirl (gray regions of the first and third arrows in Figure 2.7) increasing the local downward angle of the jet. Roughly horizontal regions correspond with the upward portions of the swirl canceling the general downward motion. Moreover, the staircase wobbles with time, as the initial angle alternates between almost horizontal and vertical steep. The time scale of this wobbling motion can be visually estimated to be of the order of 0.4s. Close to the NF, the vectors tend to become more horizontal. The velocity vectors at a given point change angle without specific pattern, as a result of both up-down and presumably also in-out motion.

The overall jet angle alternates without any definite pattern between the two extreme cases of a shallow and a deep penetrating jet. The shallow jet bends to become horizontal close to the port outlet and continues to remain horizontal as seen in figure 2.9. The deep penetrating jet, on the other hand, continues at an average downward angle of 30^o as seen in figure 2.8.

In addition to the small time scale (0.4s) in-out motion of the jet there is a large scale in-out motion of the jet as evidenced by the alternate appearance and disappearance of vectors near the narrow face in the sequence of four instantaneous velocity vector plots spaced 2.4s apart in figure 2.10. This sequence again has been chosen to best illustrate this phenomenon and the time scale of 7.2s for this motion to occur.

2.4.2 Upper Roll

Figure 2.11 is a set of instantaneous velocity vector plots of the top region with a smaller reference vector compared to figures 2.8-2.10 to observe the large scale structures in the upper roll. Figures 2.11 a) and (b) are representative of the two flow scenarios that exist above the main jet. In figure 2.11 a) the upper roll is seen as a single large recirculation region with the upper wall jet flowing along the top surface until it recirculates into the main jet more than halfway across the mold from the narrow face. In figure 2.11 b) no specific pattern of flow exists for the upper wall jet and the region above the main jet consists of a number of distinct vortices with sizes comparable to the upper roll. The flow in the upper roll alternates without specific pattern or time scale between these two extremes.

Recall that the top surface velocity is crucial to the shear entrainment of liquid flux. Figure 2.12 is a representative plot of time variation of horizontal velocity at a point close to the top surface, halfway between the SEN and the narrow face. The points are spaced 0.2s apart evidenced in the symbol spacing. This velocity variation was compiled from two consecutive measurement runs resulting in a break in the x axis. The negative sign for the velocities indicates flow towards the nozzle, which is characteristic of a classic double roll pattern.

Closer observation of the results suggests the existence two predominant time scales. The lower one is about 0.7s. The consecutive PIV measurements were close enough (0.2s) to capture this time scale as there are more than five points per 0.7s time cycle. The higher time scale is at least 45s. This results in periods of 5s or more when the velocity close to the top surface is three to four times the corresponding mean value (for example the 10-20s range in figure 2.12). This period of high velocity could shear the liquid flux layer and cause shear entraiment deep into the caster. The occurance of these high velocity periods can be correlated to the large variations in the jet angle in the center plane. When the jet is shallow the impingement point will be closer to the top surface resulting in more flow along the upper wall jet with lower flow for a deep penetrating jet. This larger flow will cause higher velocities close to the water surface. However, as mentioned in the jet section, the pattern of jet angle variation in the center plane is complex making a direct correlation difficult.

2.4.3 Lower Roll

Figure 2.13 is a time averaged velocity vector plot of both lower rolls. The vectors were averaged over 30 min of flow with 2000 instantaneous measurements. Flow in either lower roll consists of the lower wall jet that flows towards the mold exit and flow being entrained by the low pressure in the main jet from below the nozzle. There is some cross flow between the two resulting in the roll-like appearance of these recirculation regions.

Considerable asymmetry can be seen between the left and right rolls. Considering the large time period and high sampling rate over which this mean flow field has been measured, this asymmetry is persistent and is not a transient phenomenon. There are two main features of this asymmetry that are especially significant. One is the region of very low velocity around the impingement point on the right, which contrasts with the higher downward flow on the left. This follows from the instantaneous asymmetry between the left and right jets seen in the dye injection snapshot in figure 2.3. Persistence of this asymmetry with time would cause the right jet to curve upwards steeply and therefore lower velocities in the jet region on the right (see figure 2.13). The second is the upward flow from below the SEN being directed slightly towards the left. This suggests a significant period of time when the right roll is larger than the left.

Figure 2.14 shows an instantaneous snapshot when both the rolls are about the same size. This flow configuration lasts for about 12s. This is followed by a period of around 17s when the right roll is larger than the left, which is represented in figure 2.15. The upward flow below the nozzle is directed to the left squeezing the left roll in the downward direction, while expanding the right roll. In this flow configuration the location of the eye or center of the left roll oscillates in the vertical direction but is never high enough to make both rolls of equal size. This in turn is followed by the flow sequence seen in the instantaneous vector plots shown in figures 2.16, which span over 14s. Here the flow from the lower jet turns sharply to the right, to form a short-circuited roll structure. This might be caused by fluctuations at the inlet or instabilities inherent in any turbulent flow field. This structure then expands downwards over a 8s period finally merging into the lower roll. This sequence repeats every 60s. This phenomenon is important when studying bubble or particle entrapment as it changes the transport phenomena in the lower roll. Together these three flow configurations constitute the flow transients observed in the lower. There is a probable correlation between the asymmetry of the two jets and the lower rolls although no satisfactory explanation has been found.

2.5 Summary

The present work has quantified the flow field in the mold region of a water model of a continuous caster using Particle Image Velocimetry (PIV) measurements. The mold region was subdivided into measurement areas of suitable size for accurate measurement of the various large scale structures. Instantaneous measurements were made over long enough time to include all the time scales of flow field and obtain an invariant mean flow field. Using the mean flow field, time animations of instantaneous velocity vector plots and time signals at key points the flow transients were studied and where possible a correlation to its effect on defect formation was made.

The flow near the top surface is found by more than 100% of its mean value. This variation consists of a high frequency component of around 1.5 Hz. This is probably caused by the motion of small scale vortex structures present in the upper roll past the point of measurement. It also consists of a low frequency component with a time period of the order of 45s, which results in durations of 5s or more when the horizontal velocities are three to four times their mean values. These high surface velocities are of considerable significance as they will enhance the shear entrainment of the liquid flux.

The swirl in the jet at the port outlet persists at least halfway across the mold. Also the experimental jet has considerable in-out of center plane and up-down motion and its downward angle decreases progressively away from the inlet resulting in nearly horizontal impingement on the narrow face. The overall angle of the jet in both the horizontal and vertical directions varies considerably with a large time scale (> 7s). This wide variation is the probable reason for the appearance of high velocities close to the water surface, which would enhance the shear entrainment of liquid flux.

Although the entire geometry including the inlet nozzle and its ports were symmetric, there was considerable, persistent, asymmetry between the two lower rolls. The flow in the lower rolls is not stationary but consists of a sequence of flow configurations, which repeats in a specific pattern but with varying time scale. One of the flow features involving a diversion of part of the lower wall jet flow to the flow being entrained from below the nozzle occurs over a period of 14s and is seen to repeat around every 60s. It might be caused by fluctuations in the inlet flow field or by instabilities present in any turbulent flow. This feature is important for particle inclusion and bubble entrapment defects.

There is a region of low velocity near the top corner of the mold between the flow in the upper wall jet and near the water surface. This is seen both in instantaneous and time averaged velocity vector plots. For mass balance of the flow to be satisfied there has to be some out of plane motion between the two regions of high velocity. The exact nature of this flow however, is unknown.

Table 2.1 Water model conditions

Dimension / Condition	Value
Port width x height	31mm x 32mm
Port thickness	11 mm
Port angle, lower edge	15^{o} down
Port angle, upper edge	40^{o} down
Bottom well recess depth	4.8 mm
Slide-gate diameter	28 mm
Slide-gate thickness	18 mm
Liquid flow rate at inlet	7.07×10^{-4} m^3/s
Slide-gate orientation	90°
SEN submergence depth	80 mm
Slide-gate opening (FL)	52%
Liquid kinematic viscosity	1.0×10^{-6} m^2/s
Gas volume fraction	0 %
Water model length	950 mm
Water model thickness	95 mm (top) to 65 mm (bottom)
Top surface	Free surface
Flow rate through each port	3.528×10^{-4} m^3/s (5.6gal/min)
Average inlet velocity	424 mm/s
Average jet inlet angle	30^{o}
SEN Submergence depth (top of port to top surface)	75 ± 3mm
Outlets at bottom	1.5 round 35mm diameter outlets along each half

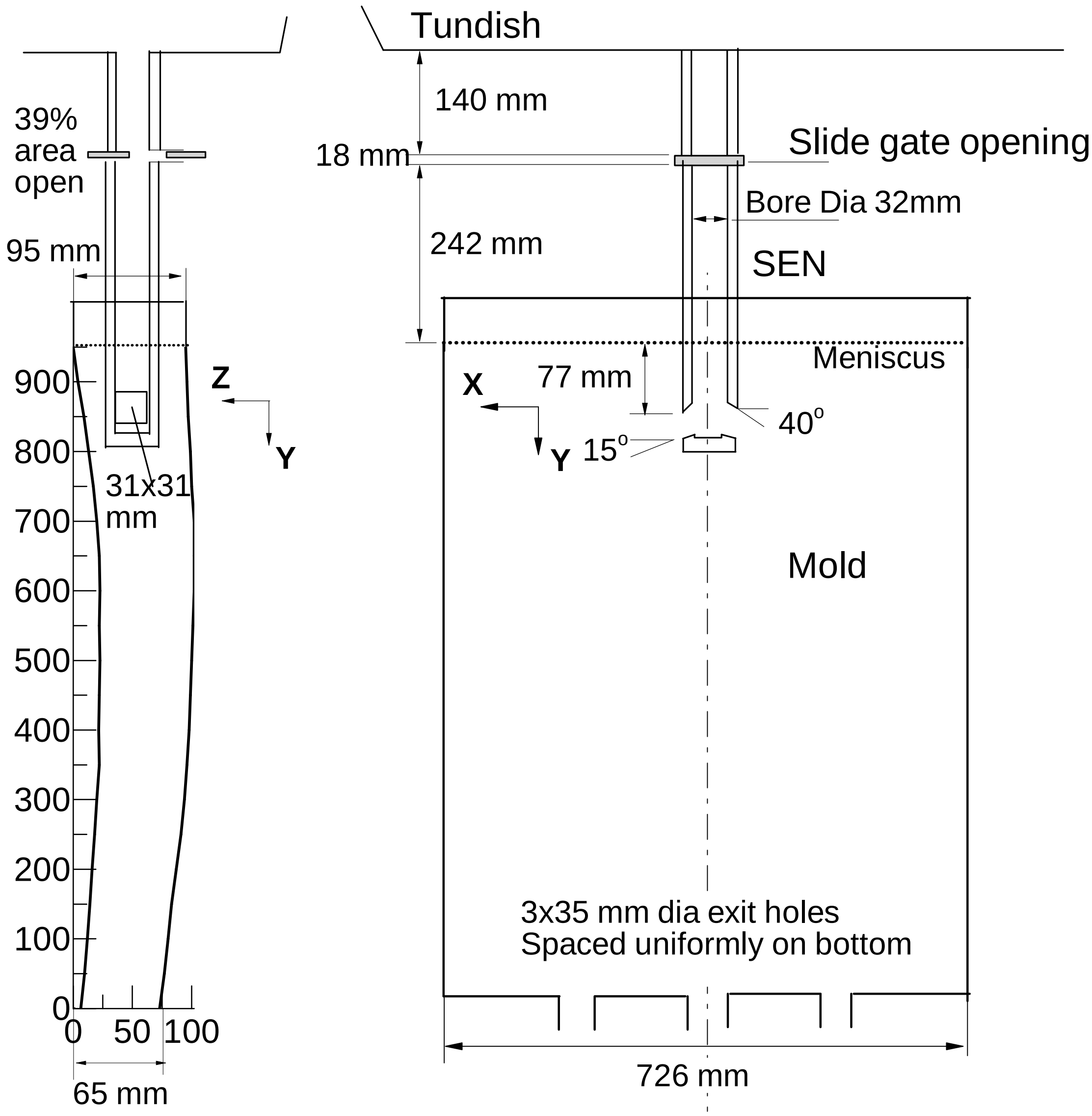

Figure 2.1 Schematic of water model domain

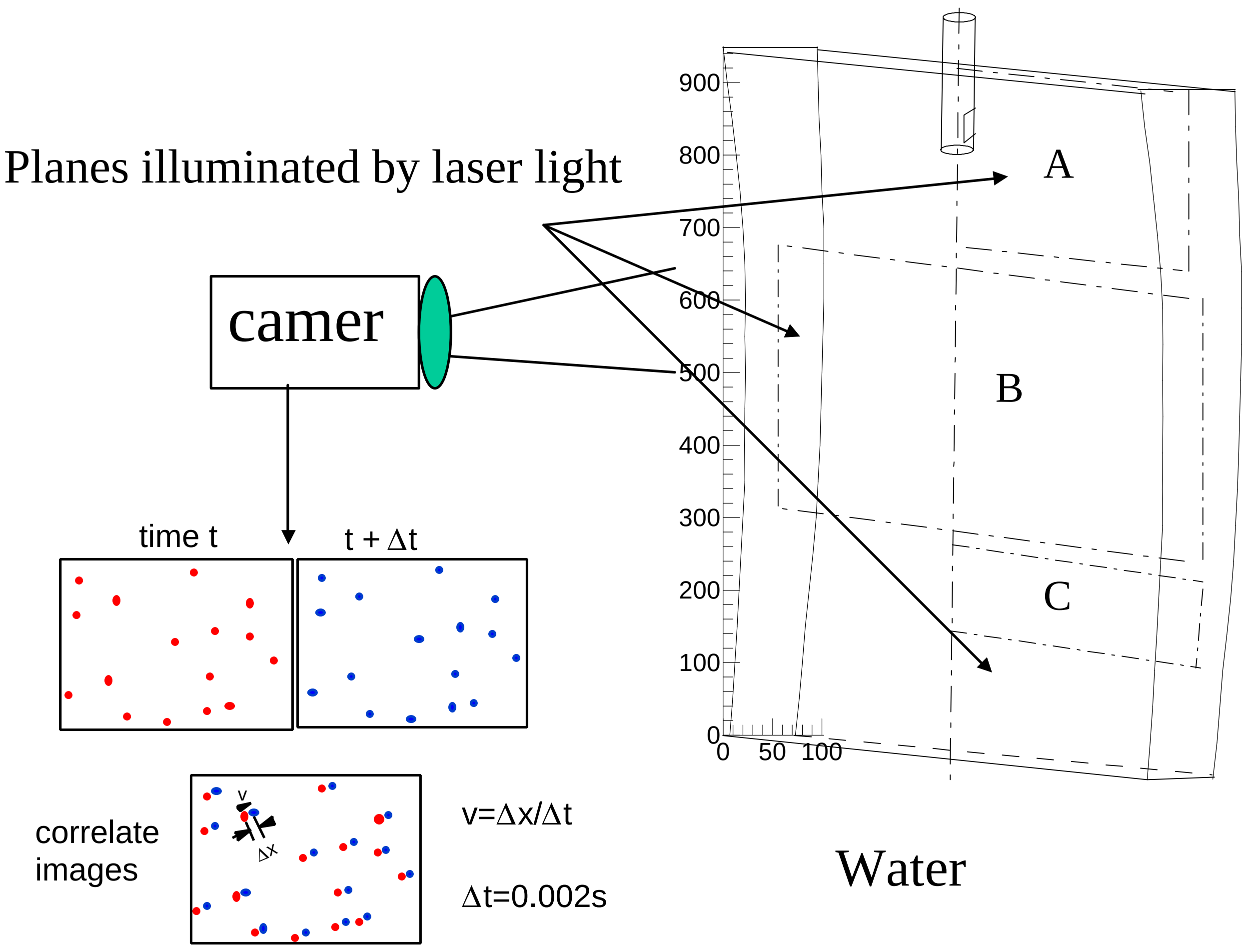

Figure 2.2 Principle of Particle Image Velocimetry (PIV)

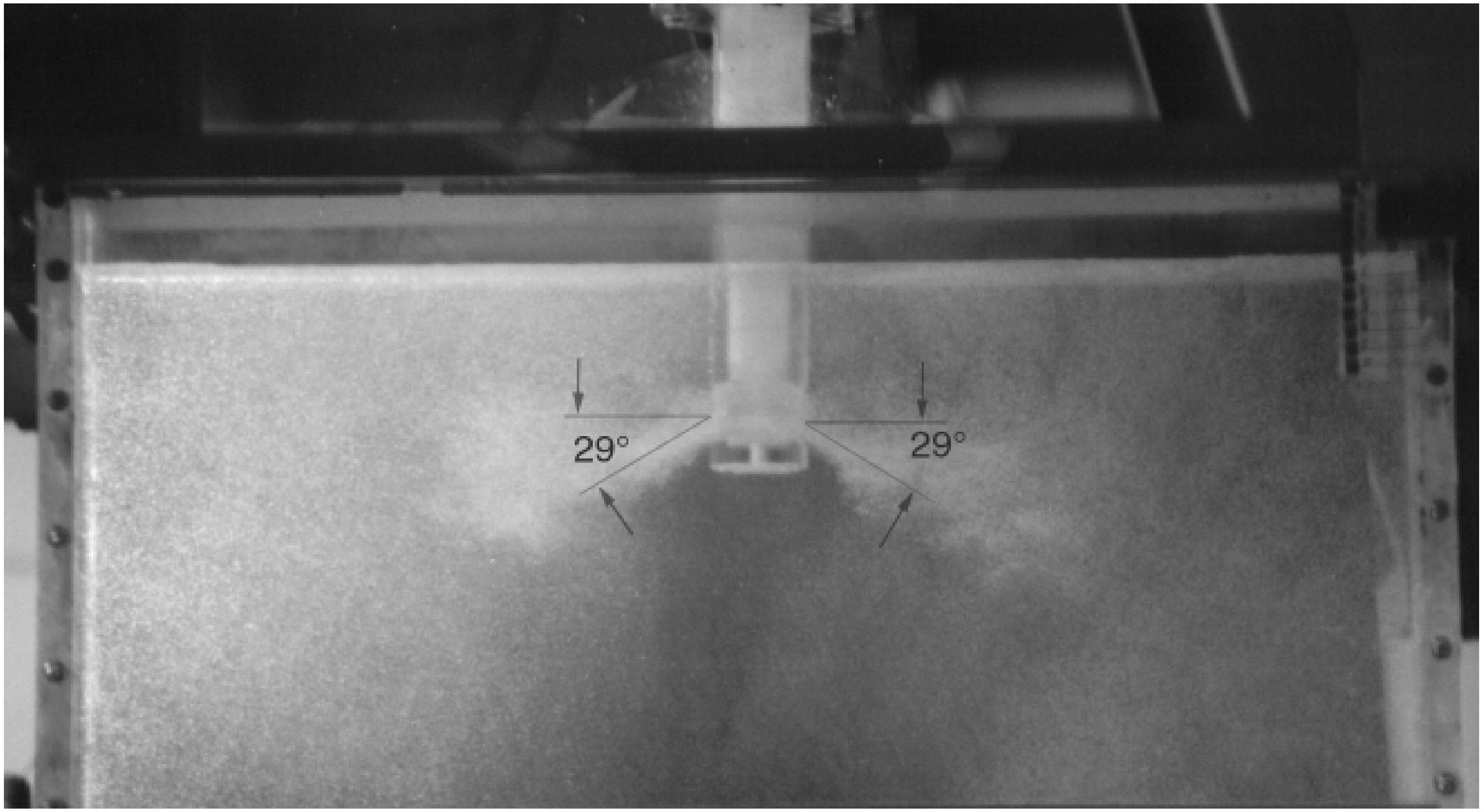

Figure 2.3 Snapshot of mold flow pattern and jet angle

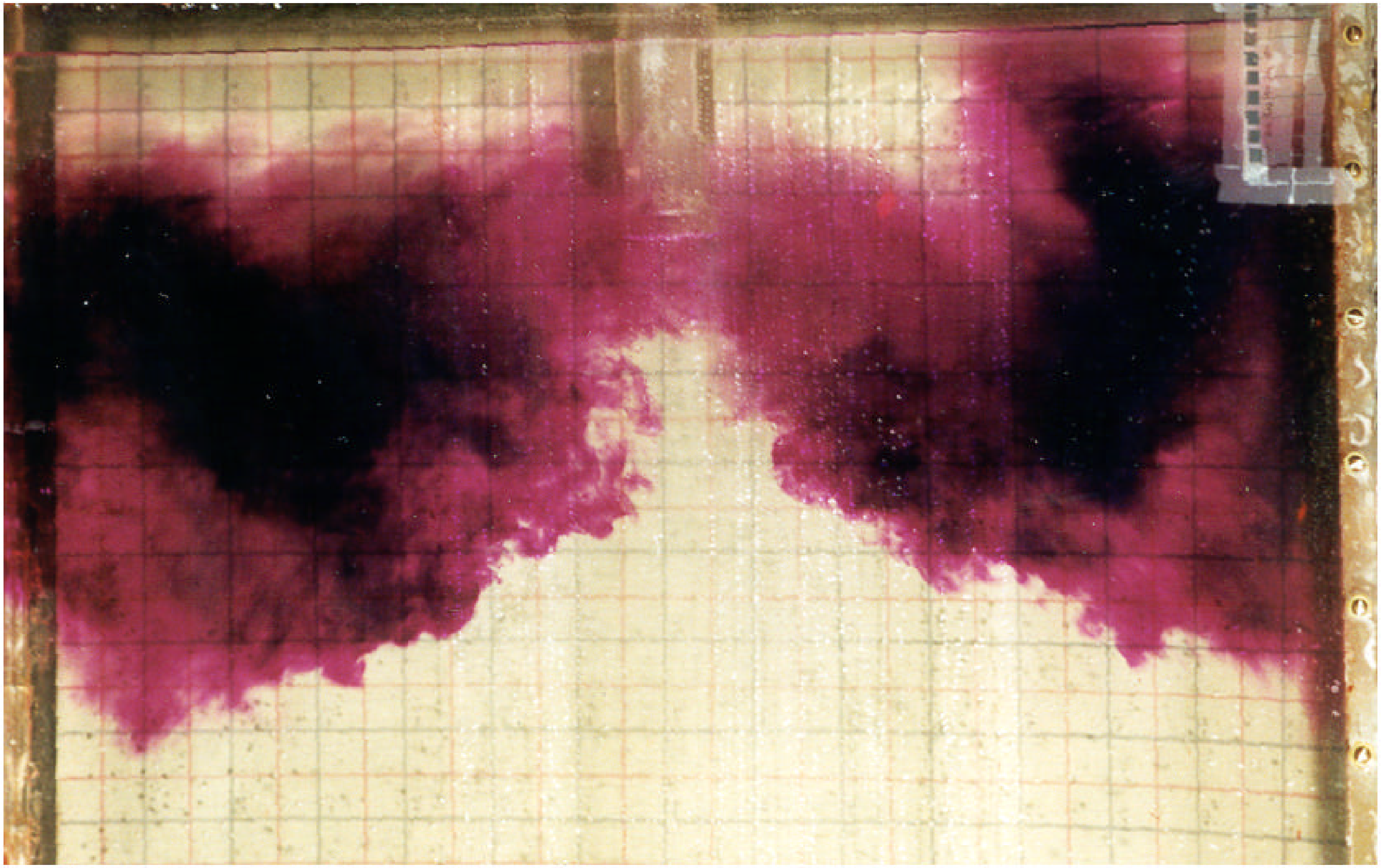

Figure 2.4 Snapshot of mold flow with dye injection showing asymmetry between jets

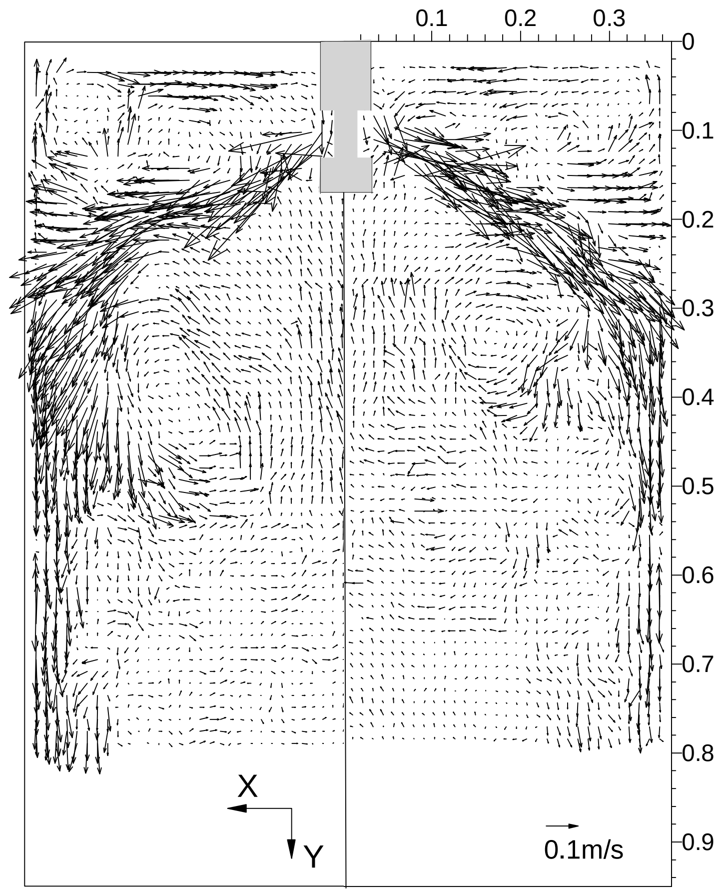

Figure 2.5 Instantaneous PIV measurement, velocity vector plot

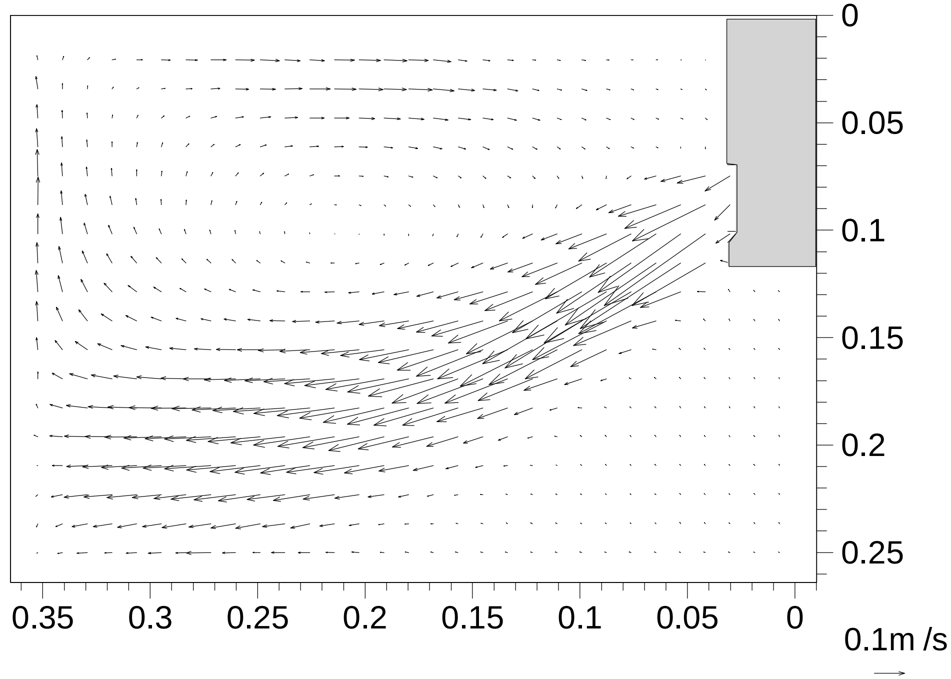

Figure 2.6 Time averaged PIV measurement, velocity vector plot of the jet and upper roll

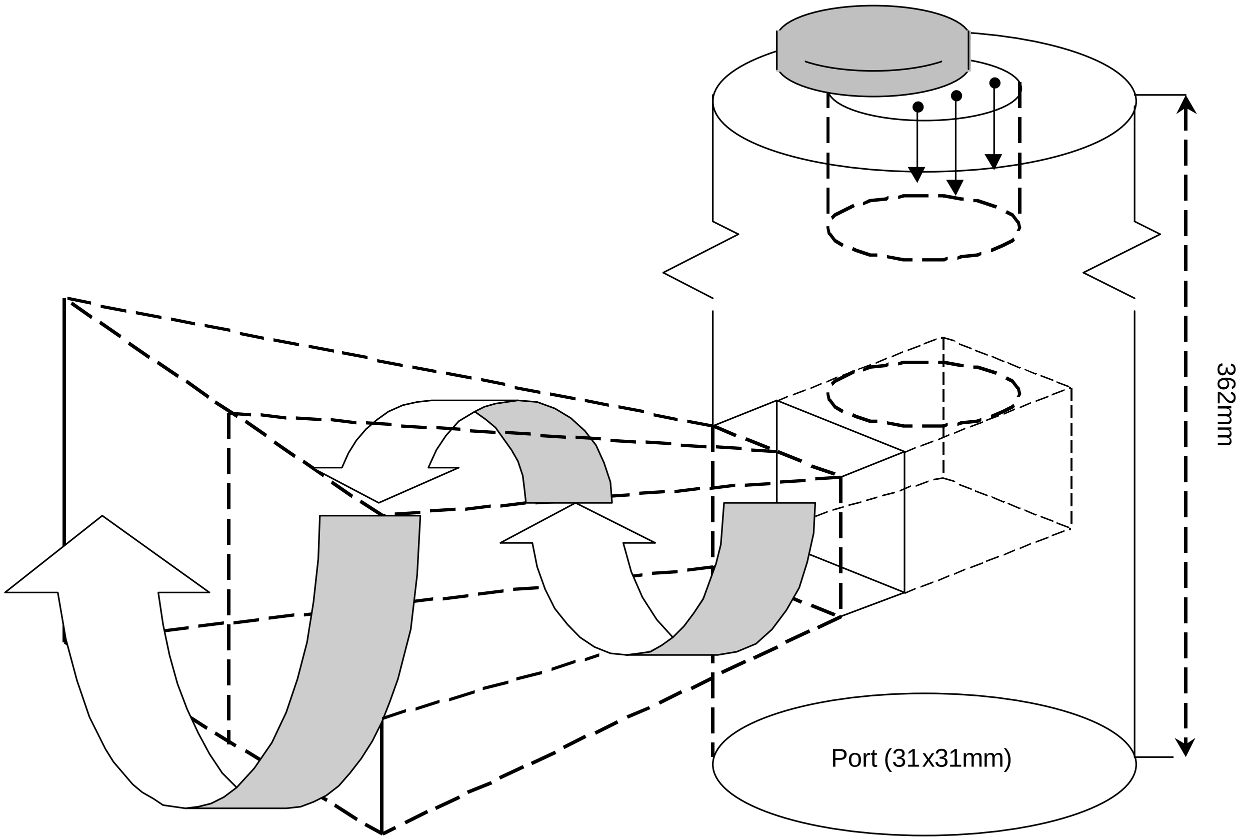

Figure 2.7 Schematic of swirling flow in the experimental jet

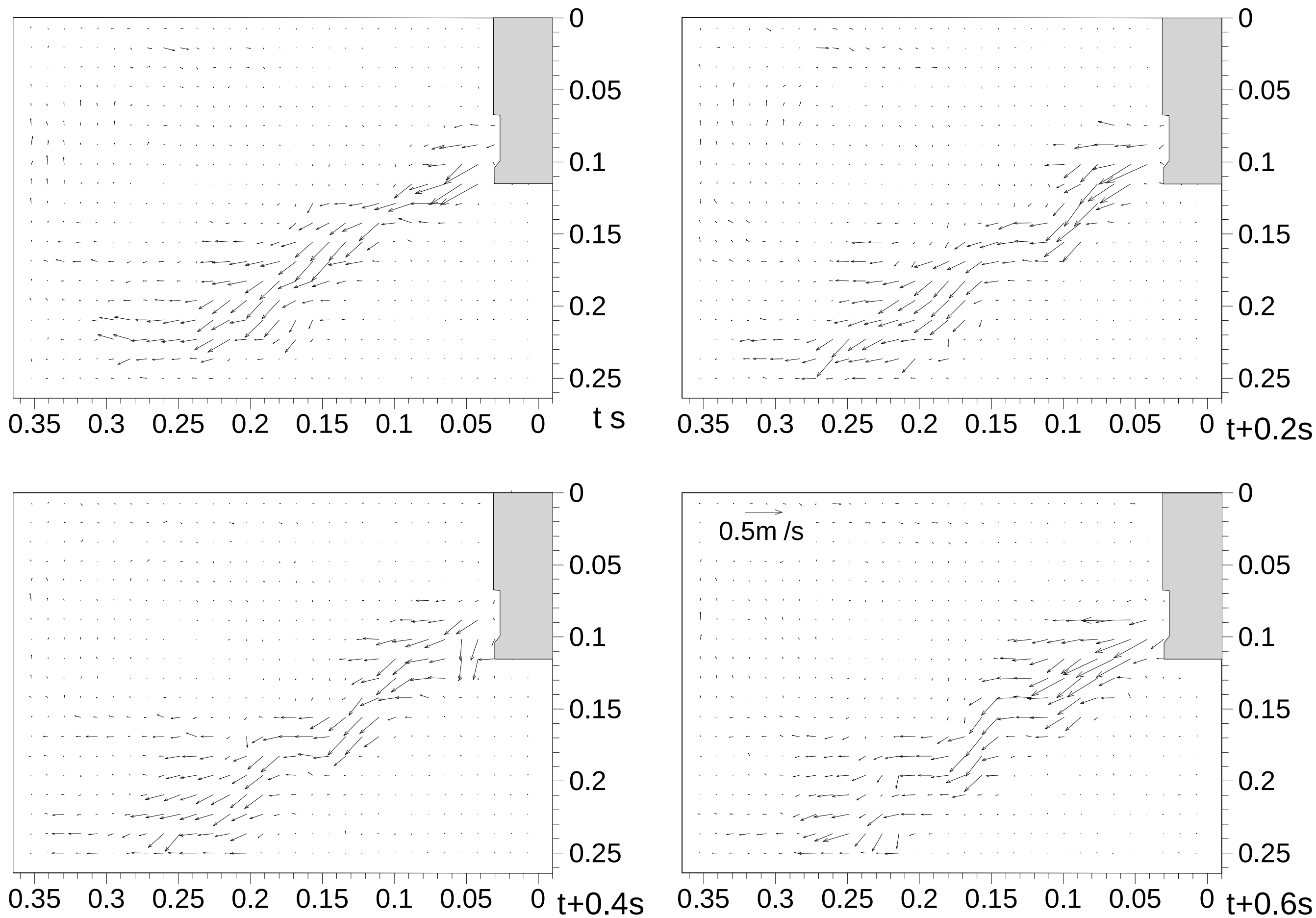

Figure 2.8 Sequence of instantaneous velocity vector plots from PIV measurements 0.2s apart

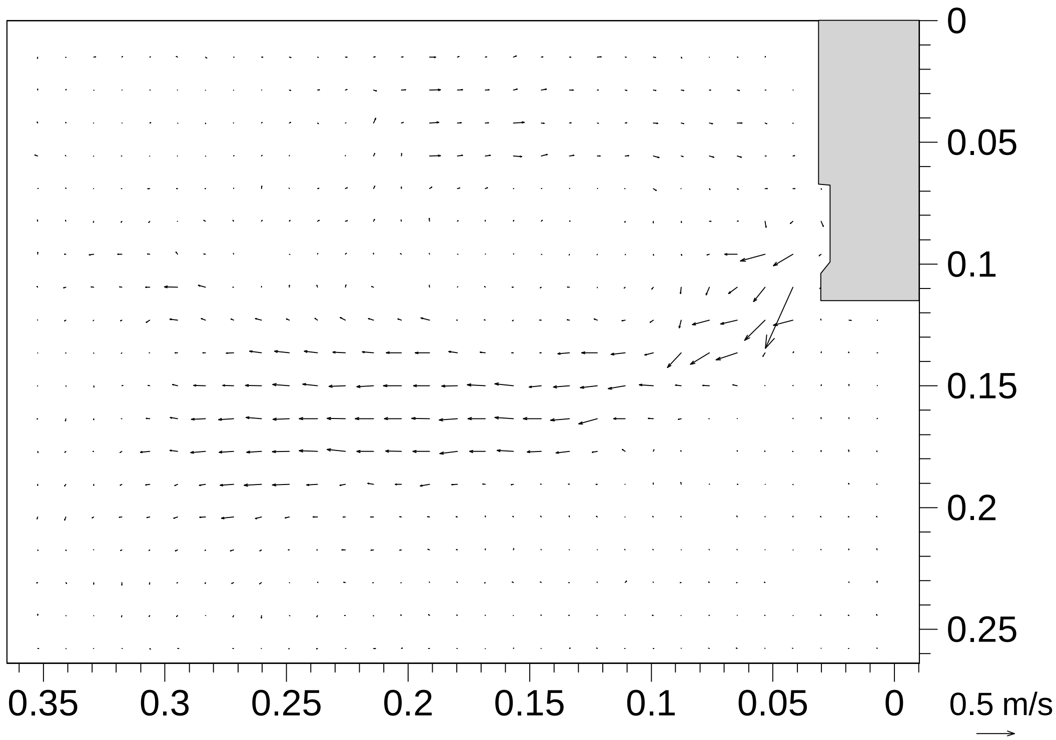

Figure 2.9 Instantaneous velocity vector plot of PIV measurement with shallow jet

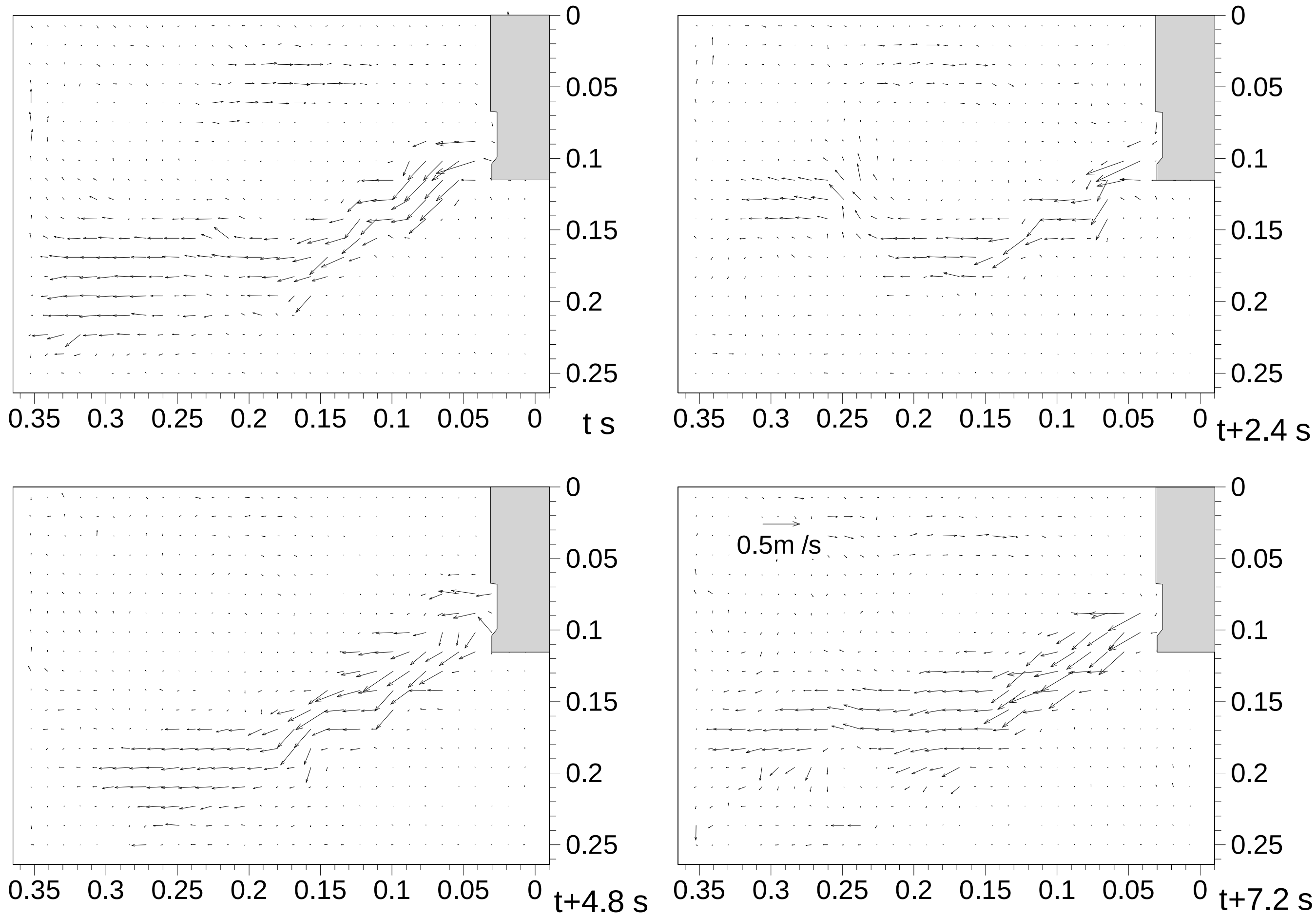

Figure 2.10 Sequence of instantaneous velocity vector plots from PIV measurements spaced 2.4s apart

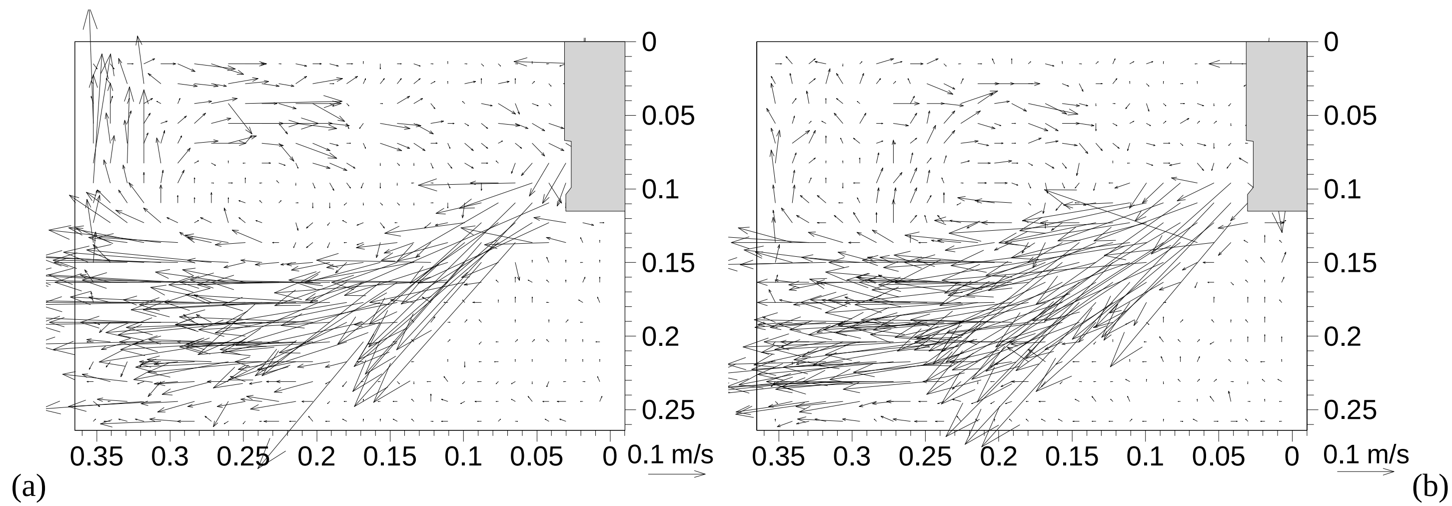

Figure 2.11 Instantaneous velocity vector plot from PIV measurement with (a) single and (b) broken upper roll

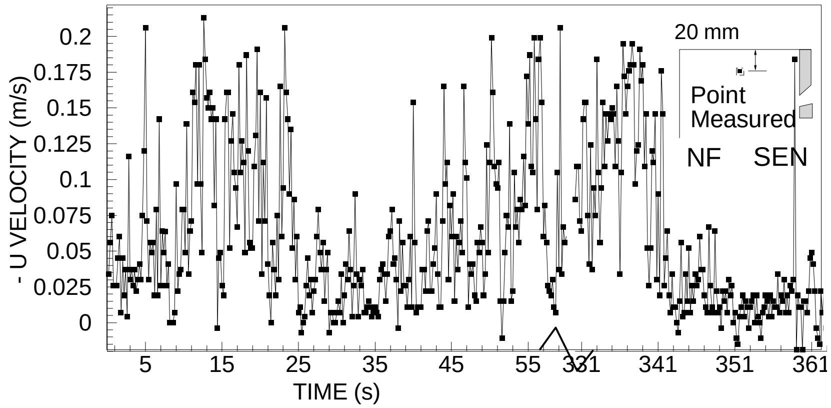

Figure 2.12 Typical history of U velocity component below water surface measured using PIV

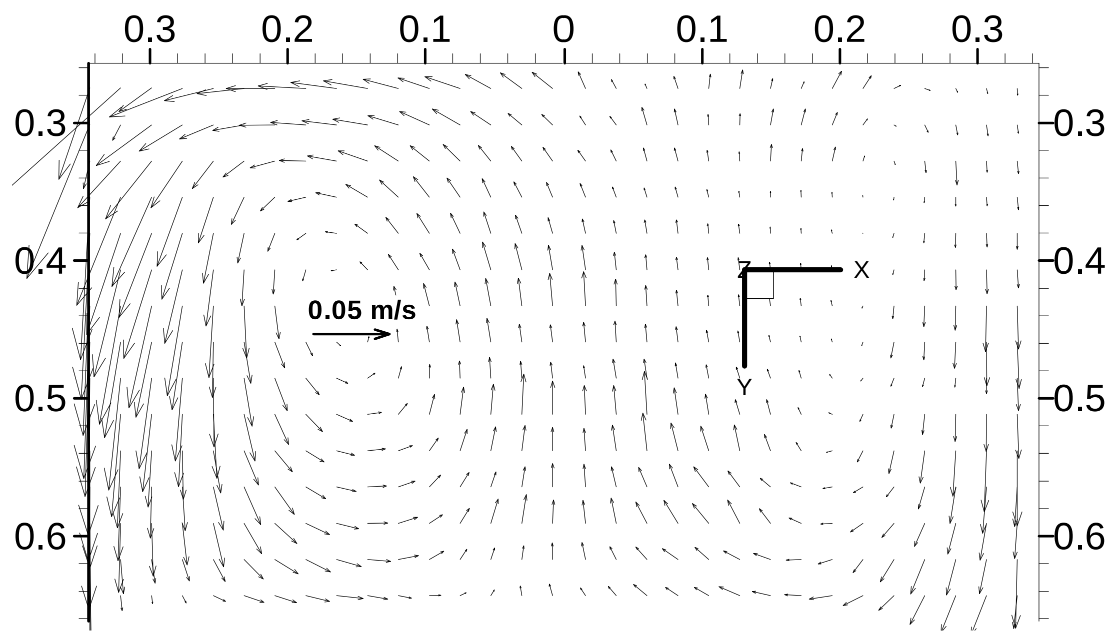

Figure 2.13 Time averaged velocity vector plot of lower rolls from PIV measurement

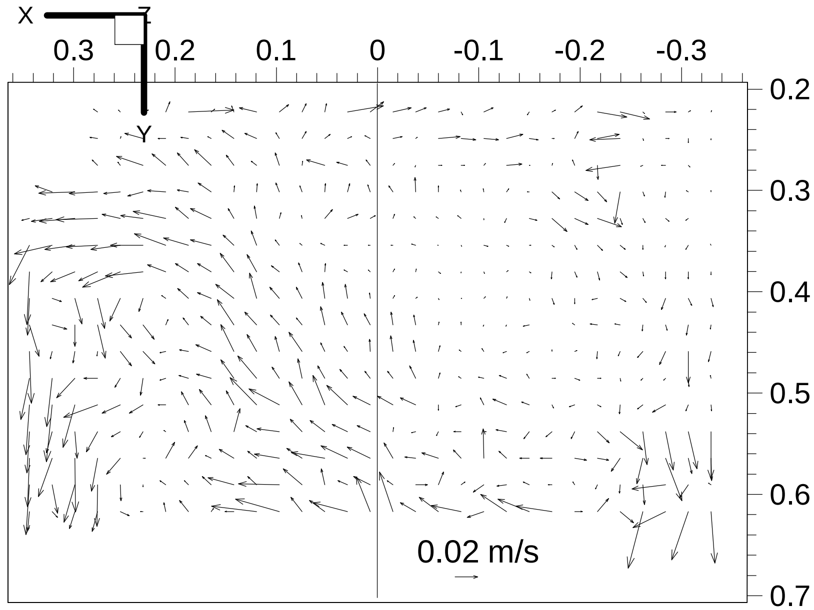

Figure 2.14 Instantaneous velocity vector plot of lower rolls with right roll larger than left

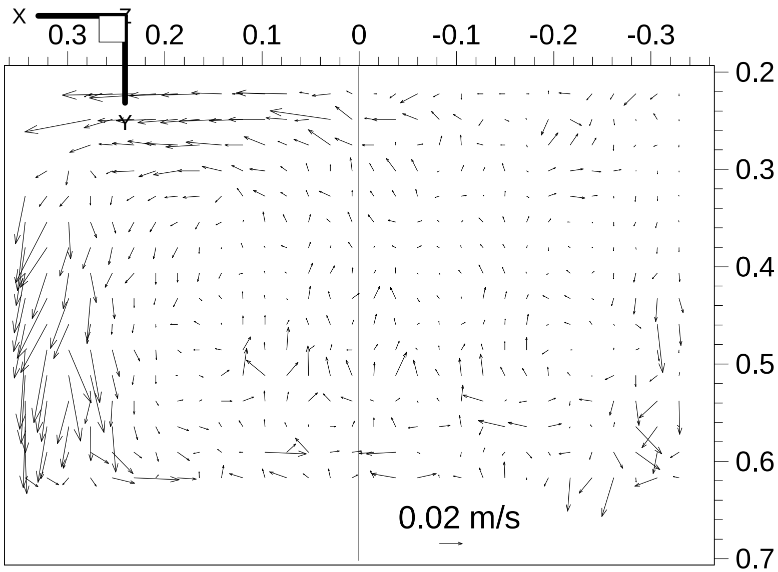

Figure 2.15 Instantaneous velocity vector plot of lower rolls with both rolls about the same size

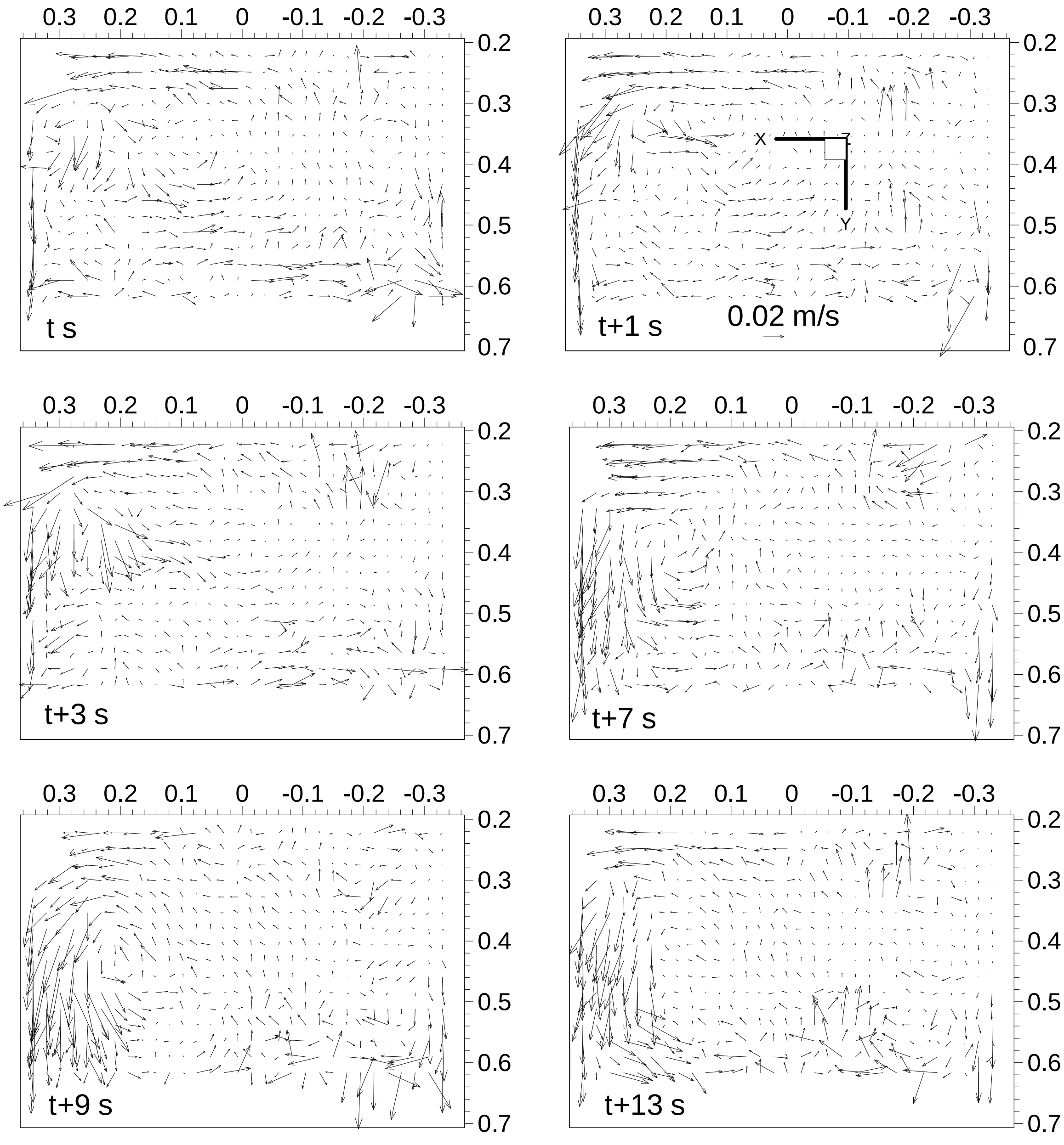

Figure 2.16 Sequence of instantaneous velocity vector plots of lower rolls from PIV measurements showing formation and motion of structure

CHAPTER 3. NUMERICAL STUDY OF TRANSIENT FLOW STRUCTURES IN A MODEL CONTINUOUS CASTER OF STEEL

3.1 Introduction

The present paper is concerned with study of turbulent flow structures in the mold region of a continuous caster of steel. Continuous casting is used to solidify most of the several hundred million tons of steel produced in the world every year. Continuous casting of steel is a very complex process involving transport and two-phase flow. A description of the process is given in the text by Schrewe[19] and is described below. A representative picture of the continuous casting process can be found in chapter 1. Molten steel flows from a ladle through a tundish into the mold. The flow from the tundish into the nozzle is turbulent and has a high Reynolds number, around 100,000. Flow through the submerged nozzle is gravity driven by the pressure difference between the liquid levels of the tundish and the mold free surface. In practice the flow into the SEN is controlled either by a "stopper rod " or by a "slide gate". These flow control devices strongly influence the flow pattern in the nozzle and beyond. Argon gas is injected into the nozzle to prevent clogging. The resulting bubbles provide buoyancy that greatly affects the flow pattern both in the nozzle and the mold. The jet leaving the nozzle flows across the mold and impinges against the shell, solidifying at the narrow face. Here, the heat transfer is due to oblique impingement of the fluid, with the jet bifurcating into an upward wall jet and a downward wall jet. The jet carries superheat, which can erode the shell where it impinges on locally thin regions.

The upward flowing wall-jet travels towards the free surface, and may become transitional or laminar. Liquid flow along the top surface of the mold is very important to steel quality. The horizontal velocity along the interface induces flow and controls heat transfer in the liquid and solid flux layers, which float on the top free surface. Beneath the jet, a large recirculation region is formed, which may be also transitional or mildly turbulent. This flow pattern changes radically with increasing argon injection rate and with the application of electromagnetic forces used to brake and stir the liquid. The flow pattern can fluctuate with time, leading to defects, so transient behaviour is important.

Lower in the caster, fluid flow is driven by thermal and solutal buoyancy effects, caused by density differences between the different compositions created by microsegregation. This flow leads to macrosegregation and associated defects such as centerline porosity, cracks and undesired property variations. Thus understanding the detailed fluid flow and heat transfer phenomena is of considerable importance to defect reduction in continuous casting.

3.2 Previous work

Much of the previous analyses of the flow in the mold region and in the nozzle have been carried out using the Reynolds-averaged approach. As the flow is turbulent, it is necessary to account for turbulent mixing and momentum transport. In the past, the Reynolds-averaged approach has been the preferred route to analyze the flow and heat transfer because of its low computational cost and the unavailability of powerful computers. This situation has however changed recently with the rapid increases in computing speeds even at personal computer level.

Extensive literature on work done using the Reynolds-averaged approach is available. Following is a brief discussion of selected references to provide an overview of the effect of various process variables on the fluid flow, heat transfer and solidification in the mold region. Thomas et al [5] simulated the fluid flow with a two-dimensional finite element model in FIDAP using a K-ε turbulence model. For domain lengths less than 6m, the domain length was found to have an effect on the lower roll velocities, indicating the need for long simulation domains to predict the flow pattern accurately. The downward momentum of the flow in the nozzle was found to produce jet angles steeper than nozzle port bottom angle, whose increase was found to further increase the downward jet angle. Increasing casting speed was not found to have a significant effect on the flow pattern while increasing wideface width was found to significantly increase the jet spread. Changing nozzle submergence was not found to affect the flow pattern, with the impingement point moving almost exactly by submergence depth. Lan et al [11] evaluated six K-ε turbulence models by comparison with laser Doppler anemometry experiments in a physical plexiglass model of a billet mold. The high Reynolds number K-ε model was found to give good results for the central core whereas the low Reynolds number K-ε model was superior for the reverse flow region close to the mold. A finding of significant importance was that the velocity fluctuations in the three directions, obtained using the experiment, were significantly different. All three components were different close to the jet inlet, whereas far away from it the cross-stream components were almost identical but different from the axial component. The high Reynolds number K-ε model better predicted the turbulence kinetic energy whereas low Reynolds number K-ε did better for the mean axial velocity component. Although turbulence kinetic energy (one half the sum of the squares of the velocity fluctuations) was predicted with reasonable accuracy, the K-ε model with the assumption of isotropic turbulence cannot predict the velocity fluctuations. Another example of Reynolds averaged modeling is the work of Aboutalebi et al [20]. The fluid flow, heat transfer and solidification were simulated in a fully coupled manner using a finite volume approach and a low Reynolds number K-ε model. Source terms were added to the momentum equations to model the mushy zone. A Fe-C binary system was used to obtain the solute composition in the solid and liquid phases. The probability of entrapment of particles within the mushy zone was found to increase with decreasing particle size.

Transient flow modeling has been done using an unsteady Reynolds averaged approach by Huang and Thomas [1]. A three-dimensional, finite volume, two-phase approach was used with fully implicit backward Eulerian scheme for time discretization. The transition from a steady biased flow to a steady symmetric flow was simulated to study such effects as de-clogging of nozzles. For biased flow the steady state result showed a large difference in the velocities near the meniscus even though the nozzle blocked only 62% of the cross flow area. As the flow transitioned a large lower vortex was shed. Comparison with experiment indicated a good correlation between turbulent kinetic energy and level fluctuation. This could be used in future work when using a no-slip boundary in place of a free surface. The maximum turbulent kinetic energy and hence level fluctuations occurred at the wall for zero argon injection, moving towards the nozzle with increased argon injection, as buoyancy decreases the jet angle and raises the impingement point. The surface turbulence kinetic energy was found to decrease with increasing submergence depth and decreasing casting speed.

The effect of argon gas on the flow field in the mold has been studied in detail by Thomas et al.[6] using a three-dimensional finite volume model. A continuum model was used for the gas phase wherein the vertical gas bubble velocity relative to the fluid was set to the terminal velocity with an additional transport equation solved for the continuum gas bubble concentration. Increasing gas concentration was found to decrease the jet angle, the size of the upper recirculation region shrinks towards the nozzle and the lower recirculation region eye and impingement point move up markedly. At high gas concentrations the direction of flow at the surface was reversed. Bubble size was found to have a significant effect on the flow pattern. Smaller bubbles traveled further across the mold with the jet causing the jet to bend more. The gas fraction contours indicated a greater probability of deep penetration for smaller bubbles.

With increasing argon injection more heat was removed in the mold due to more shallow jet and higher impingement point. Smaller bubble size was seen to amplify this effect.

Although the present work is focused on the mold, the flow in the nozzle influences it, hence a brief review of the work done on nozzle flow follows. Hershey et al. [16] studied the fluid flow through bifurcated nozzles in both two and three-dimensions using the commercial finite element code FIDAP and the standard K-ε turbulence model. Najjar et al [15] simulated the fluid flow through bifurcated nozzles. They found the bottom port angle was the most important parameter influencing the jet angle. Increasing bottom port angle increased the jet angle. As the fraction of the port area with strong flow increased the jet was found to conform further to the port angle. Unless the combined area of the ports was less than the bore area of the nozzle there was a recirculation region observed at the top of the port. Casting speed was found not to change either the jet angle or any other characteristic of the jet.

The steel fluid flow near the steel-slag interface significantly influences the steel quality and hence is of interest. Theodorakakos and Bergeles [4] simulated the flow in a water model of the mold with an oil film for a slag layer to study the mechanism of break up of the steel-slag interface. The discretized steady state two-dimensional Navier-Stokes equations were solved on a non-orthogonal grid of changing shape, to resolve the interface accurately. A K-ε turbulence model was used and two sets of conservation equations for the two fluids were solved separately and iteratively. The amplitude of the interface waves was found to depend on the Froude number, requiring a minimum oil thickness in order to cover the entire surface without breakup. The model compared well with experiments demonstrating its ability to work for a steel-flux interface by changing fluid properties. Gupta and Lahiri[9] studied the fluid flow at the free surface of water models. They found the meniscus to have a wavy shape with the wave amplitude varying parabolically with the nozzle exit velocity. The kinetic energy along the surface was found to be maximum at the trough. Panaras et al.[21] studied the evolution of the free surface of a water model with time from a flat no-slip boundary. In accordance with Gupta [9] they found the elevation of the free surface to be proportional to the square of the velocity of the fluid entering the domain. Beyond a certain inlet velocity a surface discontinuity was found which indicates emulsification. The stability criterion for occurrence of this instability is the ratio of the maximum wave amplitude to the wave length and the critical value for this ratio was found to be 0.21.

Schulte et al [22] used water model experiments, numerical simulations and plant measurements to study the fluid flow in the mold. A K-ε turbulence model was used, with argon gas injection accounted for by treating the flow as a one-phase mixture with an equivalent density and viscosity based on volume fraction. An important result of this work is that quantifies an 'operating window' with respect to casting speed and argon flow rate to minimize defects in the final slab. For operating conditions in this window there is no meniscus agitation, the sub-meniscus velocity is below 0.4m/s, there are no flow oscillations, lower velocities along the narrowface to reduce bubble entrapment and no stagnation of flow close to the meniscus.

3.3 Current methodology

Certainly, the Reynolds-averaged approach is economical and several sensitivity studies can be performed. However, representation of the complex turbulence phenomena using a simplistic isotropic eddy viscosity model does not produce accurate results of the defect causing phenomena. As mentioned earlier, the transient turbulence structures play an important role in particle transport and flux entrainment. A proper analysis must therefore consider these transient phenomena.

We have recently embarked on the computation of these transient structures by numerically integrating the three-dimensional unsteady Navier-Stokes equations. Figure 3.1 is a schematic of the mold domain and coordinate system used in this study. Our intent is to perform a large-eddy simulation of the mold flow region. However, for Reynolds number considered (of the order of 12000 based on jet parameters) and the grid fineness used (1.5 million nodes), we did not find it necessary to activate the sub-grid scale viscosity (Smagorinsky model). The calculations were stable, and did not reveal any spatial oscillations or non-linear instability. Although the calculation may not have resolved the scales upto dissipation length scales, most of the large scales have been resolved thus capturing the important physics. For higher Reynolds numbers and coarser grids, we found that the sub-grid model was necessary to be activated.

The governing equations solved are the time-dependent Navier-Stokes equations for the filtered velocities, where the filtered velocities imply here a grid based filtering procedure. The filtered Navier-Stokes equations can then be written as:

Mass continuity $$\frac{\partial \bar{u}_i}{\partial x_i} = 0.0 \qquad (1)$$

Momentum $$\rho\left[\frac{\partial \bar{u}_i}{\partial t} + \frac{\partial\left(\bar{u}_i \bar{u}_j\right)}{\partial x_j}\right] = -\frac{\partial \bar{p}}{\partial x_i} + \frac{\partial}{\partial x_j}\mu\left(\frac{\partial \bar{u}_i}{\partial x_j} + \frac{\partial \bar{u}_j}{\partial x_i}\right) + \frac{\partial Q_{ij}}{\partial x_j} \qquad (2\text{-}4)$$

where $\bar{u}_i, \bar{u}_j$ are the filtered velocities, $\bar{p}$ is the filtered pressure, ρ is the density, and μ is the dynamic viscosity. The term Q_{ij} represents the sub-grid momentum fluxes given by the difference

$$Q_{ij} = \bar{u}_i \bar{u}_j - \overline{u_i u_j} \qquad (5)$$

The trace-free part of the sub-grid flux is modeled in terms of the resolved scales. Models based on eddy viscosity are frequently used, in which the trace free part τ_{ij} is assumed to be proportional to the symmetric strain rate tensor of the resolved scales. The proportionality constant μ_T is defined by:

$$\tau_{ij} = Q_{ij} - \frac{1}{3} Q_{kk} = 2\mu_T \bar{S}_{ij} \quad (6)$$

$$\bar{S}_{ij} = \frac{1}{2}\left(\frac{\partial \bar{u}_i}{\partial x_j} + \frac{\partial \bar{u}_j}{\partial x_i}\right) \quad (7)$$

The eddy viscosity μ_T is commonly calculated from a length scale and a sub-grid velocity scale. The most widely used model is due to Smagorinsky [23] in which the characteristic length scale is assumed to be proportional to the filter width (or grid spacing). The eddy viscosity is given by

$$\mu_T = C_S \Delta^2 \left| S_{ij} \right| \quad (8)$$

$$\left| S_{ij} \right| = \sqrt{2 S_{ij} S_{ij}} \quad (9)$$

The filter width is given by

$$\Delta = \left(\Delta_x \, \Delta_y \, \Delta_z \right)^{1/3} \quad (10)$$

where $\Delta_x, \Delta_y, \Delta_z$ are the mesh sizes in the three directions. In the conventional Smagorinsky model, the coefficient C_S is assumed to have a constant value, around 0.01. However, near walls, damping functions have to be used since the size of the sub-grid scales near the walls is smaller than the filter width.

The Smagorinsky model[23] has been widely used by a number of researchers. This model is easy to implement and serves the purpose of appropriately draining energy from the large scales of turbulent motion, such that energy does not build up at the high wave numbers. Recently, a more sophisticated sub-grid scale model has been proposed. In this model, the Smagorinsky coefficient is computed dynamically through a least-squares regression model. The resolved flow fields are once again filtered by a test filter, and the Smagorinsky constant is evaluated by relations between the test scale stresses and the grid scale stresses. The dynamic model gives the Smagorinsky constant as a function of time and space. The model has been evaluated in several model flows by a number of researchers. It is to be mentioned that the K-ε model also can be used as a sub-grid model if the turbulent viscosity can be interpreted as the viscosity due to the filtered small scales. In the present work, we have used the conventional Smagorinsky model as our initial choice. This model can initially produce results of sufficient accuracy to evaluate the importance of large-scale flow structures.

3.4 Numerical aspects

3.4.1 Numerical scheme

A finite-volume approach was used to solve equations (1) to (4). Central differencing with second order accuracy was used to discretize the equations on a staggered grid i.e. the flow velocities u,v and w are defined on the cell faces whereas pressure was defined at the cell center. The time integration of the equations was done using a semi-implicit, fractional step method. In the semi-implicit technique the y-diffusion has been treated implicitly whereas x and z diffusion are explicit. The viscous term is advanced implicitly using the Crank-Nicolson method whereas the remaining terms (convective and source terms from SGS stresses) are advanced explicitly using the second-order Adams-Bashforth method. After applying the semi-implicit procedure, the momentum equations take the following form:

$$\frac{\overline{u_i^{n+1}} - \overline{u_i^{n}}}{\Delta t} = \frac{3}{2} H_i^n - \frac{1}{2} H_i^{n-1} + \frac{1}{2}\left(\frac{1}{\mathrm{Re}_t} + \langle n_T \rangle\right) \times \left(\frac{\partial^2 (\overline{u_i^{n+1}})}{\partial x_j \partial x_j} + \frac{\partial^2 (\overline{u_i^{n}})}{\partial x_j \partial x_j}\right) - \frac{\partial \overline{P^{n+1}}}{\partial x_i} \quad (11)$$

where H_i is given by

$$H_i = -\frac{\partial}{\partial x_j}(\overline{u_i}\,\overline{u_j}) + 4d_{i3} + \frac{\partial}{\partial x_3}((n_T - \langle n_T \rangle)\frac{\partial \overline{u_i}}{\partial x_3}) + (n_T - \langle n_T \rangle)(\frac{\partial^2 \overline{u_i}}{\partial x_1{}^2} + \frac{\partial^2 \overline{u_i}}{\partial x_2{}^2})$$

$$+\frac{\partial n_T}{\partial x_1}(\frac{\partial \overline{u_i}}{\partial x_1} + \frac{\partial \overline{u_1}}{\partial x_i}) + \frac{\partial n_T}{\partial x_2}(\frac{\partial \overline{u_i}}{\partial x_2} + \frac{\partial \overline{u_2}}{\partial x_i}) + \frac{\partial n_T}{\partial x_3}\frac{\partial \overline{u_3}}{\partial x_i} \qquad (12)$$

where $<\nu_T>$ is the average of ν_T taken in the entire interior domain at a given instant.

In the fractional step method an intermediate velocity field $(\overline{\tilde{u}}_i)$ is calculated by neglecting the pressure gradient term in the momentum equations. The semi-implicit procedure involves solving for the y-diffusion terms using Alternate Line Inversion (ALI), whereas the x and z diffusion terms are treated explicitly. Subsequently the $(\overline{\tilde{u}}_i)$ field is corrected to satisfy continuity by solving for the pressure field at time (n+1) as seen in equations (13) to (15) below

$$\frac{\overline{\tilde{u}_i} - \overline{u_i{}^n}}{\Delta t} = \frac{3}{2}H_i{}^n - \frac{1}{2}H_i{}^{n-1} + \frac{1}{2}(\frac{1}{\mathrm{Re}_t} + \langle n_T \rangle)\times(\frac{\partial^2(\overline{\tilde{u}_i})}{\partial x_j \partial x_j} + \frac{\partial^2(\overline{u_i{}^n})}{\partial x_j \partial x_j}) \qquad (13)$$

$$\frac{\overline{u_i{}^{n+1}} - \overline{\tilde{u}_i}}{\Delta t} = -\frac{\partial f^{n+1}}{\partial x_i} \quad \text{and} \quad \nabla^2 f^{n+1} = \frac{1}{\Delta t}\frac{\partial \overline{\tilde{u}_i}}{\partial x_i}, \qquad (14)$$

where $\overline{f^{n+1}}$ and $\overline{P^{n+1}}$ are related through

$$\overline{P^{n+1}} = \overline{f^{n+1}} - \frac{\Delta t}{2}(\frac{1}{\mathrm{Re}_t} + \langle n_T \rangle)\nabla^2 \overline{f^{n+1}} \qquad (15)$$

Equations (13) and (14) are solved to obtain the velocity field at the (n+1)th time level.

3.4.2 Initial and boundary conditions

Since the scheme involves time integration of a turbulent flow field the initial condition will not effect the accuracy of the final solution, although it will influence the integration time to reach a statistically stationary state. Recall from the introduction that the structure and turbulence level varies widely through the flow field. In order to avoid any residual flow regions resulting from initial conditions, which would require longer integration time to attain stationarity, zero flow velocities are assumed initially throughout the domain.

The mold domain in figure 3.1 is one half of a water model of a continuous caster. The partition is therefore a symmetry boundary whereas the wideface and narrowface are wall boundaries. Three 35mm diameter openings uniformly spaced on a bottom plate are used to drain out the flow from the water model. This translates into one and a half 35mm square mass flow boundaries along the bottom of the model domain. Water model studies without argon injection for the flow rate studied show less than 3mm variation in the meniscus level in space and time. Considering this the free surface is replaced by a rigid free slip boundary.

Though the inlet condition influences the mold flow, the extent and nature of this influence on the transients has not been studied. The nozzle is replaced by an inlet window equal in size to the nozzle port opening. Two different inlet conditions, namely a plug flow with velocity corresponding to the flow rate and the fully developed turbulent flow from a square duct changing at each time step in accordance to the duct flow are used. The fully developed turbulent flow in a square duct was simulated using the same numerical scheme described earlier using a FORTRAN computer program LES3D developed at the CFD lab at the University of Illinois at Urbana Chmapaign. The duct length chosen was six times the duct side. The duct walls were essentially wall boundaries and periodicity was imposed along the axial direction. The computational grid used for this simulation consisted of 64x64x128 grid cells in the two crosswise and streamwise directions respectively. For the duct Reynolds number of 12000 and grid fineness (0.5 million) used, activation of the sub-grid scale (Smagorinsky) model was not found necessary. A suitable pressure gradient was imposed in the axial direction to induce the desired flow rate. Following is a brief discussion of the results of the square duct flow. Figure 3.2 a) is time mean plot of cross-stream velocities. Since the axial direction is homogeneous the mean includes an average of all axial planes simulated. The cross-stream velocities are seen to convect mean flow from the center to the corners of the duct, which is in agreement with previous work[24]. Figure 3.2 b) is a similar mean axial velocity contour plot. Figure 3.3 a) and (b) are instantaneous cross-stream velocity vector and axial velocity contour plots respectively showing the turbulent mixing flow with randomly distributed structures in both cross-stream and axial directions. The results of this simulation compared favorably to the work of Madabushi and Vanka [24] validating the numerical scheme and computer program used.

3.4.5 Computational details

A computational grid consisting of 128x185x64 cells in the x,y and z directions (see figure 3.1) was used. The maximum gradients in the flow field occur in the jet and its shear layer, requiring finest grid sizes in this region. Hence the grid was stretched in the y direction using a ratio of 1.03 from the edges of the inlet opening to both the top and bottom of the mold. A uniform grid of 32 cells in the y and 24 cells in the z was used at the inlet. Uniform grid spacing was used in both x and z directions. The FORTRAN computer program LES3D was used for the computations. A time step Δt of 0.001s, satisfying the Courant-Friedrichs-Lewy (CFL)[24] stability condition for the convective terms and diffusion time step was used. The computations were performed at the National Center for Supercomputing Applications (NCSA) and the CFD lab at the University of Illinois at Urbana Champaign, requiring 18(CPU) sec per time step. Message Passing Interface (MPI) was used to parallelize the FORTRAN program. Almost linear speedup was found up to eight processors. Considering queuing time and additional post processing time for increased processors four processors were used for NCSA computations.

3.5 Results and discussion

The discretized governing equations were integrated in time until a statistically stationary flow field was attained. Time averaged velocity statistics were computed over the entire flow field. Root mean square velocities were computed along the jet and at specific locations in the upper and lower recirculation regions. Time animations of instantaneous velocity vector and contour plots and monitoring points were used to study the transient flow structures in different parts of the mold. In the following sections an overview of the instantaneous and time averaged flow is discussed first. This is followed by a detailed discussion of the various flow transients in jet, upper and lower rolls. A discussion of time averaged and root mean square statistics and comparison with Particle Image Velocimetry (PIV) measurements is next. Finally the implications of the transient flow results on sensor location in an actual caster are considered.

3.5.1 Overview of mold flow

Figure 3.4 is an instantaneous velocity vector plot with simulation results on the left and PIV measurements on the right. The flow is turbulent consisting of a range of flow scales, as witnessed by the velocity fluctuations across the flow field. Most of the instantaneous flow features in the PIV measurement are duplicated by the simulation. The flow emerges from the nozzle as a jet, which is seen to diffuse as it travels across the mold, impinging on the narrow face and spreading into upper and lower wall jets. The upper wall jet is found to flow along the narrow face and meniscus, finally recirculating into the main jet. The lower wall jet flows down along the narrowface towards the mold exit at the bottom. The low pressure in the main jet is seen to entrain flow from below the nozzle causing a recirculation region below the main jet. Some crossflow from the lower wall jet to the flow entrained by the main jet is observed in both the simulation and PIV measurement. Averaging several instantaneous results, such as figure 3.4, the time averaged flow field in figure 3.5 for both simulation and experiment is obtained. Most of the flow features in the instantaneous result, discussed above, are also observed in the time averaged plot. The shape of the upper and lower rolls and their eye locations agree very well between simulation and experiment. A region of low velocity vectors exists at the intersection of the meniscus and the narrowface in experiment and simulation. In order to conserve mass the additional flow from the upper wall jet must exit the center plane. The cross plane flow in the simulation is examined later, in the time averaged results section. The biggest discrepancy between the results is the lower entrainment of the flow from below the nozzle in the PIV measurement compared to the simulation.

3.5.2 Flow transients

The variation of the horizontal velocity component with time at four different points along the jet centerline is shown in figure 3.6. The location of points 1-4 is seen in the figure and they are progressively away from the jet inlet in the center plane. Stationarity of the flow field has been ensured before the results are collected. At all four points the flow is seen to be turbulent with the velocity fluctuating with time about a mean value. The highest frequency of the fluctuations is found to decrease away from the inlet. Since the highest frequency is associated with the smallest length scale, the size of the smallest turbulent length scale decreases away from the inlet. The diffusion of jet momentum decreases both the mean velocity and the amplitude of the turbulent fluctuations along the jet. Close to the impingement point (4 in figure 3.6) the horizontal velocity frequently reverses direction, as the turbulent fluctuations are comparable to the mean value. Figure 3.7 is a representative instantaneous velocity vector plot of the center plane of the simulated jet. The jet diffuses and spreads away from the inlet with the jet angle not varying significantly from the 30^{o} inlet value.

Recall that the upward wall jet flows along the narrowface, meniscus and back into the main jet, forming a recirculation region called the upper roll. In the time averaged velocity vector plot the upper roll appears to be a single flow loop, which is also seen in the instantaneous simulated velocity vector plot in figure 3.8. Though the velocity fluctuations throughout the upper roll confirm the existence of smaller length scales, none are comparable in size to this single flow loop. Figure 3.9 is another simulated instantaneous velocity vector plot. The single flow loop in the previous results is replaced by distinct vortices comparable in size to the upper roll. These vortices transport the flow from the upward jet to the main jet. The flow alternates without definite pattern between the two extremes of a single flow loop and a set of distinct vortex structures, a feature also observed in PIV measurements in chapter 1. The presence of vortices instead of a single loop causes greater mixing and turbulent transport, which would aid inclusion particle entrapment. This is especially true for bubbles, which must be aspirated through the upper roll and slag layers. Though this simulation only considers single phase flow, the results will be equally applicable for low gas flow rates (eg. 1 cubic ft per hour) and small particle concentrations.

Figure 3.10 shows a sample plot of time variation of velocity at a point close to the top surface, halfway between the nozzle and the narrow face. The PIV measurement points are spaced 0.2s apart as compared to 0.001s increments in the simulation. As discussed in chapter 1, the PIV velocity variation shows the existence of two prominent time scales. The short time scale is about 0.7s and is predicted well by the simulation. The large time scale variation in PIV measurements of 45s or more, which was seen to cause periods of 5-10s wherein the velocities are four to five times their mean values in chapter 1, is absent in the simulation. This was attributed this to the large variations in the spatial average jet angle, based on the similar time scales for the jet angle and surface velocity variation. The simulation jet, as discussed earlier, has an almost time invariant spatial average angle. This nearly constant angle would not provide for large changes in the flow rate close to the water surface resulting in smaller velocity fluctuations compared to the PIV measurement. This discrepancy between simulation and PIV measurement adds strength to the correlation in chapter 1, between large variations in jet angle and appearance of periods of high velocities close to the water surface. The sudden appearance of higher velocities close to the top surface could cause shear entrainment of liquid flux in a caster and hence inlet conditions should be modified to be closer to that used in the present work.

Figure 3.11 is a representative set of simulated instantaneous velocity vector plots of the flow in the lower recirculation region. The flow from the lower wall jet travels to the bottom of the mold before part of it recirculates into the main jet from below the nozzle. The flow in this region is turbulent, evidenced by the spatial and temporal velocity fluctuations. The center and shape of the lower recirculation region is seen to vary with time. Figure 3.12 is a sequence of simulated instantaneous velocity vector plots of the flow in the lower recirculation region spaced 2.5s apart. At t(s), higher up in the mold (at 0.45m) the flow from the lower wall jet recirculates into the flow being entrained by the main jet from below the nozzle, forming a flow structure which is seen to expand downwards over a 7.5s period, finally merging into the lower roll. This flow phenomenon is found to occur at irregular intervals. The formation and evolution of this flow structure and the time scale over which it occurs is similar to that observed in the PIV measurements in chapter 1. The difference in the inlet condition of the present work from that used in the PIV measurements of chapter 1 confirms that this flow structure is caused by instabilities inherent in any turbulent flow and not by fluctuations in the flow field at the inlet.

3.5.3 Mean flow field

The stationary simulated flow field was averaged until a time invariant mean flow field was obtained. The time period needed for an invariant mean varies over the flow field and an average over 60s was found adequate. Following is a discussion of the mean flow results in the jet, upper and lower roll region. The results are compared with PIV measurements where available.

Figure 3.13 is a plot of the jet speed in the center plane along the extrapolated jet centerline (from the inlet at an angle of 30^o downwards), from simulation and PIV measurements. The simulated jet velocity is found to decrease from its initial square duct flow centerline value of 0.5m/s to near zero values close to the impingement point on the narrowface. This decrease follows from the diffusion of jet momentum in the direction perpendicular to its centerline. Close to the inlet the diffusion rate is very low followed by a region of constant slope and finally a sharp drop close to the impingement point. Three sets of PIV measurements, each time averaged over 60s with 300 instantaneous measurements (a measurement consists of two correlated snapshots), are plotted in figure 3.13. The three sets are found to be highly consistent with each other confirming the time invariance of the PIV measurements. Except close to the inlet the PIV measurement is consistently lower than the simulated value. Both in the central region and close to the impingement point the PIV measurement has the same slope as the simulation indicating equal diffusion rates along most of the jet. The experimental setup for the PIV measurements has a 90^o slide-gate causing a swirl at the inlet, which is absent in the simulation. The results presented in chapter 1 suggested that the swirl in the experimental jet persists more than halfway across the mold. The maximum velocity in a swirling jet occurs outside the center plane as opposed to the near logarithmic square duct inlet profile with its maximum at the centerline. Thus the existence of the swirl is confirmed in the lower PIV measurements along the jet centerline. In addition to the information on jet diffusion obtained from figure 3.13 the jet profile and spread are of interest to quantify the mean jet behaviour. Figure 3.14 shows the variation of the time mean jet profile along the extrapolated jet centerline, in simulation and PIV measurement. Both the simulated and PIV measurement jets are seen to diffuse and spread away from the inlet. The jet spread is more on the side of the upper roll than the lower roll, as evidenced by the more gradual decrease in velocity away from the jet peak on the upper roll side. The peak value of the simulated jet remains along the extrapolated jet centerline whereas the PIV measurement peak progressively shifts above it. This confirms the decreasing downward angle of the PIV measurement jet away from the inlet, also seen in the time averaged velocity vector plot in figure 3.5. The consistently lower peak value of the PIV measurement compared to the corresponding simulated value follows from the discussion of figure 3.13 above. The simulated time averaged cross plane jet spread and diffusion are seen in figure 3.15. The jet is seen to spread and diffuse smoothly in the cross plane. A portion of the jet flow recirculates back along the wide faces after impingement on the narrow face.

Recall from the overview section, the region of low velocity vectors in the top left corner region of the mold (see figure 3.5) in both simulation and PIV measurement. The time mean flow in the cross plane direction in this region is seen in figure 3.16, which is a time averaged velocity vector plot of a plane parallel to the narrowface, 20mm from it. The jet impingement point is seen at the bottom of the plot, with velocity vectors in opposite directions on either side of it. After impingement the jet spreads in the cross plane resulting in more upward flow along the wide faces than in the center plane. This bias in cross plane flow gradually diffuses resulting in more or less even flow in the cross plane near the top surface. The flow out of the center plane of the jet, finally diffusing across the cross section along the top surface explains the region of low velocity vectors seen in figure 3.5.

The time mean flow at the intersection of the narrow face and top surface, in the center plane is seen in figure 3.17. The flow from the upper wall jet is unable to follow the sharp bend resulting in a shear driven recirculation region in this corner. This recirculation region is found to extend across the thickness of the mold and is also seen in dye injection studies in the water model. The sizes of it in experiment and simulation are comparable. The reversed low velocity flow near the corner will affect the shear driven motion of the liquid flux layer on the surface of the caster. In addition it is significant to meniscus solidification and feeding of flux into the gap between the shell and narrowface.

The time mean flow velocities below the water surface, in the center plane, halfway between the nozzle and narrowface are seen in figure 3.18. The plot includes three PIV measurement sets and the simulated mean. In both the simulation and measurement the flow is found to be nearly horizontal with the vertical component of velocity nearly zero. Except close to the water surface the simulated and measured values compare very well. Near the water surface two measurement data sets compare well with the simulation. Set 3, if extrapolated to the water surface gives more than twice as large values for the measurement and could be considered inaccurate. Detailed PIV measurements of the region very close to the water surface reveal set 3 to be accurate with the low velocities in sets 1 and 2 caused by improper correlation between the snap shots used to obtain an instantaneous PIV measurement. The larger velocities in the mean PIV measurement are a result of the time periods with three to four times mean velocity present in the experiment but absent in the simulation, as discussed earlier in the flow transients section.

The mean flow field in the lower roll is quantified by figure 3.19. The simulated and PIV measurements of vertical velocity in the center plane, along the wideface, at four locations (0.3, 0.4, 0.5 and 0.6m) below the top surface are plotted. The PIV measurement consists of 10 sets each averaged over 200s with 200 instantaneous measurements. The mean and range of these 10 sets are indicated in figure 3.19 by the symbols and error bars respectively. The velocities of all plots in figure 3.19 change sign close to the center of the graph in accordance with the opposite flow directions of the lower jet and flow being entrained by the jet from below the nozzle. Close to the narrow face the simulated plot at 0.3m is significantly different from those at 0.4, 0.5 and 0.6m. The simulated impingement point is close to 0.3m, causing the plot at 0.3m to pass through the simulated jet. The experimental downward jet angle, as discussed earlier, decreases progressively towards the narrow face raising the impingement point towards the top surface and decreasing the vertical velocities at 0.3m compared to the simulation. Close to the narrow face the lower wall jet causes a sharp increase in the vertical velocities from 0.3 to 0.4m. Further below the velocity decreases from 0.4 to 0.6m due to diffusion of the lower wall jet parallel to the narrow face. In the left half of the plot, close to the narrowface, the simulated and PIV measurements agree well from 0.4 to 0.6m. The biggest discrepancy between simulated and experimental values, remarked earlier in the time averaged velocity vector plot of figure 3.5, is the significantly lower vertical velocities below the nozzle. In chapter 1 persistent asymmetry between the two lower rolls was found to exist. For extended periods of time one roll was found to be larger than the other, which would cause the central portion of one or the other rolls to be present below the nozzle. When time averaged this will result in very low vertical velocities below the nozzle, explaining the discrepancy.

3.5.4 Root mean square (RMS) statistics

Figure 3.20 is a plot of RMS speed along the jet centerline in simulation and PIV measurement. The RMS values for the simulation and PIV measurement were computed over 60s using a time invariant mean value. The simulated RMS values in different cross planes are also seen in the plot. Except close to the inlet, both simulated and measured values match very well, with the RMS speed remaining nearly constant over most of the jet length. Close to the inlet the measured values are much larger than the simulated values. Significant out of center plane motion of the experimental jet was seen in the results presented in chapter 1. This can be accounted for in the simulation considering cross plane simulated values. Moving from 1-1 to 3-3 results in near perfect agreement between simulation and experiment. This confirms the similar turbulent fluctuation magnitudes in simulation and measurement, if the out of plane motion of the experimental jet is accounted for. The RMS velocity below the water surface in simulation and measurement is seen in figure 3.21. Close to the top surface the measured values are more than twice that simulated, in accordance to the periodic appearance of three to four times larger than mean velocity flow in the experiment (see figure 3.10), which is absent in the simulation. Finally the representative RMS velocities in the lower roll are plotted in figure 3.22. This plot is similar to the time-averaged version discussed earlier consisting of RMS of the vertical velocity component in the center plane, along the wideface and 0.5m below the top surface. The simulation results have been computed over 60s using a time invariant mean value. There is a sharp peak in the simulated results close to the narrow face. This corresponds to the highly turbulent lower wall jet, which passes through this region. Except this sharp peak close to the narrow face the RMS values are almost constant on the narrow face half of the lower roll. The RMS values on the nozzle half of the lower roll are lower by a factor of two over the narrow face half. Similar to the time averaged results the PIV measurement consists of 10 sets each over a 200s period with 200 instantaneous measurements, for both halves of the mold. The overall RMS and range of these results is plotted in figure 3.22 for the left and right halves of the mold. The large range of the RMS values suggests that the statistics are not time invariant. This is confirmed by the results in chapter 1, that the flow in the lower roll goes through a sequence of at least three different configurations each persisting for as long as 40s. The asymmetry between the lower rolls causes a difference between the statistics for the two halves of the lower roll. The RMS values of the PIV measurements agree very well with the simulated results, both in trend and actual values. The peak close to the narrow face in the simulation is considerably spread out on the left half whereas it is similar on the right half of the mold in the PIV measurement.

3.5.5 Implication of flow transients on use of electromagnetic sensors on casters

Figure 3.23 shows location of two MFC velocity sensors on half of the wideface of the mold, with dimensions scaled by 0.4 to correspond with the water model. The sensors can be used to determine whether the flow pattern in the molten steel has only a single lower roll or a lower and upper (double) roll [14].The signals can also provide a measure of the strength of the velocities close to the top surface.

Each MFC sensor consists of two probes located close to each other behind the copper mold plates. Both probes emit a magnetic field. The flow of conducting steel through this magnetic field induces an electrical signal in each of the probes, according to Faraday's third law of electromagnetism. The time shift between prominent features of the two signals is a measure of the time taken by the flow to convect from one probe to the other. The average velocity in the region between the probes is then the distance between the probes divided by this time shift.

To enable comparisons of the MFC sensor signals with the numerical model, simulation results were extracted to predict the output of the probes. The horizontal velocity component convects the flow structures from one probe to the other. Prominent flow features appear in both signals, with a time shift corresponding to the average horizontal velocity between the probes. Thus, the horizontal velocity components calculated within the cells in the area beneath each probe head were first averaged in each plane parallel to the wideface. Next, the attenuation of the magnetic field strength with distance into the flow was taken into account by assuming that the induced signal strength decreased inversely with the square of the distance from the wideface, according to figure 3.24. Thus, the overall simulated signal was calculated by taking a weighted average of the horizontal velocities calculated in the different planes beneath the probe head. Weighting factors were taken from figure 3.24. The average of the two signals predicted at each probe indicates the best possible sensor output.

Figures 3.25 a) and (b) show the simulated probe signals and the sensor output predicted at locations A and B (see figure 3.23). At position A, near the surface, the two probe signals are very similar, except for an obvious time shift, so it is quite feasible that the average of the two signals could be extracted by the sensor logic. At position B, however, the two probe signals are very different. They are clearly not always the same basic signal offset in time, so it is likely that large errors might arise in predicting their average by the sensor. The reason for this difference in behavior of the signals at A and B can be understood by looking at the flow fields near the two sensors.

Figures 3.26 and 3.27 are samples of instantaneous velocity-vector plots taken in two planes parallel to the wideface in the top region of the simulation. The upper roll at this instant is seen to consist of a set of distinct vortex structures, as opposed to the single large recirculation structure seen in the time average vector plot. The upper roll alternates chaotically between these two extremes. Flow at position A near the surface is seen to be relatively consistent, as the velocities are generally horizontal and similar at both probes. The variation through the mold thickness is not significant, so the attenuation of the electromagnetic signal should not be important. Flow at position B is very different, however. The mean convection of vortices is not always horizontal. Flow past one probe may not be seen by the other probe. Thus, the probe signals may not be correlated (Figure 3.25 b). Figures 3.26 and 3.27 also show how vortex structures traverse almost randomly across the caster, especially near the center of the roll. Velocities recorded by the probes could suggest a change in the direction of flow for several seconds (Figure 3.25 b; probe 2-B; 32-35s and 62-65s) that could be falsely interpreted as a change between single and double roll patterns. In conclusion, for accurate predictions, the sensor probes must be placed near the top surface.

3.6 Summary

The Large Eddy Simulation (LES) approach has been used to simulate the turbulent, transient fluid flow in a water model of a continuous caster. The results of the simulation agree well with the PIV measurements of presented in chapter 1. Together the two approaches provide insight into the flow transients in continuous casting molds. An electromagnetic sensor (MFC) located on the actual caster provides point velocity signals, which provide information about the fluid flow in the caster. The simulated results are also compared to the MFC output signals and have been used to both better interpret the sensor measurement technique and study its optimum location.

The highest frequency of velocity fluctuations along the jet centerline decreases away from the inlet. Due to jet diffusion both the mean and RMS velocity decrease away from the inlet along the jet centerline. The mean, however, drops faster than the RMS resulting in frequent flow reversal close to the impingement point. The upper roll structure is seen to alternate between a single large recirculation region and a set of distinct vortex structures of size comparable to the upper roll. This observation is consistent with the PIV measurement results. The horizontal velocity variation with time close to the water surface shows the existence of a prominent 0.7s time scale, which is also seen in the experiment. In accordance with the correlation made in chapter 1, due to the absence of large variations in simulated jet angle the larger time scale of 45s seen in the PIV measurement is not captured by the simulation.

In the lower roll, periodic diversion of flow from the lower wall jet to the flow entrained by the jet from below the nozzle results in the formation of a flow structure, which then expands downwards and finally merges into the lower roll. A similar flow structure is seen in PIV measurements, which confirms that this flow structure is caused by instabilities inherent in any turbulent flow and not by fluctuations in the flow field at the inlet of the mold.

In time averaged velocity vector plots of PIV measurements in the center plane, low velocity vectors were found in the region formed by the intersection of the narrow face and top surface. This region is also seen in the simulation and had been attributed earlier in chapter 1 to three dimensional flow in this region. Examination of the flow across planes parallel to the center plane in the simulated result shows that the jet after impingement spreads out, with larger flow along the wide faces than the center plane. This biased flow diffuses, finally resulting in uniform flow across planes along the top surface. This leaves a region of low velocity in the center plane where most of the flow has been diverted out of it.

A small recirculation region is seen in the simulation at the intersection of the narrow face and top surface. This has also been observed in dye injection studies in water models. The flow from the upper wall jet is unable to follow the sharp bend shear driving a recirculation region in this corner. The reversed low velocity flow near the corner, resulting from the recirculation region, will affect the shear driven motion of the liquid flux layer on the surface of the caster. In addition it is significant to meniscus solidification and feeding of flux into the gap between the shell and narrowface.

The simulation of the MFC sensor signals illustrates the great importance of locating the sensor in a stable region of the flow if accurate velocities are to be extracted. Sensors positioned in the current location just beneath the top surface should accurately output both the roll pattern and velocity history. The individual probes of sensors positioned deep in the recirculation zone experience very different transient flow fields, so cannot be relied upon to produce accurate velocities.

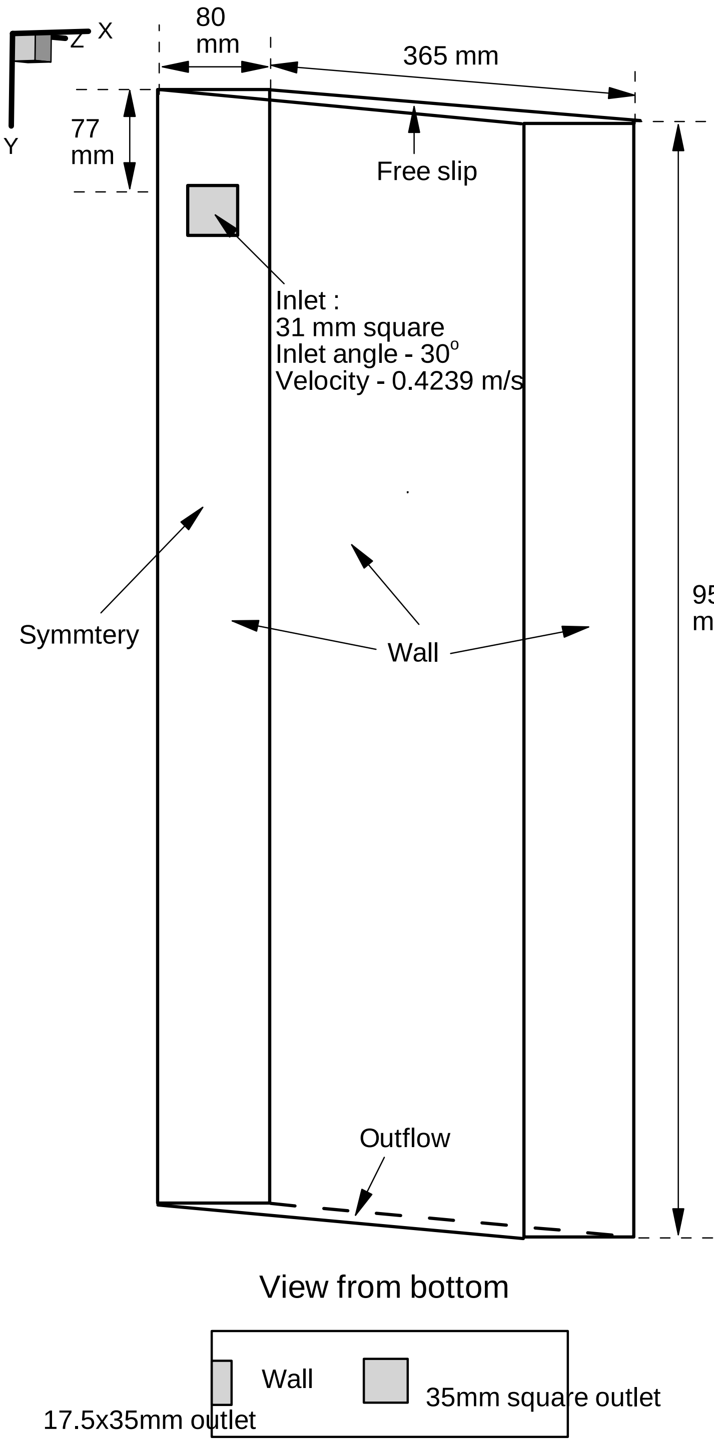

Figure 3.1 Schematic of domain used for simulation

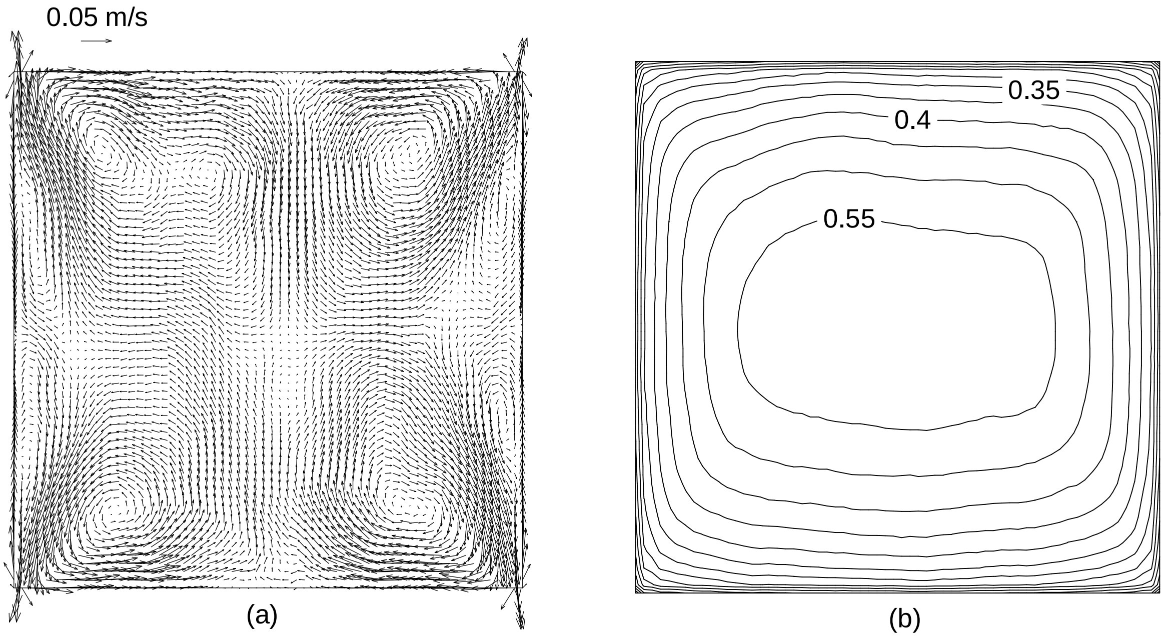

Fig. 3.2 (a) Mean secondary flow velocity vectors and (b) axial velocity contours in cross sectional plane

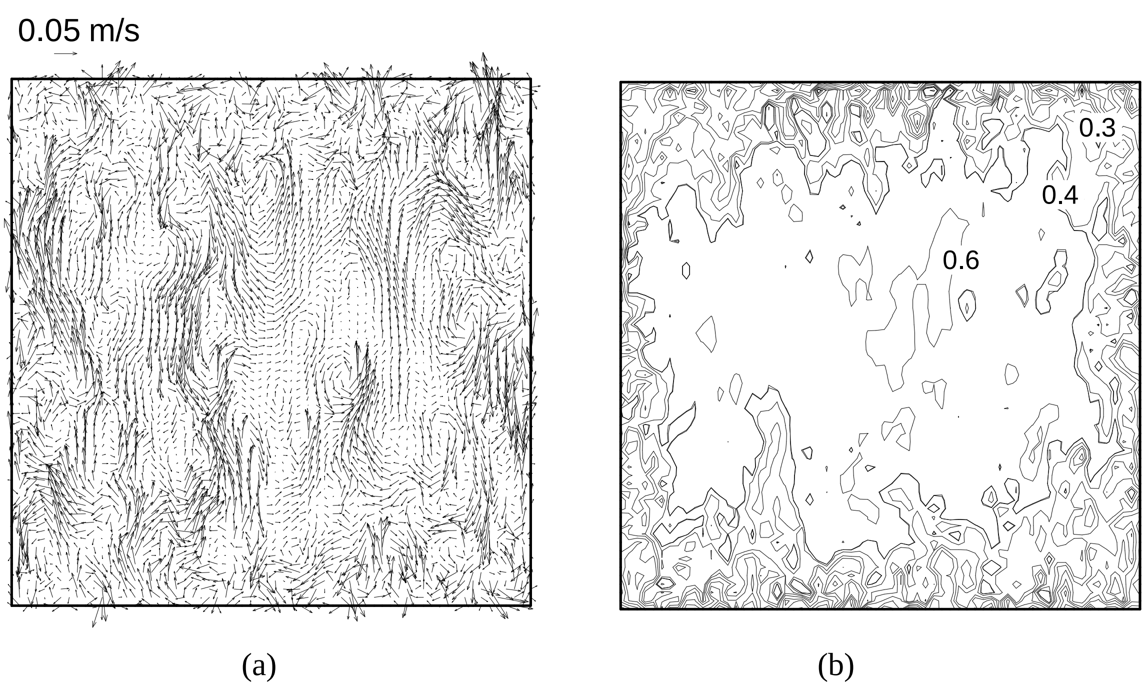

Fig 3.3 (a) Instantaneous cross-stream velocity vector and (b) Instantaneous axial velocity contour plots in a cross sectional plane

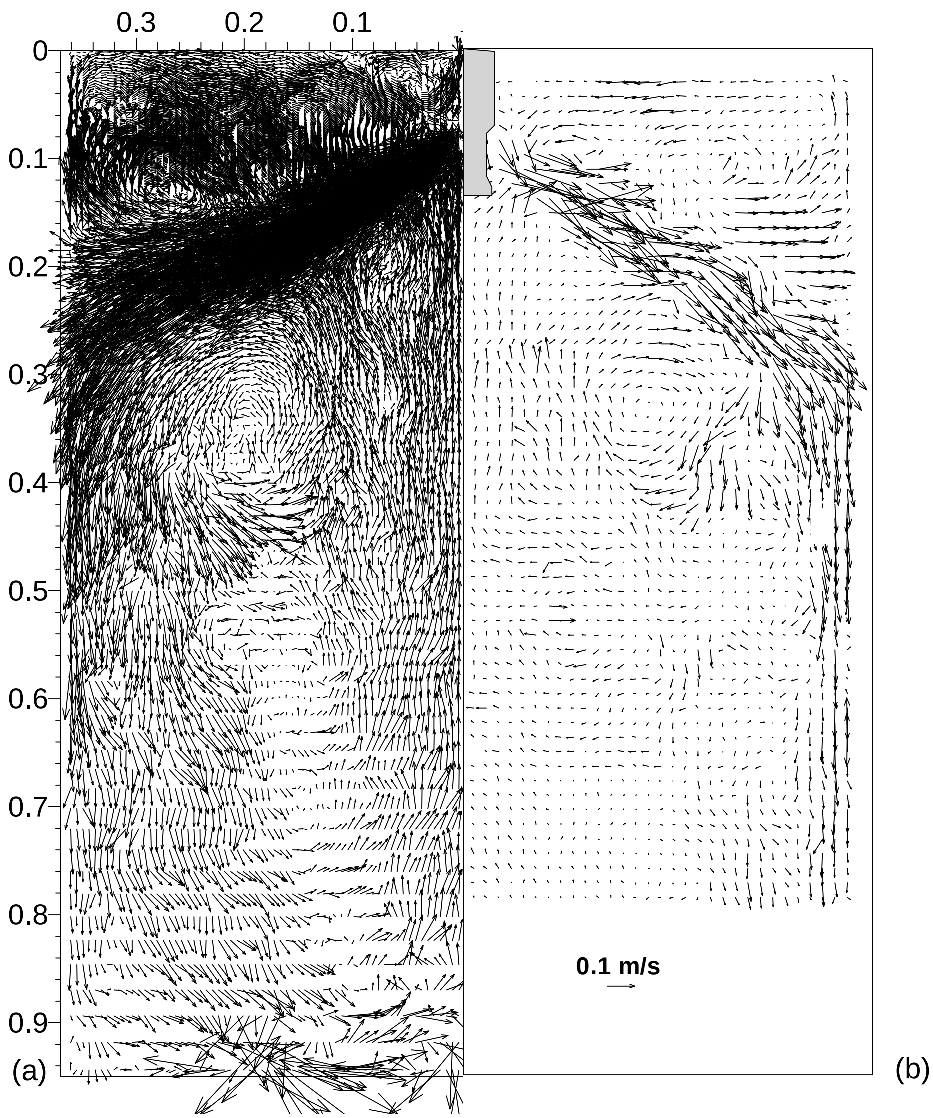

Figure 3.4 Instantaneous velocity vector plots of (a) simulation and (b) PIV measurement

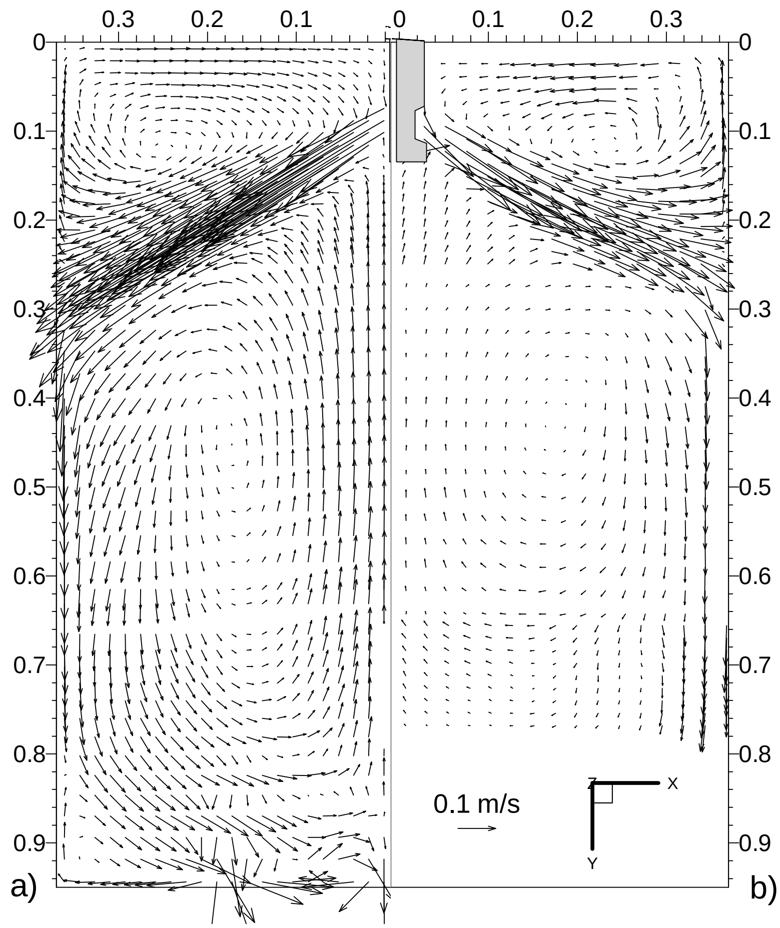

Figure 3.5 Time averaged velocity vector plot of (a) simulation and (b) PIV measurement

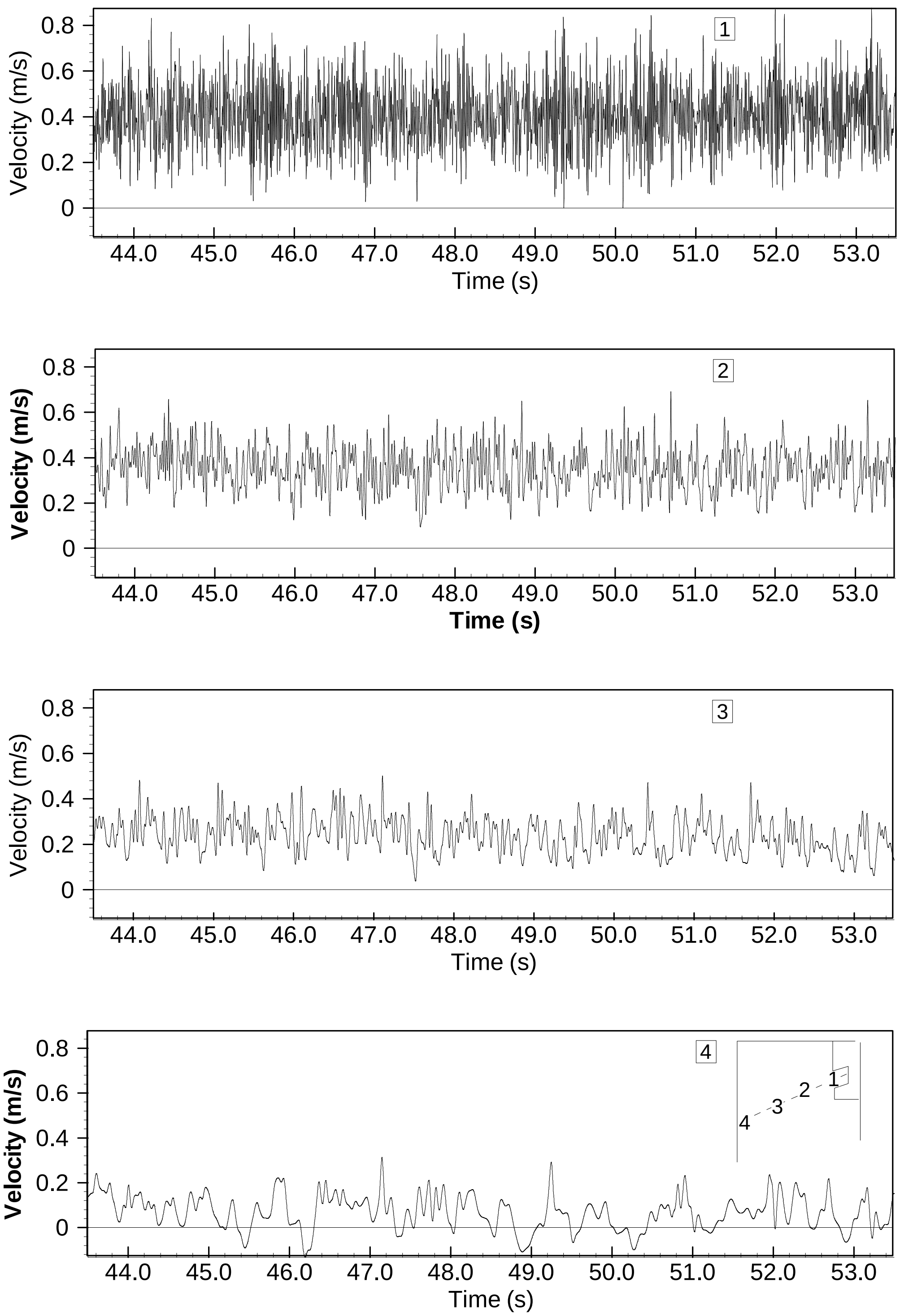

Figure 3.6 U velocity variation with time at points along jet centerline

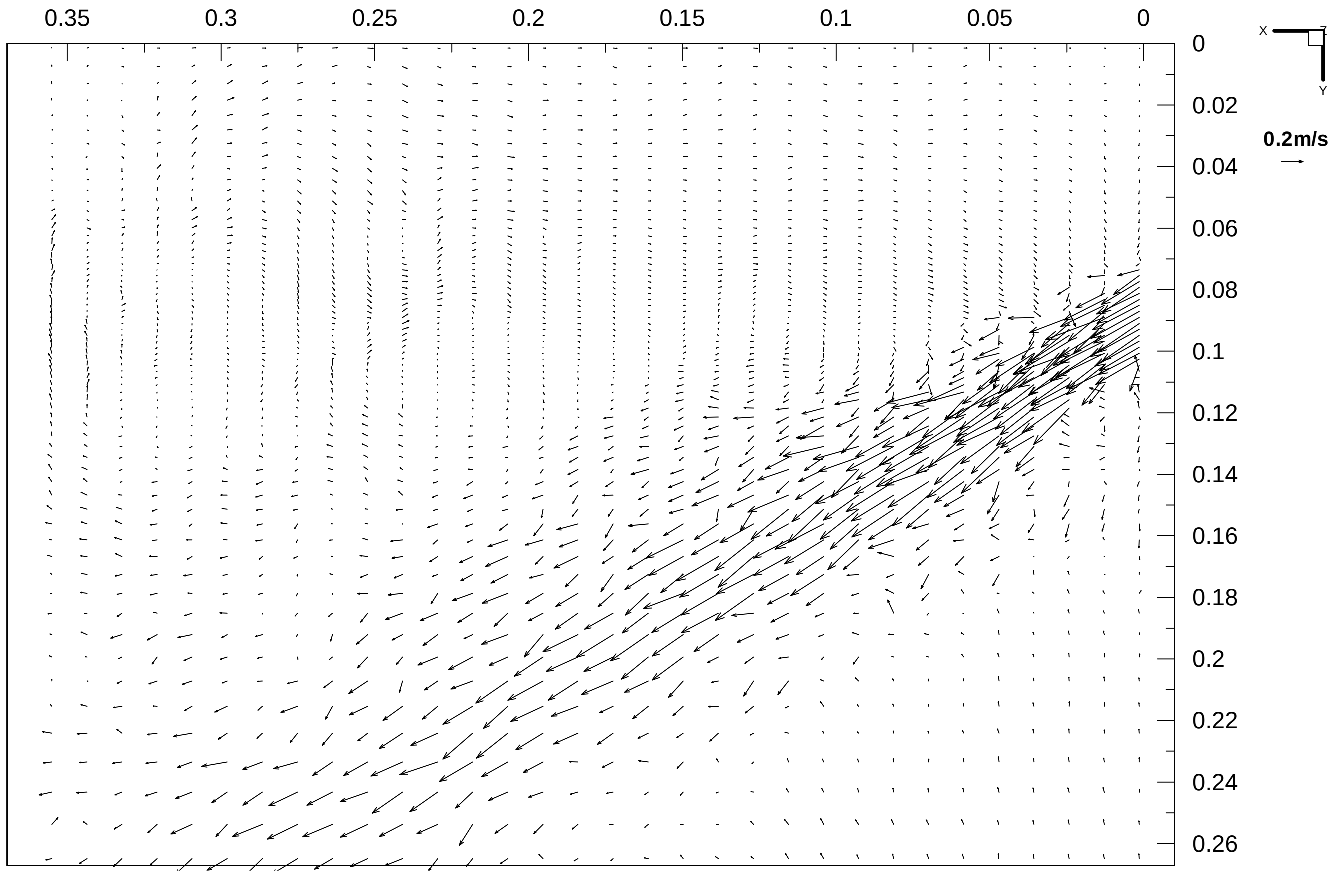

Figure 3.7 Instantaneous snap shot of simulation jet

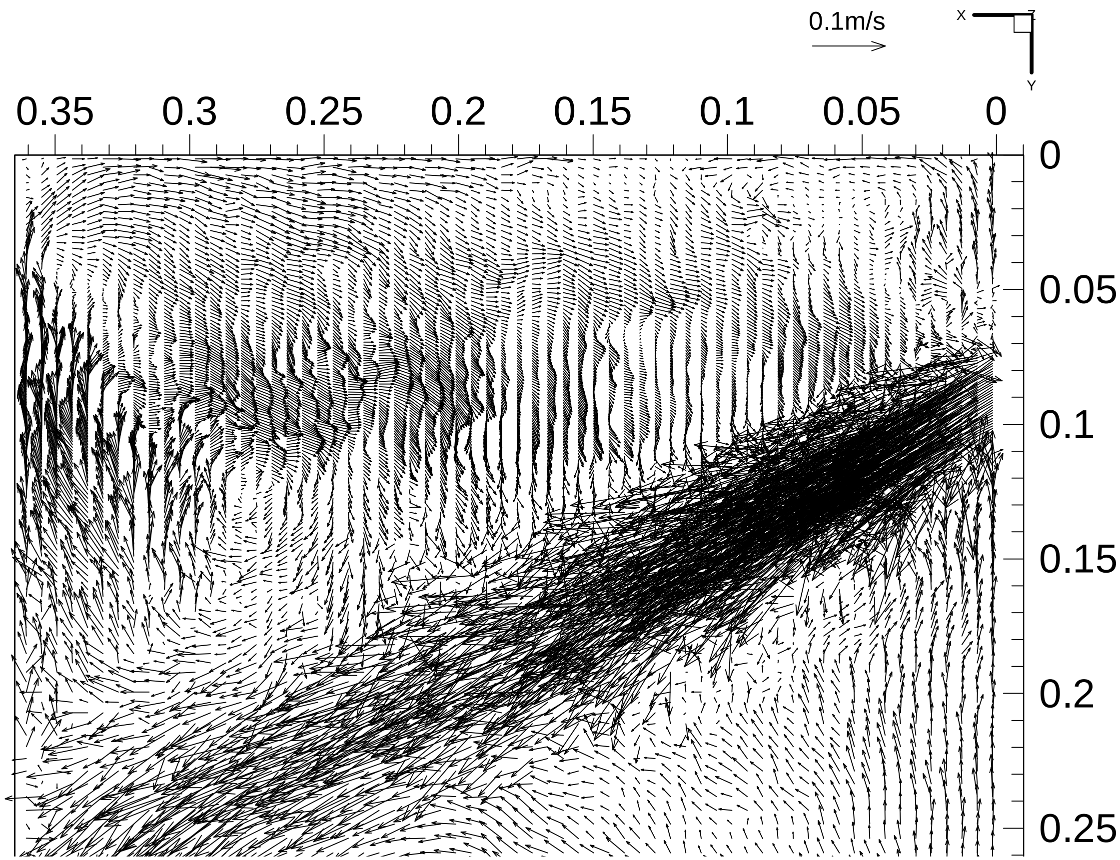

Figure 3.8 Instantaneous simulated velocity vector plot with upper roll as a single recirculation region

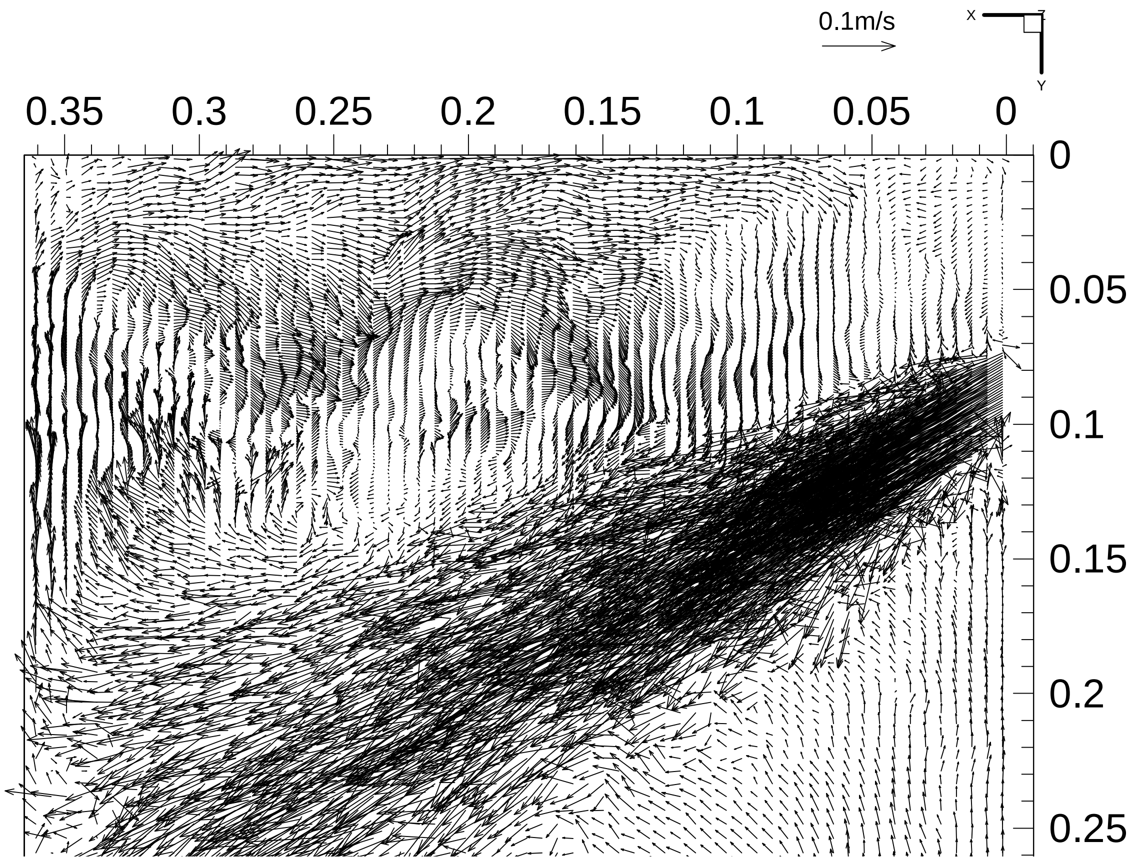

Figure 3.9 Instantaneous simulated velocity vector plot with upper roll as a set of distinct vortices

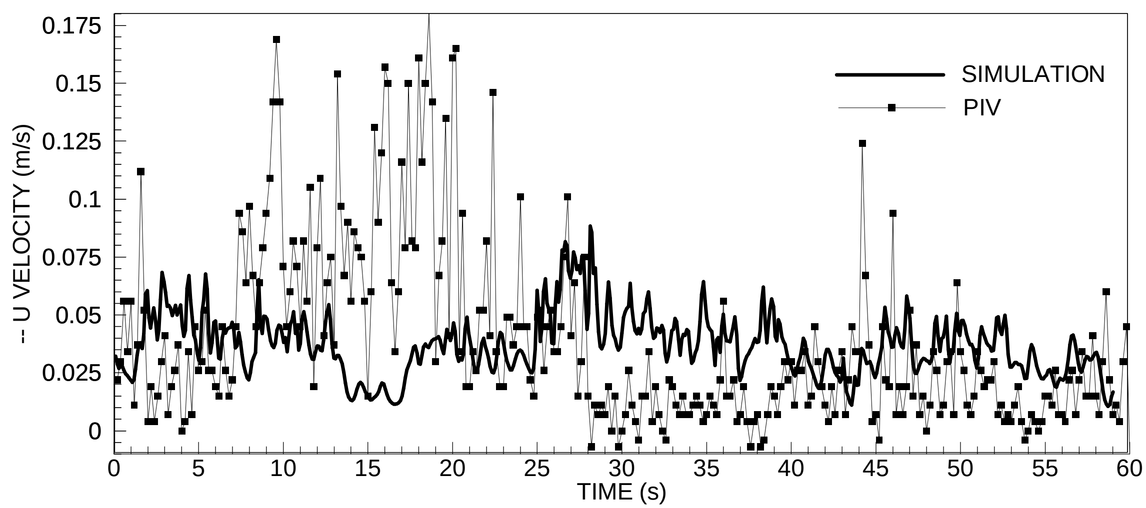

Figure 3.10 Plot of velocity variation with time at a point close to the water surface halfway between the nozzle and narrow face

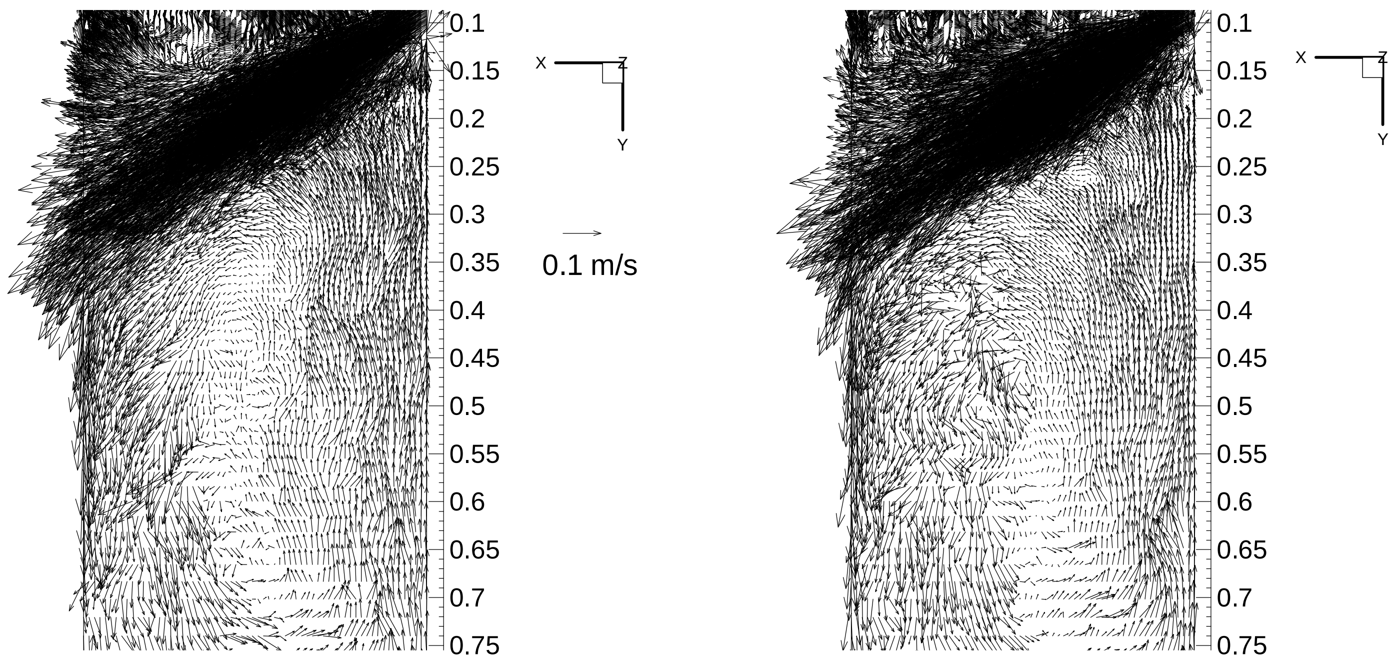

Figure 3.11 Instantaneous simulated velocity vector plots

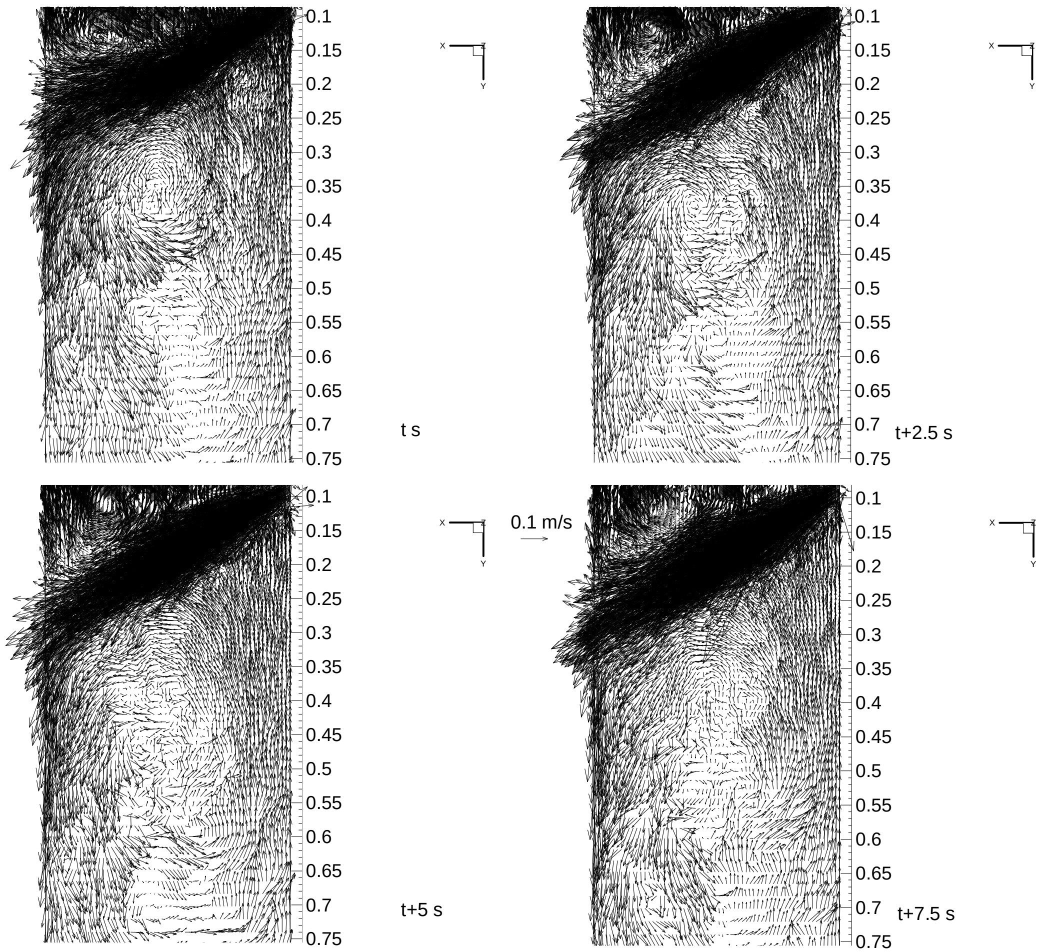

Figure 3.12 Instantaneous simulated velocity vector plots showing structure formation and motion

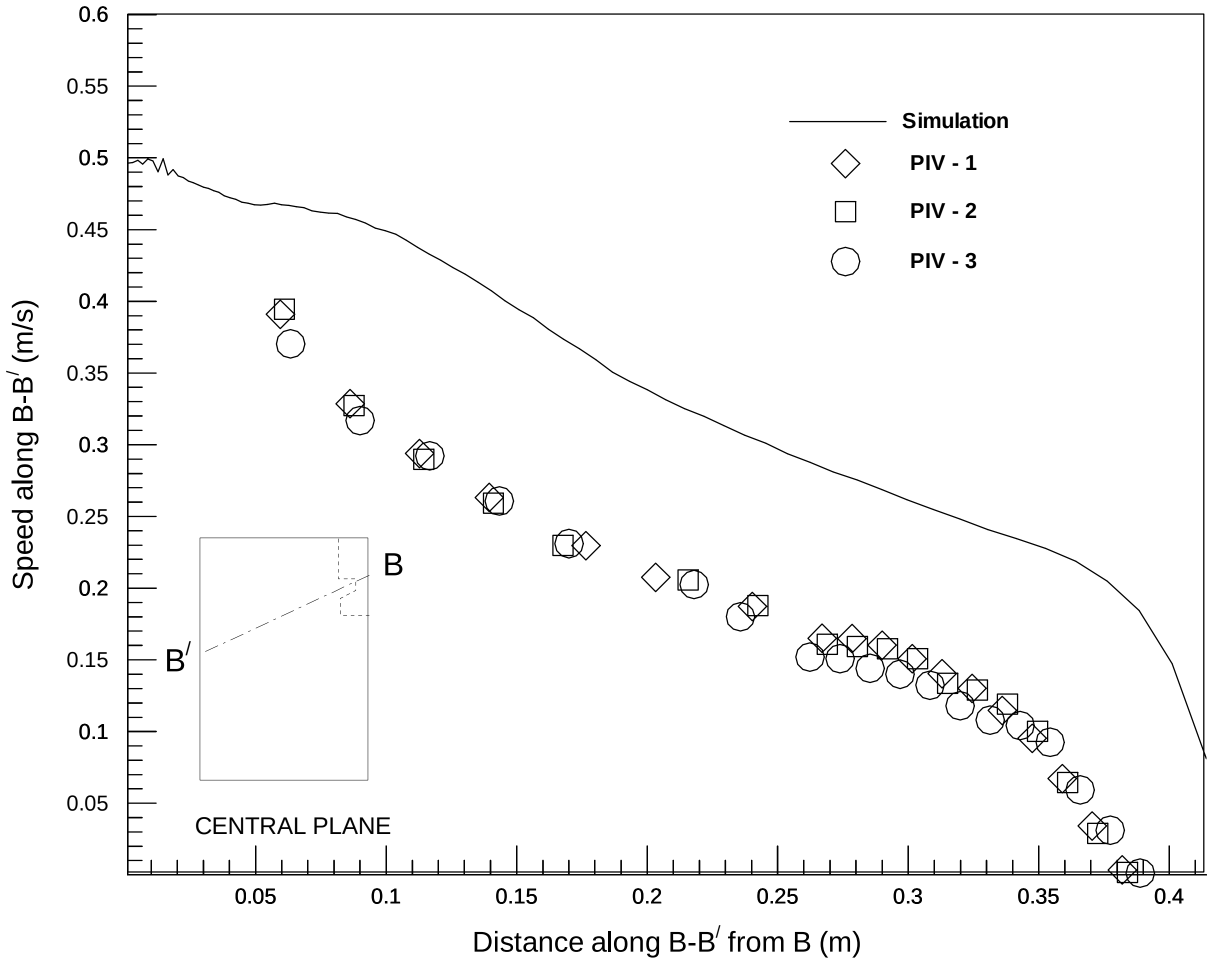

Figure 3.13 Plot of speed variation along the center of the jet starting at the inlet

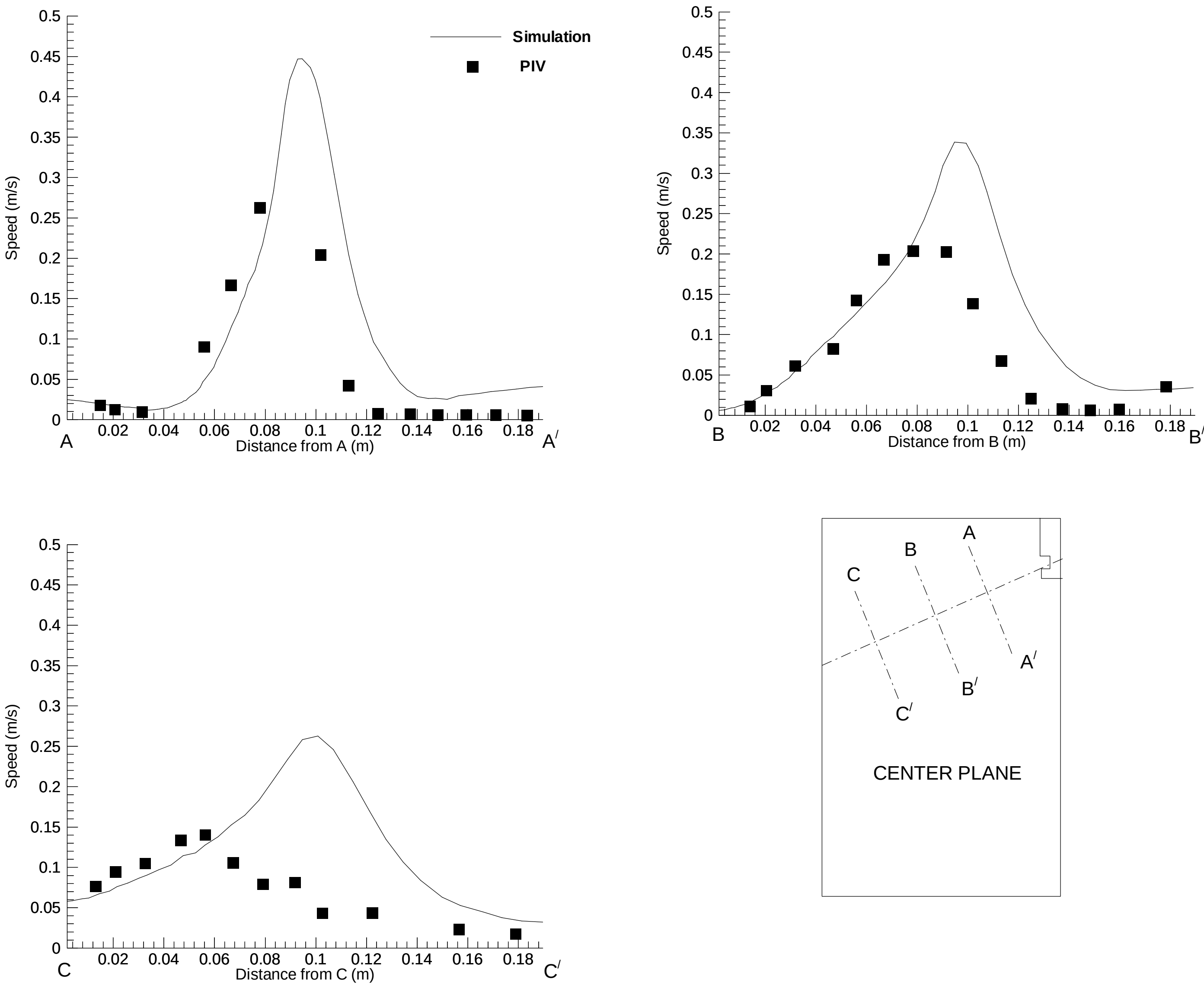

Figure 3.14 Plot of jet speed profile at three different locations along the jet

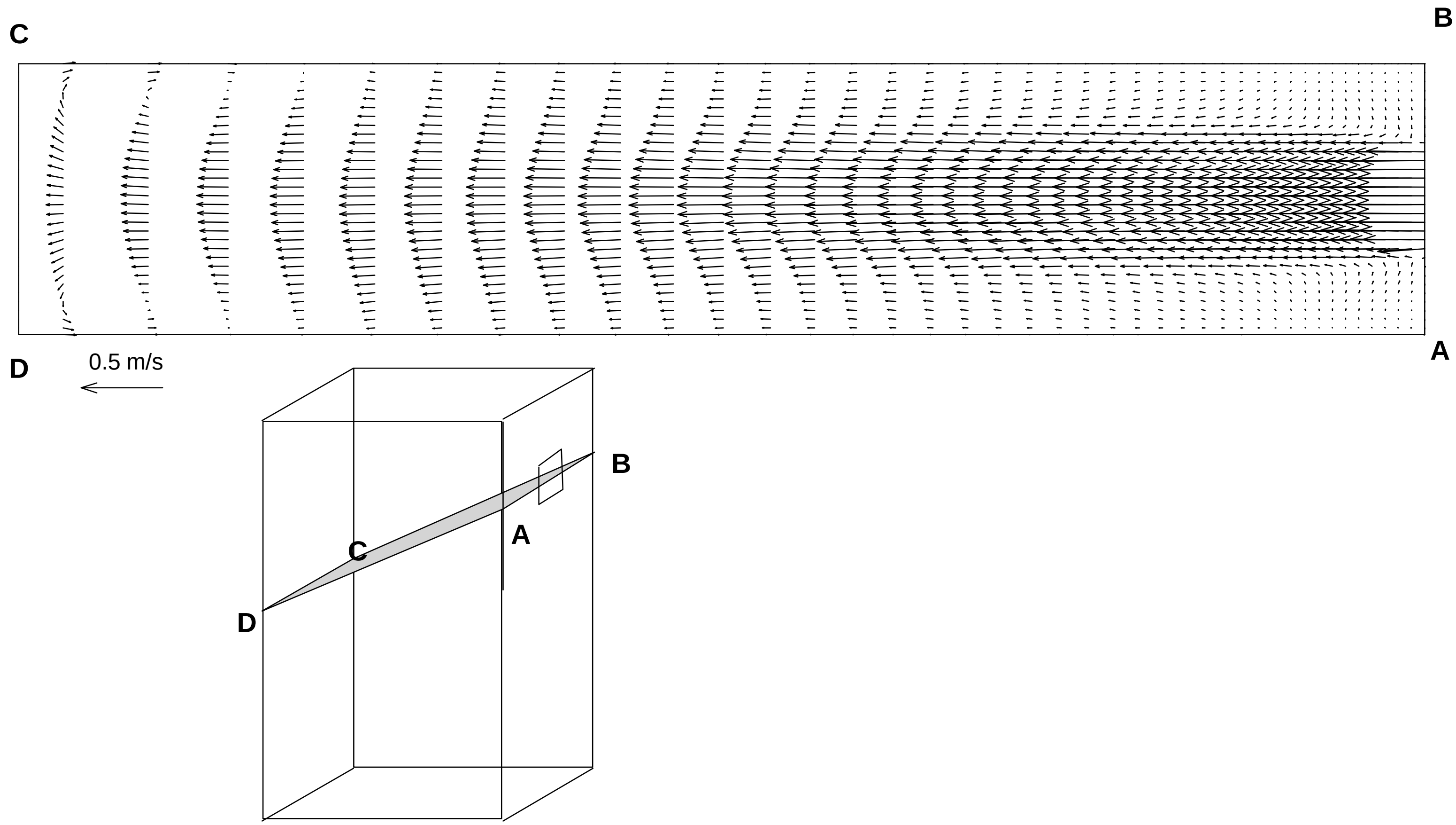

Figure 3.15 Vector plot through cross section of the jet

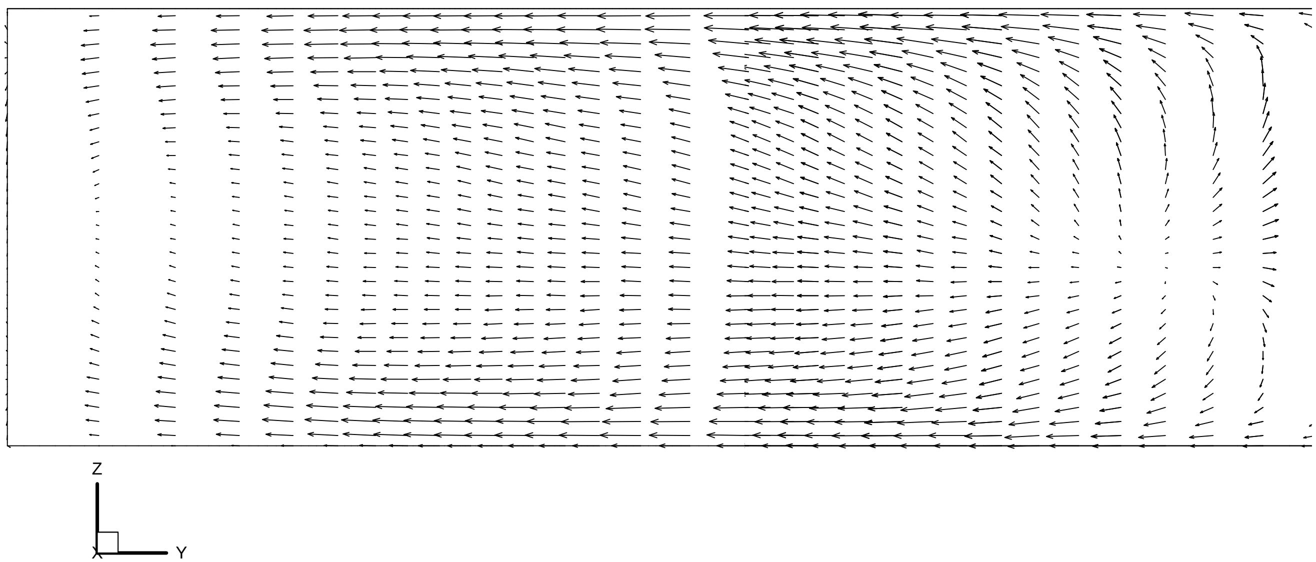

Figure 3.16 Time averaged vector plot of plane parallel to the narrow face, 20mm from it

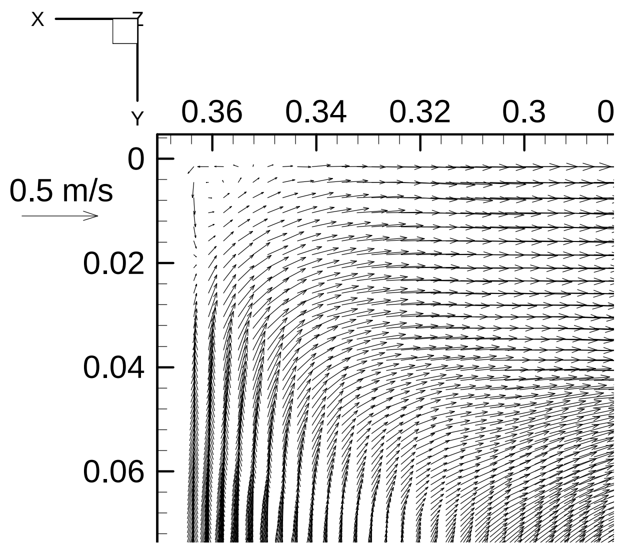

Figure 3.17 Simulated top left corner recirculation region

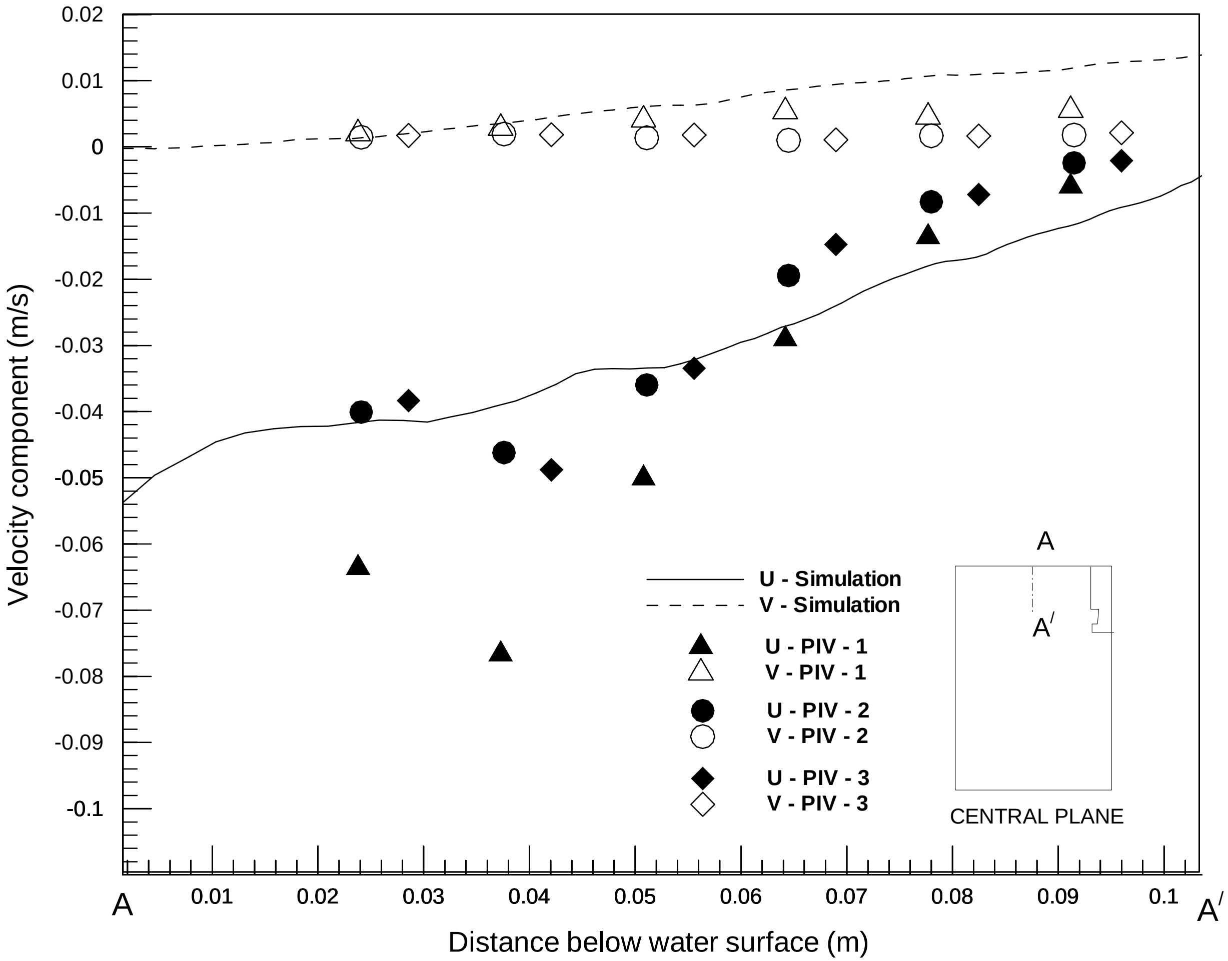

Figure 3.18 Plot of velocity variation in the casting direction at the center of the wideface and narrowface

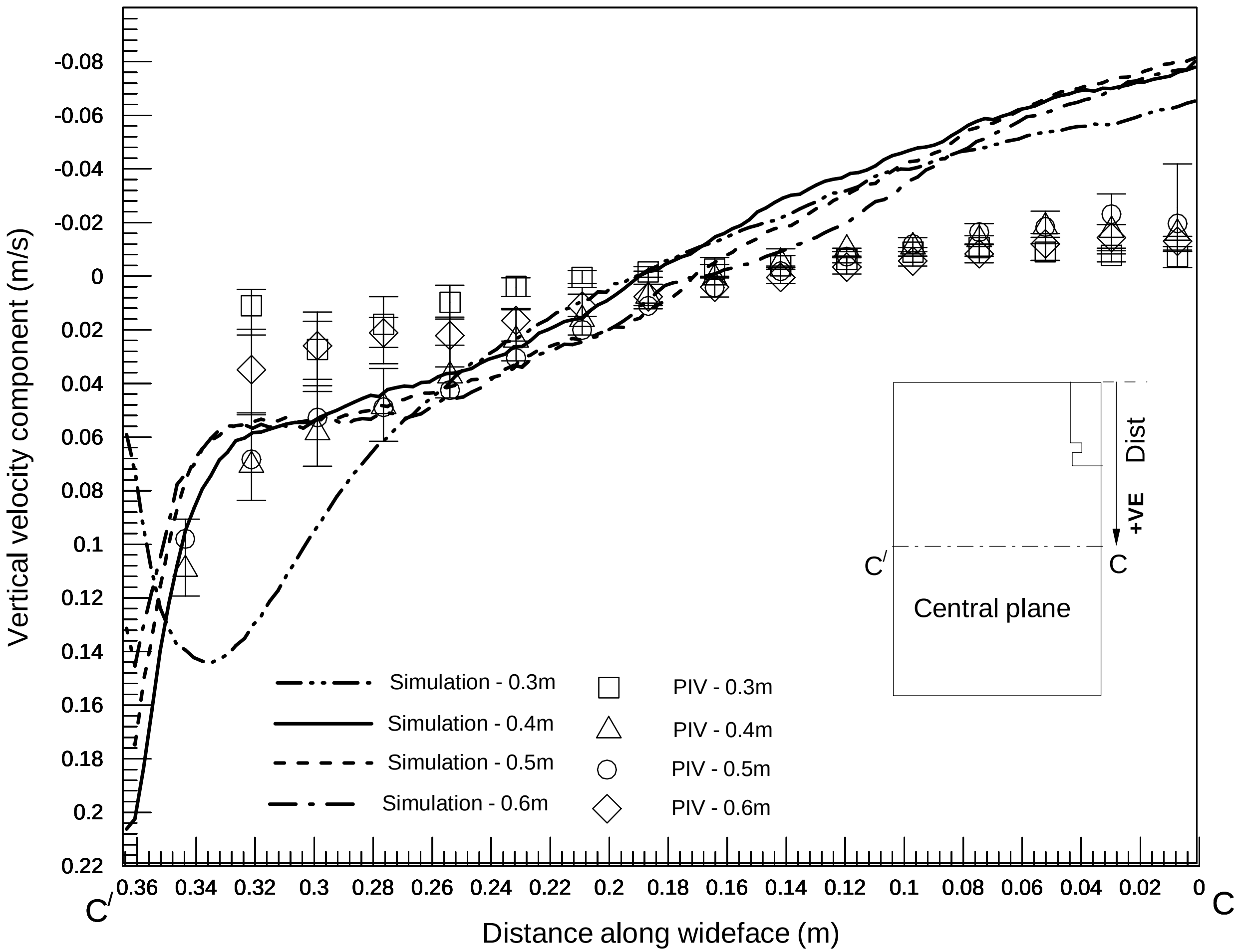

Figure 3.19 Plot of time average vertical component of velocity from the simulation and PIV measurement along the wideface, at a given distance below the water surface

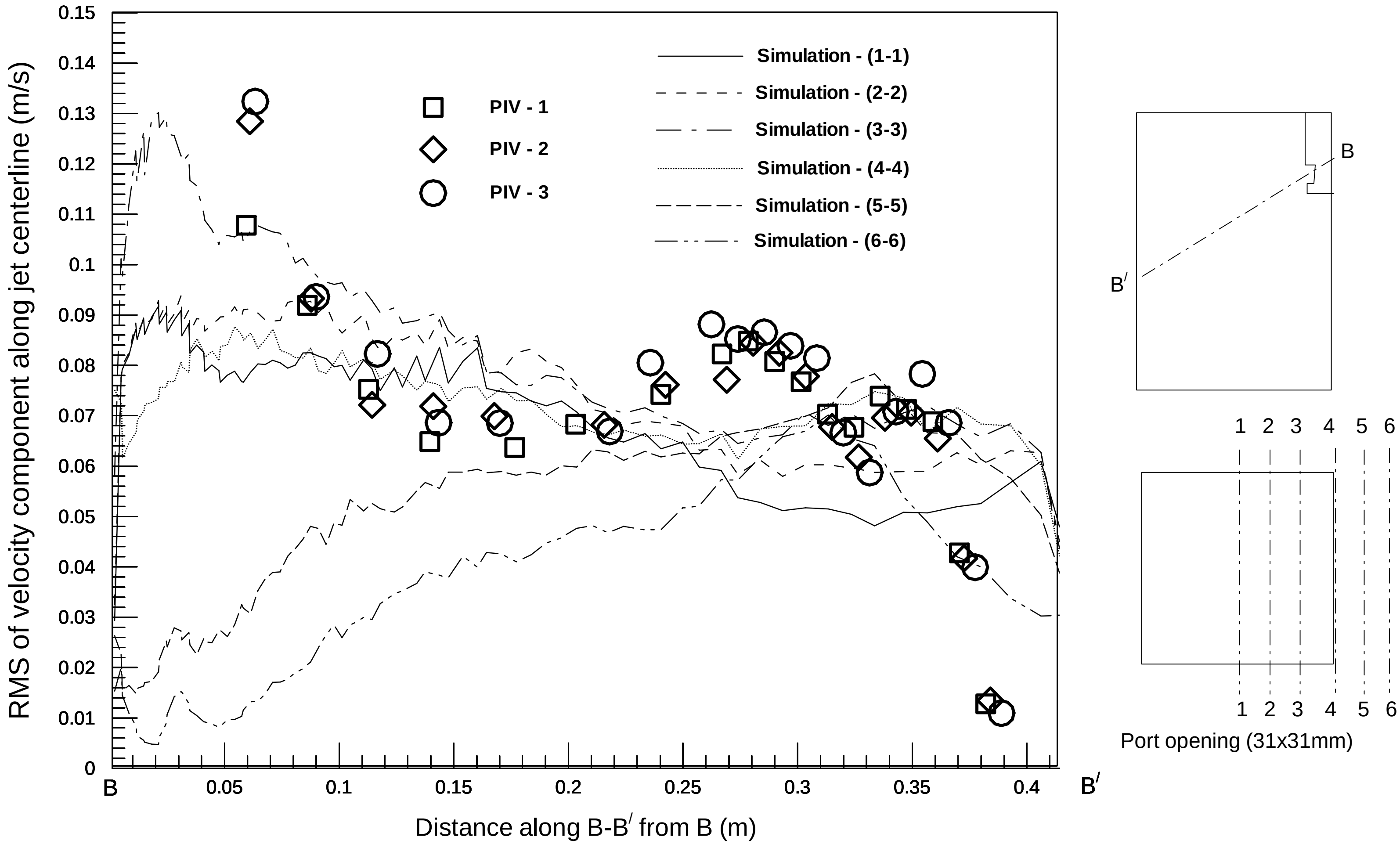

Figure 3.20 Plot of variation of RMS speed along the jet centerline starting at the inlet

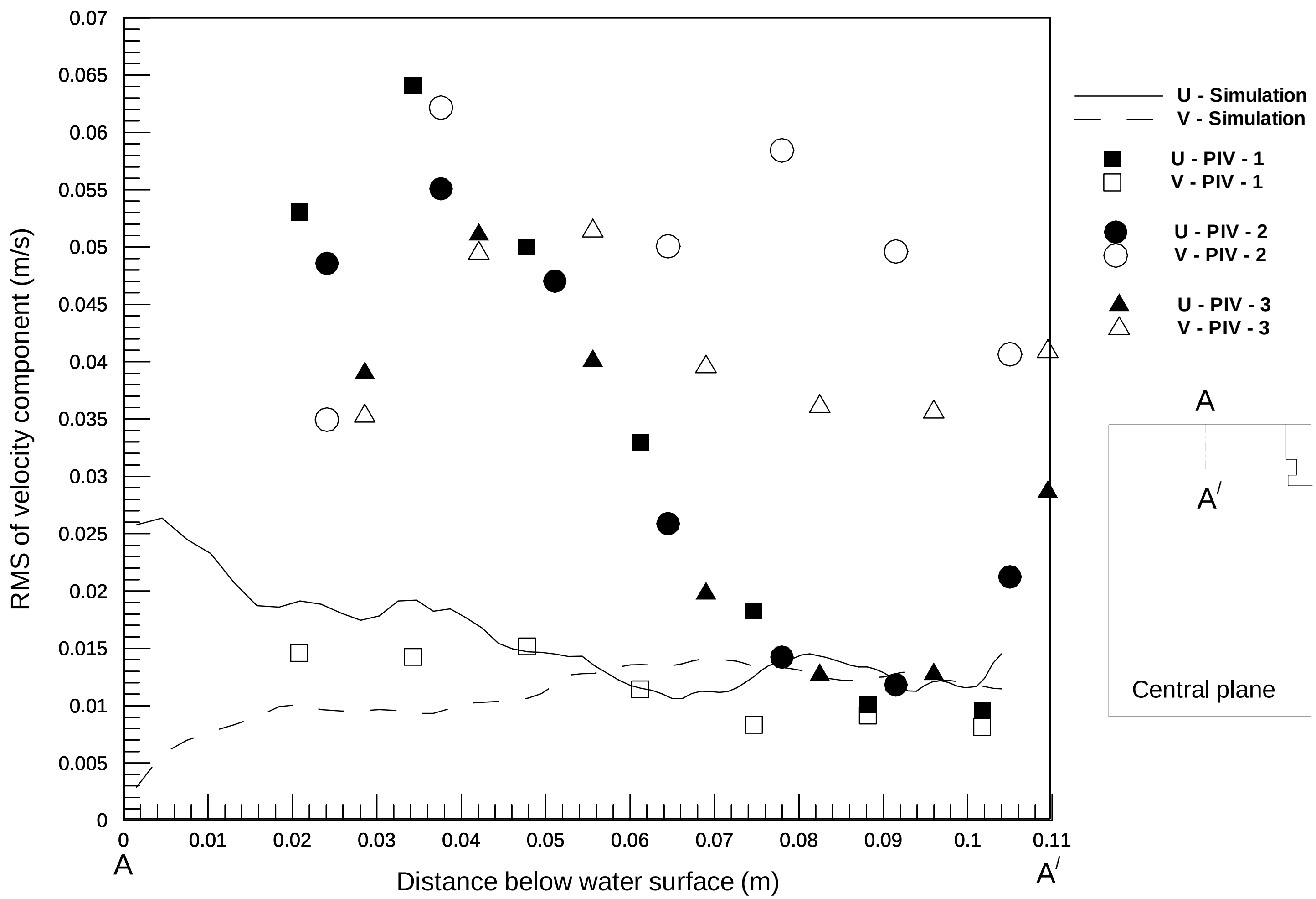

Figure 3.21 Plot of RMS of U and V components of velocity below the water surface in the center plane

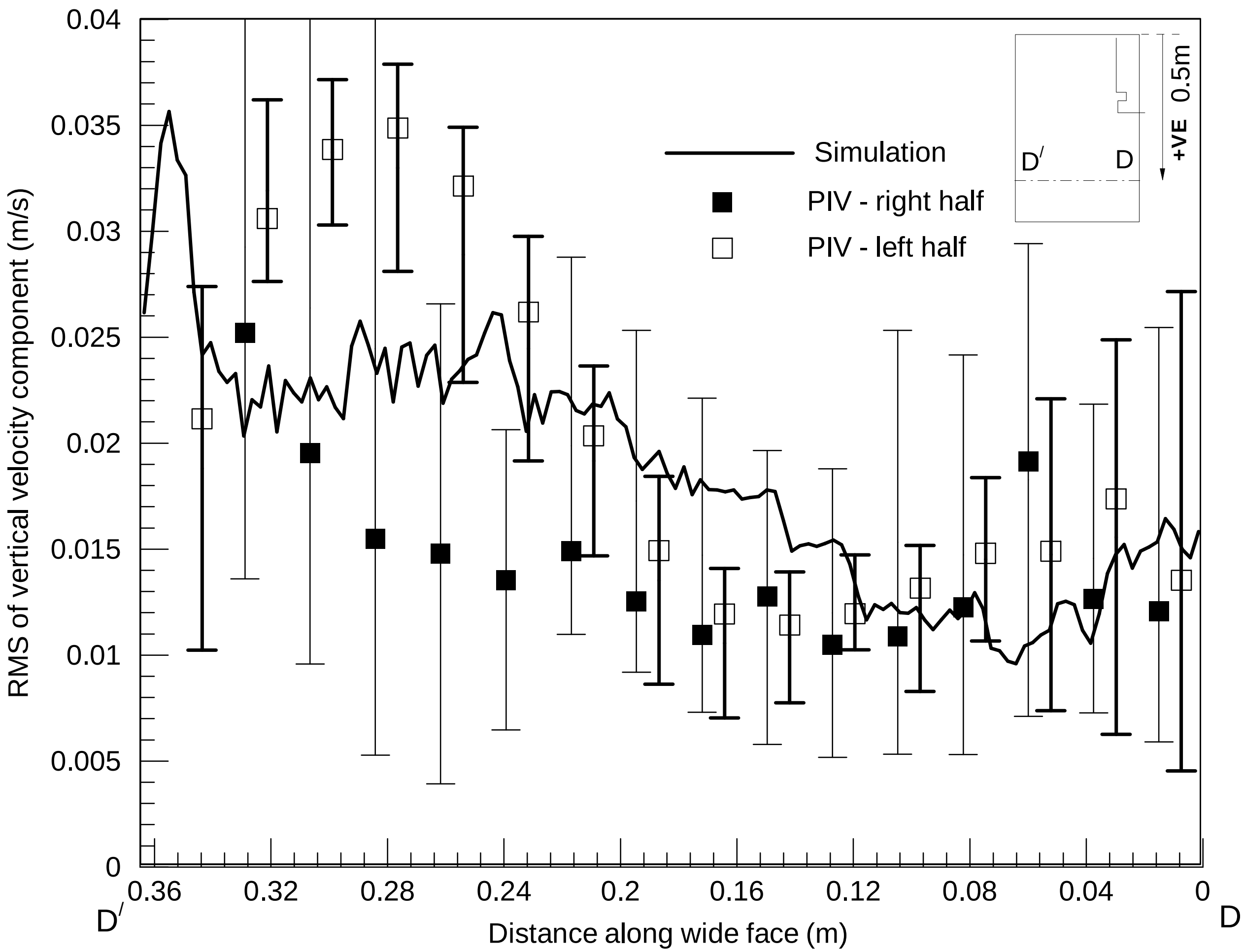

Figure 3.22 Plot of RMS of V component of velocity 0.5m below the top surface in the center plane

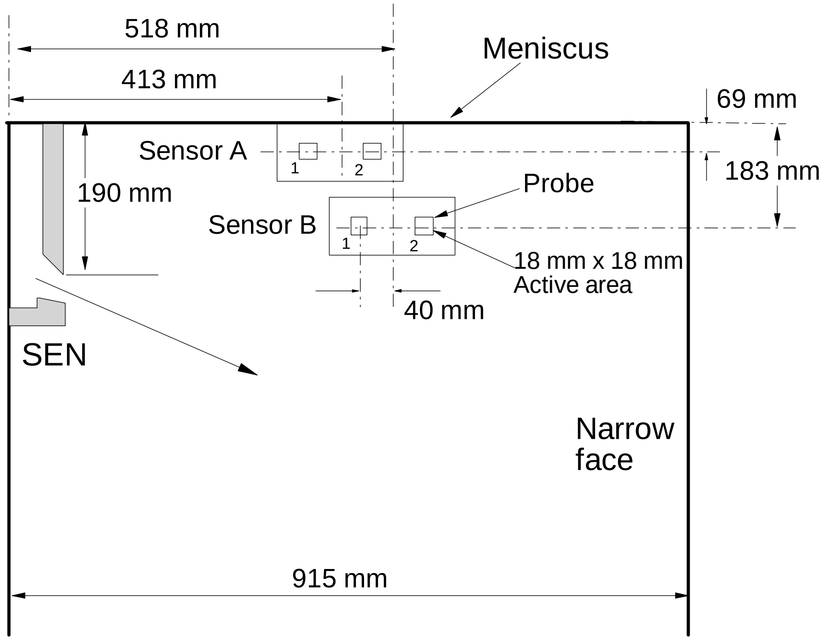

Figure 3.23 MFC sensor location on water model

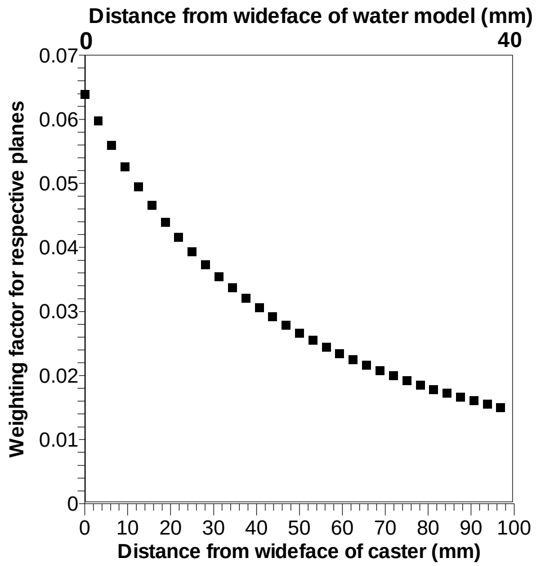

Figure 3.24 Assumed weightage of velocities with distance from wideface by MFC probes

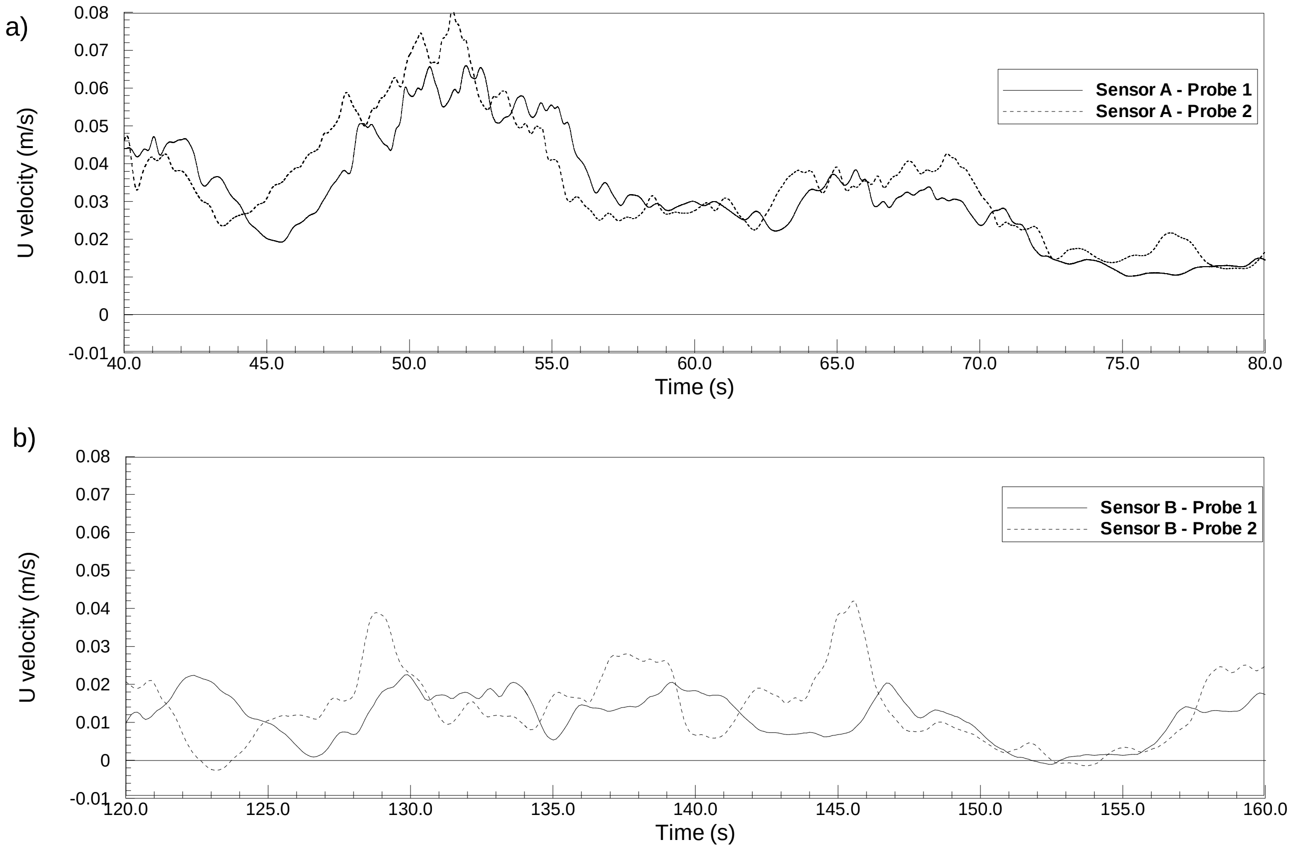

Figure 3.25 Simulated probe signals and MFC sensor output locations A (a) and B (b)

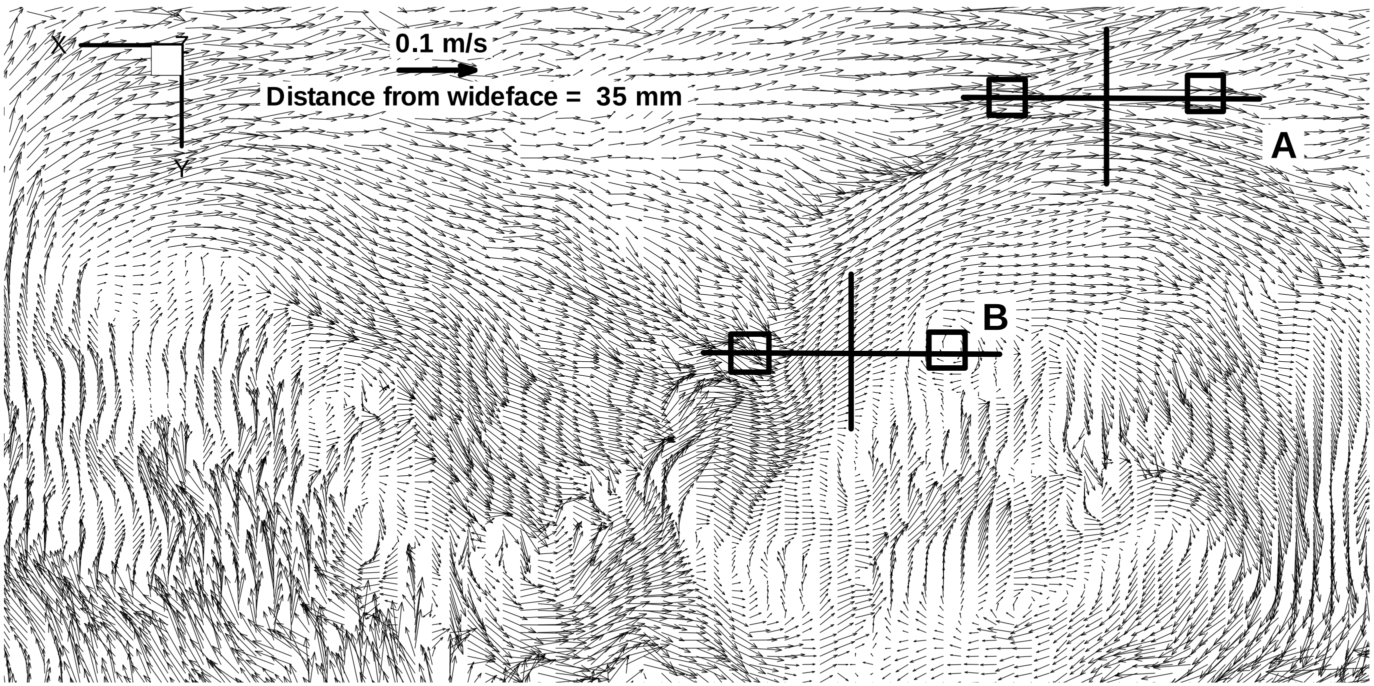

Figure 3.26 Instantaneous simulated vector plot of the upper roll 35mm from wideface

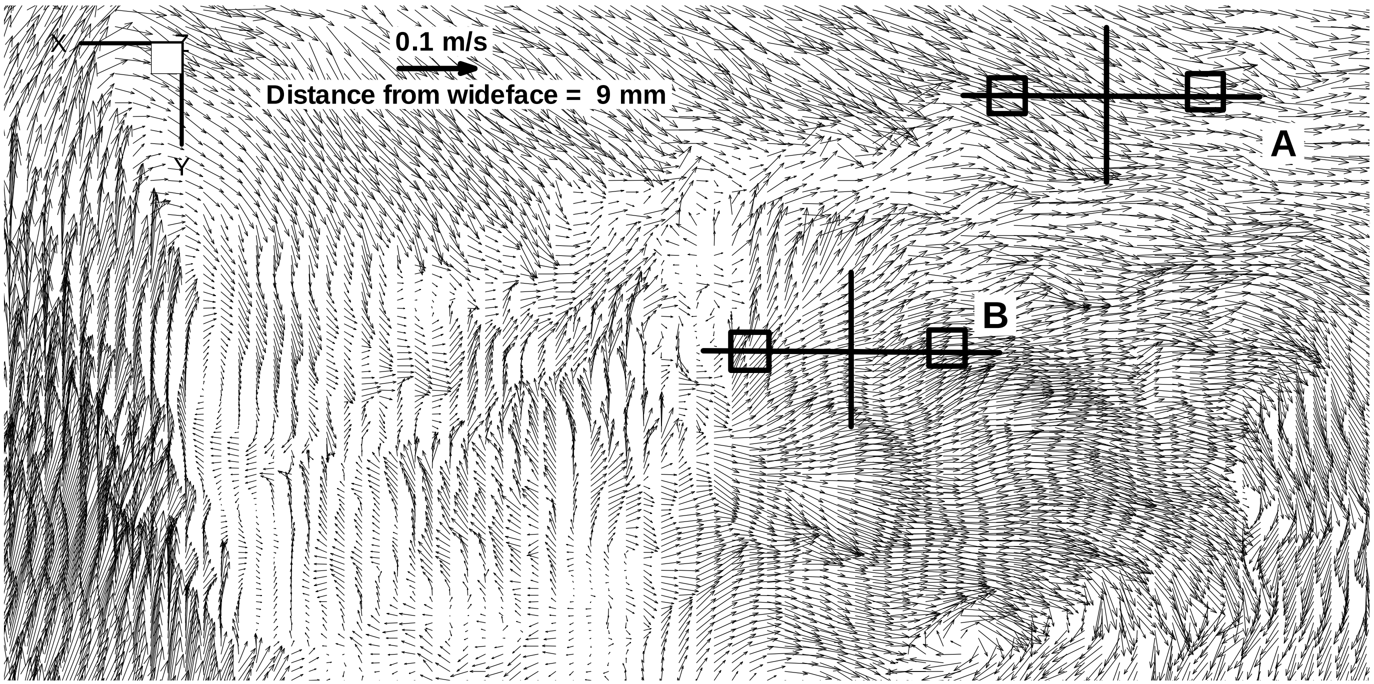

Figure 3.27 Instantaneous simulated vector plot of the upper roll 9mm from wideface

CHAPTER 4. NUMERICAL STUDY OF HIGH PRANDTL NUMBER NATURAL CONVECTION IN A SHALLOW CAVITY WITH IMPOSED SHEAR

4.1 Introduction

Buoyancy driven convection is an important mechanism of heat and mass transfer in a variety of industrial applications. Fluid slag layers in materials processing, with large temperature differences and temperature dependent density, experience buoyant forces [25]. Other examples include glass layers in melting furnaces [26] and dendrite growth during solidification [27]. Fluid viscosity dissipates the buoyant force. The strength of the buoyant force relative to viscous dissipation is characterized by the Rayleigh number (Ra, defined in the nomenclature). For low Ra viscosity dominates and the fluid layer is stationary. Beyond a Ra of 1707 (as determined by linear stability analysis [28]) buoyancy induces fluid flow. The flow pattern is steady consisting of plumes transporting hot low-density fluid upward and cold high-density fluid downward in accordance to the buoyant forces. These are arranged alternately and merge to form cells. The resulting fluid flow and heat transfer for layers with large length to thickness (A) and length to width ratio (B) in excess of one has been studied extensively and is called Rayleigh-Benard convection [28-30]. For B>1 fluid flow is two-dimensional with the cell axis along the width.

The impinging plumes increase the local heat transfer rate. This increases the overall heat transfer beyond pure conduction through the stationary fluid layer. With increasing Ra and hence the relative magnitude of the buoyant force the plume velocity increases further increasing the overall heat transfer through the fluid layer. Another parameter which influences the fluid flow and heat transfer through the fluid layer is the Prandtl number (Pr), which is the ratio of the momentum diffusivity to the thermal diffusivity. The fluids of interest for this study are characterized by a low thermal conductivity and a high molecular viscosity, hence a high Pr (Pr

> 50). For these fluids the momentum diffusion rate is high compared to the thermal diffusion, requiring low flow rates and hence velocities for the heat flux transport. With increasing Ra transition occurs from two to three dimensional steady flow. The critical Ra for this transition increases with Pr saturating at a Ra of 50000 beyond a Pr of 100 [31, 32]. Further increase in Ra causes transition to oscillatory convection. The critical Ra for this transition also increases with Pr saturating at a Ra of 100000 for a Pr of 100 [31, 32]. Low Prandtl number fluids such as liquid metals are characterized by a high thermal conductivity and low viscosity. For these fluids the low momentum diffusion rate compared to thermal diffusion necessitates higher flow rates to transport the heat flux. Also the low viscosity implies lower diffusion resulting in lower Ra for transition to oscillatory and turbulent convection than high Pr fluids. Mercury (Pr = 0.025) has a critical Ra for transition to oscillatory convection of around 2000 [31]. Slag layers, glass layers etc are characterized by a very large aspect ratios A>>10. This aspect ratio (A) also influences the fluid flow and heat transfer in the fluid layer. The critical Ra for onset of natural convection decreases with increase in A and asymptotes to 1 beyond A of 10 [33-35]. All practical applications have fluid layers of finite width. As mentioned earlier for length to width ratio larger than 1 (B ≥ 1.5) the problem is two dimensional with cells aligned with their axis parallel to the width. For B close to 1 a symmetric cell pattern is formed which is discussed in great detail in Stork [36]. For B < 1 the cells align themselves parallel to the length. In addition to influencing the critical Ra for onset of natural convection lateral confining walls distort the rolls adjacent to them [36].

Knowledge of the overall heat transfer through the fluid layer is important, and is quantified by the average Nusselt number (Nu_{avg}) over the length of the fluid layer. Extensive experiments have been done to quantify Nu_{avg}, for large aspect ratio (A > 10 and B > 1) fluid layers, as a function of Ra and Pr [37-39]. As mentioned earlier Nu_{avg} is found to increase with Ra. Rossby

[38] presents a summary of power exponents for Ra to quantify this increase. For high Pr ($50 < Pr < 1673$) the results of Koschimeder [39] suggest Nu_{avg} to be independent of Pr. The results of Globe [37] indicate a slight Pr dependence ($Pr^{0.074}$) over a much larger range of Pr ($0.02 < Pr < 8750$).

In addition to the buoyant force most differentially heated fluid layers in industrial applications are suspended over a fluid bed. Flow in this underlying fluid shear drives the fluid layer. This results in forced convection, which for laminar natural convection conditions in the fluid layer tends to annihilate the natural convection cells. The resulting flow pattern is complex and depends on the relative magnitude of the buoyancy and inertia force resulting from shear. Low Pr shallow fluid layers ($A >> 1$) with natural convection and top shear have been studied numerically by Mohammad and Viskanta [40]. In this study water ($Pr = 5.84$) was used as the fluid and the Ra was kept low to avoid transition to oscillatory convection ($3500 < Ra < 4000$). With increasing shear and hence top surface velocity the natural convection cells are progressively annihilated. The final flow pattern for large velocities is a single recirculation region. The resulting flow pattern for any shear velocity depends on the relative magnitude of the buoyant and inertial forces and is quantified by Gr/Re^2 (definitions in nomenclature). For $Gr/Re^2 >> 1$ buoyancy is dominant and the natural convection cells persist with the bottom shear. For $Gr/Re^2 << 1$ inertia dominates and natural convection does not contribute to the fluid flow and heat transfer. For $Gr/Re^2 \sim 1$ both forces influence the flow. The study of Mohammad and Viskanta [40] has a detailed qualitative description of the fluid flow and heat transfer for a range of Gr/Re^2. As mentioned earlier low Pr fluids ($Pr < 1$) have a low Ra for transition to oscillatory and turbulent convection ($Ra < 5000$). Addition of shear to such fluid layers makes the flow pattern extremely complicated. The work of Mohammad and Viskanta [41] is an example of experimental and numerical study of turbulent flow in low Pr fluids ($Pr << 1$) in lid driven cavities with large aspect ratios (A >> 1). The time averaged flow behaviour with increasing shear is similar to that in the laminar regime. For turbulent stationary convection Nu_{avg} fluctuates about a mean value. The frequency of this fluctuation increases with Ra [31].

No previous work on forced convection fluid flow and heat transfer in shallow liquid layers at high Pr has been found even though it is highly relevant and influential for many industrial applications. The present work aims to quantify the fluid flow and heat transfer in high Pr fluid layers subject to natural convection and shear. The range of Ra and Pr is $2500 < Ra < 100000$ and $100 < Pr < 700$. The shear is varied from zero to beyond complete annihilation of the natural convection cells. One objective is to quantify the critical shear velocity to annihilate the natural convection cells. This is of crucial importance as the fluid flow and heat transfer are completely different for buoyancy and shear dominated flows. In addition there is need to quantify the fluid flow and heat transfer (Nu_{avg} , cell pattern, velocity distribution etc) over the range of shear. This study will serve as a ready reference to determine both qualitatively and quantitatively the fluid flow and heat transfer in shear driven fluid layers with natural convection at high Pr.

4.2 Mathematical Model

Figure 4.1 is a sketch of the computational domain, mesh and boundary conditions used in this study. It consists of a rectangular cavity of aspect ratio (A) of ten. The lower wall is heated to a constant temperature T_h while the upper walled is cooled to a constant value of T_c. The lateral walls are adiabatic to emulate the heat transfer in a piece of a longer domain. Shear is added by moving the lower wall in the positive x direction at a constant velocity U. The domain is two-dimensional in accordance with the flow over most of the Ra and Pr range under study. In addition the flow is steady over this range.

4.2.1 Governing equations

In order to compute the fluid flow and heat transfer in this problem the following non-dimensional Navier Stokes equations including buoyant body forces are solved for mass, x and y momentum and heat balance.

$$\frac{\partial u^*}{\partial x^*} + \frac{\partial v^*}{\partial y^*} = 0 \tag{1}$$

$$u^* \frac{\partial u^*}{\partial x^*} + v^* \frac{\partial u^*}{\partial y^*} = -\frac{\partial p^*}{\partial x^*} + \frac{\Pr}{\sqrt{Ra}} \left(\frac{\partial^2 u^*}{\partial x^{*2}} + \frac{\partial^2 u^*}{\partial y^{*2}}\right) \tag{2}$$

$$u^* \frac{\partial v^*}{\partial x^*} + v^* \frac{\partial v^*}{\partial y^*} = -\frac{\partial p^*}{\partial y^*} + \frac{\Pr}{\sqrt{Ra}} \left(\frac{\partial^2 v^*}{\partial x^{*2}} + \frac{\partial^2 v^*}{\partial y^{*2}}\right) + \sqrt{Ra}\, \Pr\, \Theta \tag{3}$$

$$\left(u^* \frac{\partial \Theta}{\partial x^*} + v^* \frac{\partial \Theta}{\partial y^*}\right) = \frac{1}{\sqrt{Ra}} \left(\frac{\partial^2 \Theta}{\partial x^{*2}} + \frac{\partial^2 \Theta}{\partial y^{*2}}\right) \tag{4}$$

In these equations $u^* = V_x/U_o$, $v^* = V_y/U_o$, $x^* = x/H$, $y^* = y/H$, $p^* = p/(\mu U_o/H\sqrt{Ra})$, $\Theta = (T-T_c)/(T_h-T_c)$. All terms are defined in the nomenclature.

The Boussinesq approximation is made meaning that buoyant forces are taken into account solely through the last term in equation (3) and all physical properties are considered independent of temperature. The non-dimensional form of the Y-momentum equation can be used to analyze the relative magnitude of the buoyant and viscous force terms and is found to be a function of Ra and Pr (equation (3)). The characteristic velocity U_o selected such that the critical velocity for annihilation of natural convection cells is independent of Pr and is defined as

$$U_o = \sqrt{gb\Delta TH / an} \tag{4a}$$

This will be discussed in more detail in subsequent sections.

4.2.2 Boundary conditions

The boundary conditions for the governing equations of the problem are

At the lateral walls, x = 0, $V_x = 0$, $V_y = 0$, dT/dx = 0

At bottom wall, y = 0, $T = T_h$, $V_x = U$, $V_y = 0$

At top wall, y = H, $T = T_c$, $V_x = 0$, $V_y = 0$

4.2.3 Numerical method

The governing equations (1-4) are discretized using a finite element approach in the commercial code FIDAP (v 7.5.2) [42]. A penalty function approach is used in FIDAP, essentially to avoid explicit solution of the continuity equation by an adding an infinitesimal compressibility to the fluid. To accomplish this, the continuity equation is changed to

$$\frac{\partial u^*}{\partial x^*} + \frac{\partial v^*}{\partial y^*} = -ep^* \tag{5}$$

Here the penalty parameter 'ε' should be chosen to be small enough to reduce the error added by compressibility but large enough to avoid convergence problems. For the present study ε was set at 10^{-8}. Substituting for p* from equation (5) into equations (2-4) the number of equations to be solved simultaneously is reduced to three with a total of three unknown fields u*,v* and Θ. p* is then calculated using (5).

The domain is divided into quadrilateral elements each with four nodes at the four corners. The highest order derivative in the equations (1-4), for pressure is one and velocity and temperature is two. Hence variables u*,v* and Θ are defined at each node while there is only one p* per element. At any point within the element u*,v* , Θ and p* are defined using interpolation 'shape' functions which relate them to the nodal values as follows:

$$u^*(\mathbf{x}) = F^{\mathbf{T}}\mathbf{u^*},\ v^*(\mathbf{x}) = F^{\mathbf{T}}\mathbf{v^*},\ \Theta(\mathbf{x}) = F^{\mathbf{T}}Q,\ \ p^*(\mathbf{x}) = Y^{\mathbf{T}}\mathbf{p^*} \tag{6}$$

where Q**,u*,v*,p*** are column vectors for the element nodal values and F and Y are column vectors of interpolation functions in this case bilinear and constant respectively [42]. Substituting equation (6) into governing equations (2-5) a set of residuals corresponding to the inaccuracy of the discrete formulation (6) are obtained. Applying Galerkin's method, the residuals are made orthogonal to the shape functions, thereby setting the weighted average error over the entire domain to zero. Assembly of the resulting equations integrated numerically over each element produces a global system of non-linear algebraic equations expressed as

$$[\mathbf{S}(r)]\cdot\{\mathbf{r}\} = \{\mathbf{F}\} \tag{7}$$

where [**S**(**r**)] is the coefficient matrix containing stiffness, advection, buoyancy and penalty matrices, {**r**} contains the unknowns {**u***,**v***,**p***, Q} and {**F**} is the force vector containing the discretized loads due to buoyancy. Fixed velocity and temperature on the appropriate boundary segments are imposed in the solution phase by partitioning the corresponding degrees of freedom together in the matrix, deleting them, and substituting the imposed values into the other equations. The fixed heat flux boundary conditions add source terms equivalent to the heat flux in the force vector {**F**}. Equation (7) is solved for {**r**} using a relaxed successive substitution scheme.

$$[\mathbf{S}(r^{i-1})] \cdot \{\mathbf{r}^*\} = \{\mathbf{F}\} \qquad (8)$$

$$\{\mathbf{r}^{\,i+1}\} = RF\{\mathbf{r}^*\} + (1\text{-}RF)\{\mathbf{r}^{\,i}\} \qquad (9)$$

where RF is the relaxation factor, $0 \le RF \le 1$, and the superscripts refer to the iteration number. The discretized equations (8-9) are solved in a fully coupled manner at each iteration using a fully implicit equation solver based on Gaussian elimination. This is done because the temperature and velocity in this problem are highly interdependent through the buoyancy and advection leading to poor conditioning. The drawback is that the method is computationally intensive, especially for a fine mesh. Further details on the numerical method are found in the FIDAP manual [42].

4.2.4 Convergence behaviour and criteria

The choice of relaxation factor needed to achieve convergence depends on the solution behaviour over the iteration range. Iteration proceeds until error in the solution is reduced to an acceptable level. Error is defined as

$\mathbf{R}_i = \sqrt{\sum_{j=1}^{n} X_j^{\,2} / n}$ where 'n' is the number of equations being solved, X_j is the j^{th} element of the column vector **X**

$\mathbf{X} = [\mathbf{S}(r_i)] \cdot \{\mathbf{r}_i\} - \{\mathbf{F}_i\}$ and 'i' refers to the iteration number.

For RF near 1, most of the computed solution values are used for the next iteration. This accelerates convergence but may lead to an oscillating error resulting from large changes in variables at each iteration level. For RF near 0, most of the previous iteration solution is used in the next iteration. This must be used when the solution changes very rapidly at each iteration in order to reduce oscillation in residue but it slows down convergence and may lead to a stagnant convergence profile. Natural convection flows inherently have convergence problems because the velocity field is dominated by the buoyancy term in the governing equations, which in turn is controlled by the temperature field.

In order to quantify the convergence criteria the convergence behaviour of the stationary natural convection computations done for validation study, described in the next section, was evaluated. A stationary fluid layer was the initial flow field for all computations. The residual, **R** is found to follow a decrease-increase-decrease pattern with iteration number. For stationary natural convection starting with a stationary fluid layer as the initial solution, the velocity field begins to converge before the temperature field. For low velocities the convective heat transfer is negligible so the temperature field is relatively unaffected. Thus the residual falls. After the velocities have increased, the temperature field begins to converge, which in turn disturbs the velocity field. This increases the residual error **R**. Finally, when both the velocity and temperature fields become close to their ultimate converged values, the residual falls. Convergence to an accurate solution was found to be achieved when **R** has decreased by three orders of magnitude or more.

In this study, a RF of 0.5 was found to achieve converged solutions for all stationary natural convection computations. The number of iterations needed increases with increasing Ra and Pr and averaged around 100.

A relaxation factor, RF of 0.5 was also found to yield converged solutions for problems involving large shear velocities if there are no natural convection cells. For these problems **R** decreases continuously with iteration number, similar to shear driven flow problems without natural convection.

For problems close to cell annihilation the convergence behaviour of **R,** for a RF of 0.5 is a decrease then increase and level off at a constant value. To get the solution to converge, further iterations with RF greater than 0.5 are necessary For most problems **R** oscillates about a large unconverged value so further iterations with RF progressively decreasing towards 0.05 were needed.

4.3 Model Validation

4.3.1 Grid refinement study

A systematic grid independence study was done to determine the grid required to achieve acceptable accuracy for this type of problem. A square portion of the shallow cavity domain was modeled. The specific conditions were chosen to match the previous bench mark study of de Vahl Davis [43] on stationary natural convection in a two-dimensional square cavity with differentially heated side walls and air (Pr = 0.71) as the fluid. The temperature gradients for this problem are larger than encountered with a shear driven flow as shown in the results section 4. Recalling that lower Pr also increases the natural convection cell velocities and hence increases temperature gradients, this problem is a more rigorous test of the resolution of the computational grid than the problems of interest. The fluid flow and heat transfer solutions for three different meshes 16x16, 32x32 and 64x64 were computed. The meshes were stretched from the center to the walls along the horizontal and vertical directions to better resolve the boundary layer flow and hence compute the heat transfer more accurately. The results of this study for Ra of 10000 and 100000 were compared to the bench marked results of de Vahl Davis [43]. With increasing grid refinement the solutions converged to the bench marked solutions. The maximum disagreement in the maximum horizontal velocity of the 64x64 grid was found to be 1.9% and occurred on the vertical mid-plane of the cavity and occurred for a Ra of 100000. Typical errors on the finest grid were less than 0.5 %, which indicates that the model is accurate for solving natural convection problems.

Each simulation required 100-400 iterations which required For computational efficiency, the grid size of 160x16 was chosen for all simulations. The maximum disagreement on this grid (for a Ra of 100000) was a 4.5% overestimation of the Nusselt number. Typical errors for this grid were of the order of 1%.

4.3.2 Qualitative comparison with experimental interferogram

In order to study the ability of the model to simulate the fluid flow and heat transfer patterns accurately the results of a stationary liquid flux layer simulation were compared to an experimental interferogram. The experimental work was done by Oertel [35] using two cavities with aspect ratio of 10:4:1(length:depth:thickness) and 4:2:1. The study was performed using varying angles of inclination of the cavity to the horizontal with three fluids namely air (Pr = 0.71), water (Pr = 7.0) and silicone oil (Pr =1780). The critical Ra for onset of natural convection was found to decrease with increasing aspect ratio and asymptote to 1707 beyond A of 10. This is in agreement with the theoretical work of Catton[34], Davis[33] and Oertel(1976). The lateral walls in the experiment are made perfectly conducting (thermal conductivity much larger than that of fluid) so there is a linear temperature gradient along the lateral walls. The differential interferometer used in this work consists of a light beam from a monochromatic source which, using suitable optical equipment, is split into two beams polarized in perpendicular directions. After passing through the test section the beams are made to interfere. Sufficiently large temperature gradients in the cavity will produce interference fringes, which can be evaluated for qualitative information on cell distribution. For additional sensitivity a laser beam is used instead of a monochromatic light source.

Figure 4.2 is a sample set of plots for stationary natural convection for the above test conditions (Ra = 4000, Pr = 1780). These results were computed by the numerical method described in the previous section using FIDAP [42]. Recall that since the Ra is less than 50000, for a Pr of 1780, the flow is steady and two dimensional with the natural convection cell axes perpendicular to the largest side of the 10:4:1 aspect ratio cavity. Assuming the lateral walls to be perfectly conducting a linear temperature gradient is imposed from the bottom to the top along the lateral walls. A stationary fluid layer was used as the initial guess before iterating with a relaxation factor, RF of 0.5. The solution converged in 40 iterations. Since the Ra is larger than the critical value for onset of natural convection, cell formation occurs with a total of ten cells with aspect ratio 1. Recall that adjacent cells rotate in opposite directions causing alternate upward and downward moving plumes, which transport heat from the bottom to the top layer. In the central region, away from the walls, the alternate cells are identical. The increased heat transfer of the impinging plumes causes high temperature gradients, as seen in the close grouping of contour lines near the impingement point in the temperature contour plot. This is also reflected in the Nusselt number distribution along the top and bottom surfaces as seen in the last plot of figure 4.2. Close to the impingement points on the top and bottom surfaces the local Nusselt number peaks, whereas away from this it drops resulting in a wavy distribution characteristic of natural convection. The Nusselt number distributions along the top and bottom surfaces are out of phase, a consequence of the alternate rising and falling plumes. Also there is a peak in the distributions along both the top and bottom surfaces near both the lateral walls and is a consequence of the linear temperature distribution along these walls. The presence of the wall and the linear temperature boundary condition affects the shape of the cell near the wall. This last plot also includes a vertical velocity profile along the horizontal centerline, which is similar to the Nusselt number distribution graphs and has equal maximum and minimum values.

Figure 4.3 is a comparison of interferograms obtained using simulation and experiment [35]. The results are for a horizontal, rectangular cavity of aspect ratio 10:4:1, for Ra = 4000, Pr = 1780. The interferogram is in the central vertical plane with lines of uniform horizontal density gradient. To obtain horizontal density gradient in the simulation the Boussinesq approximation is used i.e. β is independent of temperature. By definition, $\beta = -d\rho/dT$ or $d\rho = -\beta dT$. Differentiating with respect to x, $d\rho/dx = -\beta dT/dx$. Hence lines of uniform horizontal density gradient are also lines of uniform horizontal temperature gradient. The experiment and simulation agree very well. The ten natural convection cells seen in the vector plot of the simulation are also seen in the interferograms. The alternate cells in the central region away from the walls are identical in shape and orientation. Recall that the difference between adjacent cells is caused by their opposite directions of rotation. The simulation shows white patches between adjacent cells above and below the centerline, also seen in the experimental interferogram as dark regions. This is due to large density of the contour lines in these regions. The conducting side walls affect the cells adjacent to them both in the simulation and experiment. The cells close to the lateral walls are smaller than those in the central region and there appear to be two smaller recirculation regions in the interferograms of both simulation and experiment adjacent to the walls. This is confirmed by the vector plot in figure 4.2.

4.3.3 Quantitative comparison with experimental Nu_{avg} at high Pr

One of the most important results of this study is the overall heat transfer rate through the liquid layer or Nu_{avg}. Recall from the introduction section that the average Nusselt number (Nu_{avg}) for pure natural convection flow in shallow liquid layers for high Pr has been quantified by extensive experimental work. Koschimeder (1974) [39] conducted experiments using silicone oil of viscosity varying from 5-200cs i.e. Pr varying from 50-1670. The experimental setup consisted of a shallow horizontal circular fluid layer heated from below. Beyond the critical Ra for onset of natural convection (Ra_c) natural convection cells in the form of concentric rings were formed increasing Nu_{avg} above one. With increasing Ra the concentric rings broke up and cells were formed until at large Ra the flow transitioned to time dependent. The Nu_{avg} increases non-linearly with Ra. The Nu_{avg} plots for different Pr seem to suggest that the results are independent of Pr over a wide range of Ra from Ra_c to $200Ra_c$. Experiments have been done by Rossby (1969) [38] using water (Pr = 6.8), mercury (Pr = 0.025) and silicone oil (Pr = 100, 200). The apparatus setup is similar to Koschimeder (1974) [39] consisting of a fluid layer sandwiched between two copper blocks and surrounded by an aluminum cylinder. The depth of the fluid layer and temperature difference were varied to vary the Ra. The lower disk was rotated at varying speeds to study the effect of Taylor number (Ta). Flow visualization was done by illuminating a suspension of aluminum powder in the fluid using a light beam. The natural convection cell pattern for a Ta of 0 was found to consist predominantly of roll and roll-like cells similar to the observation of Koschimeder(1974) [39]. With increasing Ra the roll pattern lost its two dimensional structure and transitioned at large Ra to time dependent convection. Using the results for various Ra and silicone oil with a Pr of 200 an experimental correlation was obtained between Nu_{avg} and Ra for this Pr namely $Nu_{avg} = 0.184Ra^{0.281\pm 0.005}$.

In order to make a quantitative comparison with experimental data the discretized governing equations were solved for Pr of 100 and 667 for different Ra above the critical value for onset of natural convection and below 100000, which is the critical Ra for transition to oscillatory convection. Figure 4.4 is a plot of the Nu_{avg} results obtained from computation and experiments of Koschimeder (1974) [39] and Rossby (1969) [38]. The experiment and simulation compare very well. The Nu_{avg} is found to increase linearly with the logarithm of Ra. There is some divergence between the computations and experiments at the high Ra of 100000. This is most probably due to the onset of oscillatory convection at Ra of 100000. Though all four results presented are for different Pr they line up almost exactly. This confirms the trend of Koschimeder (1974) [39], that the results are independent of Pr for Pr in the range 50-1670.

The present numerical method using FIDAP [42] for computations was able to predict accurately (to within 4.5%) the results for a test case with larger temperature gradients than the problem under study (Recall that the largest temperature gradients occur at lower Pr with zero shear velocity). It also accurately reproduced the natural convection cell shape, size and distribution as was seen in the comparison with the experimental interferogram. Finally it was able to reproduce quantitatively accurate results for two different Pr over a wide range of Ra. This confirms the ability of the numerical method (discussed in detail in section 2) on the computational grid of size (160x16) to give both qualitatively and quantitatively accurate results for the entire range of Ra, Pr and shear velocities in this study.

4.4 Results and Discussion

4.4.1 Overview

The objective of this study is to conduct many simulations over a wide range of Ra, Pr and shear velocities. Simulations were done with Ra varying from near critical for onset of natural convection to 100000, which is the critical Ra for transition to oscillatory convection and beyond which the steady state assumption is no longer valid. Also the flow is assumed to be two-dimensional over the range of study. Two different high Pr namely 100 and 667 were chosen to study the effect of Pr on fluid flow and heat transfer. For each Ra and Pr shear velocity was added and effects of progressively increasing shear velocity were observed. Recall that natural convection computations inherently have convergence problems because of the strong coupling between the momentum and energy equations resulting from the buoyancy and advection terms.

Thus the relaxation factors necessary to achieve convergence, particularly for shear velocities close to when natural convection cells are almost annihilated, vary with iteration number requiring more iterations for convergence to an accurate solution. The entire study required over 12000 iterations.

4.4.2 Effect of shear velocity

Figure 4.5 is a set of plots similar to figure 4.2, for Ra = 2500, Pr = 100, with added bottom shear velocity. Recall that the characteristic velocity used to non-dimensionalize the governing equations was defined as $\sqrt{gb\Delta TH / an}$ and termed U_o. The non-dimensional shear velocity (U/U_o) for this example case is 0.25. As seen in the velocity vector plot in figure 4.5 those rolls which rotate with this bottom shear velocity get enlarged, while those opposed get smaller and the number of rolls has decreased from 10 to 9. The flow in the rolls, which for pure natural convection was in the form of plumes impinging vertically on the top and bottom, is now directed at the angle of around 45^o to the surfaces. This is reflected in the temperature contour plot with the contour lines corresponding to the plumes symmetric about an inclined line rather than the vertical for pure natural convection (figure 4.2). This inclination of the symmetry line in the temperature contour plot reduces the normal temperature gradient reducing the local Nusselt number as seen in the fall of the peaks in the Nusselt number distribution. Due to the shear additional flow is set up in the domain, which causes more flow to impinge on the top and bottom surfaces on the right and left hand corners respectively. This is seen in the vertical velocity distribution as a larger peak at the left end and smaller but broader peak at the right end of the plot. These cause increased temperature gradients as seen by the closer grouping of temperature contours and corresponding peaks in the Nusselt number distribution. The peak on the left is larger and causes increased heat transfer on the bottom surface whereas the smaller but broader peak on the right increases the top surface heat transfer making the overall heat flux through the top and bottom layers equal (Note: The lateral walls are adiabatic).

With increasing shear velocity the cells rotating in the same direction as the velocity get larger and the number of cells continues to decrease. The angle of the plume velocity with the vertical continues to increase and is reflected in the increased inclination of the symmetry line of the temperature contour plot. This in turn decreases the normal temperature gradient close to the impingement point, decreasing the peak and increasing the valley values in the Nusselt number distribution along the top and bottom surfaces. The increased shear further increases the flow rate increasing the peak Nusselt number on the bottom surface left end and increasing and broadening the peak Nusselt number on the top surface right end.

Beyond a certain velocity all remaining cells merge to form a single large recirculation region. The bottom velocity at which this occurs is defined to be the critical velocity (U_c). Parametric studies confirm the existence of such a critical velocity for each Ra and Pr. Figure 4.6 is a set of velocity vector, temperature contour, Nusselt number and vertical velocity distribution for bottom shear velocity greater than U_c. The non-dimensional shear velocity (U/U_o) in figure 4.6 is 0.59. The velocity vector plot shows the existence of a single large recirculation region. There is no natural convection effect as seen in the horizontal, equally spaced contour lines in the central region of the temperature contour plot. This is reflected in the flat Nusselt number distribution in the central region along both top and bottom surfaces. As a result of the single recirculation region all the flow resulting from the shear of the bottom surface flows in the recirculating loop as opposed to flow with natural convection where part of the flow is carried by the cells. This large flow, seen in the large vertical velocities near the lateral walls, impinges to produce large temperature gradients along the top and bottom surfaces on the right and left end respectively, seen in the close grouping of contour lines in these regions. This results in a large Nusselt number peak of 4.5 on the bottom surface and a smaller but much broader peak of 2.5 (Nu_R) on the top surface. Further increase of shear velocity increases the flow rate in the recirculation region, increasing the peak Nusselt numbers on the top and bottom surface on the right and left end respectively.

4.4.3 Critical velocity

As mentioned in the previous section a critical velocity was identified for each Ra and Pr, beyond which the bottom shear velocity annihilated the natural convection cells resulting in the formation of a single large recirculation region. From figures 4.5 and 4.6 it can be seen that there are significant differences between sub-critical and post-critical flow and thermal fields. These differences were discussed in detail in the previous section suffice to state here that it is necessary to quantify the critical velocity as a function of Ra and Pr. To this end a number of simulations were done for each Ra and Pr varying the velocity in each case from zero until shear annihilates the natural convection cells. Using this procedure a sub-critical (cells present) and post-critical (cells annihilated) bottom shear velocity are obtained. More simulations with shear velocities in this range were needed to narrow the gap between sub-critical and post-critical shear velocity to the required accuracy.

Figure 4.7 is a plot of the dimensionless sub-critical and post-critical velocities as a function of Ra for two different Pr of 100 and 667. At and above post-critical bottom velocities the multiple natural convection cells are annihilated by the shear and natural convection does not effect the flow pattern. At and below sub-critical bottom velocities there are multiple natural convection cells with number of cells increasing with decreasing velocity. Recall that the lower limit of 1707 on the Ra axis corresponds to the critical Ra for onset of natural convection in shallow cavities of aspect ratio (A) 10 or more, obtained using linear stability analysis [28]. For this Ra, the roll velocities are infinitesimally small so that an infinitesimal bottom shear velocity would be sufficient to annihilate the rolls. Thus for a Ra of 1707 a U/U_o infinitesimally larger than zero would be the critical velocity. From figure 4.7, for both Pr the dimensionless critical velocity is seen to increase with increasing Ra. This is expected as with increasing Ra the strength of the natural convection cells increases, increasing the bottom velocity required to annihilate the cells. The rate of increase in not constant being large for low Ra and then tending to zero for Ra of order 100000. There is significant overlap between the critical regions (region between sub-critical and post-critical) of the two Pr. This is due to the appropriate selection of the characteristic velocity (U_o), which eliminates the effect of Pr on the critical velocity.

4.4.4 Variation of Nu_{avg} , Nu_R , Cell Aspect Ratio and Nu profile with U, Ra and Pr

Having quantified the critical velocity as a function of Ra and Pr the variation of fluid flow and heat transfer below and above critical velocity is of interest and is plotted in figures 4.8-4.11. In order to distinguish between the points of two different Pr all points on future graphs, with Pr of 100 are closed or filled while points for Pr of 667 are open or not filled. This can be observed in figure 4.8 which is a plot of Nu_{avg} as a function of bottom shear velocity for different Ra and Pr. For zero bottom shear velocity or along the Y axis increasing Ra is found to increase Nu_{avg}. On the other hand increasing Pr decreases the Nu_{avg} for zero bottom shear velocity as seen from the points for two different Pr and Ra of 100000. Increasing bottom shear velocity (U/U_o) for any Ra and Pr decreases Nu_{avg} for bottom shear velocity (U/U_o) much below critical (U_c/U_o). Close to critical bottom shear velocity Nu_{avg} reaches a minimum after which the trend reverses and Nu_{avg} is found to increase with (U/U_o) although the rate of increase after minimum is much lower than the rate of decrease before the minimum Nu_{avg}. The explanation for this behaviour follows from the discussion about the effect of shear velocity in an earlier section. Recall that with increasing bottom shear velocity the cells rotating in the same direction are enlarged at the expense of the cells rotating in the opposite direction. The vertically moving plumes carrying hot fluid up and cold fluid down for pure natural convection are replaced by inclined plumes whose angle of inclination to the vertical increases with bottom shear velocity until they become horizontal when all natural convection cells are annihilated. The effect of the inclination of these plumes, as discussed earlier, is to reduce the normal temperature gradient which dictates the heat flux and hence the Nusselt number. Thus with increasing bottom shear velocity the peaks in the Nusselt number distributions along the top and bottom surfaces decrease and the Nusselt number profile progressively evens out with the increasing bottom shear velocity. With decreasing peak values Nu_{avg} also decreases as is seen in figure 4.8. However with increasing bottom shear velocity the shear driven flow rate increases, increasing the peak values on the top and bottom surface at the right and left end respectively as seen in the Nusselt number distributions in figures 4.5 and 4.6. The increase in Nu_{avg} due to increase in Nu_R and decrease due to decrease in the peaks along the central region counteract to produce a minimum close to critical velocity. Above critical velocity the Nusselt number distribution in the central region is flat but increases slightly resulting from increased heat transfer from increased shear. This in addition to the increase in Nu_R causes Nu_{avg} to increase after the minimum. Figure 4.9 is a plot of variation of the right peak Nusselt number (Nu_R) along the top surface with bottom shear velocity (U/U_o). For pure natural convection Nu_R is the same as the peak value of the Nusselt number distribution in the central region. With increasing bottom shear velocity the decreasing peak values in Nusselt number distribution in the central region also decrease Nu_R but beyond critical velocity Nu_R increases. The rate of increase is low contributing to the slow rise in Nu_{avg} beyond its minimum in figure 4.8. In figure 4.8 there is some overlap between the two Pr curves for Ra of 100000 although not sufficient to be called identical. The critical velocity contour in figure 4.8 and 4.9 is a curve fit through the critical (U/U_o) values for the different Ra, Pr simulations. As observed earlier in figure 4.7 the critical velocity saturates close to (U/U_o) of 1 around a Ra of 100000 for both Pr.

The cell distribution in the cavity has been quantified by the average cell aspect ratio defined as C = A/(Number of cells in the cavity), A = 10 for present study. Figure 4.10 is a plot of variation of average cell aspect ratio (C) with bottom shear velocity (U/U_o). For pure natural convection the number of cells is approximately equal to the aspect ratio of the cavity or C is nearly 1. With increasing bottom shear velocity (U/U_o) the cells rotating opposite to the shear start getting annihilated decreasing the total number of cells in the cavity and hence increases C. When the shear velocity has annihilated all the natural convection cells only one large recirculation region or cell remains hence C becomes 10. There is no clear trend of the results with Ra or Pr. For a given Pr increasing Ra increases the strength of the natural convection cells and hence should, in general, increase the number of cells or decrease C for a given (U/U_o). For both Pr, for a given (U/U_o), increasing Ra is seen to first decrease then increase C close to Ra of 100000. The present study was carried out for A of 10. For a fluid layer of larger A, C will asymptote to that aspect ratio A.

One of the effects of natural convection cells is uneven heat transfer through the fluid layer as seen in the Nusselt number distribution in figure 4.2. In general for industrial applications uniform heat transfer is preferred. Hence the unevenness in the Nu distribution quantified by the ratio of difference between maximum and minimum Nu to Nu_{avg} as a function of (U/U_o) is quantified for different Ra and Pr in figure 4.11. For stationary natural convection this ratio is greater than 1 i.e. a highly uneven Nu distribution. For bottom shear velocities in excess of U_c the Nu distribution along the top and bottom surfaces away from the walls is flat hence the ratio is 0. Between these extremes there is no clear trend with Ra and Pr.

4.4.5 Some aspects of flow pattern variation with U

In this section some aspects of flow pattern variation with bottom shear velocity (U) are discussed for a Ra of 2500 and a Pr of 100. The discussion also applies for other Ra and Pr. The variation of velocity distribution across the center of the roll in the vertical direction with bottom velocity is shown in figure 4.12. For stationary natural convection this velocity distribution is along the vertical centerline of any cell. For mixed convection with sub-critical bottom shear velocities the velocity distribution is along the vertical centerline of one of the large cells rotating in the same direction as the shear velocity. For post-critical bottom shear velocities the velocity distribution is obtained at the center of the domain length. For stationary natural convection ($U/U_o = 0$) the pattern is symmetric about the halfway height of the liquid flux layer ($y/H = 0.5$). This follows from the symmetric rolls of aspect ratio one seen for stationary natural convection in figure 4.2. The horizontal velocity (V_x/U_o) decreases to zero at the no-slip top and bottom walls giving the velocity distribution a sinusoidal appearance. With increasing bottom velocity (increasing V_x/U_o at $y/H = 0$) the center of the roll ((y/H) where velocity (V_x/U_o) changes sign in figure 4.12) is found to drop toward the bottom surface. With increasing bottom velocity, the shear increases, increasing the flow rate close to the bottom, evidenced by the larger area under the curves from y/H of 0 to 0.5 in figure 4.12. Since the flow is two-dimensional, in order to satisfy continuity, the net area under the curve must be zero. Since the effect of increased bottom shear velocity on the velocities on the top half of the fluid layer is not significant for sub-critical velocities, continuity can be satisfied only by lowering of the roll center. This is also seen in figure 4.13, which is a plot of the location of the roll center above the bottom surface with increasing bottom shear velocity (U/U_o). Beyond the critical bottom shear velocity the effect of increased bottom shear velocity is felt directly by the upper half of the liquid flux layer, through the single recirculating flow, causing the roll center location in figure 4.13 to stabilize around y/H = 0.333.

The roll speed variation with the bottom velocity is seen in figure 4.14. The roll speed is quantified as the maximum horizontal velocity above the center of the roll, rotating in the same direction as the bottom shear velocity. For low bottom shear velocities the roll speed is found to increase with increasing shear i.e. the bottom shear velocity accelerates the rolls rotating in the same direction. Close to critical increasing bottom shear velocity is seen to decrease the roll speed. This implies slip between the bottom shear flow and the roll flow close to critical velocities. For post-critical velocities roll speed is the same as the maximum horizontal velocity in the region above the eye of the single recirculating roll. Increased bottom shear velocity for this flow configuration increases the flow rate along the bottom through shear. This increased flow recirculates along the top half of the liquid layer increasing velocities in this region. Thus, as observed in figure 4.14 increased post-critical velocities increase the roll speed.

4.4.6 Relation between U and Interface Shear (t)

For most industrial applications (e.g. slag layers) the fluid layer is suspended on an underlying fluid bed. Flow in this bed can shear drive the fluid layer through the bottom interface which forms an equal shear boundary. The fluid flow in the underlying fluid bed can be computed using numerical methods. Using a suitable discretized form the local gradient of horizontal velocity in the vertical direction, at each discrete point (cell/element) on the interface, can be computed. Knowing the molecular viscosity of the underlying fluid the average shear stress exerted on the suspended fluid layer can then be computed. Now it is necessary to make a correlation between the imposed interface shear and the resulting velocity of the bottom surface of the fluid layer. This can be done by computing the average shear exerted by the flow in the fluid layer on the bottom surface for each Ra, Pr and bottom shear velocity. A second order accurate, three-point differencing scheme was used to compute the dimensionless vertical gradient of the horizontal velocity ($\partial u^*/ \partial y^*$) for each finite element along the bottom surface. These local gradients act over the length of the corresponding element. Since the grid is uniform in the horizontal (x-direction) averaging these local gradients yields an average dimensionless gradient for the entire surface. Figure 4.15 is such a plot of average non-dimensional velocity gradient or shear stress, along the top and bottom surfaces, as a function of dimensionless interface velocity (U/U_o). The plot is made for three different Ra-Pr combinations to study the effect of Ra and Pr. The average non-dimensional shear stress along the top and bottom is seen to increase linearly with increasing non-dimensional bottom shear velocity. Also for this choice of characteristic values of shear stress and bottom velocity the graphs for different Ra and Pr merge exactly. Hence a universal correlation, applicable for all Ra and Pr, between interface shear stress and bottom shear velocity (U) can be obtained as follows:

$$\text{Bottom shear stress} = \tau_B\ (N/m^2) = 4.35\ (\mu U/ H) \tag{9}$$

$$\text{Top shear stress} = \tau_T\ (N/m^2) = 2.115\ (\mu U/ H) \tag{10}$$

The above correlations are in the dimensional form. Since the velocity terms in both the non-dimensional velocity gradient and non-dimensional bottom shear velocity are scaled by the same characteristic velocity U_o, U_o and hence Ra and Pr do not affect the correlations (9) and (10). Thus the shear stress-velocity correlation is found to be independent of the strength of natural convection, which is governed by Ra and Pr. The reason for this can be found in figures 4.16-4.18 which are plots of variation of dimensionless shear stress along the top and bottom of the fluid layer, for stationary, sub-critical and post critical bottom shear velocities. For stationary convection (figure 4.16) the shear exerted by the consecutive rolls is identical but opposite in sign, as seen in the sinusoidal variation of shear stress along both surfaces, giving a net shear of zero. Thus the net shear exerted by pure natural convection cells is the same as that exerted by a stationary fluid layer, namely zero. For sub-critical bottom velocity (figure 4.17) mixed convection exists. Natural convection rolls rotating in the same direction as the bottom shear velocity will, by virtue of more slip, experience lower shear than for the same shear flow in the absence of natural convection. The exact opposite will be true for rolls rotating in a direction opposite to bottom shear velocity. This is reflected in the sinusoidal shear stress variation over and above the mean shear seen in figure 4.7. Thus there is no net contribution of natural convection to the average interface shear. For post-critical bottom velocity (figure 4.18) natural convection is no longer found to affect the flow, as observed in the flat shear stress distribution profile in the central region. Hence for all bottom shear velocities natural convection is found to have no effect on the average top or bottom shear. Knowing the average interface shear from other computations, correlations (9-10) can be used to compute dimensional bottom shear velocity.

4.5 Summary

The critical bottom shear velocity for annihilation of multiple natural convection cells is found to increase with Ra around a Ra of 100000 for all Pr. With increasing Pr the critical bottom shear velocity is also found to increase. The average Nusselt number (Nu_{avg}), which quantifies the heat flux through the fluid layer follows a decrease-minimum-increase pattern with increasing bottom shear velocity (U/U_o), the minimum value occurring close to the critical bottom shear velocity. The rate of decrease for sub-critical bottom shear velocities is much higher than the rate of increase after the minimum value is reached. In addition Nu_{avg} is found to increase with increasing Ra irrespective of the Pr or dimensionless bottom shear velocity (U/U_o). The center of the natural convection rolls drop with increasing bottom shear velocity asymptoting around y/H = 0.33 for post-critical bottom shear values. As the bottom shear velocity increases the roll speed first rises, then drops around the critical, and rises beyond the critical bottom shear velocity. This implies that the rolls initially are accelerated by the bottom shear velocity, then close to critical values they slip with respect to the bottom shear and beyond critical the single recirculation region value causes roll speed to increase again.

The average shear stress at the top and bottom interfaces is seen to be a linear function of the bottom velocity. The alternate natural convection cells have identical interface shear distributions but with opposite signs. Thus the linear correlation is found to be independent of the Ra and Pr and hence the strength of natural convection.

Knowing the interface shear (eg. from calculations in the fluid flow beneath) the bottom velocity can be computed using correlation (9-10). Comparing this value with U_c one can determine the nature of the fluid flow in the layer. In addition the Nu_{avg}, roll aspect ratio, roll center location, roll speed etc can be computed using the plots presented in this work. Thus this study will serve as a ready reference to determine both qualitatively and quantitatively the fluid flow and heat transfer in shear driven fluid layers with natural convection at high Pr.

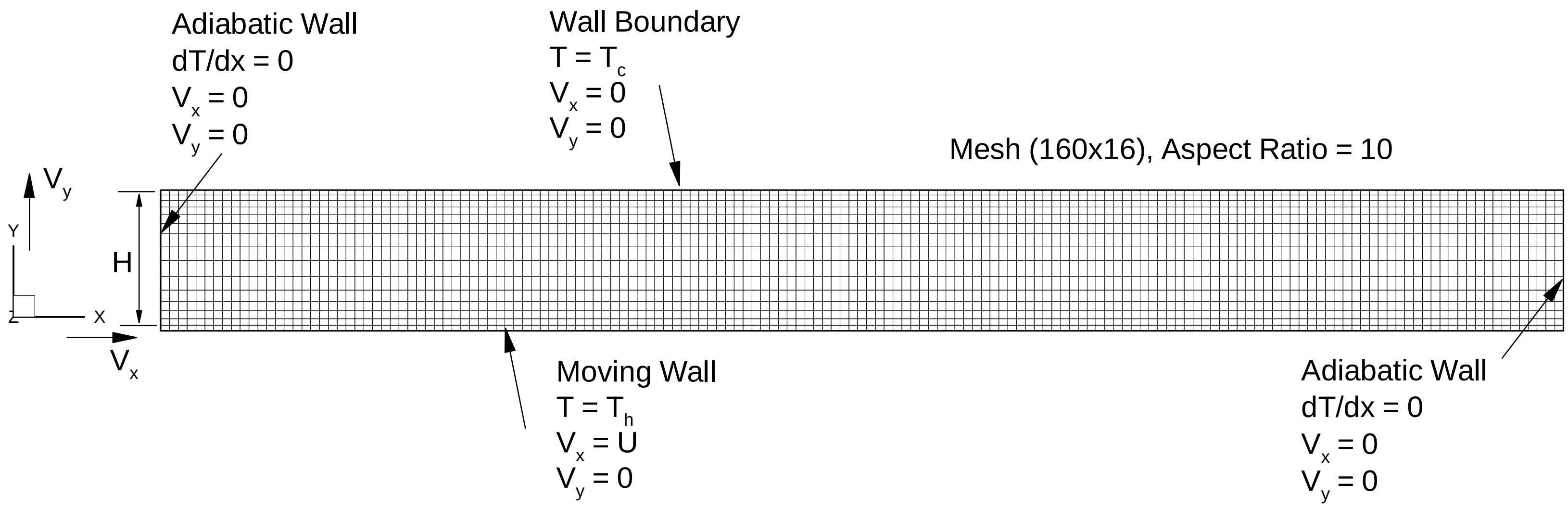

Figure 4.1 Computational domain with mesh and boundary conditions

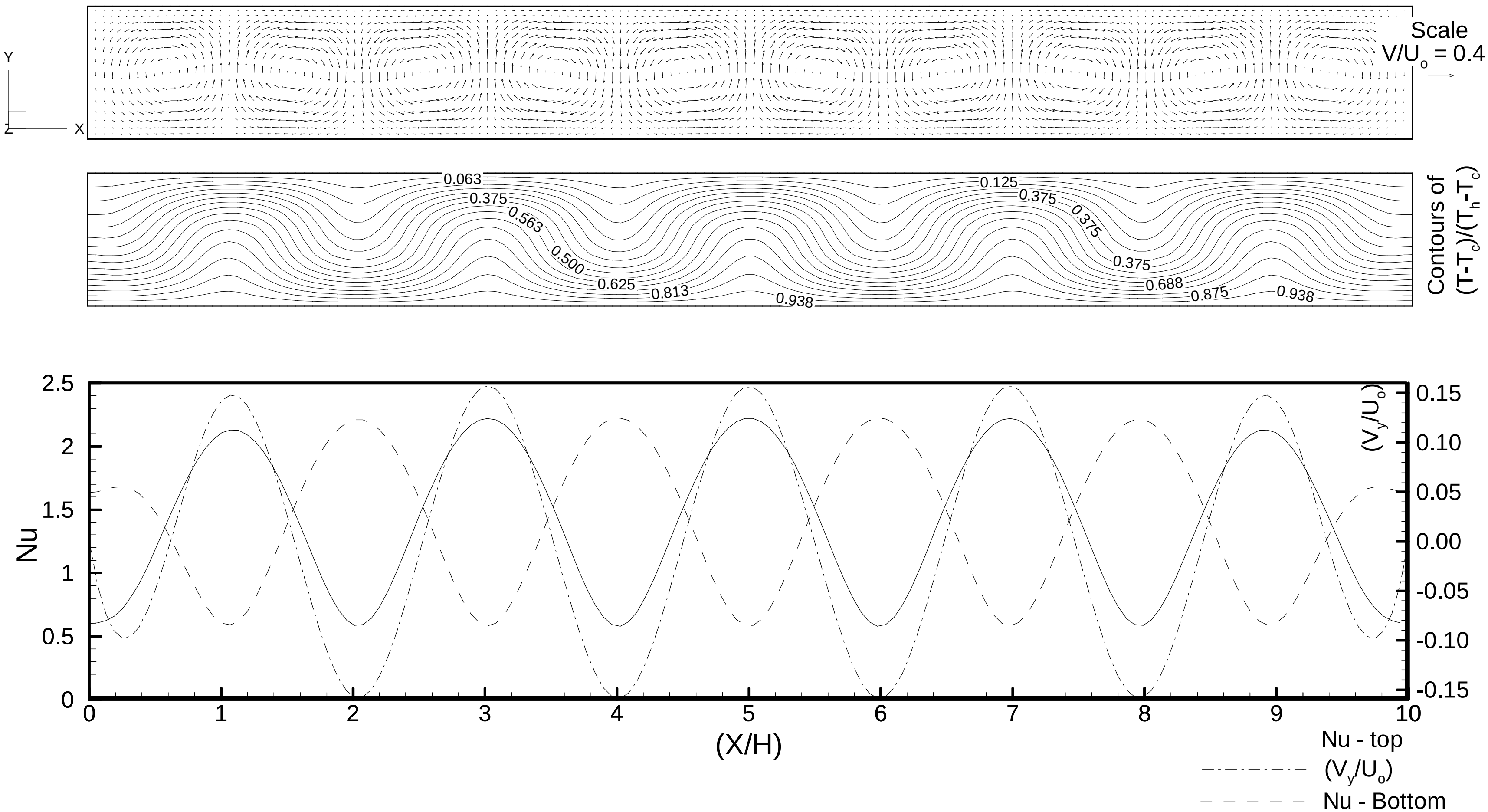

Figure 4.2 Velocity vector, temperature contour, Nu and V_y profiles for Ra = 2500, Pr = 100 and U/U_o = 0

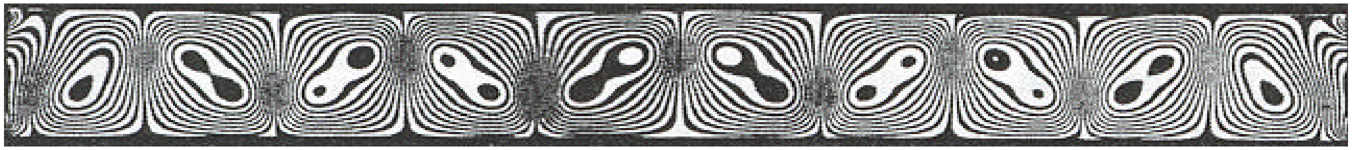

Oertel measurement (1988)

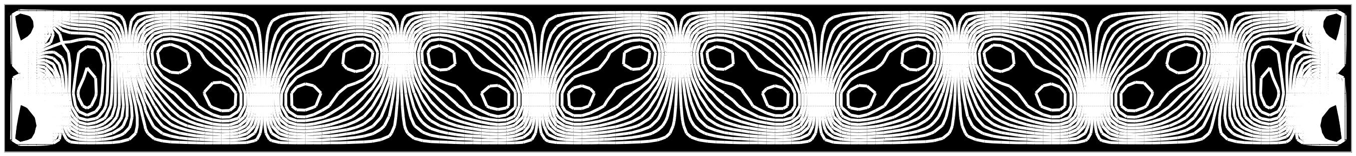

FIDAP

Figure 4.3 Comparison of contours of horizontal density gradients (calculated vs experimental interferogram)

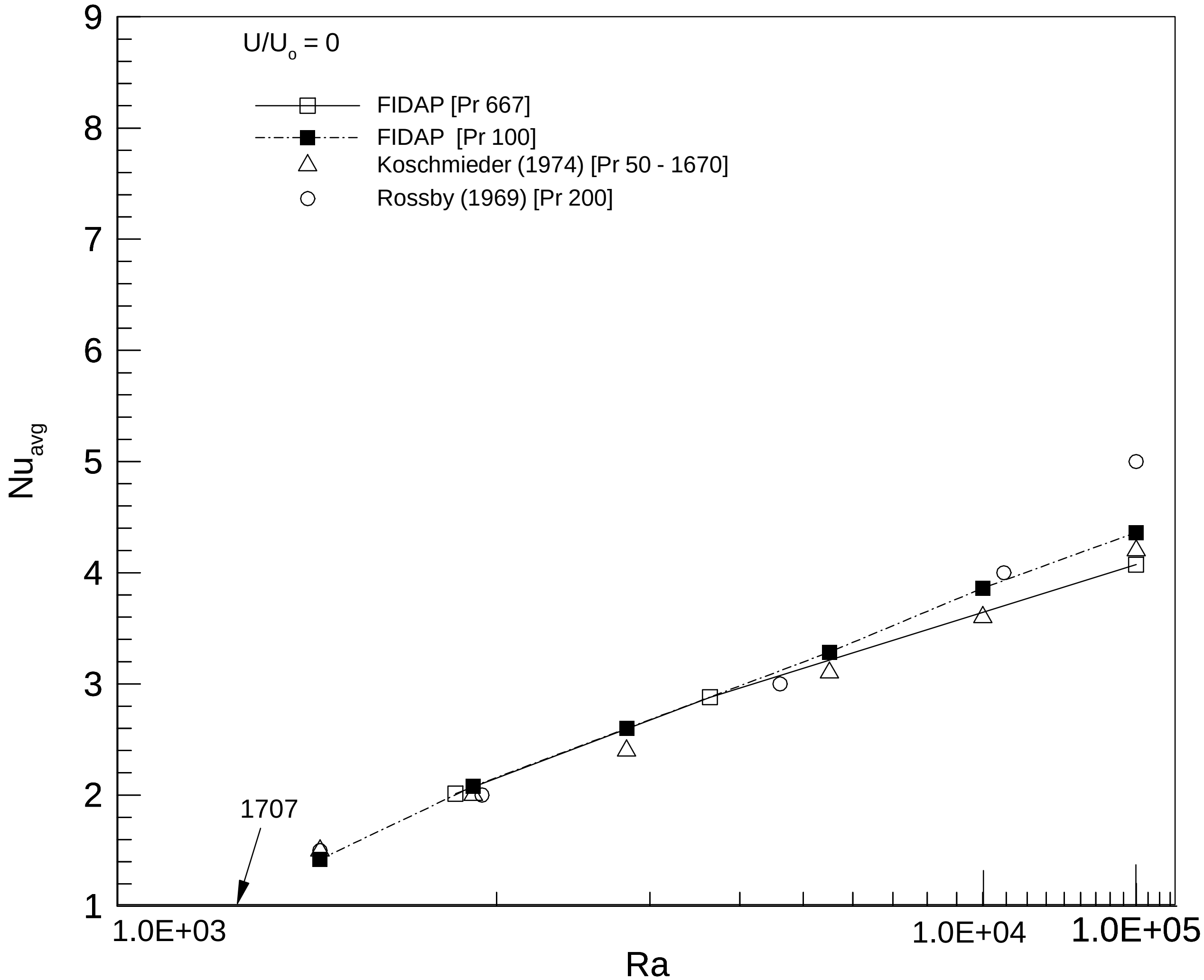

Figure 4.4 Variation of Nu_{avg} with Ra (comparison of FIDAP with experimental results)

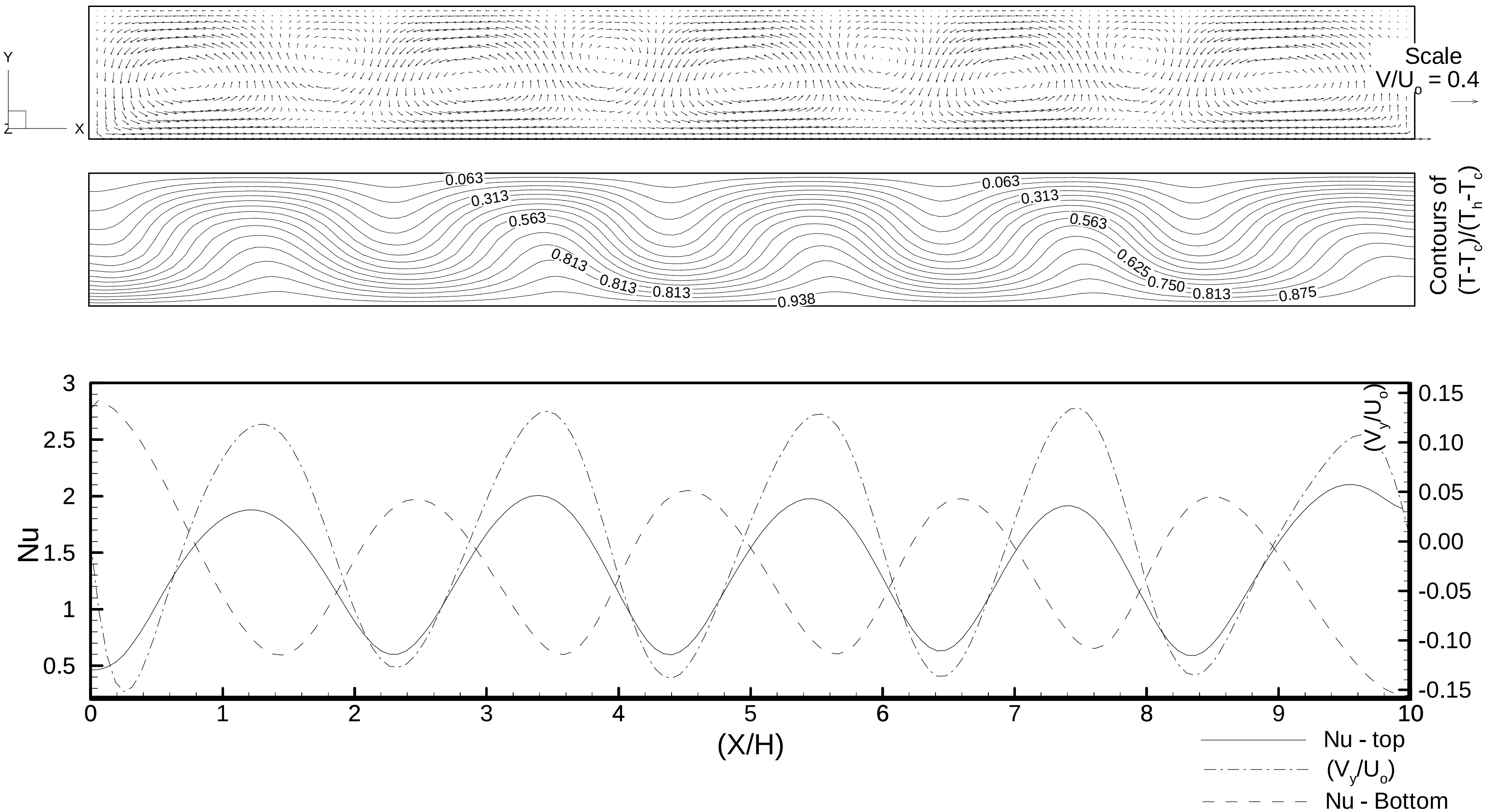

Figure 4.5 Velocity vector, temperature contour, Nu and V_y profiles for Ra = 2500, Pr = 100 and U/U_o = 0.246

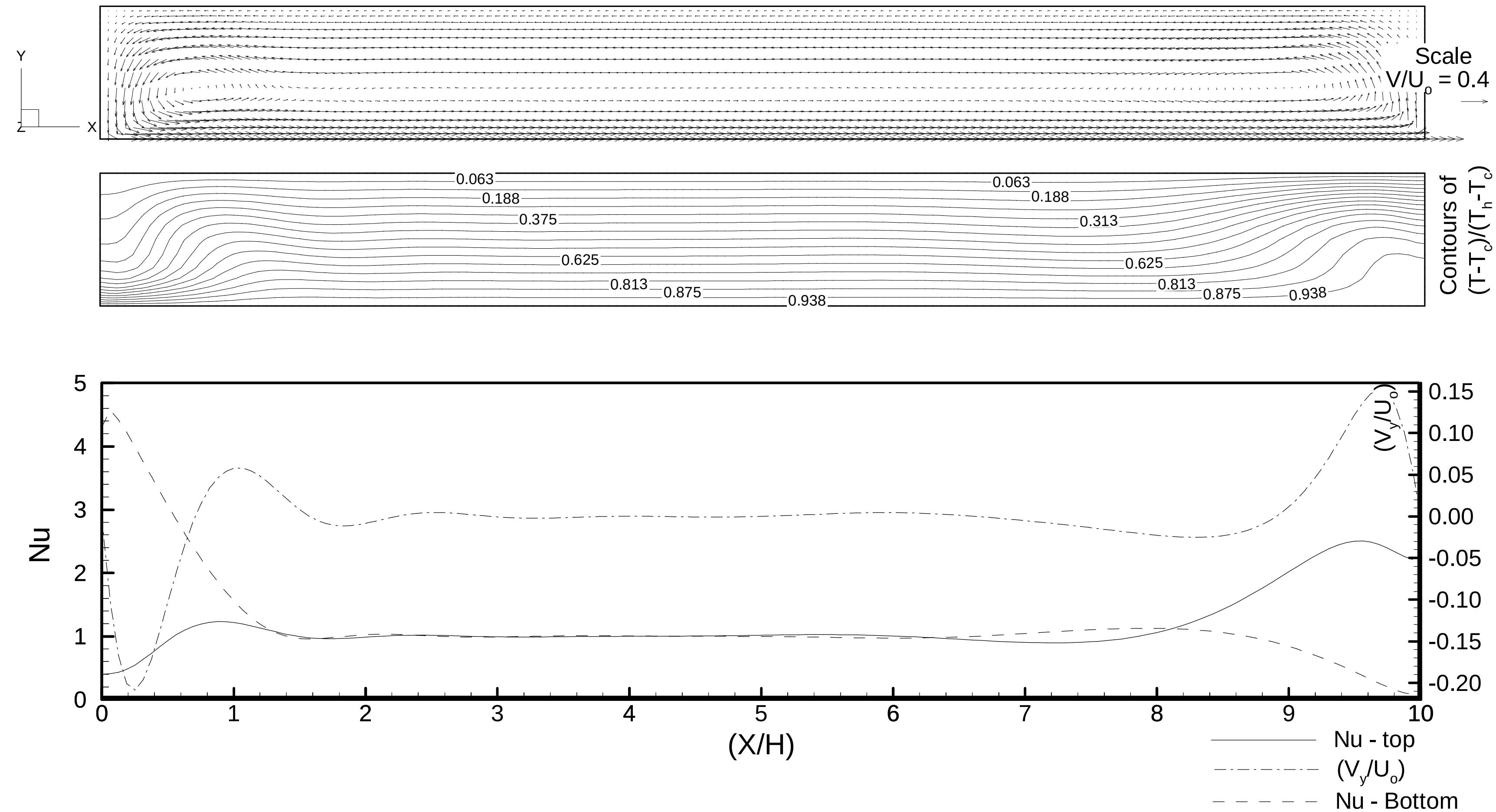

Figure 4.6 Velocity vector, temperature contour, Nu and V_y profiles for Ra = 2500, Pr = 100 and U/U_o = 0.59

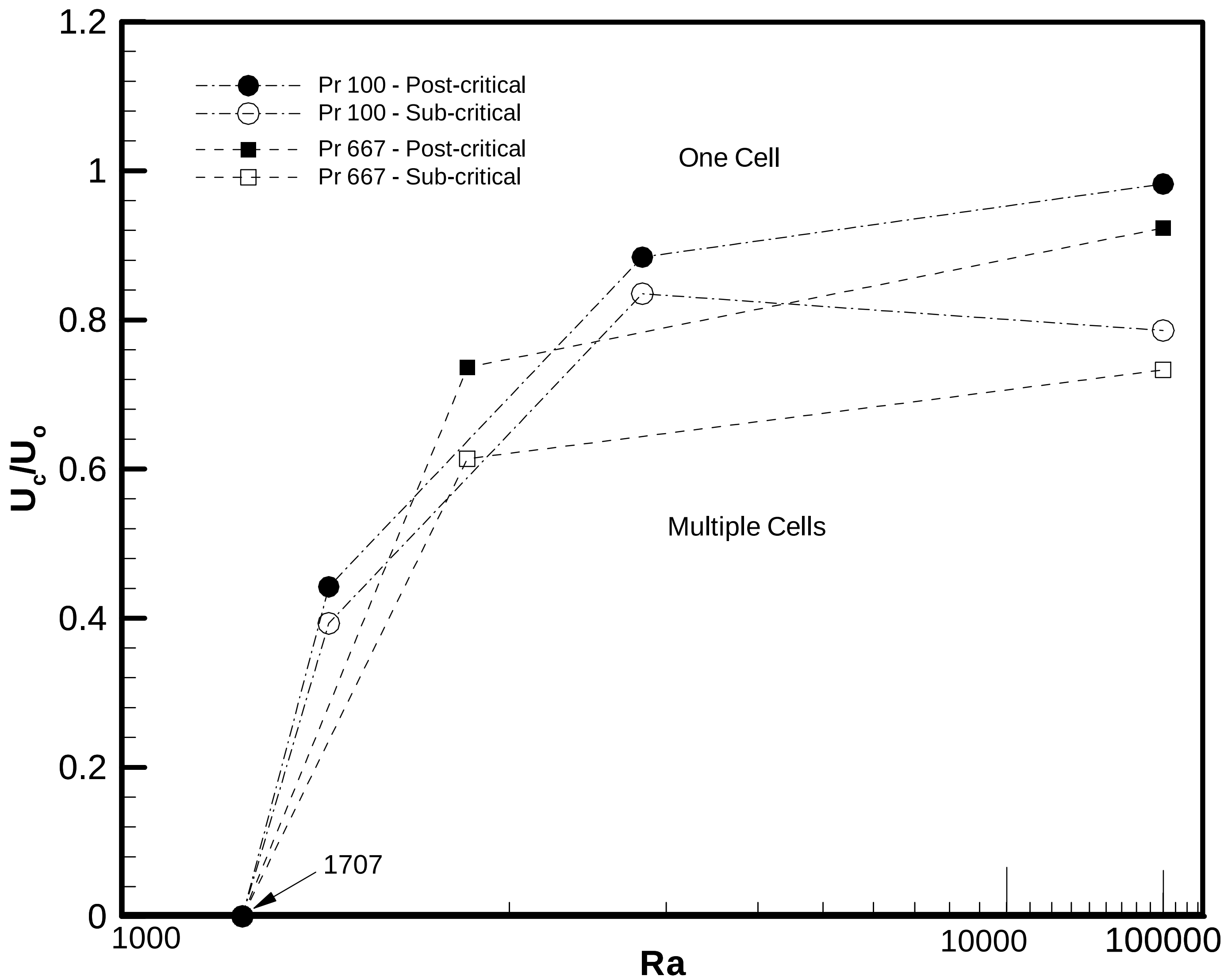

Figure 4.7 Dimensionless critical velocity as a function of Ra and Pr numbers

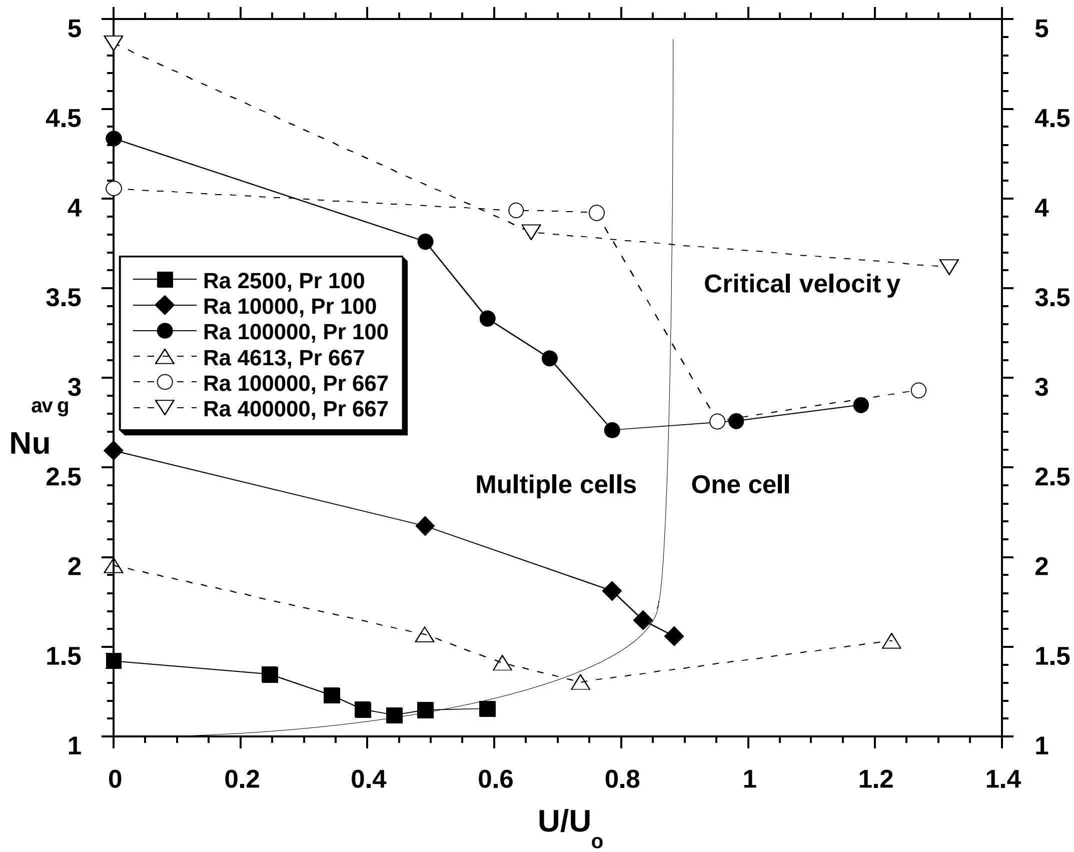

Figure 4.8 Nu_{avg} as a function of Ra, Pr and U/U_o

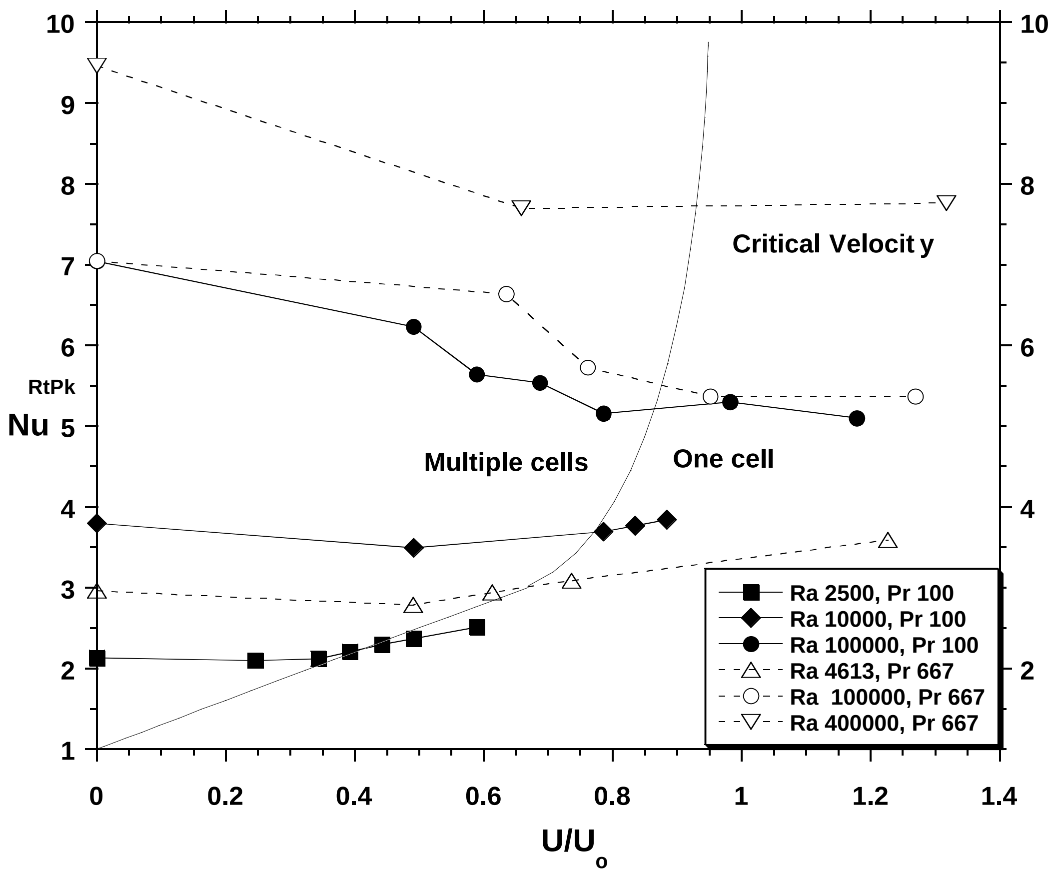

Figure 4.9 Right peak Nusselt number as a function of (U/U_o), Ra and Pr

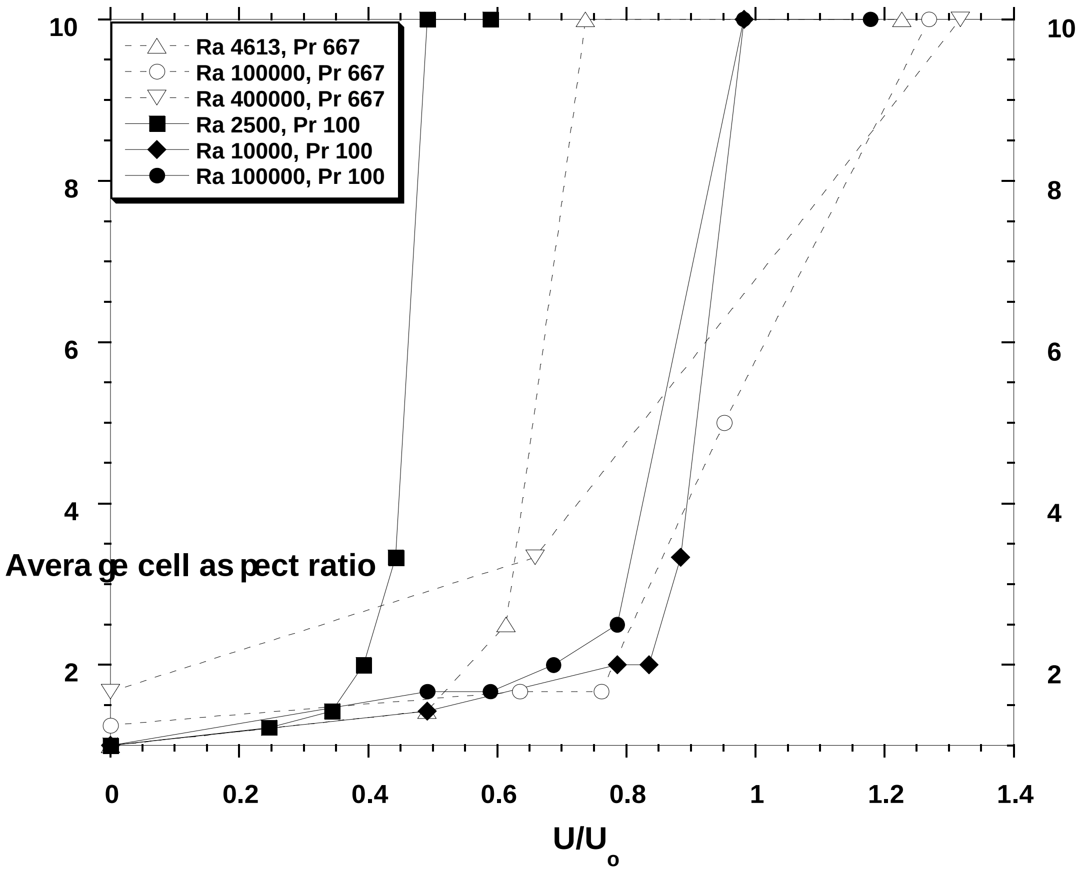

Figure 4.10 Average cell aspect ratio as a function of (U/U_o), Ra and Pr

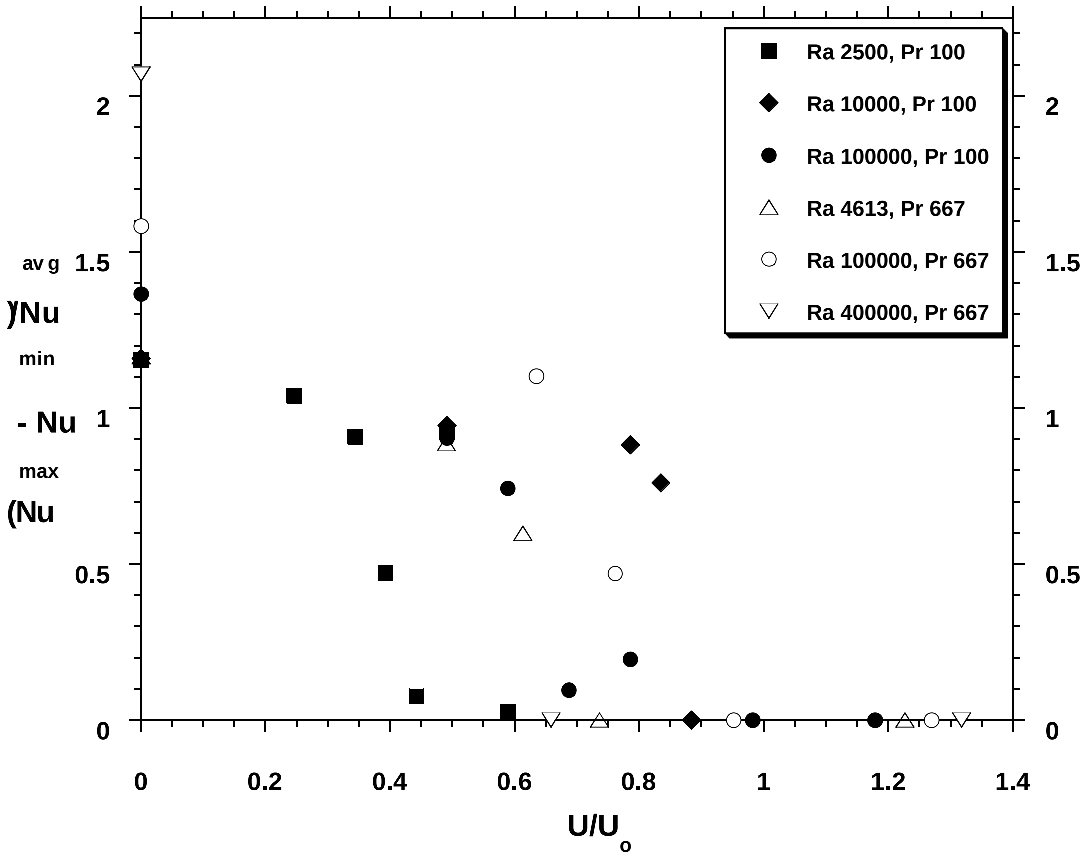

Figure 4.11 Relative uneveness of Nu profile as a function of (U/U_o), Ra and Pr

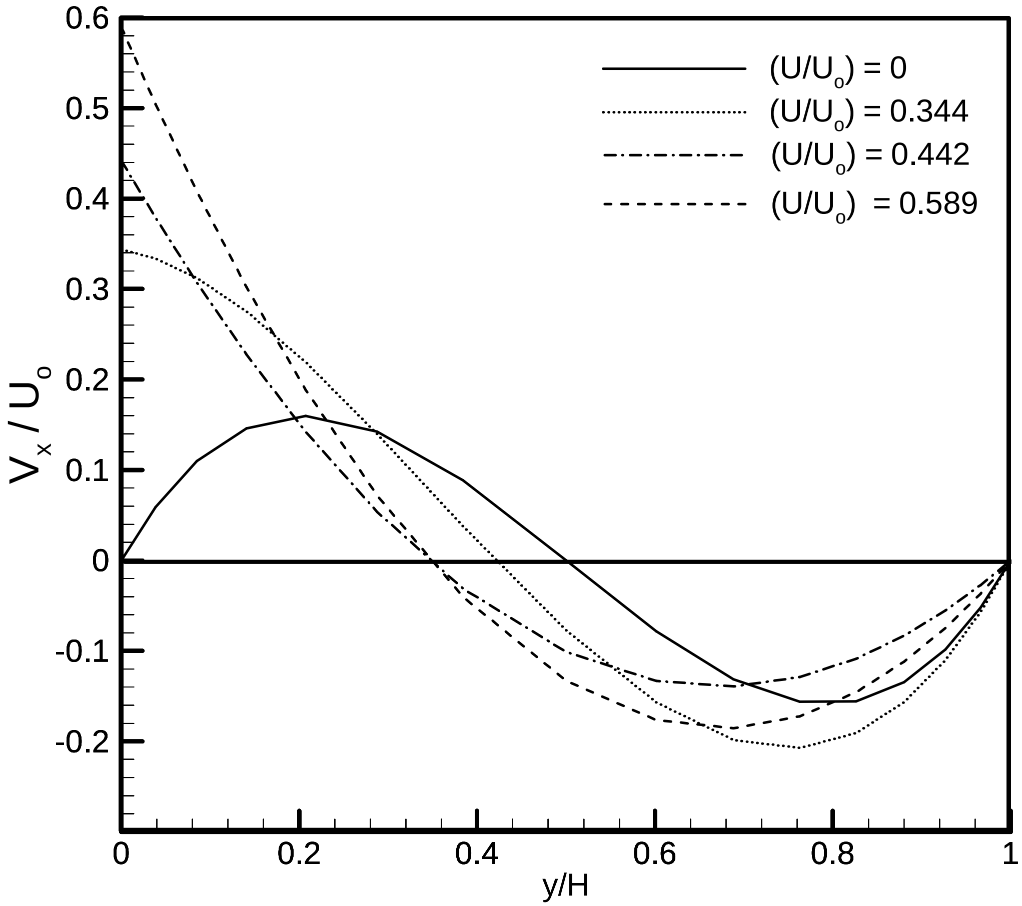

Figure 4.12 (V_x/U_o) as a function of (y/H) through the eye of the roll for different (U/U_o)

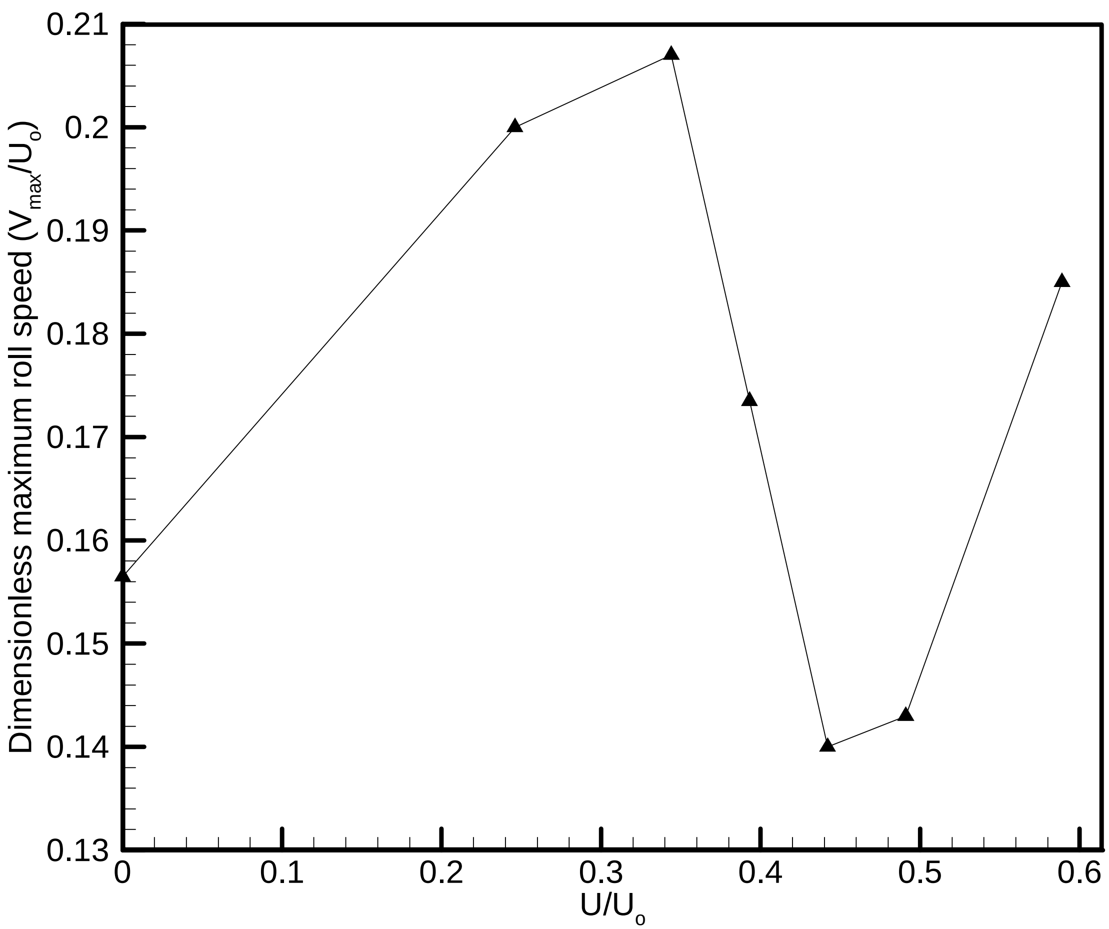

Figure 4.13 Maximum roll speed as a function of interface velocity for Ra = 2500, Pr = 100

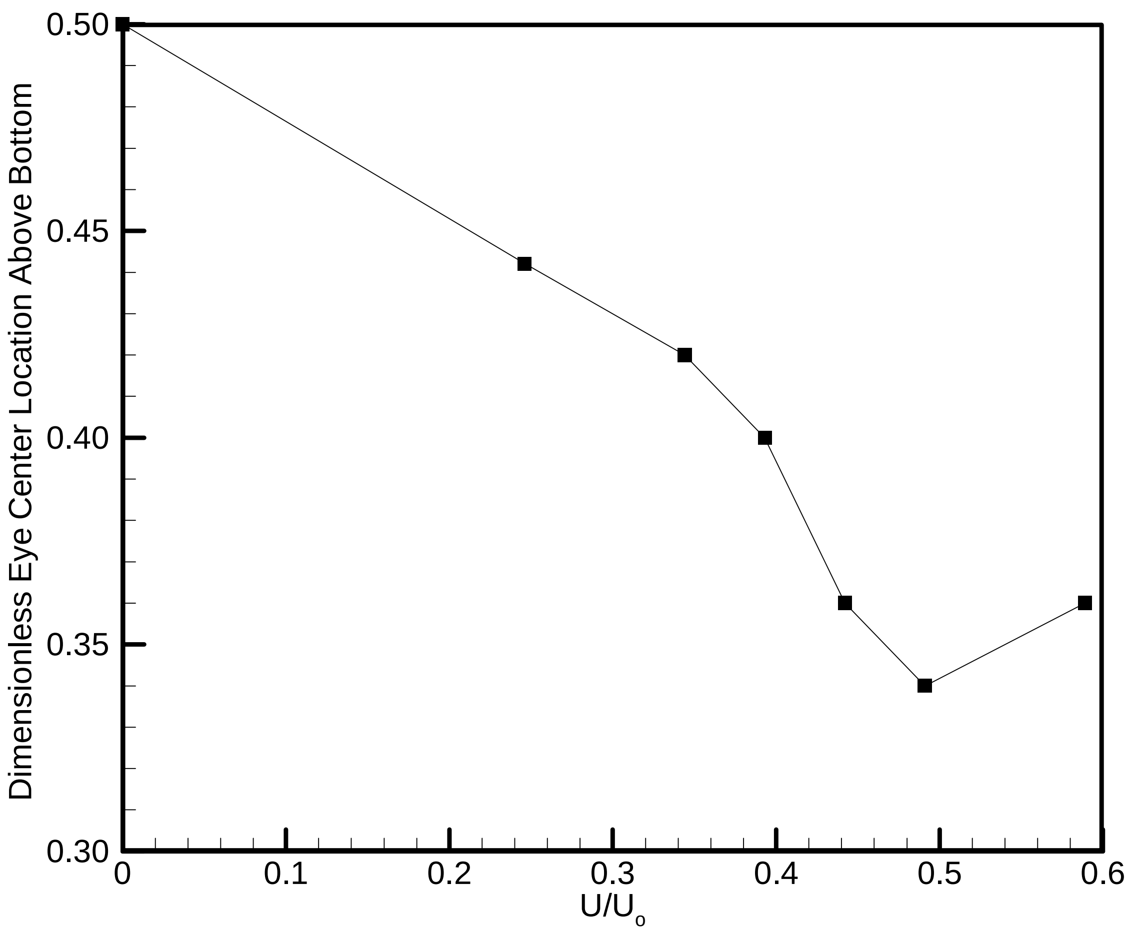

Figure 4.14 Eye center location as a function of interface velocity for Ra = 2500, Pr = 100

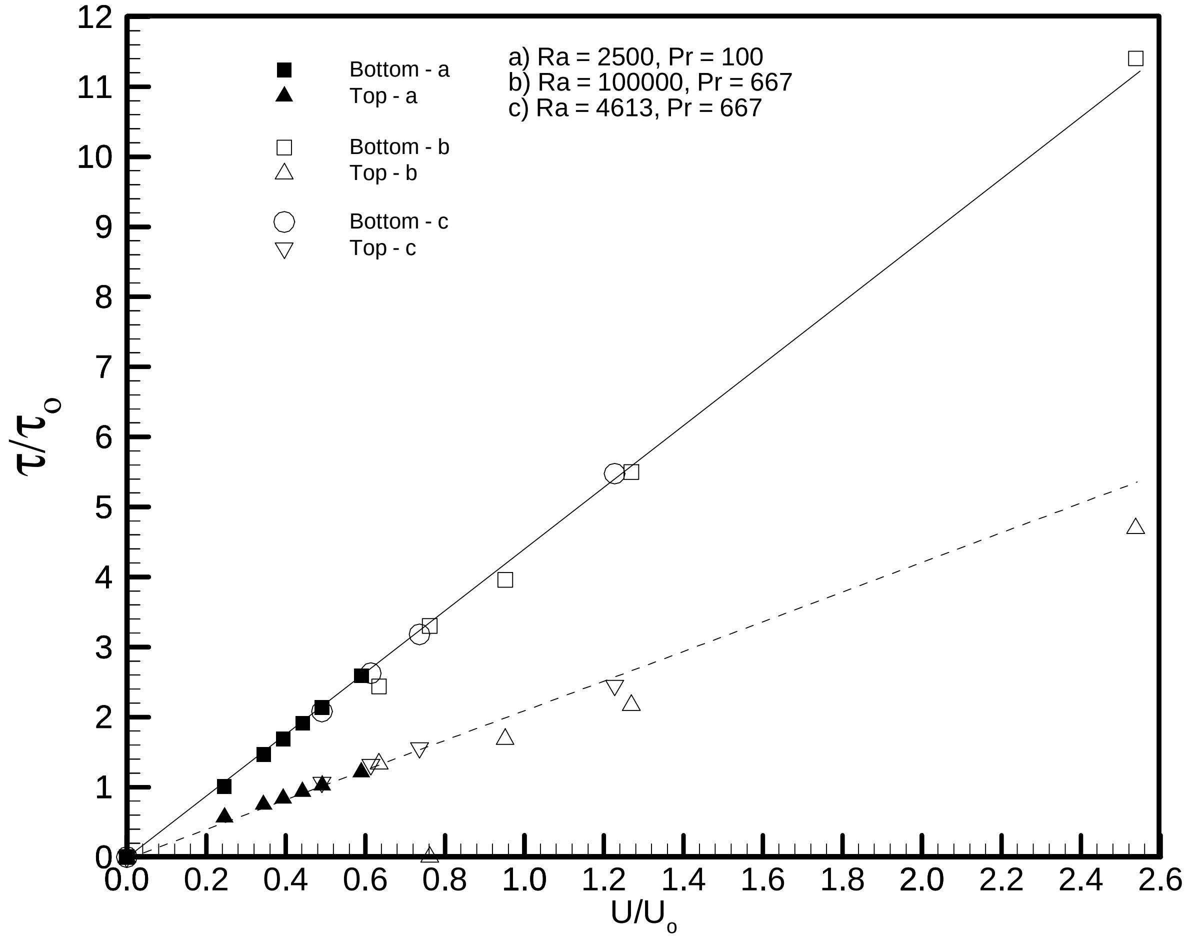

Figure 4.15 Average bottom shear stress as a function of imposed velocity

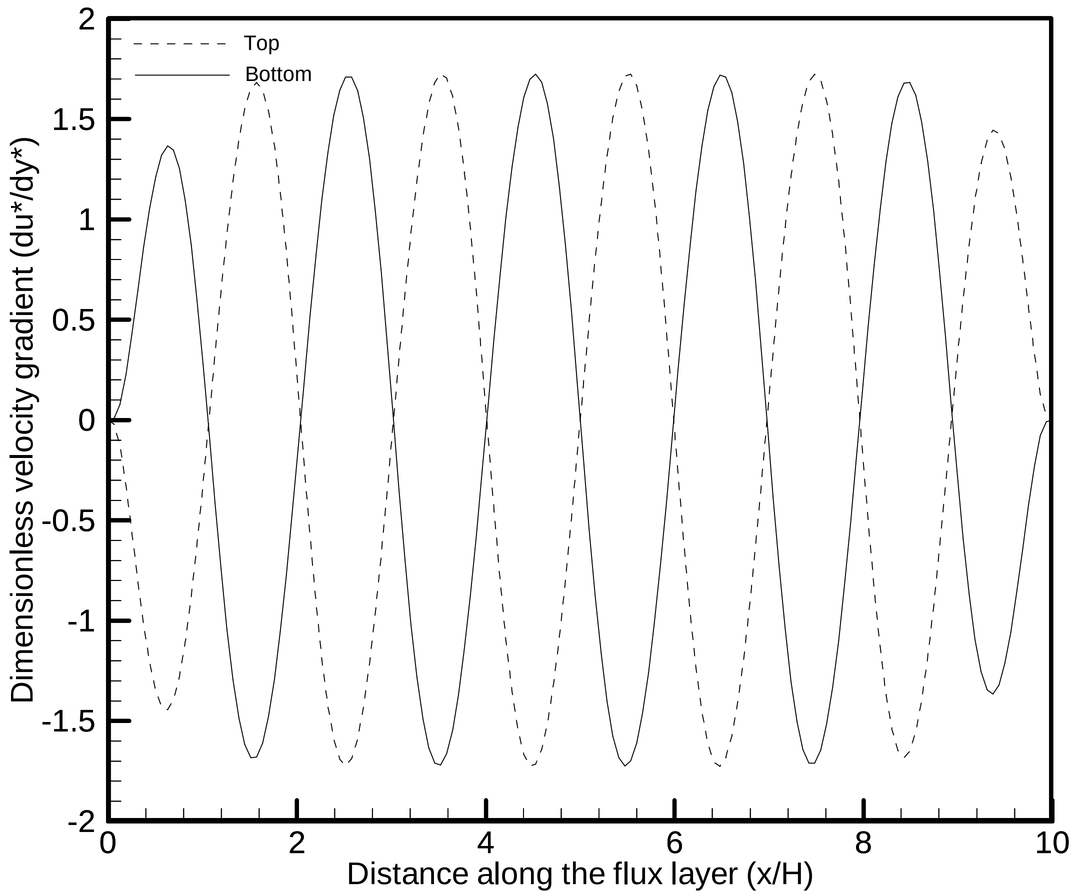

Figure 4.16 Dimensionless velocity gradient/Dimensionless shear stress distribution along the top or bottom of the flux layer for Ra = 2500, Pr = 100 and $U/U_o = 0$

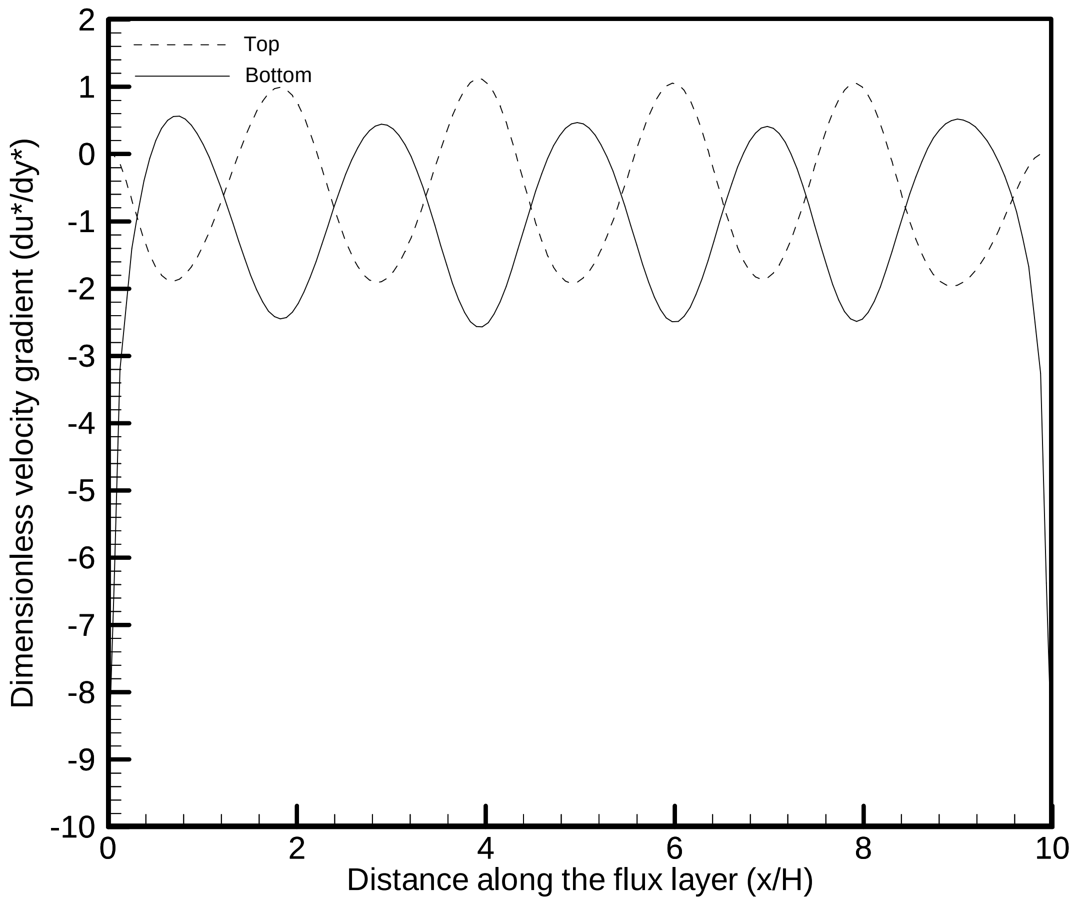

Figure 4.17 Dimensionless velocity gradient/Dimensionless shear stress distribution along the top or bottom of the flux layer for Ra = 2500, Pr = 100 and $U/U_o = 0.246$

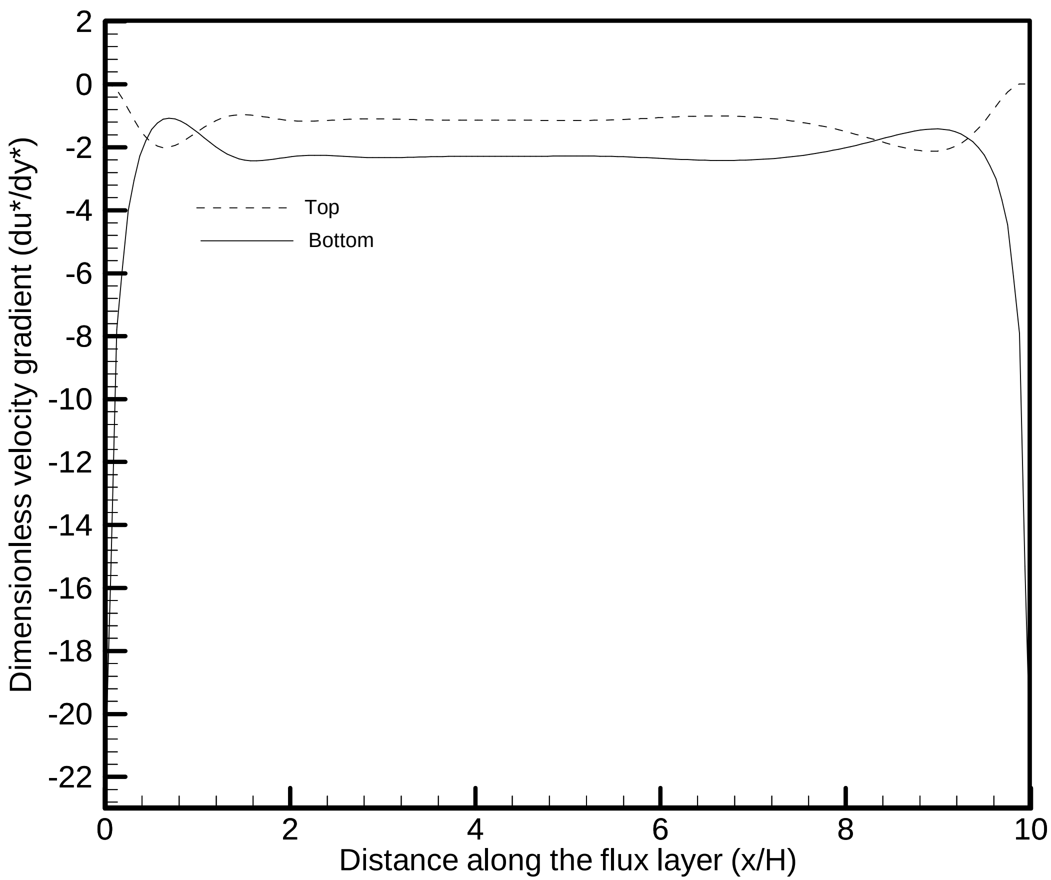

Figure 4.18 Dimensionless velocity gradient/Dimensionless shear stress distribution along the top or bottom of the flux layer for Ra = 2500, Pr = 100 and $U/U_o = 0.59$

CHAPTER 5. HEAT TRANSFER THROUGH MOLTEN SLAG LAYERS

5.1 Introduction

Slag is added to the surface of molten metals during many different processing and refining operations. The slag layer provides chemical insulation by preventing the metal from oxidizing through contact with the atmosphere. Its composition is carefully controlled to absorb impurities such as alumina inclusions in steel. In addition the slag layer has much lower thermal conductivity than the metal and provides thermal insulation. The slag is generally added as a solid on top of the metal, where it sinters and melts to form a liquid flux layer above the molten metal surface. The interface between the liquid slag and the sintering solid powder floating above is at the melting temperature of the slag and is generally quite rigid or viscous relative to the liquid below. Heat transfer through this slag layer occurs by conduction, natural convection and forced convection from motion of the liquid below. Quantifying this heat transfer is very important from a practical standpoint yet has received very little attention in previous literature. One process where this behaviour is particularly important is in continuous casting molds. A vertical cross section through the mold, figure 5.1, reveals powder, sintered and liquid layers above the molten steel surface. The liquid flux infiltrates into the gap between the solidifying steel shell and the mold where it lubricates the interface and promotes uniform heat transfer across the mold strand gap and prevents defects. Powder is added to the top surface to maintain as equilibrium. The aim of this work is to quantify the fluid flow and heat transfer through slag layers for a wide range of slag properties and process parameters (molten metal temperature, bulk velocity in molten metal etc).

5.2 Previous work

Despite the importance of this problem, it has received very little attention by the modeling community. Previous work has been predominantly experimental. This literature is reviewed by McDavid and Thomas [2] who also performed one of the few modeling studies of this system. They used a three-dimensional finite element model in FIDAP (v 6.0.1) to solve for the coupled laminar fluid flow and heat transfer in the top-surface flux layers. The steel surface velocity was computed using a three dimensional k-ε turbulent fluid flow model of the nozzle and mold region of the continuous caster. The two computations were iterated until equal shear at the interface was achieved. Flux infiltration into the mold-strand gap and the steel-liquid flux interface shape were fixed to experimentally measured values at an actual caster. Temperature dependent thermal and conductivity, viscosity etc were defined and the converged solution matched the measured flux layer thickness profile. The flow solution revealed a single large recirculation region whose depth increased with increasing liquid flux conductivity and decreasing flux viscosity. The narrowface flux consumption flow caused flow separation and non-uniformity in the temperature distribution close to the narrowface. This work ignored natural convection effects in the liquid flux layers and did not investigate the effect of varying casting speed.

Natural convection in the liquid flux layer arises because the density of the liquid flux is temperature dependent. The lower surface of the liquid flux layer is just above steel melting temperature (1550 ^{o}C) while it's top surface is at the melting temperature of the flux (800-1200^{o}C). This large temperature gradient causes a density gradient with lighter fluid at the bottom and heavier fluid at the top. This unstable system breaks down as buoyancy forces set up alternate rising and falling plumes, which transport hot low-density fluid upward and cold high-density fluid downward. These merge together to form natural convection cells. The resulting fluid flow and heat transfer in these high length to thickness ratio fluid layers has been studied extensively and is called Rayleigh-Benard convection [28-30]. For B>1 fluid flow is two-dimensional with the cell axis along the width. When the length to width ratio is also large, the fluid flow is two-dimensional with the cell axis along the width.

The mixing caused by these convection cells increases the heat transfer rate significantly beyond pure conduction through a stationary fluid layer. The relative magnitude of the buoyant and viscous forces in the liquid layer is quantified by the Rayleigh number, Ra defined as

$$\mathrm{Ra} = rgb\Delta TH^3 / ua \qquad (1)$$

For low Ra, viscous forces are large relative to the buoyancy force so the fluid layer is stationary. When Ra increases above the critical value of 1707 natural convection cells start to form [28]. With further increasing Ra the velocities increase, which further increases heat transfer through the fluid layer. Another parameter which influences the fluid flow and heat transfer through the fluid layer is the Prandtl number defined as

$$\mathrm{Pr} = n/\alpha \qquad (2)$$

Liquid flux layers are characterized by a low thermal conductivity and a high molecular viscosity, hence a high Pr (Pr > 50). For such fluids the momentum diffusion rate is high compared to the thermal diffusion, requiring lower flow rates and hence lower velocities for the heat flux transport.

Chapter 4 has studied the fluid flow and heat transfer through high Pr fluid layers over a range of Ra and shear. This work includes a detailed literature review of the effects of Ra, Pr, Aspect Ratio (A), Length to depth ratio (B) and shear (at low Pr) on the nature of the fluid flow and heat transfer through the fluid layer. They have identified the existence of a critical shear velocity at which the natural convection cells are annihilated and the flow transforms into a single recirculation region. Beyond this velocity natural convection is found to no longer effect the fluid flow and the results are comparable to the work of McDavid and Thomas [2].

Detailed study of the various properties of the liquid flux layer in section 4 reveals that the range for Ra of flux layers in continuous casters is 0-10^6 and for Pr is 1.5-1000. Thus in the absence of steel flow and for Ra greater than 1707 natural convection cells will exist in liquid flux layers and with increasing Ra their strength will increase. The overall heat transfer rate through such stationary liquid flux layers can be obtained using the correlations of Koschimeder [39], Rossby [38] and Globe [37]. The existence of steel flow below shears the liquid flux layer. The resulting flow and heat transfer fields are complex and depend on the relative magnitude of the natural convection cell and shear velocities. This in turn depends on the relative magnitude of the buoyancy and inertia forces in the liquid flux layer. No previous work has been found which studies fluid flow and heat transfer in high Pr, large aspect ratio fluid layers under the influence of natural convection and shear. The present study quantifies the fluid flow and heat transfer through slag layers in continuous casters over a wide range of slag properties and casting conditions. It also correlates the velocity of the lower surface of the liquid flux layer to the steel surface velocity. Thus knowing the steel surface velocity, flux properties and casting conditions the nature of the fluid flow, heat transfer and overall heat flux through the flux layer can be obtained.

5.3 Model description

5.3.1 Geometry

Figure 5.2 is a sketch of the domain, mesh and boundary conditions used in this study. The domain used for this study is two-dimensional with an aspect ratio (length to thickness) of ten. Recall from chapter 4 that the fluid flow and heat transfer fields become independent of aspect ratio (except for end effects) beyond an aspect ratio of ten. In addition for continuous casters the wideface width is at least a factor of two larger than the narrowface depth i.e. B>2, the rolls axes are perpendicular to the wideface. In flux layers there is a steep transition region from liquid to solid flux at the top of the liquid flux layer, where the properties change from their liquid to solid values. If the transition region is steep then the liquid and solid (sintered) flux layers can be considered divided by a flat surface, which in this study forms the top surface of the liquid flux layer and is at the flux meting temperature. The depth of the liquid flux layer varies from narrowface to SEN (defined in the nomenclature) and is maximum halfway between where the steel velocity is high[2]. For this study the flux layer thickness is assumed to be constant along the length and parametric studies are done to find the effect of varying thickness. The lower surface of the liquid flux layer is at least at steel melting temperature and could increase with increased superheat of the steel flowing into the mold. The effect of the flux infiltration into the mold strand gap is neglected. The flux infiltration flow aids either the large recirculation region for large shear and hence no natural convection effects or the natural convection cell in the corner with flow moving down along the lateral walls. The lateral walls are adiabatic to emulate the heat transfer in a piece of a longer domain.

5.3.2 Governing Equations

The two-dimensional, steady, laminar Navier-Stokes equations (1-4) are solved to compute the flow and thermal fields in the domain.

Mass conservation $$\frac{\partial u}{\partial x} + \frac{\partial v}{\partial y} = 0 \qquad (1)$$

x-momentum $$\frac{\partial u}{\partial t} + u\frac{\partial u}{\partial x} + v\frac{\partial v}{\partial y} = -\frac{1}{r}\frac{\partial p}{\partial x} + u\left(\frac{\partial^2 u}{\partial x^2} + \frac{\partial^2 u}{\partial y^2}\right) \qquad (2)$$

y-momentum $$\frac{\partial v}{\partial t}+u\frac{\partial v}{\partial x}+v\frac{\partial v}{\partial y}=-\frac{1}{r}\frac{\partial p}{\partial y}+u(\frac{\partial^2 v}{\partial x^2}+\frac{\partial^2 v}{\partial y^2})+gb\Delta T \quad (3)$$

Energy conservation $$rC_p(\frac{\partial T}{\partial t}+u\frac{\partial T}{\partial x}+v\frac{\partial T}{\partial y})=k(\frac{\partial^2 T}{\partial x^2}+\frac{\partial^2 T}{\partial y^2}) \quad (4)$$

The Boussinesq approximation is made meaning that buoyant forces are taken into account solely through the last term in equation (3) and all physical properties are considered independent of temperature

5.3.3 Boundary conditions

The boundary conditions for the governing equations of the problem are

At the lateral walls, x = 0, $V_x = 0$, $V_y = 0$, dT/dx = 0

At bottom wall, y = 0, T = T_h, $V_x = U$, $V_y = 0$

At top wall, y = H, T = T_c, $V_x = 0$, $V_y = 0$

5.4 Solution methodology

The model developed in chapter 4 is being used in this study. It uses a finite element approach to discretize the governing equations. A penalty function approach is used to avoid explicit solution of the continuity equation. The domain is divided into four node quadrilateral elements with constant and bi-linear interpolation functions for pressure and velocity variables respectively. The Galerkin method is used with the interpolation functions to obtain a global system of non-linear algebraic equations. These are solved by a relaxed successive substitution method with the equation system at each iteration solved in a fully implicit manner using Gaussian elimination. Convergence is quantified by the residual error **R,** which is defined as the root mean square error in the system of discretized equations at a given iteration number.

Further details about the numerical method can be found in chapter 4 and the FIDAP manual (v 7.5.2).

Natural convection flows inherently have convergence problems because the velocity field is dominated by the buoyancy term in the governing equations, which in turn is controlled by the temperature field. As a consequence the residual, **R** is found to follow a decrease-increase-decrease pattern with iteration number. For stationary natural convection starting with a stationary fluid layer as the initial solution, the velocity field begins to converge before the temperature field. For low velocities the convective heat transfer is negligible so the temperature field is relatively unaffected. Thus the residual falls. After the velocities have increased, the temperature field begins to converge, which in turn disturbs the velocity field. This increases the residual error **R**. Finally, when both the velocity and temperature fields become close to their ultimate converged values, the residual falls. Convergence to an accurate solution was found to be achieved when **R** has decreased by three orders of magnitude or more. Addition of shear to the liquid flux layer complicates convergence resulting in an oscillating or unchanging **R**, particularly for shear velocities when natural convection cells are close to annihilation. The relaxation factor, RF needs to be increased or decreased to get the solution to converge. For shear velocities, when all natural convection cells have been annihilated by shear, **R** decreases continuously with iteration number similar to shear driven fluid layers without natural convection. Details regarding choice of RF and number of iterations required are discussed in chapter 4.

5.5 Model validation

5.5.1 Grid refinement study

A systematic grid independence study was done to determine the grid required to achieve acceptable accuracy for this type of problem. A square portion of the shallow cavity domain was modeled. The specific conditions were chosen to match the previous bench mark study of de Vahl Davis [43] on stationary natural convection in a two-dimensional square cavity with differentially heated side walls and air (Pr = 0.71) as the fluid. The temperature gradients for this problem are larger than encountered with a shear driven flow as shown in the results section 4. Recalling that lower Pr also increases the natural convection cell velocities and hence increases temperature gradients, this problem is a more rigorous test of the resolution of the computational grid than the problems of interest. The fluid flow and heat transfer solutions for three different meshes 16x16, 32x32 and 64x64 were computed. The meshes were stretched from the center to the walls along the horizontal and vertical directions to better resolve the boundary layer flow and hence compute the heat transfer more accurately. The results of this study for Ra of 10000 and 100000 were compared to the bench marked results of de Vahl Davis [43]. With increasing grid refinement the solutions converged to the bench marked solutions. The maximum disagreement in the maximum horizontal velocity of the 64x64 grid was found to be 1.9% and occurred on the vertical mid-plane of the cavity and occurred for a Ra of 100000. Typical errors on the finest grid were less than 0.5 %, which indicates that the model is accurate for solving natural convection problems.

Each simulation required 100-400 iterations which required For computational efficiency, the grid size of 160x16 was chosen for all simulations. The maximum disagreement on this grid (for a Ra of 100000) was a 4.5% overestimation of the Nusselt number. Typical errors for this grid were of the order of 1%.

5.5.2 Qualitative comparison with experimental interferogram

In order to study the ability of the model to simulate the fluid flow and heat transfer patterns accurately the results of a stationary liquid flux layer simulation were compared to an experimental interferogram. The experimental work was done by Oertel [35] using two cavities with aspect ratio of 10:4:1(length:depth:thickness) and 4:2:1. The study was performed using varying angles of inclination of the cavity to the horizontal with three fluids namely air (Pr = 0.71), water (Pr = 7.0) and silicone oil (Pr =1780). The critical Ra for onset of natural convection was found to decrease with increasing aspect ratio and asymptote to 1707 beyond A of 10. This is in agreement with the theoretical work of Catton[34], Davis[33] and Oertel(1976). The lateral walls in the experiment are made perfectly conducting (thermal conductivity much larger than that of fluid) so there is a linear temperature gradient along the lateral walls. The differential interferometer used in this work consists of a light beam from a monochromatic source which, using suitable optical equipment, is split into two beams polarized in perpendicular directions. After passing through the test section the beams are made to interfere. Sufficiently large temperature gradients in the cavity will produce interference fringes, which can be evaluated for qualitative information on cell distribution. For additional sensitivity a laser beam is used instead of a monochromatic light source.

Figure 5.3 is a sample set of plots for stationary natural convection for the above test conditions (Ra = 4000, Pr = 1780). These results were computed by the numerical method described in the previous section using FIDAP[]. Recall that since the Ra is less than 50000, for a Pr of 1780, the flow is steady and two dimensional with the natural convection cell axes perpendicular to the largest side of the 10:4:1 aspect ratio cavity. Assuming the lateral walls to be perfectly conducting a linear temperature gradient is imposed from the bottom to the top along the lateral walls. A stationary fluid layer was used as the initial guess before iterating with a relaxation factor, RF of 0.5. The solution converged in 40 iterations. Since the Ra is larger than the critical value for onset of natural convection, cell formation occurs with a total of ten cells with aspect ratio 1. Recall that adjacent cells rotate in opposite directions causing alternate upward and downward moving plumes, which transport heat from the bottom to the top layer. In the central region, away from the walls, the alternate cells are identical. The increased heat transfer of the impinging plumes causes high temperature gradients, as seen in the close grouping of contour lines near the impingement point in the temperature contour plot. This is also reflected in the Nusselt number distribution along the top and bottom surfaces as seen in the last plot of figure 5.3. Close to the impingement points on the top and bottom surfaces the local Nusselt number peaks, whereas away from this it drops resulting in a wavy distribution characteristic of natural convection. The Nusselt number distributions along the top and bottom surfaces are out of phase, a consequence of the alternate rising and falling plumes. Also there is a peak in the distributions along both the top and bottom surfaces near both the lateral walls and is a consequence of the linear temperature distribution along these walls. The presence of the wall and the linear temperature boundary condition affects the shape of the cell near the wall. This last plot also includes a vertical velocity profile along the horizontal centerline, which is similar to the Nusselt number distribution graphs and has equal maximum and minimum values.

Figure 5.4 is a comparison of interferograms obtained using simulation and experiment [35]. The results are for a horizontal, rectangular cavity of aspect ratio 10:4:1, for Ra = 4000, Pr = 1780. The interferogram is in the central vertical plane with lines of uniform horizontal density gradient. To obtain horizontal density gradient in the simulation the Boussinesq approximation is used i.e. β is independent of temperature. By definition, $\beta = -d\rho/dT$ or $d\rho = -\beta dT$. Differentiating with respect to x, $d\rho/dx = -\beta dT/dx$. Hence lines of uniform horizontal density gradient are also lines of uniform horizontal temperature gradient. The experiment and simulation agree very well. The ten natural convection cells seen in the vector plot of the simulation are also seen in the interferograms. The alternate cells in the central region away from the walls are identical in shape and orientation. Recall that the difference between adjacent cells is caused by their opposite directions of rotation. The simulation shows white patches between adjacent cells above and below the centerline, also seen in the experimental interferogram as dark regions. This is due to large density of the contour lines in these regions. The conducting side walls affect the cells adjacent to them both in the simulation and experiment. The cells close to the lateral walls are smaller than those in the central region and there appear to be two smaller recirculation regions in the interferograms of both simulation and experiment adjacent to the walls. This is confirmed by the vector plot in figure 5.3.

5.5.3 Quantitative comparison with experimental Nu_{avg} at high Pr

One of the most important results of this study is the overall heat transfer rate through the liquid layer or Nu_{avg}. Recall from the introduction section that the average Nusselt number (Nu_{avg}) for pure natural convection flow in shallow liquid layers for high Pr has been quantified by extensive experimental work. Koschimeder (1974) [39] conducted experiments using silicone oil of viscosity varying from 5-200cs i.e. Pr varying from 50-1670. The experimental setup consisted of a shallow horizontal circular fluid layer heated from below. Beyond the critical Ra for onset of natural convection (Ra_c) natural convection cells in the form of concentric rings were formed increasing Nu_{avg} above one. With increasing Ra the concentric rings broke up and cells were formed until at large Ra the flow transitioned to time dependent. The Nu_{avg} increases non-linearly with Ra. The Nu_{avg} plots for different Pr seem to suggest that the results are independent of Pr over a wide range of Ra from Ra_c to $200Ra_c$. Experiments have been done by Rossby (1969) [38] using water (Pr = 6.8), mercury (Pr = 0.025) and silicone oil (Pr = 100, 200). The apparatus setup is similar to Koschimeder (1974) [39] consisting of a fluid layer sandwiched between two copper blocks and surrounded by an aluminum cylinder. The depth of the fluid layer and temperature difference were varied to vary the Ra. The lower disk was rotated at varying speeds to study the effect of Taylor number (Ta). Flow visualization was done by illuminating a suspension of aluminum powder in the fluid using a light beam. The natural convection cell pattern for a Ta of 0 was found to consist predominantly of roll and roll-like cells similar to the observation of Koschimeder(1974) [39]. With increasing Ra the roll pattern lost its two dimensional structure and transitioned at large Ra to time dependent convection. Using the results for various Ra and silicone oil with a Pr of 200 an experimental correlation was obtained between Nu_{avg} and Ra for this Pr namely $Nu_{avg} = 0.184Ra^{0.281 \pm 0.005}$.

In order to make a quantitative comparison with experimental data the discretized governing equations were solved for Pr of 100 and 667 for different Ra above the critical value for onset of natural convection and below 100000, which is the critical Ra for transition to oscillatory convection. Figure 5.5 is a plot of the Nu_{avg} results obtained from computation and experiments of Koschimeder (1974) [39] and Rossby (1969) [38]. The experiment and simulation compare very well. The Nu_{avg} is found to increase linearly with the logarithm of Ra. There is some divergence between the computations and experiments at the high Ra of 100000. This is most probably due to the onset of oscillatory convection at Ra of 100000. Though all four results presented are for different Pr they line up almost exactly. This confirms the trend of Koschimeder (1974) [39], that the results are independent of Pr for Pr in the range 50-1670.

The present numerical method using FIDAP for computations was able to predict accurately (to within 4.5%) the results for a test case with larger temperature gradients than the problem under study (Recall that the largest temperature gradients occur at lower Pr with zero shear velocity). It also accurately reproduced the natural convection cell shape, size and distribution as was seen in the comparison with the experimental interferogram. Finally it was able to reproduce quantitatively accurate results for two different Pr over a wide range of Ra. This confirms the ability of the numerical method (discussed in detail in section 2) on the computational grid of size (160x16) to give both qualitatively and quantitatively accurate results for the entire range of Ra, Pr and shear velocities in this study.

5.6 Material properties and casting conditions

Table I lists the standard conditions used for this study. These follow from the typical values of the various parameters found in continuous casting flux layers. A typical steel-flux interface velocity is not listed, as for each simulation it varies widely from zero to post-critical values. Unless otherwise mentioned the standard properties are assumed. Following is a detailed discussion of the range of each parameter encountered in continuous casters.

5.6.1 Molecular viscosity of the flux (m)

The viscosity of the liquid flux layer in a continuous caster is a function of its chemical composition and temperature.

First the effect of chemical composition is examined. Schrewe [19] gives the typical chemical composition and viscosity range of casting fluxes for slab, bloom, billet and round casters. The viscosity of the liquid slag of typical casting fluxes is listed as 0.1 – 0.18 Pa-s at 1300^{o}C for slabs and 0.3 – 0.7 Pa-s at 1300^{o}C for billets. Also an attribute of good casting fluxes is that their viscosity does not vary significantly from 1100^{o}C to 1500^{o}C [19]. The commercially available fluxes have three main constituents namely CaO, SiO_2 and Al_2O_3. The typical ranges of each are Al_2O_3 (0 – 13 %), CaO (22 – 45%), SiO_2 (17 – 56%) [44]. Other constituents include network modifiers, such as fluorides(NaF, CaF_2), alkalies(Na_2O, K_2O), and other basic oxides(MgO, BaO, SrO). Among the constituents SiO_2 content is the major factor that determines the viscosity. Increasing the SiO_2 content causes heavier interlacing within the silicate chain increasing viscosity [45]. As an example figure 5 in [45] shows two fluxes H and L with a 26% difference of SiO_2 content (with other constituents roughly the same) with the viscosity of L 7 times that of H. Table II shows the effect of SiO_2 content on viscosity. For an average SiO_2 content of 35% (all other contents at their average values) and average liquid flux layer temperature of 1300^oC the viscosity of the liquid flux layer is 1 Pa-s. For large SiO_2 content and low average flux layer temperatures this increases to 20 Pa-s, whereas for low SiO_2 content and high flux layer temperatures this drops to as low as 0.1 Pa-s.

Increasing Al_2O_3 content also increases the viscosity [45]. However, the viscosity increase per percent increase in Al_2O_3 content, depends on the composition of the flux. Maintaining the Al_2O_3 content within 10% is found to make the viscosity almost independent of Al_2O_3 content [45]. The Al_2O_3 content of the liquid flux varies with time, as Al_2O_3 absorption is one of the main functions of the liquid flux layer. This is particularly true of Aluminum-killed steels where aluminum is added to reduce the ferrous oxides. This absorption rate increases with basicity, which ranges from 0.75-1.5 for typical fluxes [44]. Al_2O_3 decreases the fluidity of the slag and being refractory in nature will decrease the heat transfer in the mold-shell gap. A low-end estimate of absorption rate (B_I) is $2x10^{-4}$ g/cm^2s [44].

Alumina absorption calculation:

Caster half-top surface area = A_s = 0.66m x 0.22 m = 0.1452 m^2

Alumina absorbed by the flux layer = B_I x A_s = 0.29 g/s

Flux density (ρ) = 2500 g/cm^3

Liquid layer thickness (H) = 0.020m

The mass of the liquid layer on one side of the caster (m) = (A_s x ρ x H) = 7260 g

For 10% Al_2O_3 content, total mass of Al_2O_3 on one side of the flux layer = 0.1m = 726 g.

Casting speed of 1m/min = 0.0167m/s

Steel mass flow rate (s) = 37830 g/s.

Flux consumption (f) = 0.2 –0.8 kg/t of steel [19]. = 0.0005g /g of steel

Flux consumption in g/s = s x f = 18.9 g/s

Flux consumption per half-top surface area = 9.5 g/s

If we assume that 50% of the Al_2O_3 absorbed is carried away by the flux lubricating the gap 0.145 g/s remains in the liquid flux layer. This over a period of time say 1hr could add 522.7 g of Al_2O_3 to the steel, which nearly doubles the Al_2O_3 content. This process can continue until the flux layer becomes highly viscous, stopping flux flow in the gap between the mold and shell. However, this is an extreme case, as fresh mold powder melts continuously lowering the Al_2O_3 content as liquid flux is being exhausted in the lubrication of the shell-mold interface i.e. the Al_2O_3 carried off with the liquid flux flowing into the mold gap will be much more than 50% of the quantity absorbed by the liquid flux layer. This example illustrates the need to increase the range of Al_2O_3 content of the liquid flux (which is present to a maximum of 15% in the fresh mold powder) to account for Alumina absorption. A conservative estimate would be 30%. This combined with a high SiO_2 content could give viscosity values (at 1300^oC) upto 20 Pa-s [45]. Table III summarizes the effect of Al_2O_3 content on flux viscosity. For an average Al_2O_3 content of 10% and average liquid flux layer temperature of 1300^oC the viscosity is 2 Pa-s. For high Al_2O_3 content and low liquid flux layer temperatures the viscosity is as high as 20 Pa-s whereas for no Al_2O_3 and very high liquid flux layer temperatures it drops to 0.1 Pa-s. Other constituents including CaO decrease the viscosity but not to the extent of SiO_2 and Al_2O_3 [45].

Next, we examine the effect of temperature on viscosity. The viscosity of liquid flux decreases with temperature according to the Arrhenius equation [45]. As the flux solidifies its viscosity increases to infinite values (greater than 10^4Pa-s for practical purposes). The solid and liquid regimes are separated by a solidification range, where the flux viscosity variation is not very well quantified and hence is predicted by extrapolating the behaviour in the solid and liquid regimes. Branion [44] presents one such example. The temperature of the flux steel interface is at least the steel melting temperature of 1550^{o}C. The liquid layer gradually transitions to a solid. If the flux layer is considered as a fluid between parallel wall surfaces with lower wall moving, the range of liquid temperatures is from 1550^{o}C to either crystallization temperature or transition temperature of the flux powder. This temperature ranges from 1000–1250^{o}C for typical fluxes [45]. From figure 5 of Brimacombe[45] this corresponds to a range of viscosity of (0.5 – 15 Pa-s) for most commercial fluxes.

Based on the chemical composition and temperature ranges found in liquid layers an overall range of 0.1- 20 Pa-s can be ascribed for viscosity with an average value of 1 Pa-s

5.6.2 Specific heat of the flux (Cp)

McDavid and Thomas [25] give the enthalpy vs temperature relationship for a typical liquid flux. Future modeling efforts consider the liquid flux layer to be entirely fluid and the corresponding portion of figure 9 in McDavid and Thomas[25] is used. Since the enthalpy varies linearly with temperature in this range (1000 - 1600^{o}C) the specific heat of the flux is constant i.e.

$Cp = \Delta H/\Delta T = (1.2 \times 10^6 / 600) = 2000$ J/kg –K.

5.6.3 Volumetric expansion coefficient of the flux (b)

Data on the volumetric expansion coefficient is sparse and a value of 2.4 x 10^{-5} K^{-1} is selected from McDavid and Thomas[25].

5.6.4 Temperature difference across the flux layer (DT)

As in the discussion of viscosity the modeled liquid layer top surface temperature (which corresponds to the flow temperature of the flux) varies from 1000-1250^{o}C based on the chemical composition of the flux. The lower surface temperature of the liquid flux layer is at least 1550^{o}C. Thus the temperature difference across the liquid layer, for modeling purposes, is considered to vary from 350K to 550K.

5.6.5 Thickness of the flux layer (H)

Equilibrium between flux consumption and melting of the powder causes the liquid layer to attain a certain thickness. Small thickness of the liquid layer causes more heat loss from the surface and may cause insufficient lubrication in the flux gap, whereas the equilibrium places as upper limit on the liquid layer thickness. Schrewe [19] states that the thickness of the slag and flux layer should not exceed 30mm. McDaivd and Thomas [25] give the variation in the liquid layer thickness along the wideface of the caster obtained using nail-dip measurements. It varies, for this case, from 5mm near the narrow face to a maximum of 25mm in the center. From this a range of 5-30mm can be considered for the liquid flux thickness.

5.6.6 Velocity of the steel-flux interface (U)

Chapter 2 discusses the MFC sensor located close to the steel surface, which records the variation of the average horizontal flow velocity at its location with time. It thus provides a measure of the surface velocity of steel. The sensor output velocity for a 72inch slab caster, casting at 1m/min and with no argon injection is found to vary from 0.1 to 0.35 m/s. Since the velocity decreases continuously from the surface to the center of the upper roll the steel surface velocity will be larger and hence a range of 0.1-0.5m/s can be assumed for the steel surface velocity. McDavid and Thomas [25] plot the variation of velocity of the steel flux interface along the wideface at two different locations along the narrowface. The bottom shear velocity is seen to vary from 0-6mm/s for a casting speed of 1m/min. As the casting speed increases the interface velocity will also increase. Hence a range of 0-10mm/s would be appropriate for the bottom shear velocity of the liquid flux layer. The correlation between steel surface velocity and bottom shear velocity of the liquid flux layer will be discussed in more detail later.

5.6.7 Flux density (r)

McDavid and Thomas [25] list the flux density for their model as 2500kg/m^3. Though density of the flux is a function of temperature and composition it is assumed that the flux layer is homogeneous i.e. it has a constant density throughout. A suitable density range for flux layers is 2000-3000kg/m^3.

5.6.8 Thermal Conductivity (k)

Thermal conductivity of the liquid flux layer varies over a wide range. Since the liquid flux is translucent and the lower surface of liquid flux layer is in contact with the steel, radiation from the liquid steel causes additional heat transfer. This can be accounted for by modeling radiation heat transfer as heat loss by conduction, i.e using a radiation thermal conductivity (k_R). The analogy between radiation and conduction is based on the similarity in the heat transfer process. When the heat radiated from liquid steel falls on a layer of the liquid flux some of the energy will be absorbed by that layer, the temperature of this section will increase and it will radiate heat to cooler sections. The process is repeated through the liquid layer. Consequently the radiation conductivity will increase until a certain thickness called optical thickness is reached beyond which it remains constant. The quantity absorbed and emitted depends on the absorption coefficient of the liquid flux. The following formula can be used to find the equivalent k.

This can be expressed as: $k_R = 16\sigma n^2 T^3 / 3\alpha$

σ = Stefan Boltzmann constant = 5.67×10^{-8} W/m^2 K

n = refractive index of the liquid flux layer = 1.5 – 1.6 [46, 47]

T = thermodynamic temperature(K)

α = absorption coefficient(m^{-1})

The value of the absorption coefficient depends on the quantity of transition metal oxides present in the mold powder. Based on experimental measurements in glassy slag layer the following expression has been arrived at for α.

$\alpha = \alpha + 910(\%FeO) + 410(\%NiO) + 5(\%MnO) + 390(\%Cr_2O_3) + 370(\%Cr_2O_3)^2$ [46, 47]

Two extreme cases are considered to study the magnitude of $k_{R.}$

Low transition metal oxide content - %FeO = %NiO = %Cr_2O_3 = 0 , %MnO = 2, T = 1550^{o}C yields k_R = 110 W/mK

High transitional metal oxide content - %Fe_2O_3 = 11, MnO = 2, T = 1000^{o}C yields k_R = 0.149 W/mK

The lattice or pure conduction based conductivity (k_C) lies between 0.2-0.6 W/m-K [46, 47]. Considering the relative magnitudes of k_R and k_C radiation conductivity can be seen to be significant for all mold powders and an overall thermal conductivity (lattice+radiation) range of 0.5 - 150 W/m-K can be considered.

5.6.9 Caster dimensions

The caster dimension of significance to the modeling process is the wideface width. This varies in casters with a typical value of around 1.2m. However, for a liquid layer aspect ratio (Liquid layer length over half of the caster / Thickness of the liquid flux layer) greater than 10 the flow pattern becomes independent of aspect ratio [35]. Hence to conserve computing resources and time the half-length of the wideface is assumed 10 times the liquid layer thickness modeled for all simulations in this work.

5.7 Results and discussion

The objective of this study is study the effect of natural convection on the fluid flow and heat transfer in the liquid layer of continuous casters. Since the properties of the fluxes vary widely (see earlier section on material properties and casting conditions) and so the relative strength of natural convection and shear from the steel flow beneath, it is necessary to conduct a parametric study to identify the effect of various process variables. Thus a number of simulations were done with different flux properties μ and k and process variables ΔT, H and U. The values of these variables were chosen to simulate a wide range of natural convection and shear strengths. Following is a detailed discussion of the results of these simulations.

5.7.1 Combined effect of steel-flux interface shear and natural convection

Figure 5.6 is a set of plots similar to figure 5.3, for Ra = 2500, Pr = 100, with added bottom shear velocity. Recall that the characteristic velocity used to non-dimensionalize the governing equations was defined as $\sqrt{gb\Delta TH/an}$ and termed U_o. The non-dimensional shear velocity (U/U_o) for this example case is 0.25. As seen in the velocity vector plot in figure 5.6 those rolls which rotate with this bottom shear velocity get enlarged, while those opposed get smaller and the number of rolls has decreased from 10 to 9. The flow in the rolls, which for pure natural convection was in the form of plumes impinging vertically on the top and bottom, is now directed at the angle of around 45^o to the surfaces. This is reflected in the temperature contour plot with the contour lines corresponding to the plumes symmetric about an inclined line rather than the vertical for pure natural convection (figure 5.3). This inclination of the symmetry line in the temperature contour plot reduces the normal temperature gradient reducing the local Nusselt number as seen in the fall of the peaks in the Nusselt number distribution. Due to the shear additional flow is set up in the domain, which causes more flow to impinge on the top and bottom surfaces on the right and left hand corners respectively. This is seen in the vertical velocity distribution as a larger peak at the left end and smaller but broader peak at the right end of the plot. These cause increased temperature gradients as seen by the closer grouping of temperature contours and corresponding peaks in the Nusselt number distribution. The peak on the left is larger and causes increased heat transfer on the bottom surface whereas the smaller but broader peak on the right increases the top surface heat transfer making the overall heat flux through the top and bottom layers equal (Note: The lateral walls are adiabatic).

With increasing shear velocity the cells rotating in the same direction as the velocity get larger and the number of cells continues to decrease. The angle of the plume velocity with the vertical continues to increase and is reflected in the increased inclination of the symmetry line of the temperature contour plot. This in turn decreases the normal temperature gradient close to the impingement point, decreasing the peak and increasing the valley values in the Nusselt number distribution along the top and bottom surfaces. The increased shear further increases the flow rate increasing the peak Nusselt number on the bottom surface left end and increasing and broadening the peak Nusselt number on the top surface right end.

Beyond a certain velocity all remaining cells merge to form a single large recirculation region. The bottom velocity at which this occurs is defined to be the critical velocity (U_c). Parametric studies confirm the existence of such a critical velocity for each Ra and Pr. Figure 5.7 is a set of velocity vector, temperature contour, Nusselt number and vertical velocity distribution for bottom shear velocity greater than U_c. The non-dimensional shear velocity (U/U_o) in figure 5.7 is 0.59. The velocity vector plot shows the existence of a single large recirculation region. There is no natural convection effect as seen in the horizontal, equally spaced contour lines in the central region of the temperature contour plot. This is reflected in the flat Nusselt number distribution in the central region along both top and bottom surfaces. As a result of the single recirculation region all the flow resulting from the shear of the bottom surface flows in the recirculating loop as opposed to flow with natural convection where part of the flow is carried by the cells. This large flow, seen in the large vertical velocities near the lateral walls, impinges to produce large temperature gradients along the top and bottom surfaces on the right and left end respectively, seen in the close grouping of contour lines in these regions. This results in a large Nusselt number peak of 4.5 on the bottom surface and a smaller but much broader peak of 2.5 (Nu_R) on the top surface. Further increase of shear velocity increases the flow rate in the recirculation region, increasing the peak Nusselt numbers on the top and bottom surface on the right and left end respectively.

5.7.2 Critical velocity

As mentioned in the previous section a critical velocity was identified for each Ra and Pr, beyond which the bottom shear velocity annihilated the natural convection cells resulting in the formation of a single large recirculation region. From figures 5.6 and 5.7 it can be seen that there are significant differences between sub-critical and post-critical flow and thermal fields. These differences were discussed in detail in the previous section suffice to state here that it is necessary to quantify the critical velocity as a function of Ra and Pr. To this end a number of simulations were done for each Ra and Pr varying the velocity in each case from zero until shear annihilates the natural convection cells. Using this procedure a sub-critical (cells present) and post-critical (cells annihilated) bottom shear velocity are obtained. More simulations with shear velocities in this range were needed to narrow the gap between sub-critical and post-critical shear velocity to the required accuracy.

Figure 4.7 is a plot of the dimensionless sub-critical and post-critical velocities as a function of Ra for two different Pr of 100 and 667. At and above post-critical bottom velocities the multiple natural convection cells are annihilated by the shear and natural convection does not effect the flow pattern. At and below sub-critical bottom velocities there are multiple natural convection cells with number of cells increasing with decreasing velocity. Recall that the lower limit of 1707 on the Ra axis corresponds to the critical Ra for onset of natural convection in shallow cavities of aspect ratio (A) 10 or more, obtained using linear stability analysis [28]. For this Ra, the roll velocities are infinitesimally small so that an infinitesimal bottom shear velocity would be sufficient to annihilate the rolls. Thus for a Ra of 1707 a U/U_o infinitesimally larger than zero would be the critical velocity. From Figure 4.7, for both Pr the dimensionless critical velocity is seen to increase with increasing Ra. This is expected as with increasing Ra the strength of the natural convection cells increases, increasing the bottom velocity required to annihilate the cells. The rate of increase in not constant being large for low Ra and then tending to zero for Ra of order 100000. There is significant overlap between the critical regions (region between sub-critical and post-critical) of the two Pr. This is due to the appropriate selection of the characteristic velocity (U_o), which eliminates the effect of Pr on the critical velocity.

5.7.3 Effect of thermal conductivity (k) on heat flux

Recall from the introduction section the two non-dimensional groups that control the strength of natural convection cells, namely Ra and Pr. Increasing Ra and decreasing Pr both increase the strength of the natural convection cells, increasing the advective heat transfer. Increasing k, for a given liquid layer thickness and temperature difference, increases the heat transfer by conduction and hence increases overall heat flux. Increasing k decreases both Ra and Pr hence the overall effect on heat flux is not obvious.

Figure 5.8 is a plot of variation of heat flux per unit area of the liquid layer with steel-flux interface velocity for different viscosity (μ) and thermal conductivity (k) combinations. It is found that, for a given viscosity, the heat flux is higher for a larger thermal conductivity irrespective of the steel-flux interface velocity. The heat fluxes for μ_1 = 0.254 Pa-s, k_1 = 5.089 W/mK and μ_2 = 0.2 Pa-s, k_2 = 0.6231 W/mK combinations at zero steel-flux interface velocity are $h_1 = 3.6x10^5$ W/m^2 and $h_2 = 7x10^4$ W/m^2 respectively. Thus, for a constant viscosity around 0.2 Pa-s, the heat flux increases by a factor of 5.14 for an 8.17 factor increase in thermal conductivity i.e. for a 10% rise in thermal conductivity the heat flux increases by 6%. Similarly considering the heat fluxes for the μ_3 = 0.08 Pa-s, k_3 = 1.61 W/mK and μ_4 = 0.1 Pa-s, k_4 = 0.3 W/mK a 10% rise in thermal conductivity at this viscosity will increase the heat flux by 9%, for a viscosity of 0.1 Pa-s. The two sets of cases considered have the same range of thermal conductivities but viscosities, which vary by a factor of 2. Thus the increase in heat flux with increase in thermal conductivity is lower at higher viscosities.

With increasing steel-flux interface velocity the natural convection cells begin to merge and the flow field begins to converge to a single recirculation flow. The plumes, which in pure natural convection are vertical impinge obliquely decreasing the temperature gradients and hence heat fluxes. Thus with increasing interface velocity the overall heat flux decreases. When all natural convection cells are annihilated the heat flux becomes uniform in the central region of the slag layer. With increasing post-critical velocity the increased flow rate causes the right peak in the heat flux profile to rise. In addition the increased shear increases the heat transfer in the central region. Both these effects increase the heat flux. Thus the overall heat flux for any combination of μ and k decreases to a minimum (around the critical velocity) and rises. As seen in figure 5.8 the overall heat flux decreases much faster than it rises with steel-flux interface velocity. The steel-flux interface velocity at which the overall heat flux is minimum and the rate of fall and rise of the different heat flux profiles vary with μ and k. Thus the percentage increase in heat flux with thermal conductivity (k) varies with the steel-flux interface velocity. For the cases μ_1 = 0.254 Pa-s, k_1 = 5.089 W/mK and μ_2 = 0.2 Pa-s, k_2 = 0.6231 W/mK and a velocity of 2.5mm/s a 10% increase in thermal conductivity (k) is found to increase overall heat flux by 7.6% whereas for the cases μ_3 = 0.08 Pa-s, k_3 = 1.61 W/mK and μ_4 = 0.1 Pa-s, k_4 = 0.3 W/mK and the same velocity a 10% increase in k also increases heat flux by 10%.

In summary increasing k increases heat flux irrespective of the steel-flux interface velocity and viscosity. A 10% increase in k increases heat flux by 6-10% depending on the viscosity and steel-flux interface velocity. For a given increase in k the increase in heat flux is higher for a lower viscosity flux.

5.7.4 Effect of viscosity (m) on heat flux

Increasing viscosity increases Pr and decreases Ra both of which decrease the strength of the natural convection cells decreasing the convective heat transfer through the flux layer. Conduction through the flux layer is not affected by viscosity changes. The overall effect is a decrease in heat flux with increasing viscosity μ. Figure 5.8 reflects this effect. Consider the cases μ = 1 Pa-s, k = 3 W/mK and μ = 0.254 Pa-s, k = 5.089 W/mK. The thermal conductivity increase from 3 to 5.089W/mK should, based on the discussion in section D, increase the heat flux, but the factor of 4 increase in μ from 0.254 Pa-s to 1 Pa-s decreases it as observed in figure 5.8. Since the lines for these cases are approximately parallel a correlation can be found between increase in viscosity and decrease in heat flux. A 10% increase in viscosity decreased the heat flux by around 2%.

Knowing the individual effects of μ and k on heat flux the effect of simultaneous change of μ and k can be estimated. For the sets μ_1 = 0.2 Pa-s, k_1 = 0.6231 W/mK and μ_2 = 0.1 Pa-s, k_2 = 0.3 W/mK, μ and k have changed by 100%. Using the correlations in the two sections yields a 60% increase in heat flux, which is found to be exact result (figure 5.8). Similar calculations for other cases suggest that for large changes in μ and k these correlations overestimate the change in heat flux by as much as 40%. Hence caution should be exercised in applying these correlations for large μ and k changes.

5.7.5 Effect of liquid layer thickness (H) on heat flux

Figure 5.9 is a plot of heat flux variation with steel-flux interface velocity for liquid layer thickness of 20 and 57mm. For steel-flux interface velocities ranging from 0-1.25mm/s and greater than 1.6mm/s the heat flux for 20mm layer is found to be larger than that for 57mm. In the range 1.25-1.6mm/s the heat flux for the 20mm layer is slightly lower than the 57mm one.

Conduction heat flux through the liquid layer = $(Q_{cond}) = k\Delta T/H$ (5)

Thus increasing liquid layer thickness (H) by a factor decreases conduction heat flux by the same factor. On the other hand, increasing liquid layer thickness increases Ra and hence the strength of natural convection, increasing heat flux. This increase is not linear as seen in the critical velocity variation with Ra result in chapter 4 (figure 4.7). The critical velocity is found to increase with increasing Ra saturating around a Ra of 100000 i.e. the strength of the natural convection cells increases rapidly with Ra for low Ra but levels off at high Ra. Increasing H from 20 to 57mm increases Ra from 4613 to 100000. The net effect on the heat flux depends on the relative change in conduction and convection heat fluxes. Thus from figure 5.9 the decrease in conduction heat flux due to the increase in thickness from 20mm to 57mm is much more than the increased natural convection.

Recall from section C that in the presence of natural convection effects, with increasing steel-flux interface velocity the heat flux decreases to a minimum and increases, the minimum occurring around the critical velocity. With increasing liquid layer thickness, Ra increases (see Ra definition in nomenclature), increasing the critical velocity for annihilation of natural convection cells (see figure 4.7). This in turn increases the steel-flux interface velocity at which the heat flux is minimum. Thus the steel-flux interface velocity at which the heat flux is minimum is lower for the 20mm layer. This lower minimum causes the heat flux for the 20mm layer to decrease faster than that for the 57 mm layer (see in figure 5.9) until it drops below it in the range of 1.25-1.6 mm/s. Beyond the critical for cell annihilation the heat flux for the 20mm layer rises while the heat flux for the 57mm layer continues to decrease as it is still in the sub-critical (for cell annihilation) regime.

Figure 5.10 is a similar plot of variation of heat flux with steel-flux interface velocity and liquid layer thickness but for μ of 0.51 Pa-s and k of 10.18 W/mK. Increasing H from 20 to 32mm is found to increase the overall heat flux for interface velocities ranging from 0-4mm/s. Increasing liquid layer thickness from 20 to 32mm increases Ra from 2500 to 10000. Following the argument made earlier for variation of natural convection cell strength with Ra this will result in a substantial increase in convective heat transfer which more than compensates the decrease in conduction, increasing overall heat flux. However when H is increased to 68mm, Ra increases to 100000 and convection saturates while conduction drops linearly with H causing the heat flux to drop below that for 20mm. Thus from 20 to 32 mm the convective heat flux increase is large increasing overall heat flux whereas from 32 to 68 mm the conduction heat flux drop decreases the heat flux.

In summary the effect of increasing H depends on the μ, k, H and steel-flux interface velocity values. For Ra much lower than 100000 small increase in H (less than 10mm) will increase heat flux whereas for Ra close to 100000 increasing H will decrease heat flux. The latter trend may be reversed for some ranges of steel-flux interface velocity as seen in figure 5.10.

5.7.6 Effect of temperature difference (DT) on heat flux

Figure 5.11 is a plot of heat flux variation with steel-flux interface velocity and temperature difference across the liquid flux layer for standard conditions. Increasing temperature difference is found to increase the heat flux through the liquid layer. With increasing temperature difference both the conduction and Ra increase. The increasing Ra increases the natural convection cell strength increasing convective heat transfer. The overall effect is an increase in heat flux through the liquid layer.

Since the spacing between the two temperature lines is approximately constant with increasing steel-flux interface velocity the change in heat flux with increasing temperature difference can be quantified. A 10K increase in the temperature difference across the liquid layer is found to increase the heat flux by 4%. Figure 5.12 is a similar plot for μ = 0.51 Pa-s and k = 10.18 W/mK. For these conditions a 10K increase produces a 3% increase in heat flux. Thus the heat flux change with changing temperature difference is fairly independent of the flux properties.

5.7.7 Relation between steel-flux interface velocity and interface shear

The velocity of the steel-flux interface depends on the shear imposed by the steel flow beneath. Mold flow modeling can be used to predict the bulk velocity of steel flow below the flux layer (V_o) and from knowledge of boundary layer flow, as discussed in the next section, the interface shear stress can be correlated to it. Knowing this shear stress it is necessary to correlate it to the steel-flux interface velocity in order to predict the fluid flow and heat transfer in the liquid flux layer for a given set of casting conditions.

This can be done by computing the average shear stress exerted by the fluid flow in the liquid layer on the bottom surface, for each imposed steel-flux interface velocity. A second order accurate three-point differencing scheme is used to compute the local gradient of horizontal velocity in the vertical direction at either wall (Appendix A). Since the grid is uniform in the horizontal direction averaging these local gradients yields an average gradient for the entire wall. This multiplied by the viscosity (μ) is the average wall shear stress corresponding to the imposed bottom interface velocity. This process can be repeated for different velocities and flux properties.

Figure 5.13 is such a plot for different Ra and Pr combinations for both the top and bottom surface shear stress. It is found that the steel-flux interface velocity varies linearly with top and bottom surface shear stress and is independent of the strength of the natural convection (Ra) and the relative strength of momentum and thermal diffusivity in the slag layer (Pr). This lack of dependence on natural convection effects has been studied in detail and an explanation can be found in chapter 4. The equations for the solid and dashed lines in figure 5.13, which quantify the variation of steel-flux interface velocity with average interface shear stress are

Average top shear stress = $\tau_t^{\dagger} = 2.12\mu U/H$ (6)

Average bottom shear stress = τ_b† = 4.35μU/H (7)

Knowing the steel-flux interface shear for a given steel bulk velocity(V_o) equations (6) and (7) can be used to compute the steel-flux interface velocity.

5.7.8 Relation between steel bulk velocity (V_o) and average interface shear stress (t_b)

The relation between steel bulk velocity (V_o) and average interface shear stress (τ_b) can be obtained using knowledge of boundary layer flow. In the continuous caster the flow exits the nozzle as a turbulent jet, which impinges on the narrowface splitting into an upward and downward wall flow. The upward flow recirculates into the jet forming a continuous loop, also known as the upper roll. The flow in this loop can be thought of as a turbulent flow in a pipe joined at both ends and bounded by the narrowface, liquid layer, submerged entry nozzle and jet. The equivalent diameter of this pipe would be one-fourth the wideface width (w) of the continuous caster. Since the loop length is infinite, the turbulent flow in this pipe can be considered fully developed with the boundary layer thickness equaling one half the pipe diameter or one eights the wideface width of the continuous caster. For fully developed turbulent pipe flow the following correlation between axial velocity component and distance from the wall can be made

$$u^+ = \frac{1}{m}\ln(1+my^+)+C \qquad (8)$$

This correlation is obtained from the Reynolds averaged Navier-Stokes equations (Chapter 4 - [48]) where

$$u^+ = u/(\sqrt{\frac{t_b}{r}})$$

† See appendix A

$y+ = y/(\frac{m}{\sqrt{t_b r}})$

k = Von-Karman constant = 0.4

C = Constant = 7.8 for smooth wall (This corresponds to the value of 5.5 for the modified form of equation (8) in Chapter 4 - [48]). Using these values equation (8) transforms to

$$u = 2.5\sqrt{\frac{t_b}{r}}\ln(1+0.4\ y/(\frac{m}{\sqrt{t_b r}})) + 7.8\sqrt{\frac{t_b}{r}} \qquad (9)$$

Equation (9) relates the horizontal component of steel velocity below the flux layer to the distance from the liquid layer i.e. it yields the profile of the steel flow past the liquid layer. The steel bulk velocity(V_o) is the velocity just outside the boundary layer or the u for a y in equation (9) of W/8. Using equation (9) an average interface shear stress(τ_b) can be computed for each steel bulk velocity (u at y = W/8 or V_o). A liquid steel density (ρ) of 7800 kg/m^3 and viscosity (μ) of 0.7x10^{-6} Pa-s are assumed.

Figure 5.14 is a plot of steel-flux interface shear stress variation with V_o. Due to the logarithmic relation the horizontal velocity will vary very gradually with distance from the liquid layer i.e. the steel flow past the liquid layer has a very flat profile. Thus a wide variation in the specified boundary layer thickness (y at u=V_o) will not change the steel bulk velocity significantly. This is found to be true particularly for V_o as seen in the results for two different boundary layer thicknesses of W/4 and W/8 respectively. The slope of the curve increases with increasing V_o implying that the shear stress increase with V_o is larger at higher V_o.

A direct correlation between steel bulk velocity and steel-flux interface velocity cannot be obtained as it depends on μ and H. Figure 5.15 is a plot of steel-flux interface velocity as a function of steel bulk velocity for H of 20mm and μ in the range 0.1 to 1 Pa-s. Increasing liquid layer viscosity (μ) is found to decrease the steel-flux interface velocity for a given steel bulk velocity. This follows from equation (7) where increasing μ for a given H and V_o (or τ_b) decreases U in the same proportion. In the earlier discussion on the effect of viscosity on heat flux for a given U (section D results and discussion), increasing μ by 10% was found to decrease heat flux by 2%. For the same V_o or τ_b increasing μ by 10% will decrease U by 10%. The effect of this on heat flux will depend on the value of U relative to the critical velocity for the known flux properties and casting conditions. For sub-critical U the heat flux will increase whereas for high post-critical values it will decrease. Thus for a given V_o a 10% increase in μ may decrease or increase the overall heat flux. Figure 5.16 is a similar plot of steel-flux interface velocity variation with steel bulk velocity for μ of 0.1 Pa-s and H of 20 and 30mm. Increasing H is seen to increase the steel-flux interface velocity for a given steel bulk velocity in accordance to equation (7). This increase in U could, as mentioned above, decrease or increase the heat flux. The effect of increasing H for a given U (section E of results and discussion) depends on μ, k, H and U. Thus the effect of increasing H on overall heat flux, for a given steel bulk velocity (V_o), depends on μ, k, H and U. In summary while considering the effect of change in viscosity or liquid layer thickness the steel-flux interface velocity needs to be re-computed from equation (7) using the new viscosity or liquid layer thickness.

5.8 Summary

Natural convection can substantially affect the fluid flow and heat transfer in liquid flux layers of continuous casters. In the absence of flow in the liquid steel beneath and Ra in excess of 1707, natural convection flow cells are formed in the liquid layer, increasing caster top surface heat transfer over that for pure conduction. In addition the heat transfer through the flux layer is highly uneven consisting of local peaks where the vertical thermal plumes of the convection cells impinge on the top and bottom surfaces of the flux layer. The natural convection flow is a function of Rayleigh(Ra) and Prandtl(Pr) numbers, the flow strength and heat transfer increasing with Ra. The steel flow beneath the liquid layer shear drives the steel-flux interface in the direction of the steel flow, decreasing the number of cells and the overall heat transfer through the liquid layer. Beyond a critical steel-flux interface velocity all the natural convection cells merge, a single recirculation region is formed and natural convection ceases to affect the fluid flow and heat transfer. This critical velocity increases with both Ra and Pr.

In the present work the variation of heat flux through the liquid layer with thermal conductivity (k), liquid layer viscosity (μ), temperature difference across the liquid layer (ΔT) and liquid layer thickness (H) has been studied. A 10% increase in k was found to increase overall heat transfer by 6-10% with the larger increase for lower viscosity liquid. A 10% increase in μ was found to decrease overall heat transfer by 2% for a given steel-flux interface velocity (U). However, increasing μ decreases U for a given steel bulk velocity (V_o) proportionately and the corresponding effect on heat flux depending on the exact conditions. Thus the change in U with changing μ must be taken into account in addition to the direct 2% for a 10% μ increase. A 10K increase in ΔT increases the overall heat transfer by 3-4%, this increase being independent of the other variables. The effect of increasing H depends on Ra. For low Ra (<<100000) increasing H increases the heat transfer. For Ra close to 100000 increase in H decreases the heat transfer. The exact change depends on the steel-flux interface velocity and an estimate can be obtained from figures 5.9 and 5.10. Similar to the effect of changing μ increasing H affects U except increasing it. This in turn changes the heat transfer. Thus before computing the effect of H its effect on U must be accounted for.

The steel-flux interface velocity (U) is found to vary linearly with the average interface shear (τ_b) independent of the Ra and Pr. Using basic knowledge of boundary layer flow a relationship between τ_b and steel bulk velocity (V_o) has been obtained (figure 5.14). Knowing V_o from mold flow calculations, figure 5.14 yields the interface shear stress and using equation (7) the steel-flux interface velocity can be computed for a given μ and H. Comparing this velocity with the critical value for the known flux properties and casting conditions qualitative information about the fluid flow and heat transfer in the liquid layer can be obtained (see section B of model validation and section B of results and discussion). This velocity can be used to compute the overall heat transfer rate through the flux layer (figure 5.8) and the information for variation of overall heat flux with k, μ, H and ΔT (see sections C-F of results and discussion).

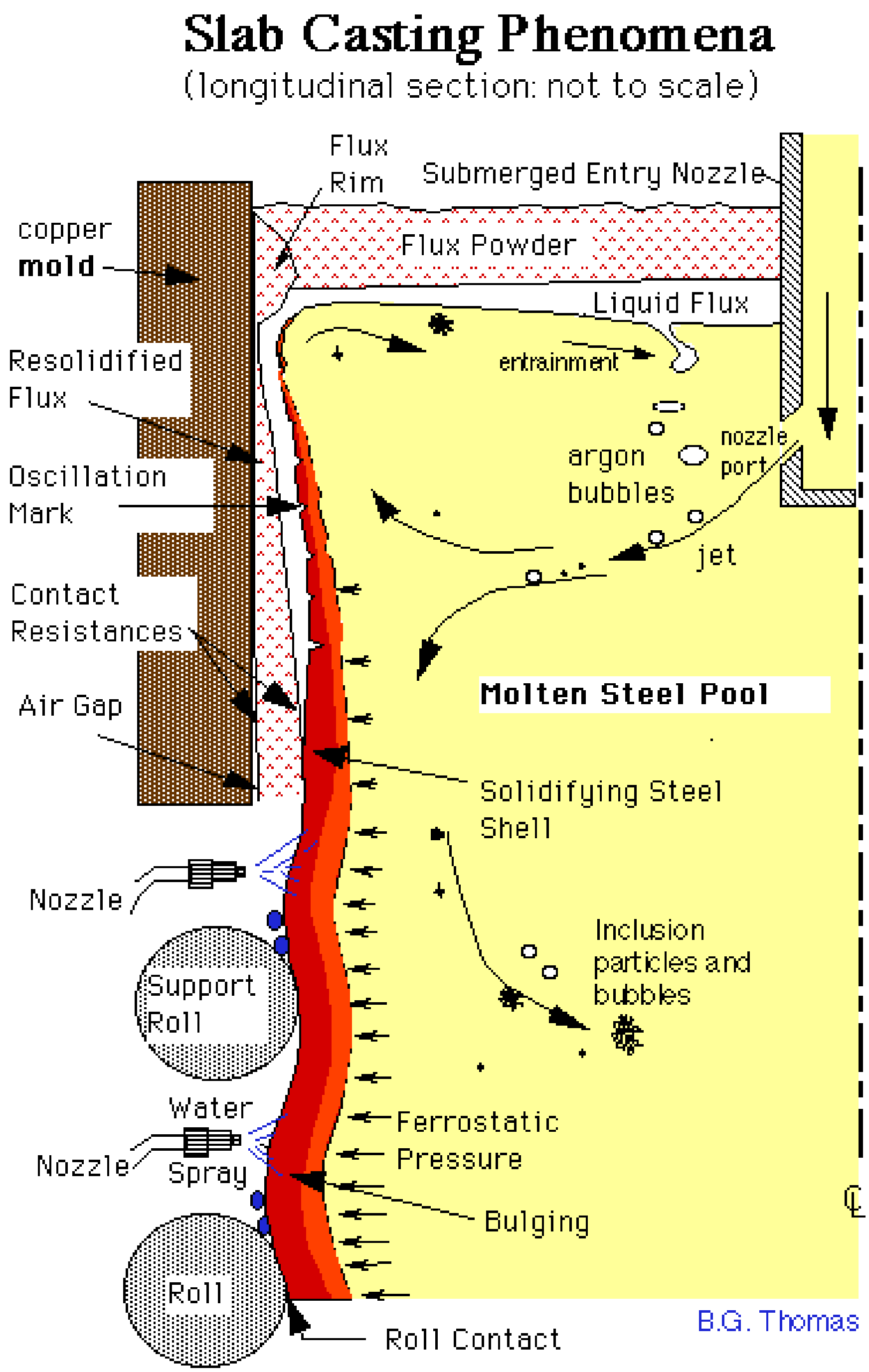

Figure 5.1 Slag layer in the continuous casting process

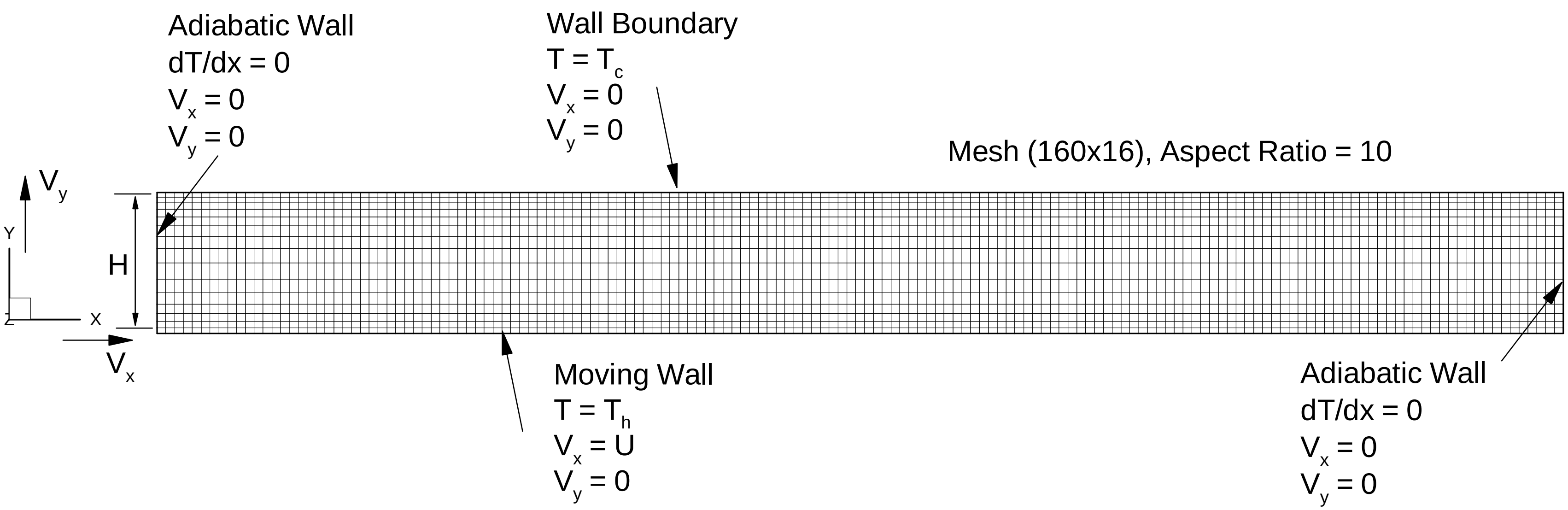

Figure 5.2 Computational domain with mesh and boundary conditions

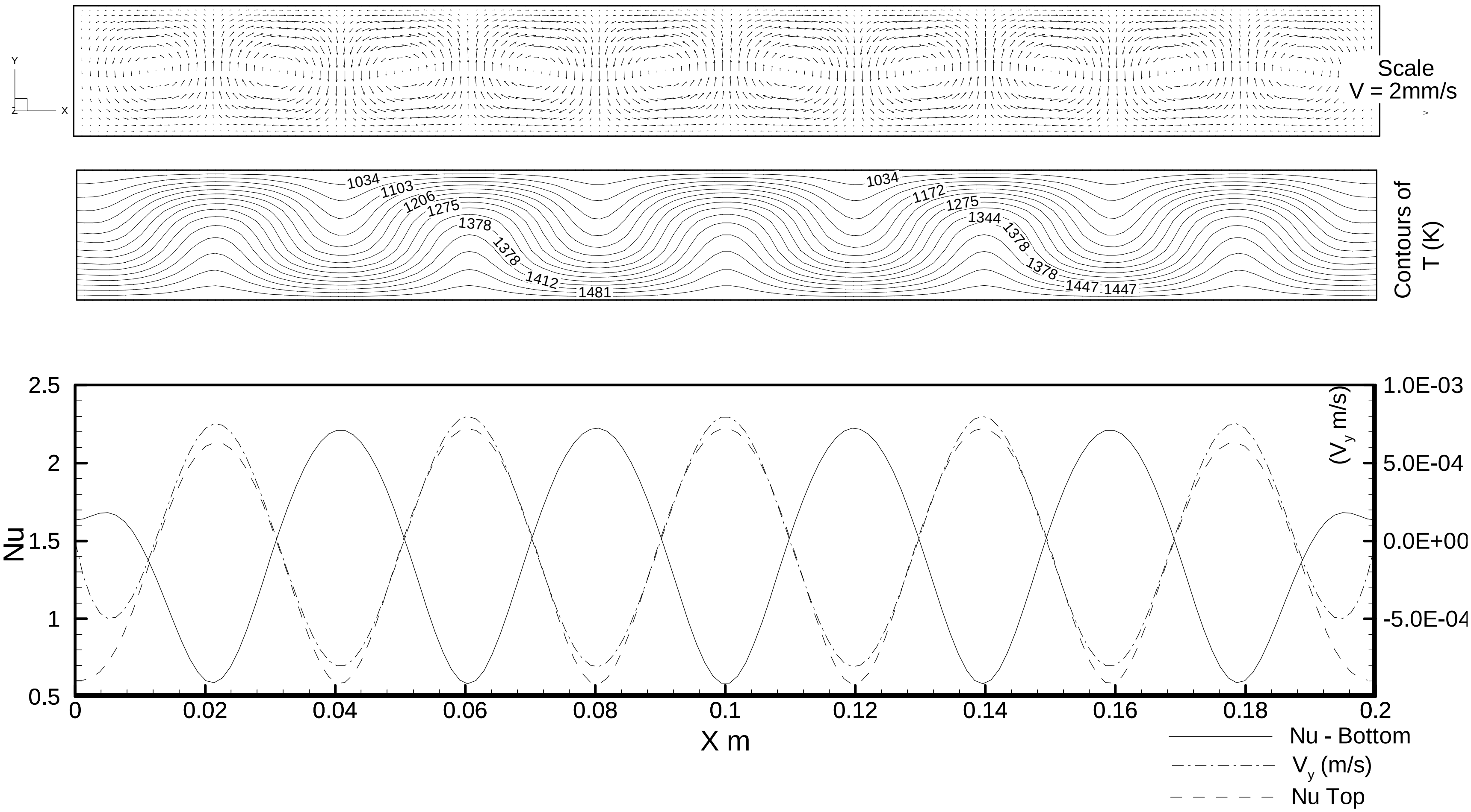

Figure 5.3 Velocity vector, temperature contour, Nu and V_y profiles for U = 0, μ = 0.51 Pa-s, k = 10.18 W/mK

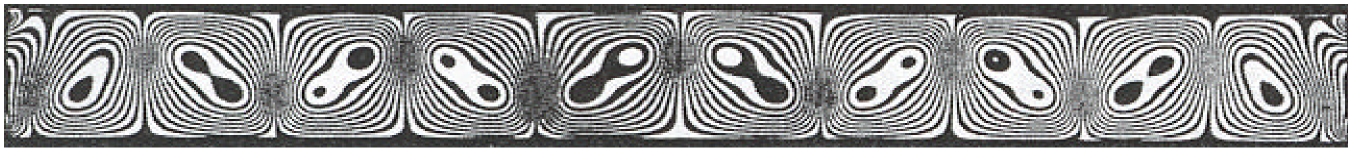

Oertel measurement (1988)

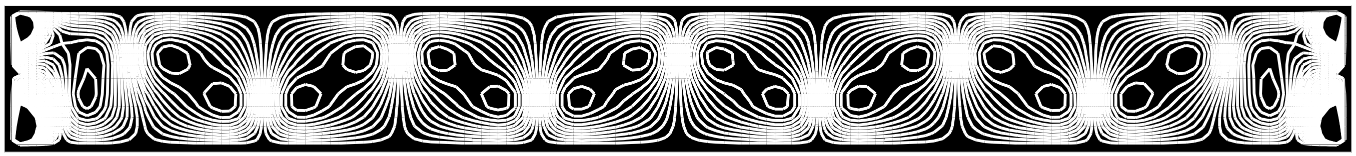

FIDAP

Figure 5.4 Comparison of contours of horizontal density gradients (calculated Vs experimental interferogram)

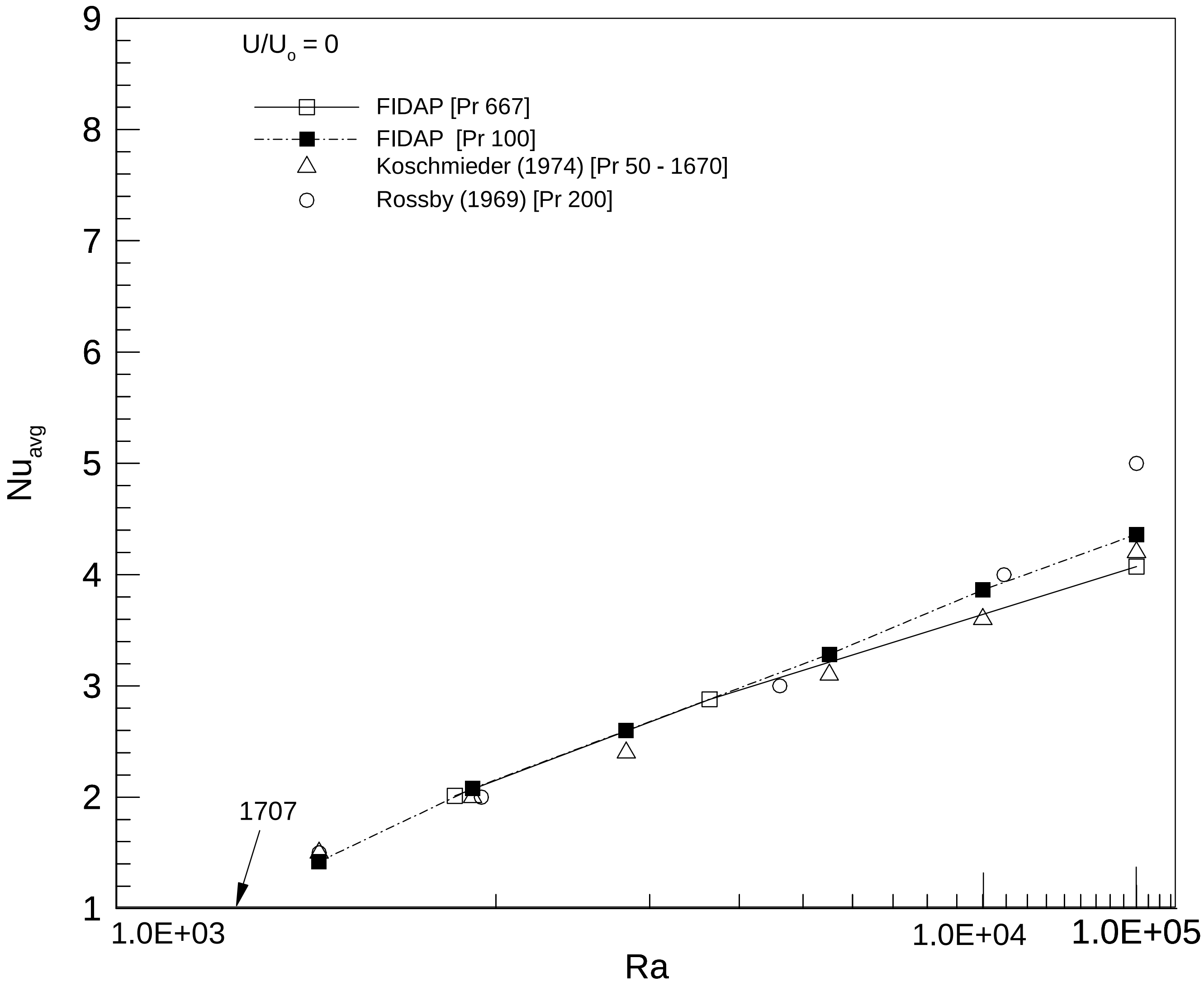

Figure 5.5 Variation of Nu_{avg} with Ra (comparison of FIDAP with experimental results)

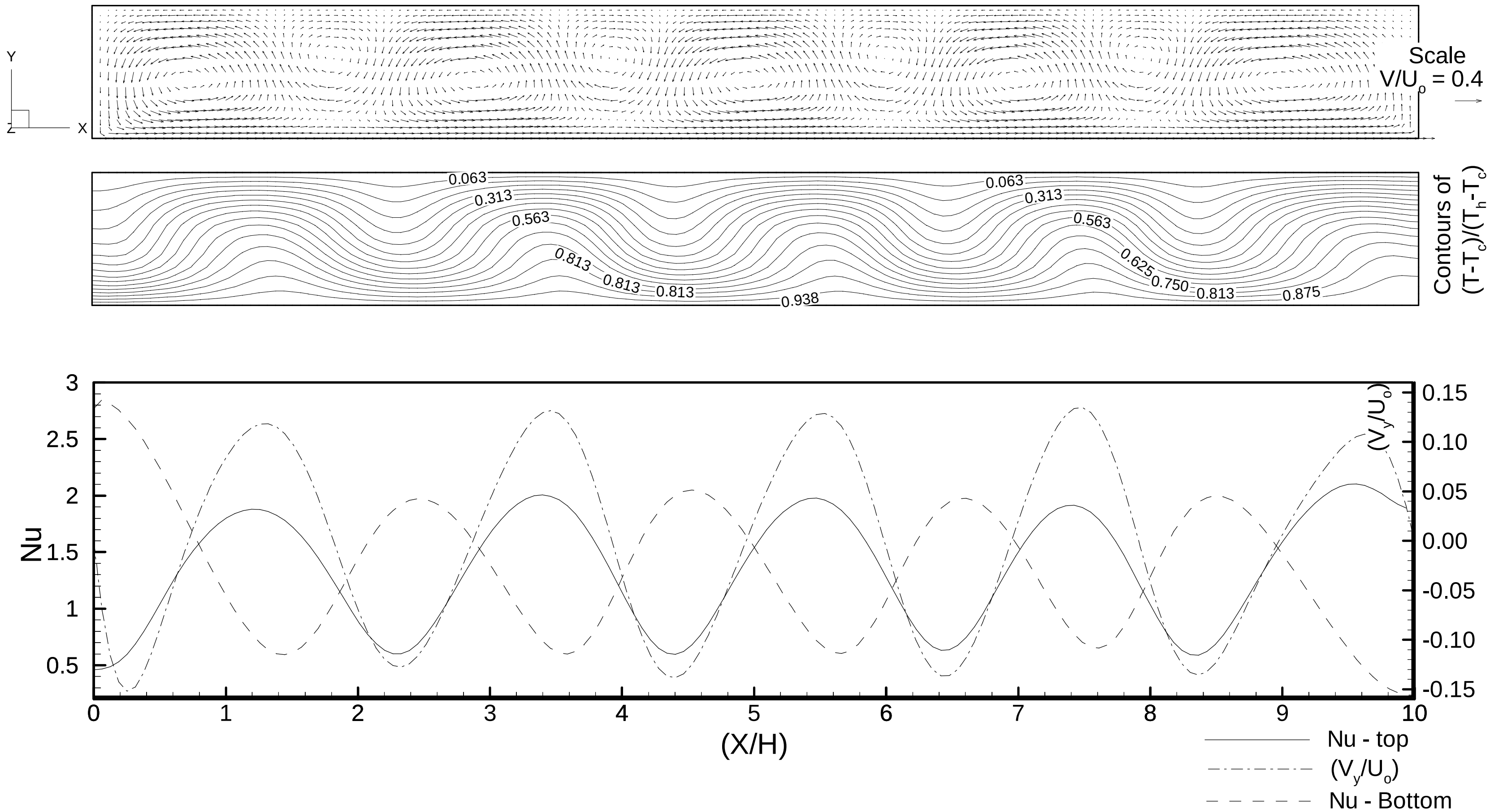

Figure 5.6 Velocity vector, temperature contour, Nu and V_y profiles for U = 1.25 mm/s, μ = 0.51 Pa-s, k = 10.18 W/mK

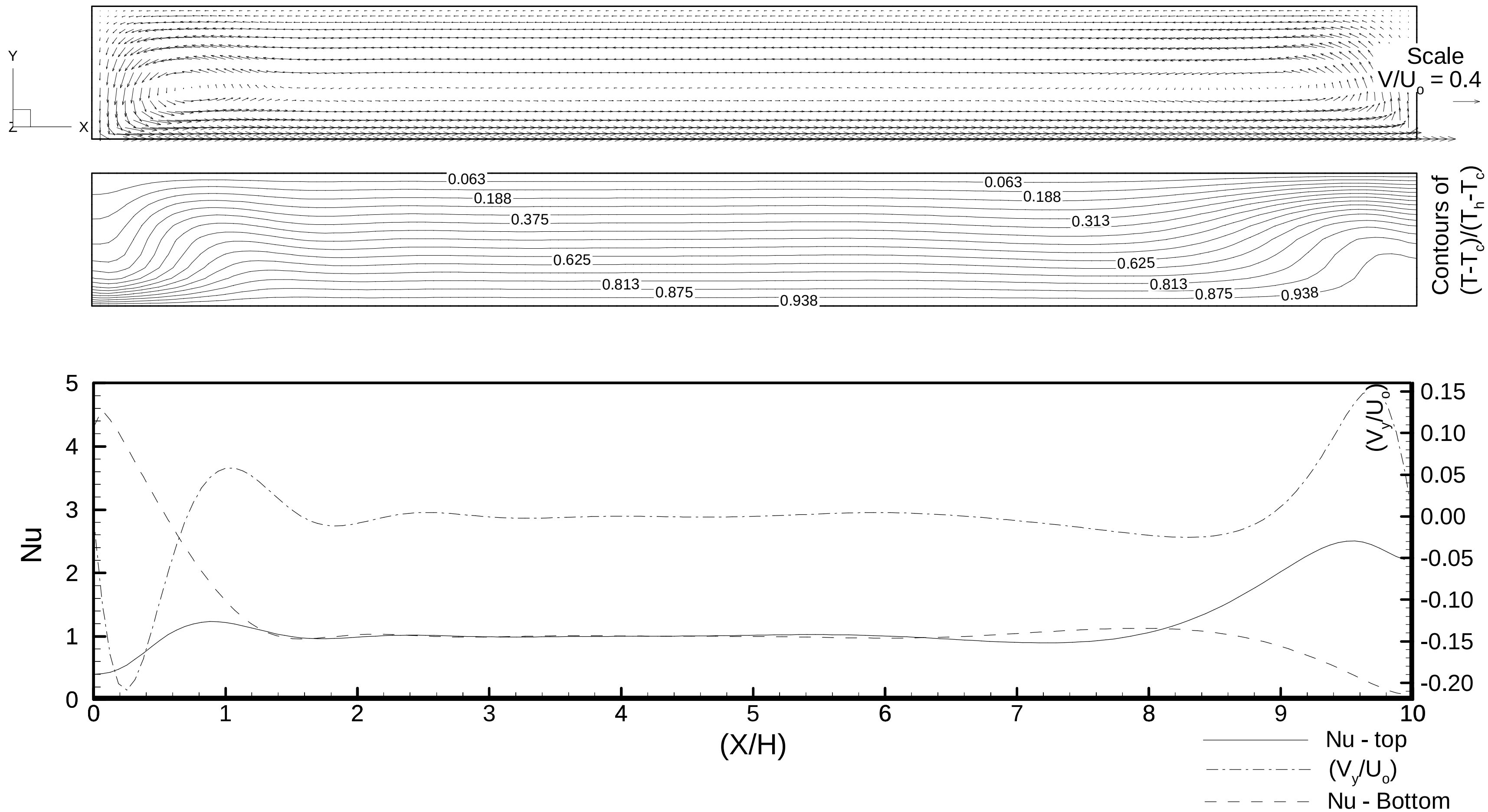

Figure 5.7 Velocity vector, temperature contour, Nu and V_y profiles for U = 3 mm/s, μ = 0.51 Pa-s, k = 10.18 W/mK

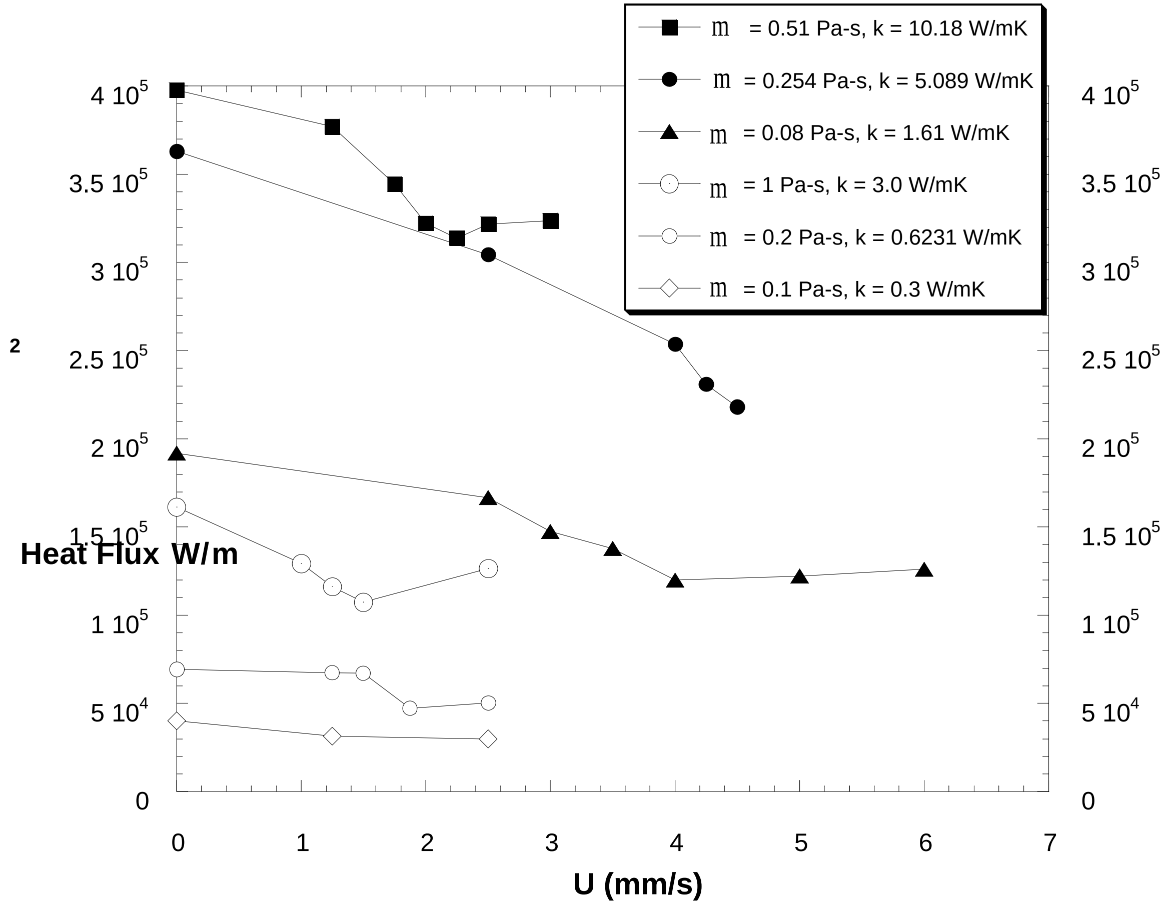

Figure 5.8 Heat flux as a function of μ, k and U

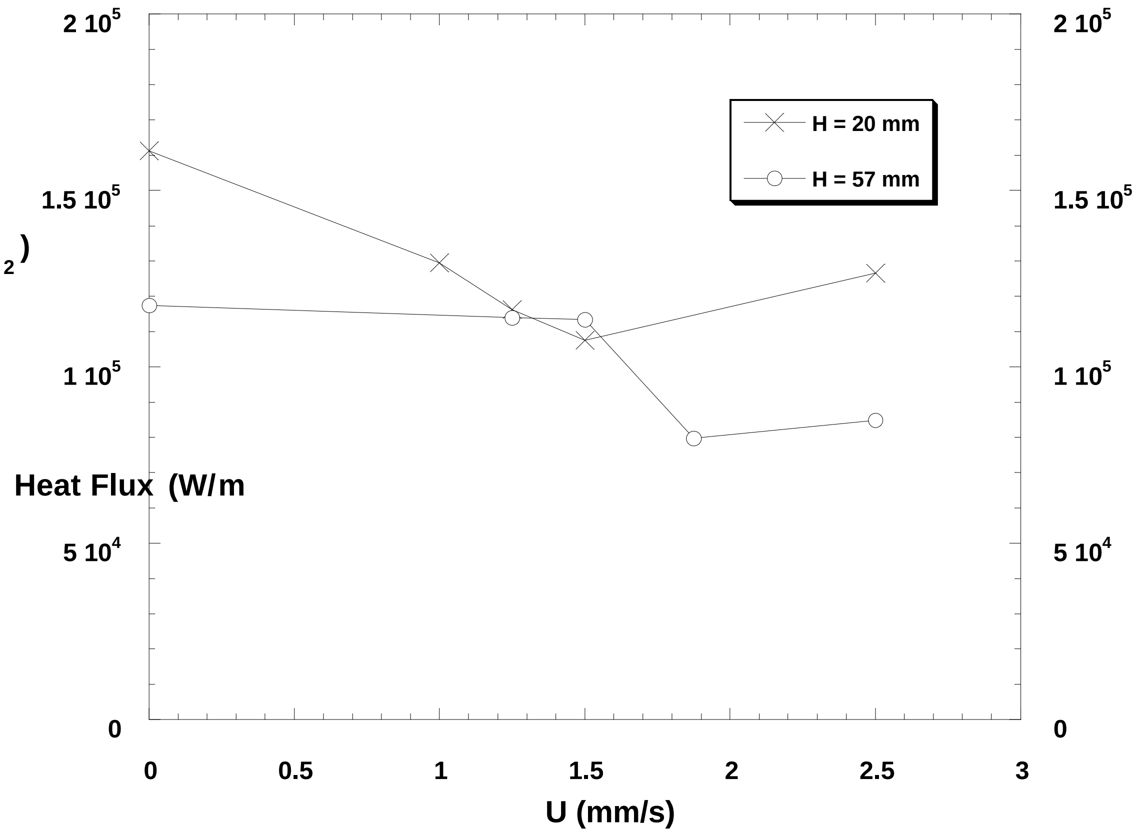

Figure 5.9 Heat flux(W/m^2) as a function of U and H for μ = 1 Pa-s and k = 3 W/mK

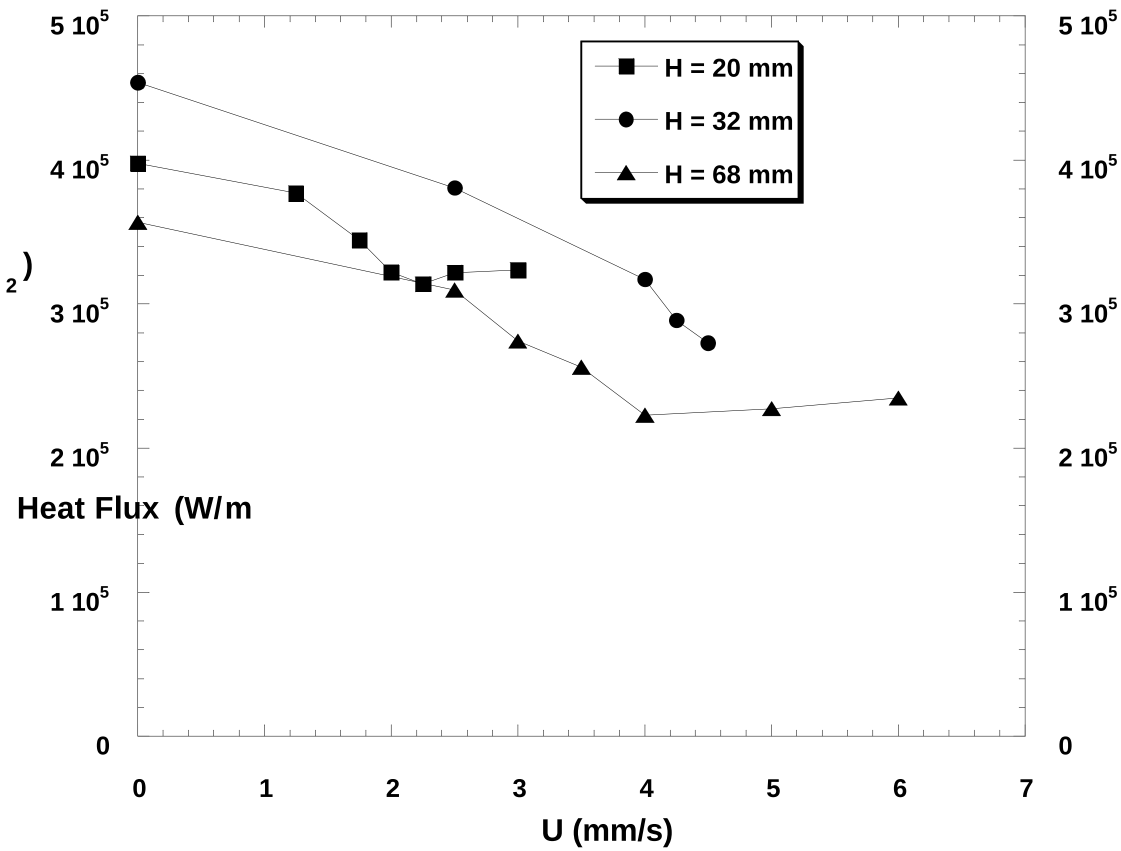

Figure 5.10 Heat flux(W/m^2) as a function of U and H for μ = 0.51 Pa-s and k = 10.18 W/mK

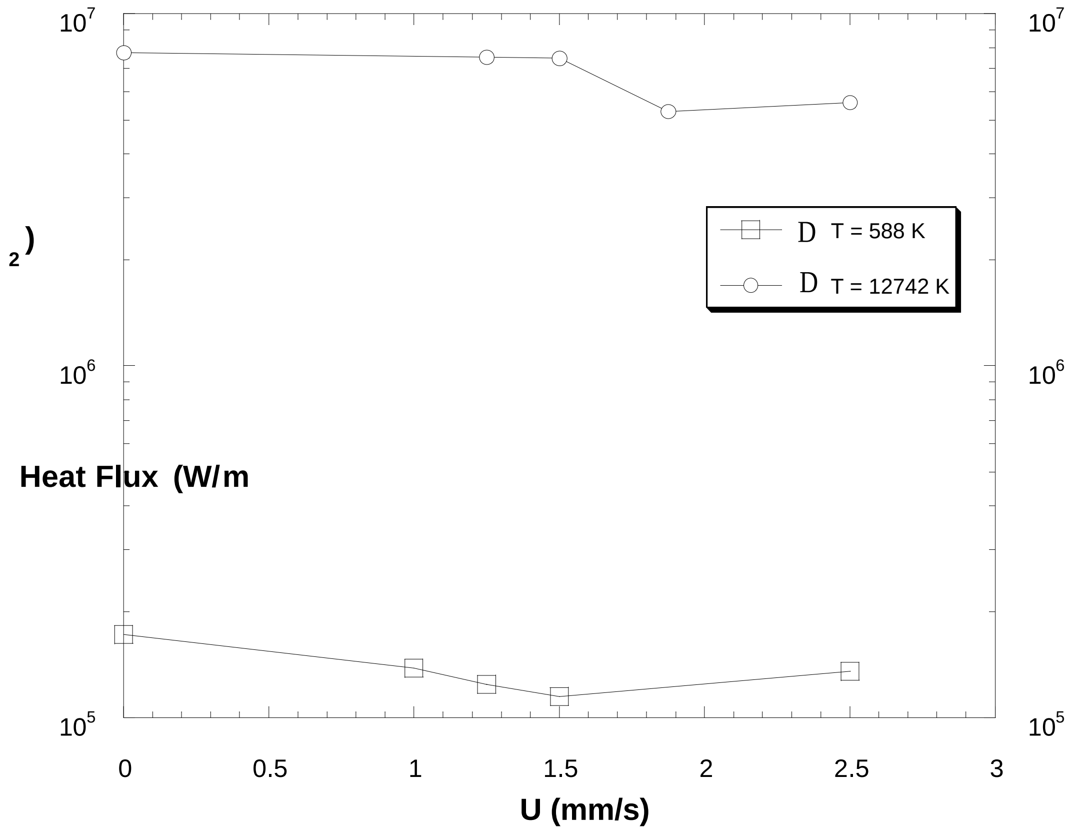

Figure 5.11 Heat flux(W/m^2) as a function of U and ΔT for μ = 1 Pa-s and k = 3 W/mK

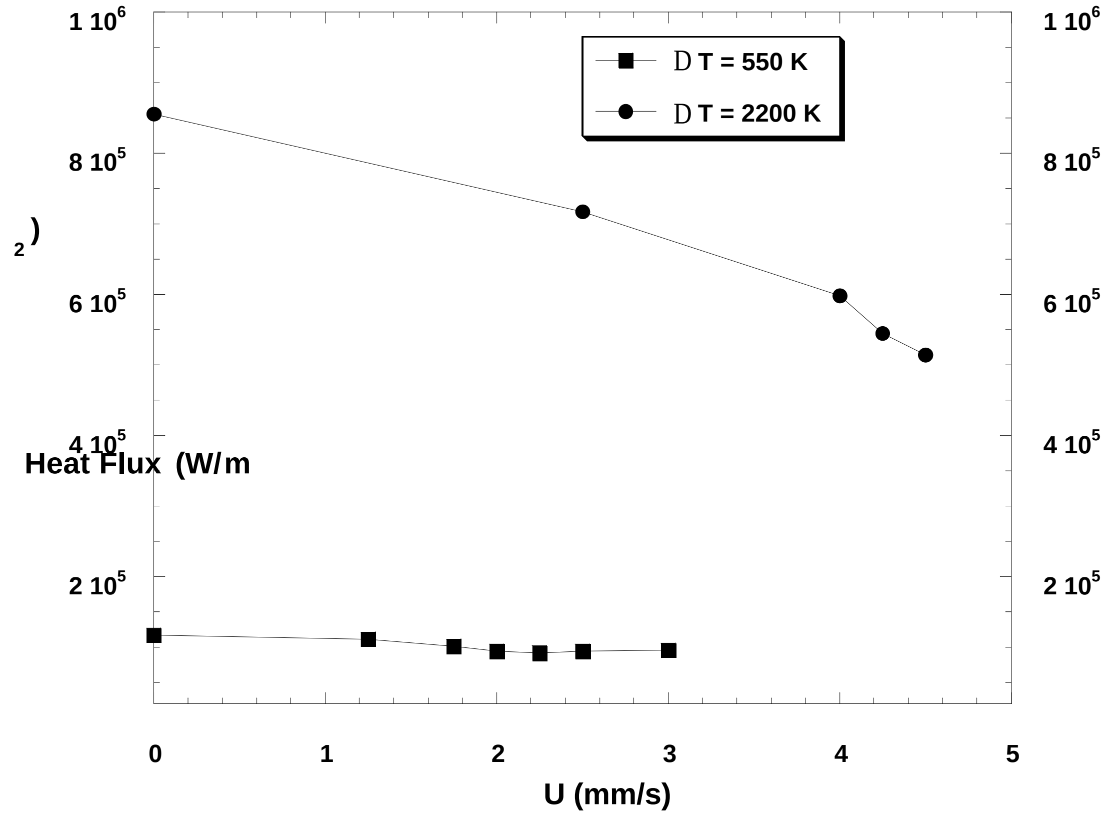

Figure 5.12 Heat flux(W/m^2) as a function of U and ΔT for μ = 0.51 Pa-s and k = 10.18 W/mK

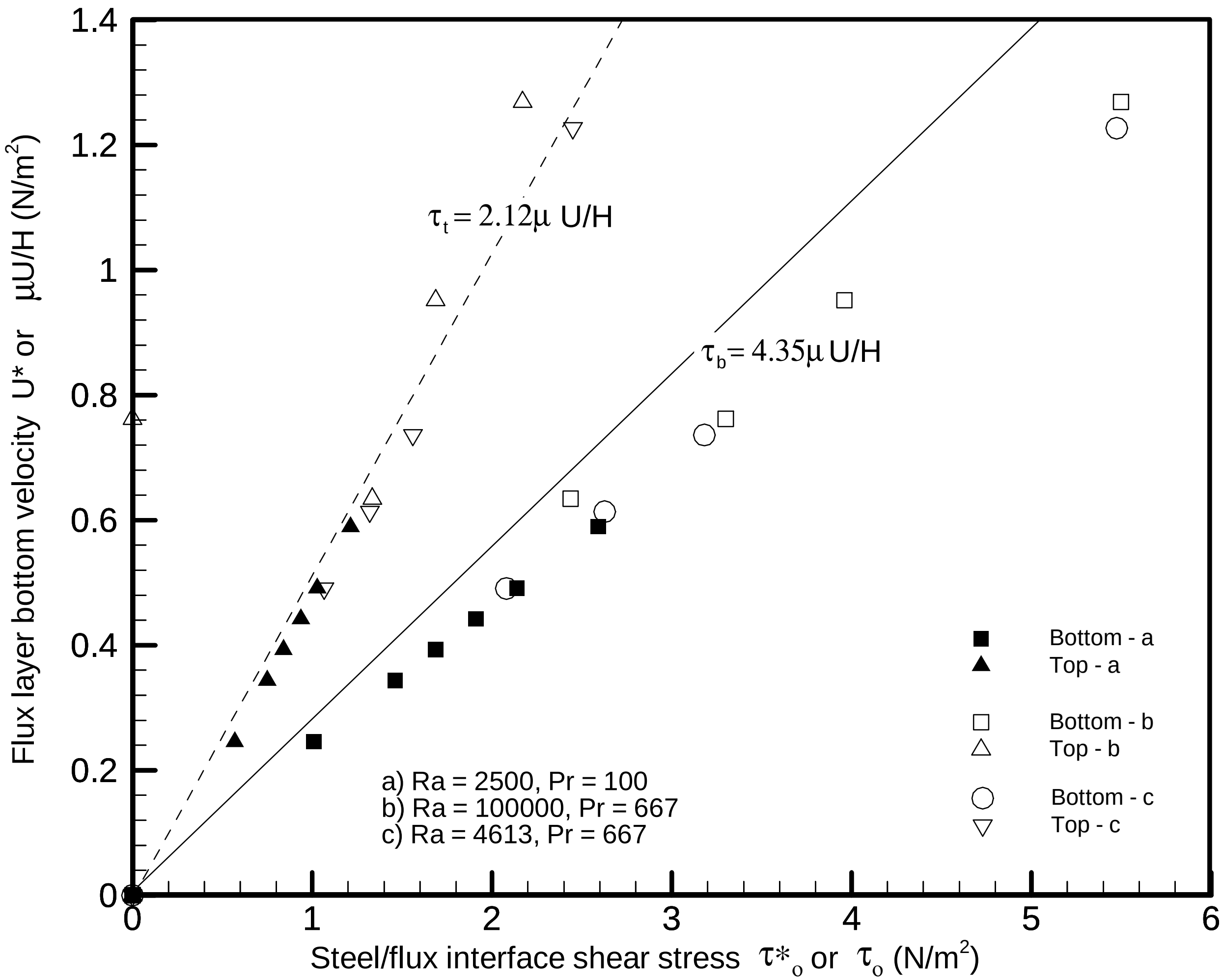

Figure 5.13 Relation between steel-flux interface velocity and interface shear stress

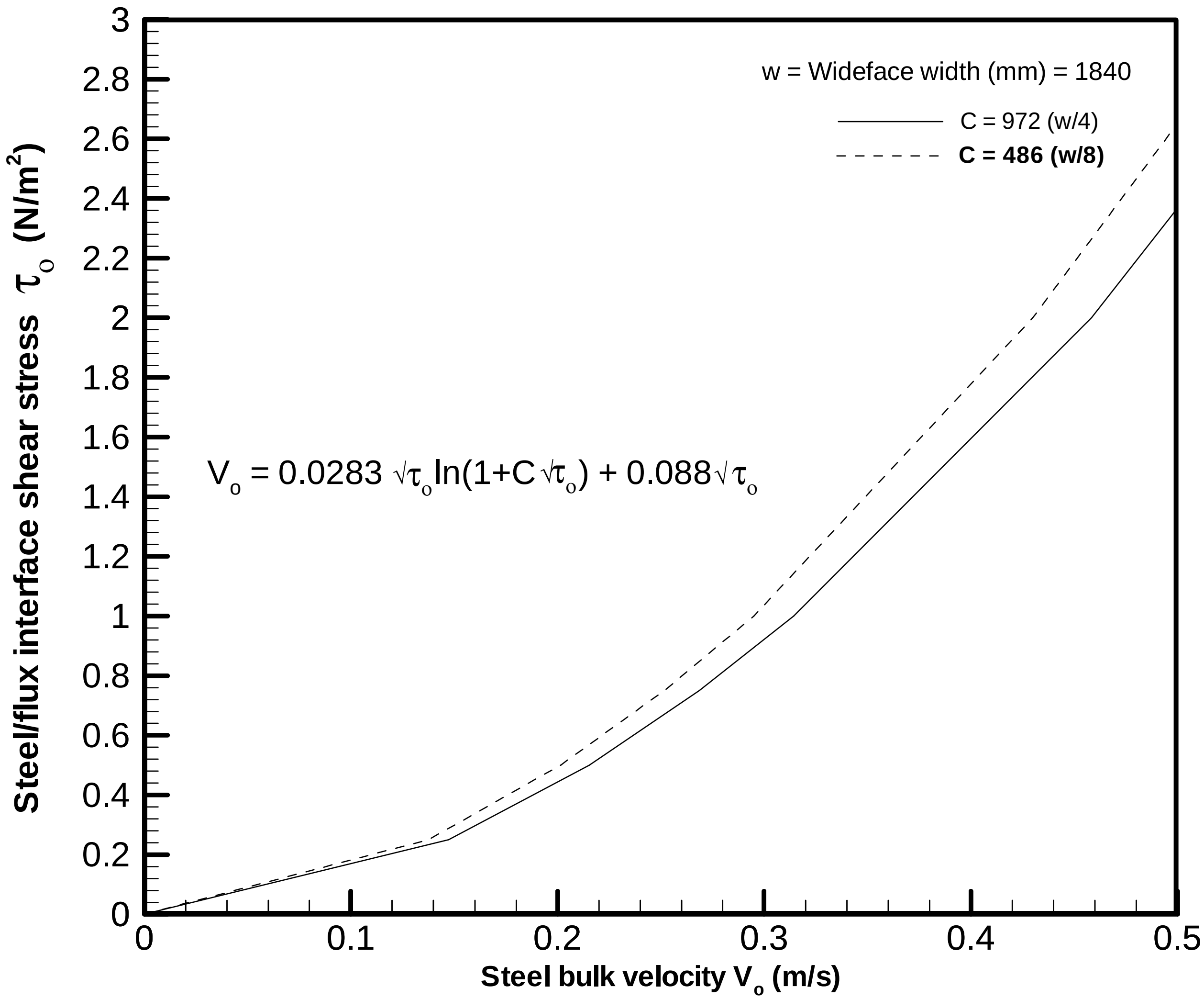

Figure 5.14 Relation between steel-flux interface shear stress and steel bulk velocity

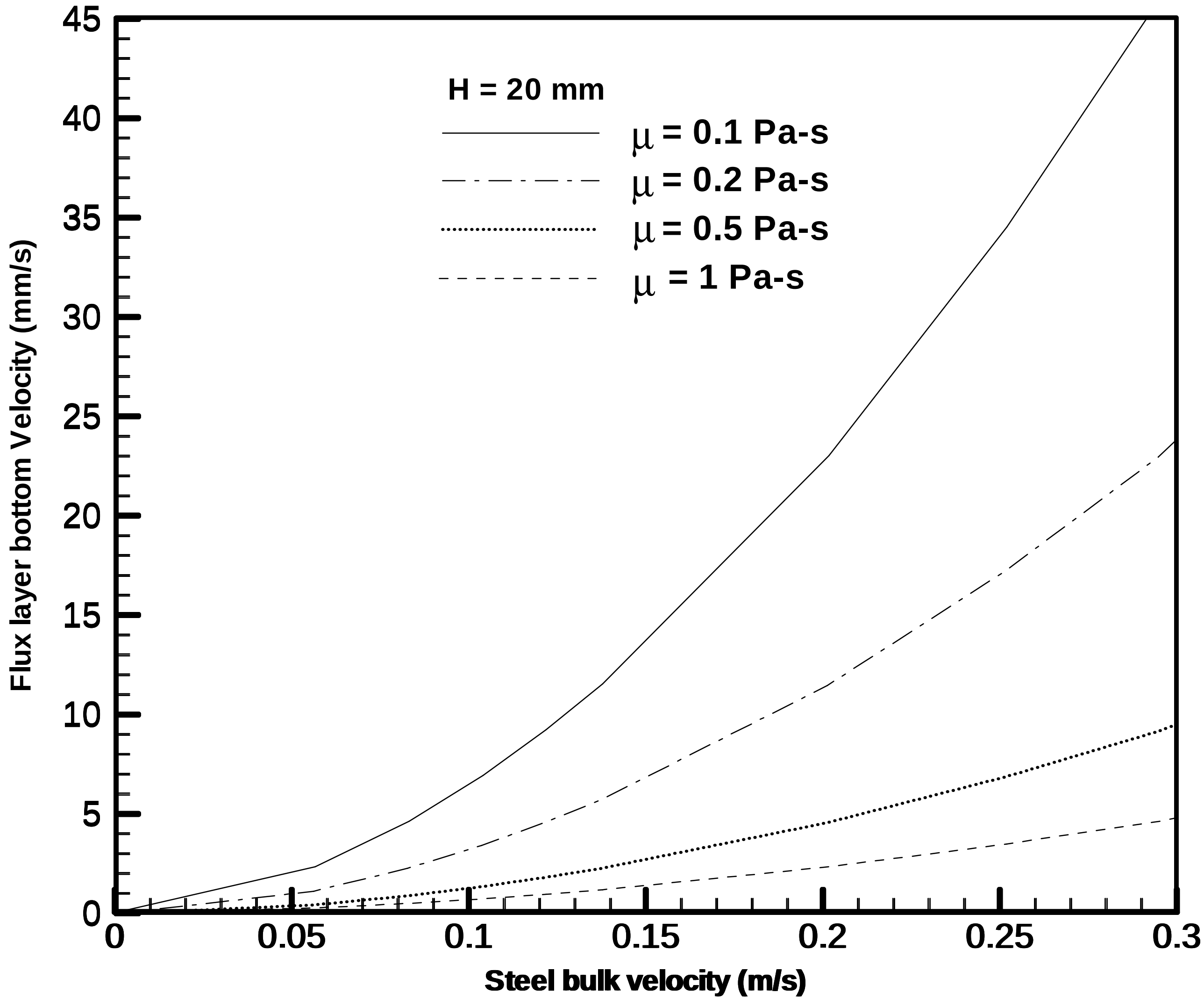

Figure 5.15 Flux layer bottom velocity vs steel bulk velocity for different viscosities

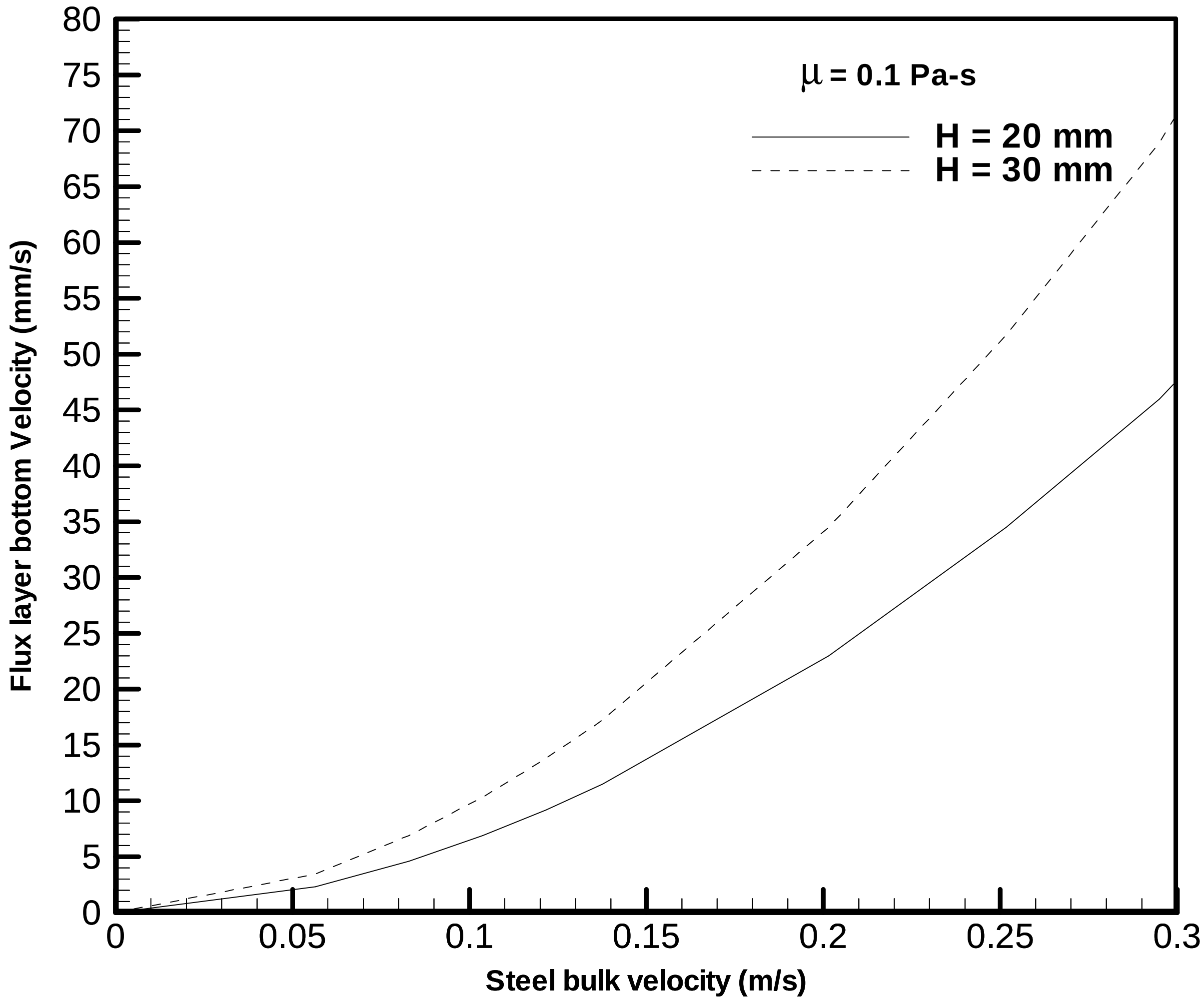

Figure 5.16 Flux layer bottom velocity vs steel bulk velocity for different liquid layer thicknesses

CHAPTER 6. CONCLUSIONS

The objective of this work was to study the fluid flow and heat transfer in continuous casting molds. Particle Image Velocimetry (PIV) measurements and Large Eddy Simulations (LES) of a water model of the continuous caster were used to study the flow transients in the mold region. Electromagnetic sensors (MFC) mounted on the mold of a caster provided further information about the flow pattern and velocities. Finite element simulations were done to study the fluid flow and heat transfer in the liquid flux layer above the steel flow in the mold, for a wide range of flux properties and casting conditions. Together these studies provide a better understanding of flow and heat transfer in continuous casting molds, both qualitative and quantitative, which can be used to improve process control and prevent defect formation.

The swirl in the jet at the nozzle port outlet is found to persist at least halfway across the mold. The overall angle of the jet, in the casting direction and into the caster depth, varies considerably with a time scale of around 7s. This wide variation is the probable cause of the appearance of periods of high velocities (three to four times the mean value) close to the water surface, which enhances the shear entrainment of the liquid flux layer. Simulating the flow without swirl does not capture either the large variations in jet angle or the periods of high velocity near the water surface. The jet after impingement spreads so there is more flow along the wide faces than in the center plane, with this bias gradually diffusing until there is nearly uniform flow into the caster depth along the top surface. This phenomenon manifests itself as a region of low velocity flow in mean velocity vector plots of the center plane. A small recirculation region is observed in both simulation and experiment, at the intersection of the narrow face and top surface. The flow from the upper wall jet is unable to follow the sharp bend, shear driving a recirculation region in this corner. The reversed low velocity flow near the corner, resulting from the recirculation region, will affect the shear driven motion of the liquid flux layer on the surface of the caster. In addition it is significant to meniscus solidification and feeding of flux into the gap between the shell and narrowface.

Considerable, persistent, asymmetry between the two lower rolls is observed in experiment. The flow in the lower rolls is not stationary but consists of a sequence of flow phenomena, which repeat at irregular intervals. One of these involves a diversion of flow from the lower wall jet to the flow entrained by the jet from below the nozzle results in the formation of a flow structure, which then expands downwards and finally merges into the lower roll. The appearance of this flow structure in experiment and simulation with significantly different inlet conditions, confirms its cause as instabilities inherent in any turbulent flow and not by fluctuations in the flow field at the inlet of the mold. This feature is important for particle inclusion and bubble entrapment defects.

The simulation of the MFC sensor signals illustrates the great importance of locating the sensor in a stable region of the flow if accurate velocities are to be extracted. Sensors positioned in the current location just beneath the top surface should accurately output both the roll pattern and velocity history. The individual probes of sensors positioned deep in the recirculation zone experience very different transient flow fields, so cannot be relied upon to produce accurate velocities.

Natural convection was found to substantially affect the fluid flow and heat transfer in liquid flux layers of continuous casters. In the absence of flow in the liquid steel beneath and Ra in excess of 1707, natural convection flow cells are formed in the liquid layer, increasing caster top surface heat transfer over that for pure conduction. In addition the heat transfer through the flux layer is highly uneven consisting of local peaks where the vertical thermal plumes of the convection cells impinge on the top and bottom surfaces of the flux layer. The natural convection flow is a function of Rayleigh(Ra) and Prandtl(Pr) numbers, the flow strength and heat transfer increasing with Ra. The steel flow beneath the liquid layer shear drives the steel-flux interface in the direction of the steel flow, decreasing the number of cells and the overall heat transfer through the liquid layer. Beyond a critical steel-flux interface velocity all the natural convection cells merge, a single recirculation region is formed and natural convection ceases to affect the fluid flow and heat transfer. This critical velocity increases with both Ra and Pr.

In the present work the variation of heat flux through the liquid layer with thermal conductivity (k), liquid layer viscosity (μ), temperature difference across the liquid layer (ΔT) and liquid layer thickness (H) has been studied. A 10% increase in k was found to increase overall heat transfer by 6-10% with the larger increase for lower viscosity liquid. A 10% increase in μ was found to decrease overall heat transfer by 2% for a given steel-flux interface velocity (U). However, increasing μ decreases U for a given steel bulk velocity (V_o) proportionately and the corresponding effect on heat flux depending on the exact conditions. Thus the change in U with changing μ must be taken into account in addition to the direct 2% for a 10% μ increase. A 10K increase in ΔT increases the overall heat transfer by 3-4%, this increase being independent of the other variables. The effect of increasing H depends on Ra. For low Ra (<<100000) increasing H increases the heat transfer. For Ra close to 100000 increase in H decreases the heat transfer. The exact change depends on the steel-flux interface velocity and an estimate can be obtained from results presented. Similar to the effect of changing μ increasing H affects U except increasing it. This in turn changes the heat transfer. Thus before computing the effect of H its effect on U must be accounted for.

The steel-flux interface velocity (U) is found to vary linearly with the average interface shear (τ_b), independent of the Ra and Pr. Using basic knowledge of boundary layer flow a relationship between τ_b and steel bulk velocity (V_o) has been obtained. Knowing V_o from mold flow calculations, the steel-flux interface velocity can be computed for a given μ and H. Comparing this velocity with the critical value for the known flux properties and casting conditions qualitative information about the fluid flow and heat transfer in the liquid layer can be obtained. The overall heat transfer rate through the flux layer and the information for variation of overall heat flux with k, μ, H and ΔT can be computed using the results of this study.

CHAPTER 7. RECOMMENDATIONS FOR FUTURE WORK

7.1 Fluid flow in the mold region

- The PIV measurements indicate the persistence of the swirl in the jet at least halfway across the mold. This swirling jet is seen to have large variations in angle, which has been correlated to the appearance of periods of high velocities close to the top surface. These high velocities are significant to shear entrainment of the liquid flux layer. There is a need for simulations of the fluid flow in the mold region with inlet swirl to study this correlation.
- The fluid flow in the lower roll has been found to be significantly asymmetric despite symmetry of geometry and inlet flow to the mold. The cause of this asymmetry is unknown and needs to be investigated by simulating both halves of the mold together.
- Parametric studies need to be conducted to study the effect of various process variables including caster dimensions, casting speed, argon gas injection etc. on the flow transients documented in this work.

7.2 Fluid flow and heat transfer in the liquid flux layer

- The present work assumes a uniform viscosity and thickness throughout the liquid flux layer. This viscosity however, increases with decrease in temperature from the bottom to the top of the flux layer. Also the liquid flux layer thickness varies, with a maximum in the center. The effect of these two differences on the results needs to be investigated.
- Only two-dimensional effects are considered in this study. At higher Ra the flow becomes three-dimensional, necessitating three-dimensional simulations.

- The level fluctuations caused by the turbulent, transient flow beneath the liquid flux layer can increase the mixing effects in liquid flux layers requiring further study.

APPENDIX A

CALCULATION OF AVERAGE SHEAR STRESS AT UPPER AND LOWER WALLS OF THE LIQUID FLUX LAYER

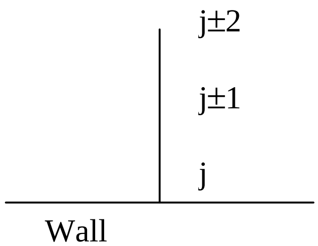

du/dy_i = ((1./c**2)*(u(i,j±2) - u(i,j)) - (1./a**2)*(u(i,j±1) - u(i,j)))/(1./c - 1./a) where

a = y(j±1) - y(j)

b = y(j±2) - y(j±1)

c = a + b

This equation is obtained by writing a Taylor expansion of (j±1) in terms of (j) and (j±2) in terms of (j) and eliminating second order derivatives.

$\tau_i = \mu\, du/dy$

$\tau_{b/t} = \sum_{i=1}^{n} t_i$ where n is the number of elements along the bottom/top surface

This formula can be used to compute the local velocity gradient at any wall providing j in the above equations is substituted for the wall co-ordinate and the positive sign is used for the lower wall, the negative being used for the upper wall.

REFERENCE

1. Huang, X. and B.G. Thomas, *Modeling of transient flow phenomena in continuous casting of steel.* Canadian metallurgical quarterly, 1998: p. 1-17.

2. McDavid, R. and B.G. Thomas, *Flow and Thermal Behavior of the Top-Surface Flux/ Powder Layers in Continuous Casting Molds.* Metallurgical Transactions B, 1996. **27B**(4): p. 672-685.

3. Panaras, G.A., A. Theodorakakos, and G. Bergeles, *Numerical Investigation of the Free Surface in a Continuous Steel Casting Mold Model.* Metallurgical and Materials Transactions B, 1998. **29B**(5): p. 1117-1126.

4. Theordorakakos, A. and G. Bergeles, *Numerical investigation of the interface in a continuous steel casting mold water model.* Metallurgical and Materials Transactions B, 1998. **29B**: p. 1321-1327.

5. Thomas, B.G., L.M. Mika, and F.M. Najjar, *Simulation of Fluid Flow Inside a Continuous Slab Casting Machine.* Metall. Trans., 1990. **21B**: p. 387-400.

6. Thomas, B.G., X. Huang, and R.C. Sussman, *Simulation of Argon Gas Flow Effects in a Continuous Slab Caster.* Metallurgical Transactions, 1994. **25B**(4): p. 527-547.

7. Gupta, D. and A.K. Lahiri, *A Water Model Study of the Flow Asymmetry Inside a Continuous Slab Casting Mold.* Met. Mat. Trans. B, 1996. **27B**(5): p. 757-764.

8. Honeyands, T. and J. Herbertson, *Flow dynamics in thin slab caster molds.* Steel Research, 1995. **66**(7): p. 287-293.

9. Gupta, D. and A.K. Lahiri, *Water-modeling study of the surface disturbances in continuous slab caster.* Metallurgical and Materials Transactions B, 1994. **25B**: p. 227-233.

10. Khodadadi, J.M., B.L. Wright, and X.K. Lan, *LDV measurements and computation of a turbulent circular jet placed non-concentrically in a confining pipe.* Metallurgical and Materials Transactions B, 1999. **30B**: p. 957-967.

11. Lan, X.K., J.M. Khodadadi, and F. Shen, *Evaluation of six k-e turbulence model predictions of flow in a continuous casting billet-mold water model using laser doppler velocimetry measurements.* Metallurgical and Materials Transactions B, 1997. **28B**: p. 321-332.

12. Xu, W.D., K.J. Jr, and J.W. Evans. *PIV physical modeling of fluid flow in the mold of continuous casting of steel*. in *The Minerals, Metals and Materials Society*. 1998.

13. Xu, D., W.K. Jones, and J.W. Evans, *The use of Particle Image Velocimetry in the physical modeling of flow in electromagnetic or direct chill casting of aluminum part II. Results of the physical model, including bag geometry, blockage and nozzle placement.* Metallurgical and Materials Transactions B, 1998. **29B**: p. 1289-1295.

14. Assar, M.A., P.H. Dauby, and G.D. Lawson. *Opening the black box: PIV and MFC measurements in a continuous caster mold*. in *Iron and Steelmaking conference*. 2000. Pittsburg: Iron and Steel Society.

15. Najjar, F.M., B.G. Thomas, and D.E. Hershey, *Turbulent Flow Simulations in Bifurcated Nozzles: Effects of Design and Casting Operation.* Metall. Trans. B, 1995. **26B**(4): p. 749-765.

16. Hershey, D.E., B.G. Thomas, and F.M. Najjar, *Turbulent Flow through Bifurcated Nozzles.* Int. J. for Numerical Methods in Fluids, 1993. **17**: p. 23-47.

17. Chanaud, R., *Observations of oscillatory motion in certain swirling flows.* Journal of Fluid Mechanics, 1965. **21**: p. 111-127.

18. Park, S. and H. Shin, *Measurements of entrainment characteristics of swirling jets.* International journal of heat mass transfer, 1993. **36**(16): p. 4409-4018.

19. Schrewe, *Continuous casting of steel*. 1989: Verlag stahleisen.

20. Aboutalebi, M.R., M. Hassan, and R.I.L. Guthrie, *Coupled turbulent flow, heat and solute transport in continuous casting processes.* Metallurgical and Materials Transactions B, 1995. **26B**: p. 731-744.

21. Panaras, G.A., A. Theodorakakos, and G. Bergeles, *Numerical Investigation of the free surface in a continuous steell casting mold model.* Metallurgical and Materials Transactions B, 1998. **29B**: p. 1117-1126.

22. Schulte, H.B.M., *et al. Study of the fluid flow in the mold for high quality slab casting*. in *ATS International Steelmaking Conference*. 1996. Paris, Dec 11-12.

23. Smagorinsky, J., *General Circulation Experiments With the Primitive Equations, General Circulation Experiments With the Primitive Equations*, . 1963, Weather Bureau: Washington. p. 99-121.

24. Madabushi, R. and S.P. Vanka, *Large Eddy Simulation of Turbulence-Driven Secondary Flow in a Square Duct.* Physics of Fluids, 1991. **3**(11): p. 2734-2475.

25. McDavid, R., *Fluid Flow and Heat Transfer Behavior of Top-Surface Flux Layers in Steel Continuous Casting*, *Fluid Flow and Heat Transfer Behavior of Top-Surface Flux Layers in Steel Continuous Casting*, . 1994, University of Illinois at Urbana-Champaign.

26. Lim, K.O., T.H. Song, and K.S. Lee, *Patterns of natural convection driven by the free surface temperature distribution in a glass melting furnace.* Glass Technology, 1998. **39**(1): p. 27-31.

27. Schrage, D.S., *A simplified model of dendritic growth in the presence of natrual convection.* Journal of Crystal Growth, 1999. **205**(3): p. 410-426.

28. Chandrashekar, S., *Hydrodynamic and Hydromagnetic Stability*. Oxford, Claredon Press, 1961.

29. Benard, H., *Les tourbillons cellularies dans une nappe liquide transportant de chaleur par convection en regime permanent.* Ann. Chim. Phys, 1901. **23**: p. 62-144.

30. Lord Rayleigh, *On convection currents in a horizontal layer of fluid when the higher temperature is on the under side.* Phil. Mag, 1916a. **32**: p. 529-546.

31. Krishnamurti, R., *Some further studies on the transition to turbulent convection.* Journal of Fluid Mechanics, 1973. **60**(2): p. 285-303.

32. Rossby, H., . 1966, Massachusetts Institute of Technology.

33. Davis, S.H., Journal of Fluid Mechanics, 1967. **30**: p. 455-478.

34. Catton, I., Journal of Heat Transfer, 1970. **92**: p. 186-188.

35. Kirchartz, K.R. and H. Oertel, *Three-Dimensional thermal cellular convection in rectangular boxes.* Journal of Fluid Mechanics, 1988. **192**: p. 249-286.

36. Stork, K. and U. Muller, *Convection in boxes: experiments.* Journal of Fluid Mechanics, 1972. **54**(4): p. 599-611.

37. Globe, S. and D. Dropkin, *Natural-Convection heat transfer in liquids confined by two horizontal plates and heated from below.* Journal of Heat Transfer, 1959. **81c**: p. 24-29.

38. Rossby, H., *A study of Benard convection with and without rotation.* Journal of Fluid Mechanics, 1969. **36**(2): p. 309-335.

39. Koschimeder, E.L. and S.G. Pallas, *Heat transfer through a shallow horizontal convecting fluid layer*. Journal of Heat Mass Transfer, 1976. **17**: p. 991-1002.

40. Mohamad, A.A. and R. Viskanta, *Laminar flow and heat transfer in Rayleigh-Benard convection with shear*. Physics of Fluids A, 1992. **4**(10): p. 2131-2140.

41. Mohamad, A.A. and R. Viskanta, *Flow structures and heat transfer in a lid-driven cavity filled with liquid and heated from below*. Experimental Thermal Fluid Science, 1994. **9**: p. 309-319.

42. *FIDAP Theory Manual*, *FIDAP Theory Manual*, , Fluid Dynamics International.

43. Davis, G.V., *Natural Convection of Air in a square cavity: A bench mark numerical solution.* International Journal for Numerical methods in fluids, 1983. **3**: p. 249-264.

44. Branion. *Mold fluxes for continuous casting*. in *Iron and Steel Society*. 1987.

45. Brimacombe, J.P., *Mold flux for continuous casting of steel*, in *Iron and Steel MakerMold flux for continuous casting of steel*, in *Iron and Steel Maker*, 1994.

46. Susa, M., K. Nagata, and K.C. Mills, *Absorption coefficients and refractive indices of snythetic glassy slags containing transition metal oxides.* Iron and Steelmaking, 1993. **20**(5): p. 372-378.

47. Taylor, R. and K.C. Mills, *Physical properties of casting powders: Part 3 Thermal conductivities of casting powders.* Ironmaking Steelmaking, 1988. **15**(4): p. 187-194.

48. Chen, C. and S. Jaw, *Fundamentals of turbulence modeling*. 1998: Taylor and Francis.